Computational modeling of atmospheric DC discharges for CO_2 conversion

Proefschrift voorgelegd tot het behalen vad de graad van doctor in de wetenschappen aan de Universiteit Antwerpen te verdedigen door

Georgi Trenchev

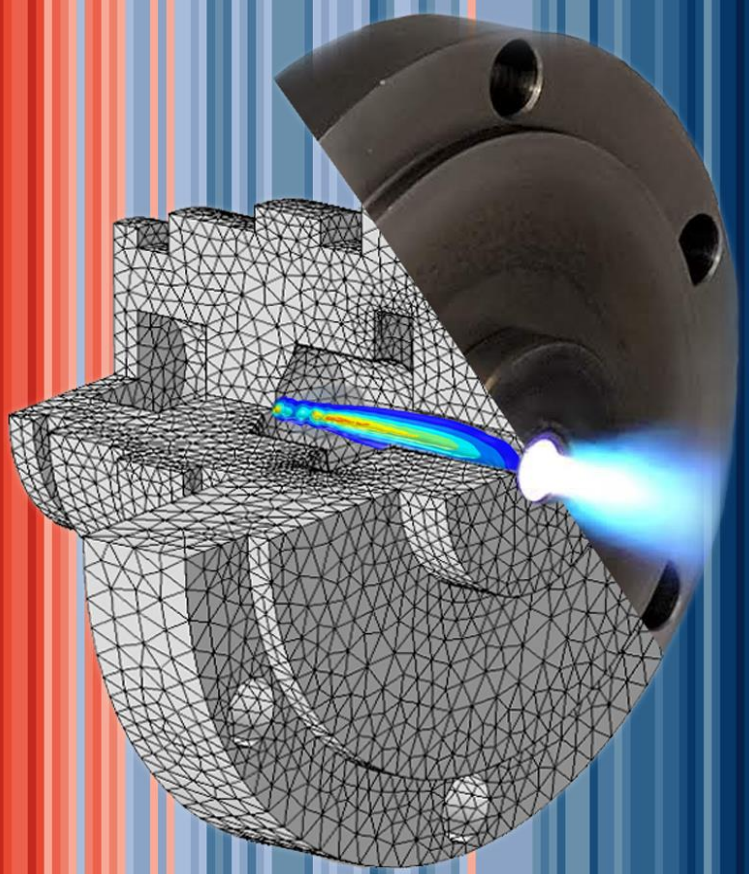

Promotor
prof. dr. Annemie Bogaerts

Faculteit Wetenschappen

Antwerpen 2019

Universiteit Antwerpen

Universiteit Antwerpen

Faculteit Wetenschappen
Departement Chemie

Computational modelling of atmospheric DC discharges for CO_2 conversion

Proefschrift voorgelegt tot het behalen van de graad van
doctor in de wetenschappen
aan de Universiteit Antwerpen
te verdedigen door

Georgi Trenchev

Promotor: prof. dr. Annemie Bogaerts

Antwerp, 2019

Note: The cover image of this thesis features the “Warming stripes” developed by climate scientist Ed Hawkins. Each stripe reflects the global temperature change over the last century, with red stripes indicating a temperature increase. In the cover background, they are placed in reverse. See http://www.climate-lab-book.ac.uk for more information.

Contents

List of figures

List of tables

Common notations and constants

Notation	Description	Unit
$\vec{v}$	Velocity	m/s
n_e	Electron density	$1/m^3$
n_i	Ion density	$1/m^3$
n_{pl}	Plasma density	$1/m^3$
n_0	Neutral density	$1/m^3$
T_e	Electron temperature	K, eV
T_i	Ion temperature	K, eV
T_g	Gas temperature	K
$\vec{E}$	Electric field	V/m
$\vec{H}$	Magnetic field	A/m
φ	Electric potential	V
$\vec{j}$	Current density	A/m^2
I	Current	A
U	Voltage	V
R	Resistance	Ω
C	Capacitance	F
L	Inductance	H
f	Frequency	Hz
μ_e	Electron mobility	$m^2/V.s$
μ_i	Ion mobility	$m^2/V.s$
D_e	Electron diffusion coefficient	m^2/s
D_i	Ion diffusion coefficient	m^2/s
σ	Electric conductivity	S/m
k	Thermal conductivity	W/m.K
k_T	Turbulent thermal conductivity	W/m.K
μ	Viscosity	Pa.s
μ_T	Turbulent viscosity	Pa.s
$\vec{u}_g$	Gas velocity	m/s
ρ	Gas density	kg/m^3
p	Gas pressure	N/m^2
P_r	Prandtl number	none
Re	Reynolds number	none
C_P	Heat capacity	J/K

Constant	Description	Value
$q_e = e$	Elementary electric charge	$1.602 * 10^{-19}$ C
k_B	Boltzmann constant	$1.380 * 10^{-23}$ J/K
N_A	Avogadro constant	$6.022 * 10^{23}$ 1/mol
m_e	Electron mass	$9.109 * 10^{-31}$ kg
h	Planck constant	$6.626 * 10^{-34}$ m^2kg/s

Acknowledgments

If called upon to describe the best part of my life after childhood – hopefully, at a *very fair* occasion – I wouldn't have a minute of doubt about the time I spent at PLASMANT as a PhD student. Spanning in almost half a decade, this was not only a period of acquiring scientific skills and writing papers, but also of personal growth, maturation, and gaining sense of belonging. This PhD position has been the first full-time job, the first stay abroad, the first time moving out of home, and the first circle of colleagues (later, friends) that I have experienced. I can certainly say that such a mix of beginnings, although difficult, can be only exciting and motivating. For there is nothing more propulsive in life than to be a beginner in something – whether it is your first time buying furniture, or writing your first paper, it is the first steps that we take with most vigour.

Not many people doing a PhD can brag about having a great promoter – and even less so, a superhero one. I was lucky to strike the former when Annemie Bogaerts made me a part of her team. Oddly enough, it all happened quickly – I still remember sending applications for a doctoral position all across Europe – in total, maybe ten or so. Annemie was the first to reply (super-positively!), and I was hired just weeks after completing my MSc thesis. Even my diploma was not ready yet, so some pre-prints had to do at the administration office of the University of Antwerp. Ever since, I still continue to be amazed by her energy and dedication to science. Annemie is a great researcher, teacher, manager, mentor, and even a 10 miles competition runner! Her passion for research set the bar in my own comprehension of what it means to be the best. And with every discussion, report, paper and grant application, this bar has been progressing upwards in a linear fashion. Annemie, thank you for the everlasting support, the freedom you gave me, the opportunities that you introduced me to, and the skills you taught me over these years.

I express exceptional gratefulness to dr. Stanimir Kolev. I met him during my Sofia University time, where he taught me various courses during my Bachelor and Master years. He is a true master of the scientific art, with enormous devotion to scientific truth, always willing to tackle, with great effort, the most difficult and obscure problems. He was the person that actually recommended me to Annemie, and, I still believe, the main reason for me becoming a PhD candidate

in her group. For me, he has been the best scientific adviser and knowledge support whenever I had difficult problems. Thank you, Stan, for teaching me how to develop, solve, and analyse science. I am also thankful to prof. Zhivko Kiss'ovski, as well as to everyone at the Faculty of Physics at Sofia University, for their impeccable teaching.

I would also like to mention my collaboration with Anton Nikiforov from Gent University, which was very fruitful, and I'm thankful for it. I also credit Peter Awakowitz and Nikita Bibinov from RUB – Bochum, who contributed to this work.

A PhD thesis is attributed to one name, but in fact, it is the result of the direct or indirect involvement of many personalities. Being in the warm group of the local *international society* was a great social pool, and a lot fun. The tradition of group dining and wine-ing was introduced by Maryam, and I soon became a regular practitioner. There I met an amazing group of like-minded friends. Thank you Maryam, Monica, Stefano, Slavisa, Radu, Amin, Saeid, Quan-Zi for the exceptional parties we've had. I'm sure that we have many more to look ahead to.

I, amongst others, am directly responsible for the catastrophic failure of no less than three coffee machines due to intensive use. Damien imported (from the Netherlands) the sub-culture of coffee-as-fuel for intensive scientific and non-scientific discussions every morning, and soon Antonin, Yannick, Vincent and Inne were regulars precisely at 10AM. Thank you all for the wonderful friendships we have developed. I'm sure these will be life-long.

I can't go ahead without mentioning the cool guys next door - Stijn, Kristof and Jonas. I will not forget the interesting discussions we had with Erik and Luc, nor the fruitful collaboration with Marleen.

Antwerp is a wonderful city, and a great place to meet others. I want to thank Carolina and Niki for the wonderful pizza-related moments we had together. I'm also grateful to having met Giulia, who is my closest friend in Belgium, and I could always rely on her support. Social outings with Victoria from the Academy of Fine Arts in Antwerp were fun and relaxing.

I could have never achieved any of this without the love and support of my girlfriend, Anja. She was my pedestal during the most demanding and stressful moments, not only at work, but also in the life we share. Thank you for being my partner.

My earliest aspirations were towards science, thanks to no other than my parents. My father, Lazar, taught me how to use a computer at the age of four, and my mother, Boryana, made sure that I get the best possible education at the right

moment. My grandfather claimed that I could read by the age of three, though I can remember reading comic books to the children at the kindergarten only a year later. I guess the seed of knowledge grows fast with the right care. I want to thank my uncle Georgi and my brother Nikola for standing by me at all times.

This work was realised with the support of Research Foundation – Flanders – FWO (Dutch: Fonds voor Wetenschappelijk Onderzoek) in Belgium. Project number: 11U5316N

CHAPTER I. Introduction

1.1. The Climate Problem

Are we a part of Nature? Are we working against it, or are we simply following an instinctive paradigm? If so, can our existence sustainably complete the natural cycles, instead of merely exploiting them for resources? The relation between human activity and Earth's natural processes consists of many unknowns. As any complex system, our habitat is constantly changing over time, with numerous alterations that may or may not be in our favour. The Earth climate – as trivial as it might seem, has long been the fundamental parameter that defines our existence.

Whether it is a natural development, or an ill-balanced equation of production and consumption, the climate change is the defining mark of the 21st century. It has been clearly proven that our activities can directly contribute in various degrees to almost any mechanism on Earth, and with no doubt, the climate is one of them. And if the lessons of the past could teach one thing, it would be to *think forward* when making decisions – as no other method has proven to be successful so far.

Since the dawn of humanity, we've kept ourselves busy with many activities, but we have always been persistent with one – technology. No matter of its form or advancement, we have always been instinctively directed towards its development. Technology drives our lives, solves our problems, and brings us new challenges to conquer. There is no question that technology is the way towards a sustainable future.

1.2 The role of CO_2

The issue of greenhouse emissions has made its own place in history. The Industrial Revolution [1] was a turning point, where the main hand production workforce was replaced with machine instalments. In the late 18th to the mid - 19th century, almost every industry in the world was completely transformed, multiplying its production output, while reducing the costs in the order of thousands. The price for this breakthrough is clearly marked on figure 1.1, where the carbon emissions from different sources are tracked over the last 200 years [2].

The problem has gained world-wide awareness, especially in the last two decades. The effects of waste gas emissions, such as CO_2, are already clear to the general public – air pollution, "greenhouse" effect (hence greenhouse gases),

rising Earth temperature and ocean levels, and harmful aftermath for natural ecosystems.

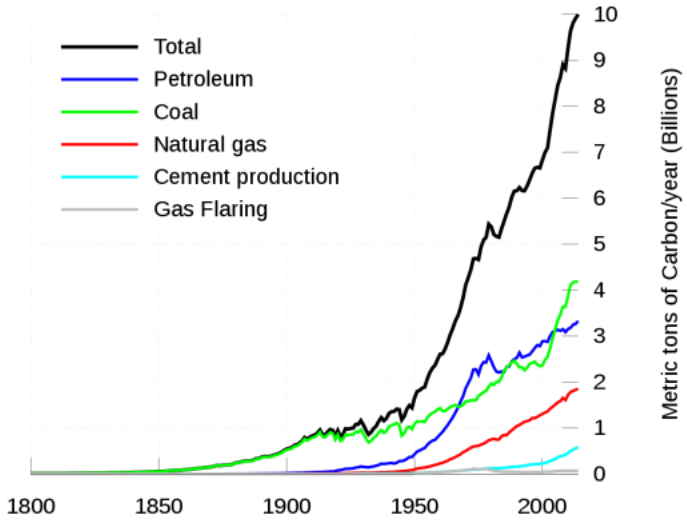

Figure 1.1 Global carbon emissions per year, from different sources. Adopted from [2].

1.3 The quest for renewable energy sources

With no doubt, certain efforts have been made, with more to come, in order to reduce the greenhouse pollutants. Many countries have adopted carbon-neutral policies, with strict regulations on the amount of greenhouse gases emitted by industries and transport. Renewable energy sources such as solar panels and wind turbines were adopted. The general public awareness clearly shows a demand for low-carbon waste products and fuel-free transport alternatives [3]. The climate strategy followed by the European Union, known as the 2020 package, dictates a 20% cut in greenhouse gas emissions, 20% of EU energy coming from renewable sources, and 20% increase in general energy efficiency, by the year 2020 [4].

While seemingly an efficient solution, renewable energy sources come with their own issues. While they produce relatively cheap (subtracting equipment costs, free), carbon-neutral energy, they do not deliver consistently. Solar panel installations suffer from an obvious problem – daily sunlight peaks around noon, while most energy is needed in the evening. Furthermore, sunlight radiation differs across the globe, and is heavily impacted by weather conditions [5].

Similar problems apply to wind farms, where power output is again variable due to changing weather. Water turbines on natural water resources (rivers, lakes…) are relatively consistent for short time periods, but can be still very variable on yearly basis. Electrical power distribution networks tackle these complications by dynamically dividing the power delivery to regions where needed, however, with a serious struggle. In periods with low overall power consumption, combined with high renewable source output, electrical providers are sometimes forced to ask customers to use the excessive energy anyway, with compensation, in order to avoid overpowering the electrical network. In essence, a lot of renewable source energy is wasted when it is in excess [6].

A number of technologies in aid to the renewable energy sources are developed. The basic approach is to store the excess energy for later use, thus eliminating the problems of overproduction and redistribution [7]. Methods for containing electrical energy vary by applicability, efficiency and cost. The most common problem is the energy density. A typical lithium battery has a specific energy of about 0.5 MJ/kg, with a limited number of recharge cycles (500~1000), which effectively increases the cost of such application [8], [9]. Super capacitors offer a much better recharge cycle capability (up to 1,000,000), but with a reduced specific energy of around 0.05 MJ/kg [10].

There exist ways other than electrochemical of storing energy on the electrical grid. A method of compressed air in underground caverns and tanks exists, but it requires a lot of space and specific infrastructure [11], [12]. Energy can be stored by pumping water from a lower water reservoir to an upper one [13], [14]. This method is in use, and is very reliable, albeit with low energy efficiency. Electrical energy can also be stored as kinetic energy by applying rotation to a flywheel storage system, known as the electromechanical method [15]. A novel alternative is plasma-based power-to-gas conversion, which is introduced in this thesis.

1.4 Thermal CO_2 splitting

Going back to the greenhouse problem, CO_2 has been targeted as one of the main pollutants. CO_2 is a very stable molecule. One carbon atom is covalently bonded to two oxygen atoms, with a formation enthalpy of 393.5 kJ/mol and bond strength of 793 kJ/mol [16]. A considerable energy input is thus required to break this bond and reform CO_2 into other gases. The splitting reaction for CO_2 at standard conditions is:

$$CO_2 \rightarrow CO + \tfrac{1}{2}O_2 \qquad \Delta H = +283\ kJ/mol \qquad (1.1)$$

Thermal CO_2 splitting is possible, but due to the high energy requirements, it is not very efficient [17]. The gas has be to heated to 3000 K and above, and still, the theoretical energy efficiency only peaks at 47% [17], decreasing rapidly at higher temperature.

1.5 Plasma-based CO_2 conversion

A practical way to insert high power into a gas, is by energizing it to a plasma discharge. Plasma-based CO_2 conversion is a rapidly growing field with many promising applications [18].

Reaction (1.1) is endothermic, and inefficient, however, as stated by Fridman [19], its energy efficiency can be improved greatly by populating the vibrational levels of CO_2. This can be effectively done in a gas discharge plasma, with an energy-efficient process known as vibrational dissociation of CO_2.

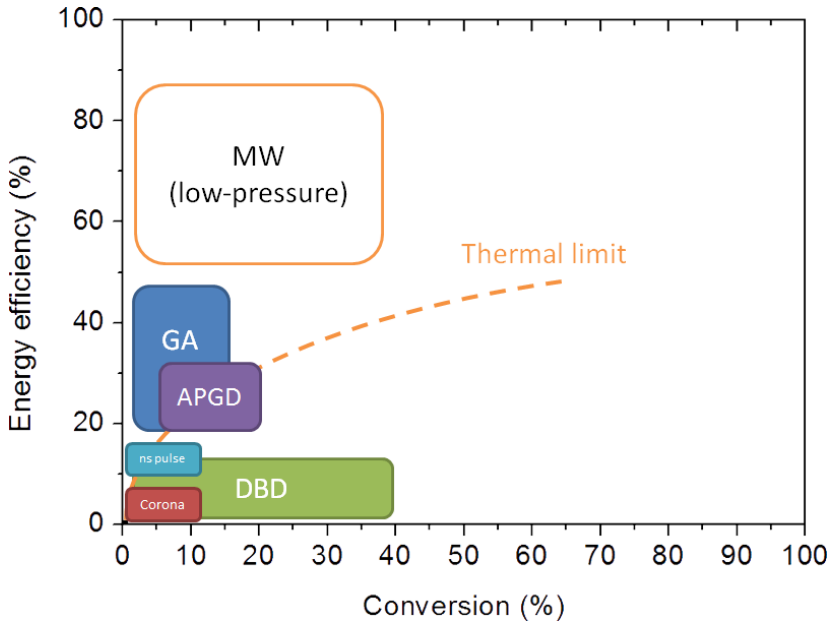

Figure 1.2 Typical performance of different plasma reactors, energy efficiency as a function of CO_2 conversion. Based on [17].

In essence, less energy is wasted on merely heating the gas (and aiming for thermal CO_2 splitting), but it is rather re-directed towards an efficient conversion

pathway in the chemically active plasma. Using this method, the energy efficiency can be brought up to 90% as claimed by [19]–[21]. Consequently, the plasma conversion method has gained a lot of interest, with highly varying results between different reactor types (see figure 1.2). See Chapter II for an overview of different plasma sources.

1.6 Plasma-based fuel production: closing the natural cycle

Hydro-carbonic fuels [22] can have specific energies of up to 60 MJ/kg, much higher than conventional electrochemical methods, which makes them a viable candidate for energy storage [23]. One way to obtain such a hydrocarbon fuel is the Fischer-Tropsch process [24], which is generally formulated as:

$$(2n+1)H_2 + nCO \rightarrow C_nH_{2n+2} + nH_2O \qquad (1.2)$$

where n is in the range of 10-20. The products of this reaction are different alkanes, typically diesel and other fuels. Water is the excess product. The connection with reaction (1.1) is now evident: with a CO_2 conversion plasma reactor as a constant CO source, electrical energy from renewables can be stored into fuels using the Fischer-Tropsch process, as shown in figure 1.3.

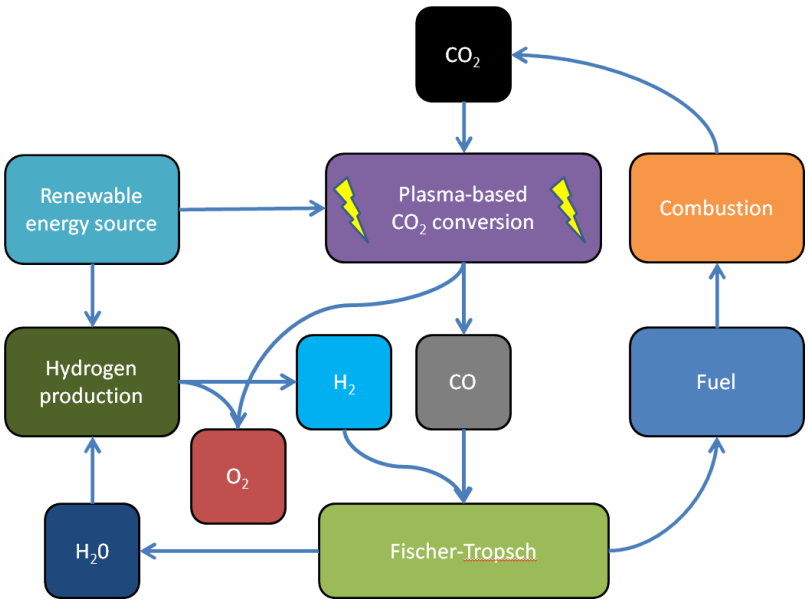

Figure 1.3 Schematic representation of plasma-assisted CO_2 utilization.

1.7 The objective of this work

The main objective of this work is to build the technical foundation of the application of DC atmospheric pressure plasma discharges for CO_2 conversion. While most of the study is undertaken through state-of the-art computer simulations, new, experimental designs are explored and put to the test. The thesis quantifies the concepts of a novel reverse-vortex gliding arc plasma reactor for CO_2 conversion through computational modelling, exposing the most critical properties and ways of improvement. Through further theoretical investigations, a new atmospheric pressure glow discharge reactor is engineered, and utilized for CO_2 conversion. Finally, a knowledge matrix of properties, principles and techniques is constructed, leading to the development of an innovative dual-vortex gliding arc plasmatron for CO_2 conversion.

CHAPTER II. Plasma sources and technology

2.1 A preface to plasma science

Although the main purpose of this work is to elucidate the application of plasma discharges for gas conversion, *plasma discharges in a gas* have existed for quite a while [25]. Plasma is not a human invention – lightings, the ionosphere, the aurorae [26], the stars, the interstellar medium, are all nature-made manifestations of the so-called *fourth state of matter* [27].

Figure 2.1. Natural occurrences of plasma – lightning [28], Aurora Borealis [29], and star formation in LH-95 [30].

First modern studies on electrical discharges date from the late 1800's with the works of John Townsend, where he described the complex process of gas ionization under strong electric fields, now known as the Townsend discharge [31]. First to introduce the term *plasma* in the context of an ionized gas was Irving Langmuir, who was studying the atomic structure in gases and electrical arcs [32]. He attributed this name to the reactive nature of the ionized gases, which reminded him of blood plasma. Today, although it still brings little confusion with the medical term, this is still the common name for an ionized gas.

Man-made plasmas exist in a vast variety [19]. Probably the most familiar technology would be neon and fluorescent lights, where an electrical glow discharge is used to produce visible light in almost every school or office. Plasma TV sets operate in a similar matter, where each pixel of the screen is an individual glow discharge cell. Artificial plasmas impact our lives in indirect ways, too. Many of the steps required to produce the integrated circuits in our computers and smartphones, are essentially based on plasma technologies. Plasmas are used for

various industrial processes, such as cutting, welding and coating [33]. Nowadays, plasma-chemical processes are used for food and air sterilization [34]. Plasma medicine is a new, rapidly growing field, where plasmas are effectively used for sterilization, treating wounds and even cancer [35]. Plasma agriculture aims to improve food production by treating seeds and plants with reactive plasma species [36]. High-temperature fusion plasmas promise to bring us an energy-independent future [37].

2.2 The states of matter

On figure 2.1, a simplified overview of the distinct states of matter is shown. Solid matter can be represented as a rigid, stationary atomic structure with high density. Liquids can have a similar density, but the solid structure between the building blocks – atoms or molecules, is broken, and there is no rigidity. Going further into a gas, the distance between the molecules is increased, creating a freely roaming medium.

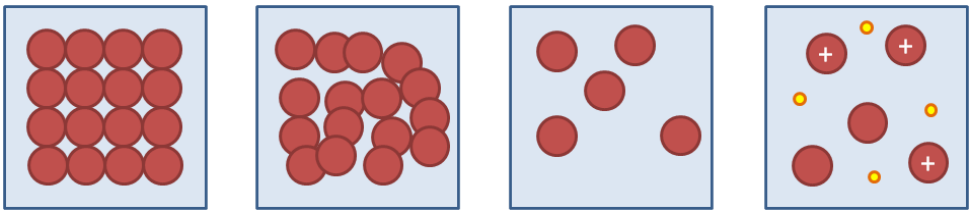

Figure 2.2 The main four states of matter

Surely, more exotic states of matter, such as the Bose-Einstein condensate [38] or the quark-gluon soup [39], exist, though strictly in very extreme conditions (absolute zero temperature and very high densities/energies). Plasma is typically produced by applying energy to a gas, which can be achieved through high temperature or high electric field. Though unlike the first three states, there is no phase change, but ionisation of the gas takes place. In this case, electrons are ripped off the atom orbitals, either through an impact with another species, or through a high electric potential. This leaves some atoms polarized, i.e. they are

now ions. A partial ionization means that some species remain neutral. The total number of free electrons (with negative potential) and ions (with positive potential) may differ, or may be similar, a case of quasi-neutral plasma. Due to the presence of free charge carriers in the form of electrons and ions, plasmas are highly electrically conductive.

2.3 Plasma properties

Plasmas are characterized by a number of direct and indirect properties. The plasma density n_{pl} typically refers to the number of electrons (or ions in quasi-neutral plasmas) per unit of volume in the plasma bulk (commonly in m^{-3} or cm^{-3}). The electron temperature T_e refers to the thermal velocity of electrons in the plasma medium, and is typically expressed in Kelvins (K) or electron-volts (1 eV = 11605 K). By plasma ion temperature, T_i, we refer to the temperature of all ionized species in the plasma. In most cases, the neutral gas temperature is assumed to be equal to T_i. The ratio between T_e and T_i serves as an important measure, as it characterizes the plasma as thermal ($T_i \approx T_e$) or non-thermal ($T_i < T_e$), also called cold plasma.

Another important feature that is directly correlated with the electron temperature, is the Electron Energy Distribution Function, or EEDF. Essentially, this is a statistical distribution of the probability density for thermal electron velocities. The EEDF in most atmospheric pressure plasmas follows a Maxwell distribution, though non-Maxwell distributions are also very common, leading to different transport properties for the electrons, and hence, different properties of the plasma.

Plasmas can also exist at different gas pressures. For instance, plasma can be generated in a low (10^{-9} to 10^{-3} bar), medium (~10^{-2} bar) or high (1 bar or above) pressure. Plasmas at regular atmospheric pressure are very favourable for industrial applications, as they do not require low-pressure vessels and vacuum pumps.

The method of plasma production has a crucial importance as well. Plasmas created in different types of plasma sources may have very different properties. For instance, an arc discharge is driven by thermionic electrons emitted from a metal surface, while a glow discharge relies on field emission, facilitated by a strong electric potential. Typically, arc discharges operate with plasma density about an order higher than glow discharges [19].

2.4. Microwave plasma (MW)

Microwave plasma sources [40] can operate at low, medium or atmospheric pressure. As shown on figure 2.3, their typical configuration consists of a dielectric tube, which is subjected to strong microwave radiation. The microwave generator, typically a magnetron at 0.815 or 2.45 GHz, is coupled with the dielectric tube through an electromagnetic waveguide. When tuned properly, the discharge results in a stationary plasma bulk in the tube centre.

Microwave sources are capable of sustaining at very high powers (over 1 kW), and typically do not suffer from reactor degradation due to the absence of electrodes. The plasma can be produced in a closed chamber, as well as in open space, depending on the reactor design [41]. Impedance matching between the source and the load, and the electromagnetic mode in the waveguide, are crucial for efficient operation.

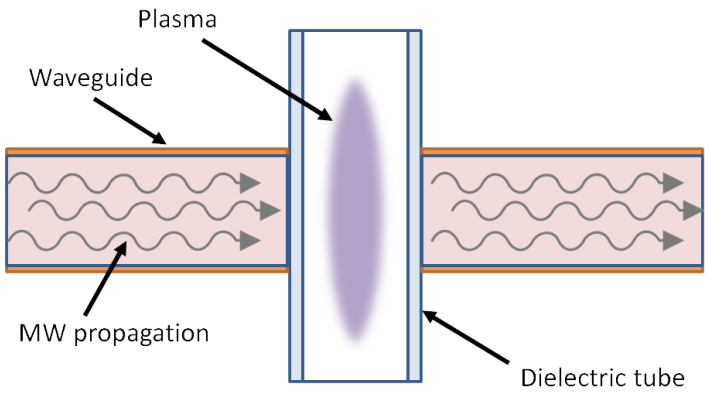

Figure 2.3 Illustration of a microwave discharge

2.5. Inductively coupled plasma (ICP)

Inductively coupled plasma (ICP) discharges [42] are another type of plasma source that utilizes electromagnetic waves to ionize the gas. As shown on figure 2.4, by applying strong AC current, typically in the radiofrequency (RF) range, a magnetic field is induced in the gas bulk, resulting in a discharge. ICP sources at atmospheric pressure typically produce a thermal plasma discharge. ICPs find applications, among others, in analytical chemistry (mass spectrometry and atomic emission spectroscopy) when working at atmospheric pressure (thermal

plasma) [43] and reactive-ion etching, when operating at reduced pressure (non-thermal plasma) [44].

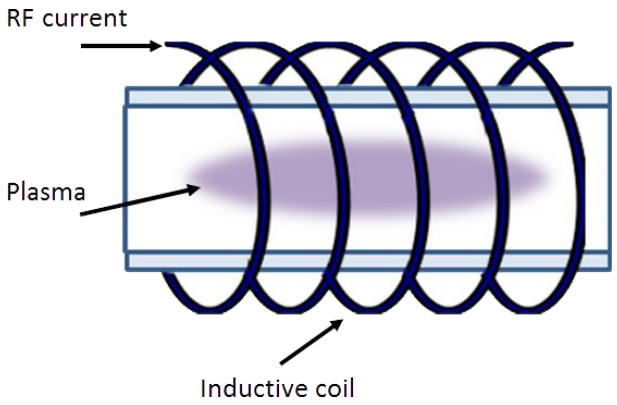

Figure 2.4 Illustration of an inductively coupled plasma (ICP)

2.6. Dielectric barrier discharge (DBD)

Dielectric barrier discharges [45] (DBD) are common atmospheric sources, suitable for a variety of applications mainly due to their simplicity and reliability.

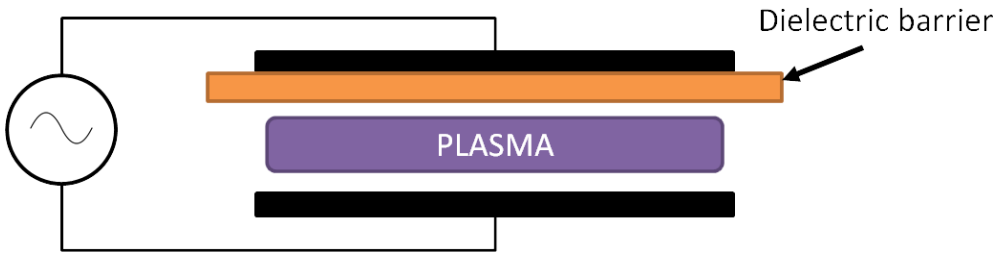

Figure 2.5 Illustration of a basic DBD plasma

As shown on figure 2.5, a basic DBD plasma source contains two electrodes (in black) connected to an AC power supply, and separated by a dielectric barrier, called also an insulation barrier. This essentially prevents the formation of electrical sparks between the electrodes. Due to the high, alternating potential difference between the electrodes, charges gather on the surface of the dielectric, and, when sufficient in magnitude, discharge at different positions. Iteratively,

they cover the entire discharge gap with plasma. DBDs are commonly used for surface treatment [46], but also for gas conversion.

2.7. Glow discharge

Glow discharges [25], [47] are another widely known plasma source, existing in many different variants. Most commonly, two opposing electrodes are biased at high voltage (high-voltage DC), whereas the negatively biased electrode is a cathode, while the other one, called anode, is typically grounded. See figure 2.6 for a schematic of a typical glow discharge.

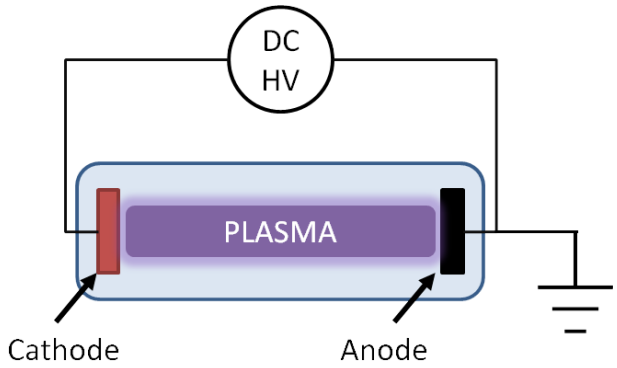

Figure 2.6 Illustration of a DC glow discharge

Glow discharges operate at high voltage (typically 3-30 kV) and low to moderate current (1-100 mA). Though they are more commonly used at low pressure, atmospheric pressure configurations exist as well.

2.8. Arc discharge

Although its electrical configuration is similar to a glow discharge, the arc discharge [25] exhibits some key differences. Typical atmospheric arcs operate at high current (0.5-100 A), in contrast to the low-current glow discharges [19]. The voltage drop across the arc is low (10V~1kV) due to the high density, and therefore high conductivity of the plasma. Arcs operate with a high-temperature cathode spot, which is its main source of electrons. The specific shape (see figure 2.7 left), and thus the name, comes from the buoyancy forces that naturally bend the hot gas in the plasma region.

Gliding arcs [19] (GA) are a particular configuration of an arc discharge. In a classical gliding arc, two diverging electrodes are subjected to a gas flow (figure 2.7 right). In this way, the arc is driven not only by the buoyancy force, but also by the gas flow velocity. Therefore, it glides along the electrodes, and elongates, until the power input is unable to sustain it anymore, leading to arc extinguishing. At the same time, as there is no more current conducted between the electrodes, the source voltage increases, and a new breakdown initiates a secondary arc at the shortest distance between the electrodes.

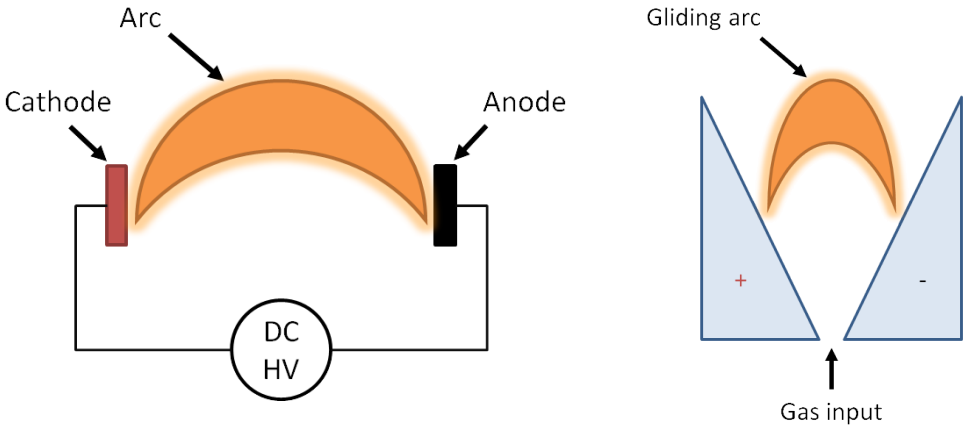

Figure 2.7 Illustration of a stationary arc discharge (left) and a classical gliding arc (right)

2.9. Glow and arc discharges – physical properties

A more detailed look into the structure of glow and arc discharges reveals even more fundamental differences. As shown on the photographs in figure 2.8, the two discharges manifest a contrasting appearance.

On figure 2.8 (a), a glow discharge in atmospheric air between two sharp pins (at a distance of 10 mm) is initiated. The luminous discharge appears as a thin column, with a noticeable gradient in brightness starting from the cathode (top). The reason for it is the gradual electron energy loss to ionization over the discharge distance. In the cathode dark space, it is not sufficient to excite the gas atoms or molecules, so almost no photons are released. This is followed by a thin bright region, called negative glow, where a lot of atomic excitation takes place,

followed by the wider Faraday dark space, and again a brighter region, the positive column (see figure 2.9).

In the positive column, the electron energy increases enough (due to the electric field, needed to guide the electrons towards the anode) to excite atoms/molecules and release photos again (hence with increased light production). The thin anode glow region typically occurs due to the increased electric field (and therefore, electron energy) in the anode layer. Due to the high conductivity of the discharge, in most cases the current is limited by a ballast resistor (R).

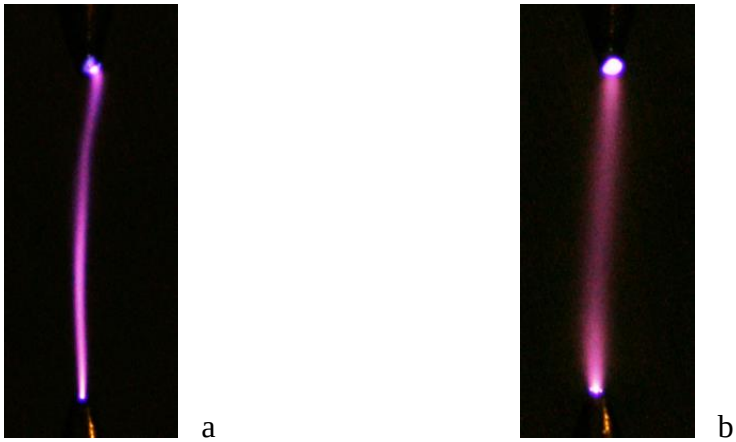

Figure 2.8 Atmospheric glow discharge (a) and arc discharge (b) between two pin electrodes.

Despite that most studies on glow discharges are carried out at reduced pressure (typically ~0.01 atm) [48], high-pressure variants were proven as early as 1933 [49]. Recent efforts to generate non-thermal plasma at atmospheric pressure have facilitated the development of such discharges again [50], [51]–[53]. However, certain distinctions have to be made.

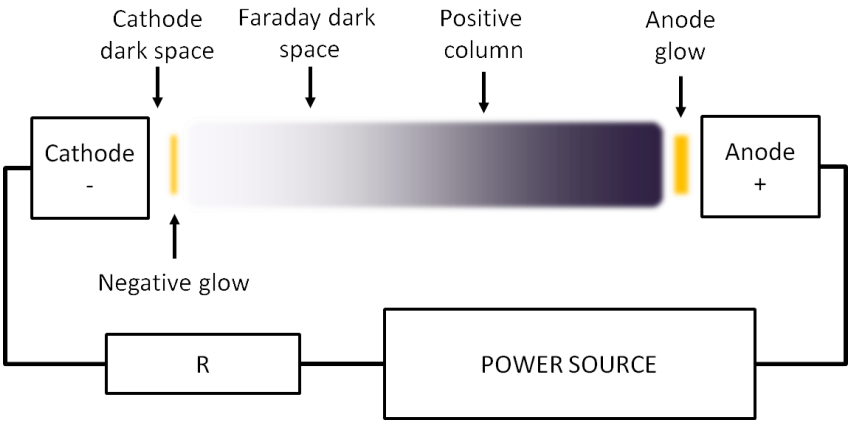

Figure 2.9 Different zones present in a glow discharge

When in normal mode, low-pressure glow discharges tend to retain their current density [54] (and hence increase area) with increasing the total discharge current, while in atmospheric discharges the current density increases due to discharge contraction. For this reason, glow discharges operating at atmospheric pressure are specifically called atmospheric pressure glow discharge (APGD).

Looking at figure 2.8 (b), the arc discharge shows some prominent specifics. A bright cathode hot spot is visible at the cathode (top electrode). This spot is a source of intense electron emission, which is driven by the surface temperature of the electrode – a process known as thermionic emission [55]. A diagram of the processes occurring in the arc discharge is shown on figure 2.10.

The main part of the arc discharge, the arc column, is characterized by a uniform luminosity. This column is electrically neutral (in charge equilibrium), with low electric field and very high conductivity. The heating process is intense Joule heating along the arc. Due to the high temperature, significant discharge contraction takes place, which leads to steep density and temperature gradients. The natural convection (i.e. the buoyancy force) drives the discharge into the characteristic shape. A wide spectrum radiation is emitted from the arc, mostly in the infrared and visible regions [56]. Evaporated metal from the cathode may be present in the plasma.

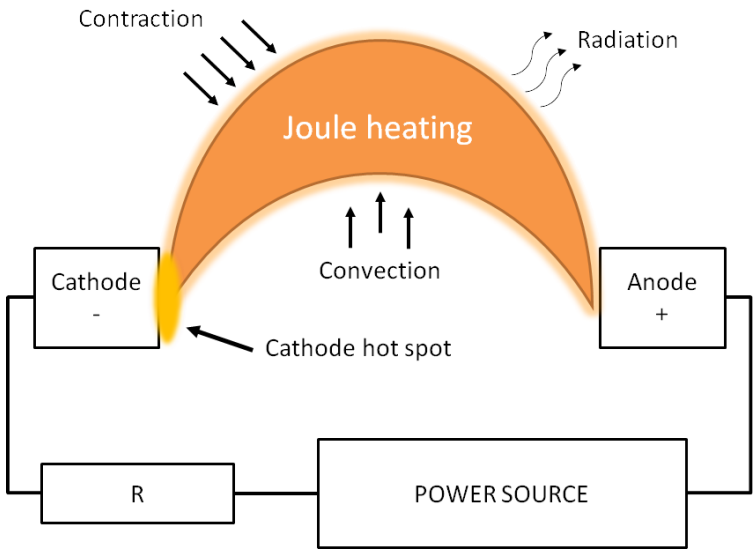

Figure 2.10 Major processes occurring in an arc discharge.

The thermionic emission can be calculated by Richardson's formula [19]:

$$J = A_G T^2 e^{-\frac{W}{kT}} \tag{2.1}$$

where J is the emission current density at the cathode, T is the surface temperature of the metal, W is the specific work function of the metal, k is the Boltzmann constant, and A_G is a constant. The exact value of A_G is still not known, but the general agreement is the following:

$$A_G = \lambda \times 1.2 \times 10^6 \tag{2.2}$$

where λ is a material-specific correction factor (usually around 0.5). The processes in the cathode spot are interesting on their own, but they fall outside of the scope of this work. In short, the cathode spot is comprised of several layers. The first layer, about 1 Debye length thick (see pg. 47) is positively charged due to the presence of slow-moving ions. This creates a cathode potential jump, which locally enhances the electric field and decreases the surface work function, accelerating the electron emission.

The transition between the different discharge stages in DC discharges (can be tracked on a V-A diagram, as shown on figure 2.11. In this example, three distinctive regions can be observed. Dark discharges occur at low-current (nA to μA range). A Townsend discharge occurs when a sufficient number of electrons starts an avalanche ionization process. Corona discharges typically fall into this region [19], [25], [57]. An electrical breakdown is marked by a sudden drop in voltage and increase in current, leading to a glow-regime discharge. In this region, electrons consistently leave the cathode surface, forming a continuous plasma column (see figure 2.8 (a)). In the glow-to-arc transition region, a peak in voltage is observed, followed by a rapid drop, accompanied by an increase in current: the discharge is now dominated by thermionic emission.

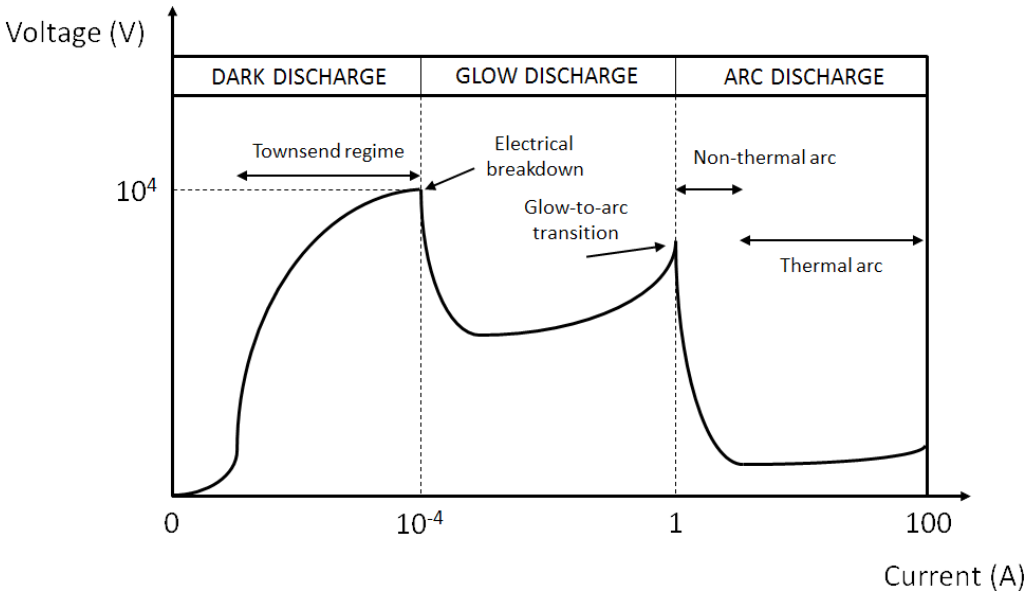

Figure 2.11 Different discharge stages in a DC discharge, showing the Townsend-to-glow-to-arc transition.

2.10. Atmospheric pressure plasmas for CO_2 conversion

Atmospheric pressure plasma reactors are promising for plasma-assisted gas conversion [19], [58]–[60]. Most studies have been executed with microwave plasma [61], [62], dielectric barrier discharge (DBD) [63], atmospheric pressure glow discharge (APGD) [60], gliding arc (GA) reactors [59], [64] and nanosecond

pulsed discharges [65]. Every reactor type has its specific advantages and drawbacks, and up to now there is no general consensus for the best technology.

For instance, microwave (MW) plasma reactors show good energy efficiency (above 50%), but typically at reduced pressure [17], although in recent years, some promising results at atmospheric pressure have been obtained at the DIFFER institute. DBD reactors are able to operate at atmospheric pressure and show relatively high gas conversion, but at very limited energy efficiency (up to 10%) [17]. Recently, certain advances have been made with APGD reactors, with an improved conversion-efficiency balance [60], though the efficiency is still limited to 25-30%.

Classical gliding arc reactors have shown promising performance in CO_2 conversion, with energy efficiency up to 29%, although still with limited conversion (up to 6%), problematic electrode degradation, and significant convective heat losses [17]. The reverse-vortex gliding arc reactor makes a compelling step forward, as it utilizes the reverse-vortex principle to insulate the discharge and reduce the heat losses towards the reactor walls. Despite its advantages, it still has a limited conversion (up to 8-9 %), at an energy efficiency of 25-35 % [59]. This has been attributed to the limited amount of gas actually passing through the discharge zone (as will be discussed in Chapter V below). Furthermore, it is accompanied by the formation of a high temperature cathode spot, which partially shifts the discharge regime into thermal. It has been shown that the temperature of this cathode spot can reach 6000K or more [66]. As will be shown in Chapter V further in the thesis, a lower gas temperature is needed for efficient vibrational CO_2 dissociation.

CHAPTER III. Modelling methods

3.1 COMSOL Multiphysics

COMSOL Multiphysics [67] is a multi-platform, finite element simulation software that can handle almost any conventional physical model. A defining feature of the software is that it comes with a variety of pre-configured physics modules that can arbitrarily interface each other (hence "Multiphysics"). The modules include workflows for solving mechanical, electrical, heat, fluid, chemistry, acoustics and particle physics problems. In addition, general ODE (Ordinary Differential Equation), PDE (Partial Differential Equation) and classical equation (Laplace, Poisson, Helmholtz…) modules are available. There is a built-in CAD (Computer-Aided Design) interface for designing geometries, and an interface for finite element mesh generation.

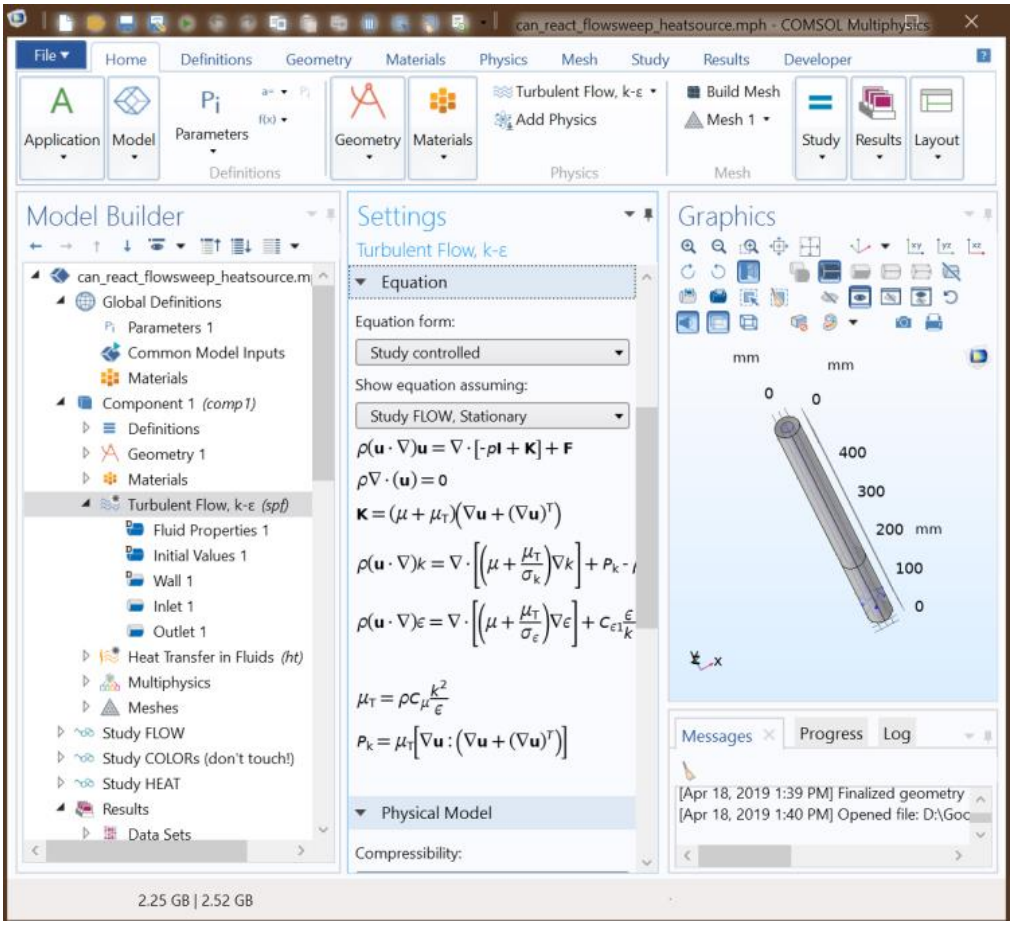

Figure 3.1 COMSOL 5.4 interface in Windows 10.

With a large emphasis on academic settings and education, COMSOL displays the equations and constants governing the physics modules as-is, with classical mathematical (Eulers') notation (see figure 3.1). Expanding each module into the actual computational code and making changes is possible.

The available solvers are proprietary, though they are highly configurable. Most problems are solved using direct solver (an automatic selection is performed upon initial problem set-up), though iterative solvers are also available. The main difference between the two is that iterative solvers approach the problem gradually, with fine computational steps, contrary to the large computational step in direct solvers. While a well-conditioned problem with sufficient mesh computes monotonically into a final solution, an ill-conditioned problem might result in the following:

```
Failed to find a solution.

The relative residual (0.06) is greater than the relative toler
ance.

Returned solution is not converged.
```

The line above is typically a problem of the finite element mesh, boundary conditions, or both. Solutions in COMSOL may take place in the time or frequency domain, and can be also stationary.

COMSOL runs mainly on CPU (x86 and x64) in Windows or Linux environment. Scalability is linear up to 7-8 CPU cores, while more cores are less efficiently utilized, though this is largely dependent on the given problem and computational solver. For small 2D problems involving fluid flow, 6-8 GB of RAM are generally sufficient, while for 3D at least 16 GB are preferable. Multiphysics problems in 3D typically require at least 32 GB. Most of the models in this work were solved on a workstation with an i7-3820 CPU and 64 GB of DDR3 RAM. GPUs are supported for graphics acceleration only.

Connecting to MATLAB [68] (and other compatible software) through the LiveLink wrapper is possible, allowing for MATLAB functions to be used directly in COMSOL.

3.2 Computational fluid dynamics

"Everything flows, nothing stands still."

Heraclitus, 501 B. C.

3.2.1. The Navier-Stokes equations

The term fluid embraces both gases and liquids, and its properties play an important role in science and engineering. The defining features of a fluid are its abilities to be deformed with ease, to take any shape in any vessel, to flow through cavities, or to remain still. A fluid, be it gas or a liquid, is composed of individual molecules with their own microscopic mechanics, yet on a macroscopic scale, it can be treated as a full, continuum body. It is this complexity that gave rise to the fluid dynamics science [69].

Early attempts to mathematically predict fluid motion date from the 19th century works of Sir George Stokes, who was studying the mechanical friction of fluids around various objects such as pendulums and metal spheres. These works led to obtaining the terminal velocity of spherical objects in a fluid flow, which is known today as Stokes' law, and gave the notion of Stokes flow [70].

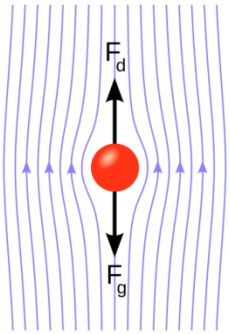

Figure 3.2 A spherical object in a Stokes flow [71]. A fluid drag force (F_d) counteracts to the gravity force (F_g).

Stokes flow is a type of steady fluid flow, where the friction forces in the fluid are much greater than its inertial forces, also called creeping flow. Generally, the motion of such a fluid is described as:

$$\nabla \cdot \boldsymbol{P} + f = 0 \tag{3.1}$$

$$\frac{\partial \rho}{\partial t} + \nabla \cdot (\rho \boldsymbol{u}) = 0 \tag{3.2}$$

Equation 3.1 represents the momentum balance in the fluid, where $\boldsymbol{P}$ stands for the Cauchy stress tensor of viscous and pressure stresses, and f represents the body force acting on the fluid. Equation 3.2 completes the Stokes equations for fluid motion by describing the conservation of the fluid mass. In the equation, ρ stands for the fluid density, and the vector $\boldsymbol{u}$ represents the fluid velocity. However, without an inertial term, these equations can describe correctly only slow-moving flows with a Reynolds number **Re** below 1.

Embedding in the inertial term in equation 3.1 leads to a system known as the Navier-Stokes equations [72]:

$$\nabla \cdot \boldsymbol{P} + f = \rho \frac{\partial \boldsymbol{u}}{\partial t} + \rho(\boldsymbol{u} \cdot \nabla)\boldsymbol{u} \tag{3.3}$$

$$\frac{\partial \rho}{\partial t} + \nabla \cdot (\rho \boldsymbol{u}) = 0 \tag{3.4}$$

Essentially being an expression of Newton's Second Law, the Navier-Stokes equations are the mathematical foundation of modern fluid mechanics. They find numerous applications in engineering, medicine, ocean exploration, meteorology, and many others. Though the Navier-Stokes equations can accurately describe the motion of a fluid, it has not been yet proven that a completely differentiable solution exits – something that still stands as an open question in mathematics.

3.2.2. Solving the Navier-Stokes equations

Early attempts to solve the Navier-Stokes equations numerically date from the first half of the 20th century. Some of the first computers, such as the ENIAC [73],

were used to calculate the equations in 1D and 2D domains. First works on 3D Navier-Stokes calculations appeared in 1967, with the works of Hess and Smith at Douglas Aircraft [74], when the calculation speed of supercomputers was up to the task, though this was an example of a bleeding edge computational science. Due to an increasing demand in many areas on science and engineering, Computational Fluid Dynamics (CFD) was established as its own field. With every new generation of computers, the approachable complexity of CFD increased, and ever since, the field has advanced proportionally with Moore's law [75].

A number of computational codes were developed over the years, each best suited for the given application and computer architecture. Naturally, first applications included aircraft, ship and automotive design, with some particular advances achieved by NASA, Boeing and Lockheed [76]–[78]. Later, CFD found application in general engineering problems regarding pipe flows, turbines, combustion, etc. Typically, a CFD problem is solved as follows:

- The computational domain geometry is created, using CAD (Computer-Aided Design) software.
- The geometry is discretized into small elements or volumes, which can be solved for individually, i.e. a computational mesh.
- The boundary conditions are applied to each entity of the mesh, i.e. walls, inlets and outlets are defined.
- The equation of interest is defined in the computational volume, i.e. Stokes flow or the full Navier-Stokes definition.
- The simulation can be then carried out with a stationary or a time-dependent solver.
- The results are post-processed and visualized.

3.2.3. A classic CFD example

On figure 3.3, an example of a computational mesh is shown. The considered problem is a common demonstration of CFD – a vortex flow pattern after a blunt body (a sphere) [79]. Figures 3.4 and 3.5 give examples of a full Navier-Stokes solution and a creeping (Stokes) flow solution.

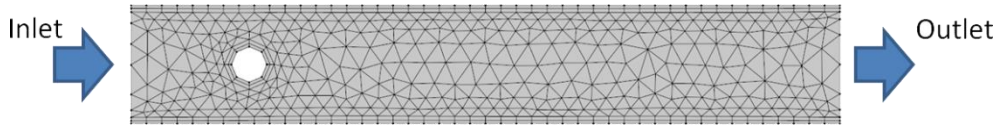

Figure 3.3 A computational mesh in a 2D domain.

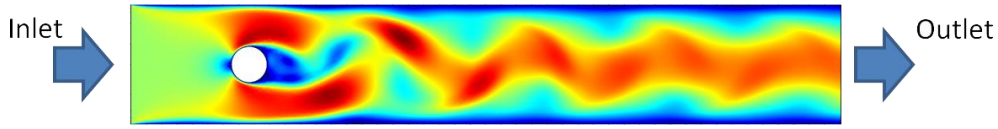

Figure 3.4 A vortex street flow pattern is developed with full Navier-Stokes equations.

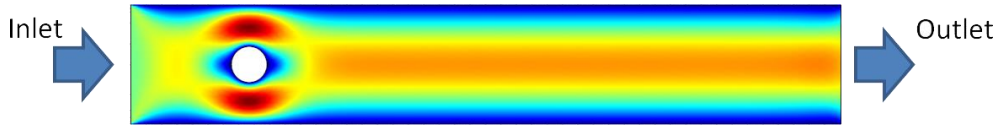

Figure 3.5 Stokes flow description – no vortex flow pattern is observed due to the lack of an inertial term.

The most common methods for computational solving of fluids are the finite volume method [80] (FVM) and the finite element method [81] (FEM). In the FVM, the governing equations are integrated as finite volumes over the mesh. Essentially, flow fluxes are balanced over the individual volumes of the computational domain. This is a straightforward computation in a regular mesh, where the domain is evenly discretized in every direction. However, more computational effort is required for complex geometries and irregular meshes, such as the one on figure 3.3. In this case, the FEM handles the computation with less effort, as it does not depend on the mesh topology. In this method, the governing equations are integrated over each element after applying a weight function, which depends on the element size and shape. Some examples of commercial CFD software and their respective computational methods are given in Table 3.1.

Table 3.1 Examples of CFD simulation software

Software	Method	Notes	References
Ansys Fluent	FVM		[82]
COMSOL	FEM	Multi-physics	[67]
OpenFOAM	FVM	Open source	[83]
STAR-CCM+	FVM		[84]
SIMSCALE		Cloud-based	[85]
Autodesk Inventor		CAD-integrated	[86]

Of course, custom CFD codes exist, and are still developed extensively. Typically, they are used for solving cutting edge problems on large-scale supercomputers, which require considerable parallel optimisation. In addition, special methods are in use for the utilization of GPUs (Graphics Processing Unit), such as the Lattice-Boltzmann Method [87] (LBM).

3.3. Flow turbulence

Flow turbulence is a naturally occurring phenomenon in fluid flows, characterized by random oscillations in fluid pressure and velocity. It can be observed almost anywhere, for example in moving clouds, fast flowing rivers, smoke from a cigarette, or even in a cup of coffee. Turbulence occurs when the kinetic energy in a fluid flow overcomes the dampening caused by the fluid viscosity. Therefore, low-viscous fluids such as atmospheric air are more prone to turbulence than highly viscous fluids, such as ordinary honey.

Figure 3.6 A submarine pours the ocean water into turbulence, visible by the white ripples [88].

Although it is a highly randomized event, certain methods for predicting turbulence exist. The Reynolds number [89] **Re** is a dimensionless quantity used to predict turbulence in fluid flows. Essentially, it is the ratio of the inertial and viscous forces acting in a fluid, and is typically defined for standard shapes such as pipes and ducts. In a cylindrical pipe, **Re** is calculated as:

$$Re = \frac{\rho u D_H}{\mu} \tag{3.5}$$

where D_H is the hydrodynamic diameter of the entity (the pipe), ρ is the fluid density, u is the mean flow velocity, and μ is the dynamic fluid viscosity. With **Re** below 1, the fluid flow in a pipe is typically assumed to be laminar, i.e. no turbulence development is to be observed.

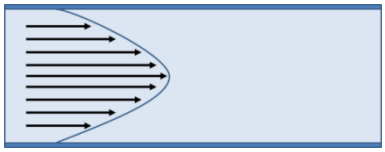

Figure 3.7 A laminar flow profile of **Re** < 1.

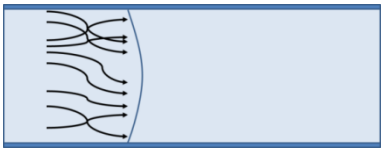

Figure 3.8 A turbulent flow profile at Re > 1000.

On figure 3.7, a textbook example of a laminar flow profile is shown. In smooth cylindrical pipes, this is the profile most fluids will take if **Re** is below or around 1. A turbulent flow is typically assumed if **Re** is above 1000, though turbulent oscillations occur at much lower values, something regarded as a transitional flow (figure 3.8). In the example, **Re** is calculated for the hydraulic diameter of the pipe.

On figure 3.9, the computational complications of turbulence are demonstrated. The simulation agrees with the theory: at **Re** = 0.66, the flow around the sphere is fully laminar. Going up just slightly higher, at **Re** = 3.33, oscillations due to the flow inertia are evident. The pattern becomes more complex and more frequent at **Re** = 33. Indeed, **Re** can serve as a direct estimation of the turbulent quantity in a given gas flow setup. With higher flow complexity, the computational load increases in two ways. First, as the oscillation physical size decreases, the gradients in velocity and pressure become steeper, which requires a finer computational mesh. Second, as the oscillations become more

frequent, the computational solver has to take smaller time steps, in order to reach a solution. In the example in figure 3.9, at **Re** = 333, the mesh and time stepping requirements would become too severe to reach a complete solution.

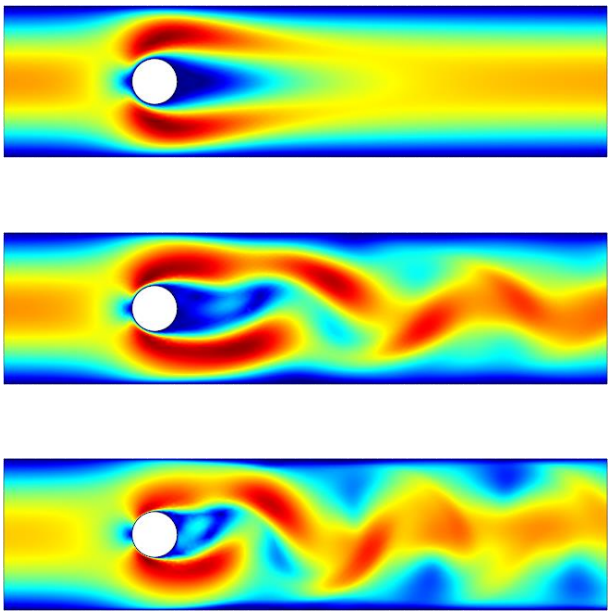

Figure 3.9 Flow patterns for different values of **Re**.

A complete solution of the Navier-Stokes equations for a turbulent flow requires extremely small space and time discretization, called Kolmogorov micro scales [90]. This is the smallest scale of the oscillations in a turbulent flow. The Kolmogorov scale for length would be:

$$\alpha = \left(\frac{\upsilon^3}{\varepsilon}\right)^{1/4} \tag{3.6}$$

In formula 3.6, α is the Kolmogorov length scale, υ is the kinematic viscosity of the fluid, and ε is the rate of turbulent kinetic energy dissipation. In laboratory systems, this scale can range to micrometers and below, which means that the fluid simulation of a typical reactor would require hundreds of millions of mesh elements – something that at the moment is only approachable for the most powerful supercomputers [91].

3.3.1 Turbulent models

To reduce this computational load, averaging mathematical models for flow turbulence exist. Most of them use average quantities of the turbulent parameters, in space and time, while still keeping the overall accuracy of the model reasonable. Most turbulent models share a common root in the Reynolds-averaged Navier-Stokes [92] (RANS) equations. RANS equations are a time-averaged decomposition of the Navier-Stokes equations. Typically, most RANS turbulent models solve two additional partial differential equations.

3.3.2 The k-ε model

The turbulence kinetic energy (k) and the dissipation of kinetic energy (ε) are solved in the case of the k-ε RANS [67], [93] model, which is an industry standard. The turbulent viscosity, μ_T, is calculated as:

$$\mu_T = \rho C_\mu \frac{k^2}{\varepsilon} \tag{3.7}$$

where C_μ is a model constant. For the turbulent kinetic energy, the equation reads:

$$\rho \frac{\partial k}{\partial t} + \rho(\boldsymbol{u} \cdot \nabla)k = \nabla \cdot \left[\left(\mu + \frac{\mu_T}{\sigma_k}\right)\nabla k\right] + P_k - \rho\varepsilon \tag{3.8}$$

where P_k is the production term:

$$P_k = \mu_T\left(\nabla \boldsymbol{u} : (\nabla \boldsymbol{u} + (\nabla \boldsymbol{u})^T)\right) - \frac{2}{3}\rho k \nabla \cdot \boldsymbol{u} \tag{3.9}$$

The equation for ε then reads:

$$\rho \frac{\partial \varepsilon}{\partial t} + \rho \boldsymbol{u} \cdot \nabla \varepsilon = \nabla \cdot \left(\left(\mu + \frac{\mu_T}{\sigma_\varepsilon}\right)\nabla \varepsilon\right) + C_{\varepsilon 1}\frac{\varepsilon}{k}P_k - C_{\varepsilon 2}\rho\frac{\varepsilon^2}{k} \tag{3.10}$$

The constants used in these equations, are determined from experiments [67]:

Table 3.2 The k-ε model constants [67].

Constant	Value
C_μ	0.09
$C_{\varepsilon 1}$	1.44
$C_{\varepsilon 2}$	1.92
σ_k	1.0
σ_ε	1.3

As with any computational model, the k-ε model relies on certain assumptions. The Reynolds number **Re** has to be high enough for the flow to be considered transitional or turbulent. The accuracy of the k-ε model at low **Re** might not be very good. Adverse pressure gradients and strongly rotating flows might not be resolved completely. In addition, the model employs wall functions for the flow near the walls, meaning that the viscous stationary layer at boundaries is not accounted for, something that might be problematic in narrow geometries. See figure 3.10 for a solution to the problem from figure 3.9 at **Re** = 3300.

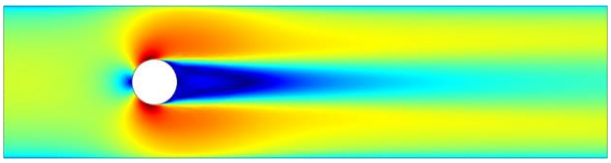

Re = 3300

Figure 3.10 The blunt-body problem is solved at a high **Re** number, using the k-ε RANS model.

3.3.3 The SST model

There exist more elaborate RANS models that resolve the disadvantages of the k-ε model, though at a higher computational cost. The Menter SST (Shear Stress Transport) model is a good example of a model that combines the robustness of the k-ε model with adequate description of the near-wall region [94]. Also, it does not depend on flow turbulence, i.e. it can solve for low **Re** numbers as well. The

mathematics behind the model are quite complex, and full details can be found in [94] and [67]. The model is formulated as follows:

$$\rho\frac{\partial k}{\partial t}+\rho\boldsymbol{u}\cdot\nabla k=P-\rho\beta_0 k\omega+\nabla\cdot\left((\mu+\sigma_k\mu_T)\nabla k\right) \tag{3.11}$$

$$\frac{\partial\omega}{\partial t}+\rho\boldsymbol{u}\cdot\nabla\omega=\frac{\rho\gamma}{\mu_T}P-\rho\beta\omega^2+\nabla\cdot\left((\mu+\sigma_\omega\mu_T)\nabla\omega\right)+2(1-f_{v1})\frac{\rho\sigma_{\omega2}}{\omega}\nabla\omega\cdot\nabla k \tag{3.12}$$

$$P=min(P_k,10\rho\beta_0 k\omega) \tag{3.13}$$

$$P_k=\mu_T\left(\nabla\boldsymbol{u}:(\nabla\boldsymbol{u}+(\nabla\boldsymbol{u})^T)\right)-\frac{2}{3}\rho k\nabla\cdot\boldsymbol{u} \tag{3.14}$$

$$\mu_T=\frac{\rho\alpha_1 k}{max(\alpha_1\omega,Sf_{v2})} \tag{3.15}$$

S is the characteristic magnitude of the mean velocity gradients:

$$S=\sqrt{2S_{ij}S_{ji}} \tag{3.16}$$

f_{v1} and f_{v2} define the model constants with the following relation:

$$\phi=f_{v1}\phi_1+(1-f_{v1})\phi_2 \text{ for } \phi=\beta,\gamma,\sigma_{k,}\sigma_\omega \tag{3.17}$$

They are interpolation functions defined as (l_w stands for the distance to the closest wall):

$$f_{v1} = tanh(\theta_1^4) \tag{3.18}$$

$$\theta_1 = min\left[max\left(\frac{\sqrt{k}}{\beta_0 \omega l_w}, \frac{500\mu}{\rho \omega l_w^2}\right), \frac{4\rho\sigma_{\omega 2} k}{CD_{k\omega} l_w^2}\right] \tag{3.19}$$

$$f_{v2} = tanh(\theta_2^2) \tag{3.20}$$

$$\theta_2 = max\left(\frac{2\sqrt{k}}{\beta_0^* \omega l_w}, \frac{500\mu}{\rho \omega l_w^2}\right) \tag{3.21}$$

In most RANS models, nothing prevents the equations for turbulent dissipation and kinetic energy (equations 3.11-3.12) from going to 0. Considering this, actual implementations require certain constraints to the turbulent viscosity, and mixing lengths:

$$l_{mix} = max\left(C_\mu \frac{k^{3/2}}{\varepsilon}, l_{mix}^{lim}\right) \tag{3.22}$$

The following model constants are defined in the SST model:

Table 3.3 The SST model constants [67].

Constant	Value
β_1	0.075
β_2	0.0828
β^*_0	0.09
γ_1	5/9
γ_2	0.44
α_1	0.31
σ_{k1}	0.85
σ_{k2}	1.0
$\sigma_{\omega 1}$	0.5
$\sigma_{\omega 2}$	0.856

3.3.4 Other turbulent models

Models of higher complexity (and lower approximation) are used when the computational power is sufficient. In LES [95] (Large Eddy Simulation) models, the Navier-Stokes equations are solved in their full form, where small turbulent oscillations are filtered out using a sub-grid model. It features no averaging in time or space, and is often utilized for high-precision fluid computations. For low **Re** numbers, direct numerical simulation (DNS) is also gaining popularity with the advancement of computer systems. In this case, the Navier-Stokes equations are solved in their full form, at Kolmogorov scale meshes and time stepping.

3.3.5 Turbulent heat flux

In gas flows, heat transfer is described by the following equation:

$$\rho C_p \frac{\partial T_g}{\partial t} + \rho C_p \boldsymbol{u} \cdot \nabla T_g - \nabla \cdot \left(k_g \nabla T_g\right) = Q \tag{3.23}$$

where ρ is the gas density, C_p is the heat capacity of the gas, k_g is the thermal conductivity of the gas, T_g is the gas temperature, $\boldsymbol{u}$ is the gas velocity vector and Q accounts for the source of gas heating.

Typical heat transfer problems involving fluids are solved using the above equation. As can be seen from the equation, the heat conductivity k_g is crucial for the heat transfer distribution, as it sets the rate of heat dissipation. Indeed, materials with low k_g are considered insulating, while materials with high k_g are conductive. In this form, heat is distributed by convection (in the case of a moving gas) and conductivity (see figure 3.11).

The case with turbulent flows is a bit more complex. By definition, turbulence is a localized flow oscillation, associated with eddies in the flow. In a computational model, where the turbulence is averaged (i.e. a turbulent model), these eddies are represented as a smooth average value of velocity and pressure.

However, when heat transfer is involved in the flow, the lack of complete turbulent flow description becomes a problem, as these turbulent eddies act as a localized heat transport enhancement. The result is that the heat is transported at a higher rate, effectively spreading the temperature gradient (see figure 3.12).

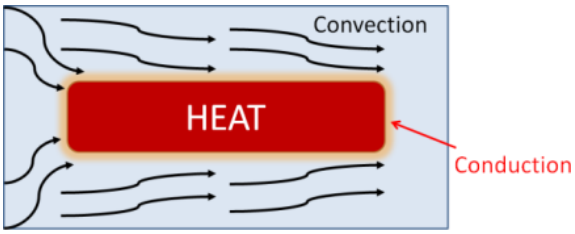

Figure 3.11 In a heated gas, energy transport consists of convection and conduction (marked by a gradient).

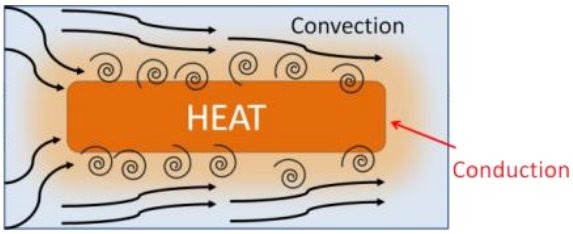

Figure 3.12 Turbulence enhances the heat transfer in a gas.

Modelling support for this effect exists, in the form of the Kays-Crawford model [96]. The model essentially calculates an additional coefficient for the heat conductivity k_T (turbulent heat conductivity) by solving for the turbulent Prandtl number Pr_T:

$$Pr_T = \left(\frac{1}{2Pr_{T\infty}} + \frac{0.3}{\sqrt{Pr_{T\infty}}} \frac{C_p \mu_T}{k_g} - \left(0.3 \frac{C_p \mu_T}{k_g} \right)^2 \left(1 - e^{-k_g/(0.3 C_p \mu_T \sqrt{Pr_{T\infty}})} \right) \right)^{-1} \tag{3.24}$$

where μ_T is the turbulent viscosity of the fluid and $Pr_{T\infty}$ is the Prandtl number at infinity (~0.85). Then, the turbulent heat conductivity is:

$$k_T = \frac{C_P \mu_T}{Pr_T} \tag{3.25}$$

The heat equation for a turbulent model is then defined as:

$$\rho C_p \frac{\partial T_g}{\partial t} + \rho C_p \boldsymbol{u} \cdot \nabla T_g - \nabla \cdot \left((k_g + k_T) \nabla T_g \right) = Q \tag{3.26}$$

3.4 Plasma modelling

"All the effects of Nature are only the mathematical consequences of a small number of immutable laws."

Pierre-Simon Laplace, 1847

The field of plasma modelling takes a considerable part of computational physics. As it deals with almost any kind of natural phenomena (particle physics, chemistry, fluid mechanics, electrodynamics…) in one self-consistent, complex system, it has drawn a lot of attention in many scientific fields. High-order plasma simulations have contributed both to the development of plasma theory and experimental techniques. In many cases, simulations are the only way of observing complex phenomena in plasmas that cannot be captured in experiments.

A theoretical, complete "model of everything", resolving every variable of every particle to the finest known scale of measure (perhaps even to Planck lengths!) would be capable of simulating almost every natural process. However, its computational cost would also be many orders of magnitude higher to what is available even in modern supercomputers, and for this reason simulation approaches of this kind are still in stand-by for a new generation of calculating machines.

Kinetic particle models are widely in use, and they can accurately predict the non-equilibrium microscopic behaviour of electrons and ions at low pressure or in very small scales, whereas macroscopic plasma properties at larger scales can be described only with approximations. 0D chemical kinetics models can employ very complex plasma chemistry involving thousands of reactions. A popular example of a chemical kinetics code is the ZDPlasKin [97] (Zero-Dimensional Plasma Kinetics) code, a kinetic plasma solver coded in Fortran. It also incorporates the BOLSIG+ Boltzmann solver, and is one of the most powerful tools available for plasma chemistry simulations.

Hybrid models [98] typically involve 2D or 3D solutions for a fluid flow (if available), coupled with selected particle kinetics. Some particles may be treated as conductive fluids. Hybrid models are often employed for high complexity problems, such as tokamak fusion reactors, but also for gas discharge plasmas.

Fluid plasma models [99] threat the plasma as a continuum fluid. Typically, the Navier-Stokes equations are solved for the flow, in full or turbulent form. This

is then coupled with macroscopic fluid equations (in 1D, 2D or 3D) governing the balance of various plasma species, as well as transport equations typically determined by drift and diffusion, also called drift-diffusion equations. Chemical reactions are incorporated as well, balancing the production and loss rates in plasma. Maxwell equations govern the electric field and potential. In addition, effects such as thermionic and field emission can be accounted for in the model. Fluid plasma models with complex chemistry, however, require a much longer calculation time than 0D chemical kinetics models. Hence, a considerable reduction in the chemistry is often needed for modelling reactor design. In addition, fluid models only work well for medium to high pressure plasmas.

For equilibrium plasmas, where $T_e = T_i$, simplified thermal models are used, also called thermal plasma models. These models are governed by the MHD [100] (Magneto-Hydro-Dynamic) equations, which are essentially a combination of Navier-Stokes equations for an electrically conductive fluid with the Maxwell equations. Since the plasma is in thermal equilibrium, it can be described by a few parameters – pressure, temperature and electrical conductivity. The chemical composition is neglected. MHD models can solve for very large systems, and are often used to describe cosmic bodies, such as galaxies, clusters, nebulae, etc [101].

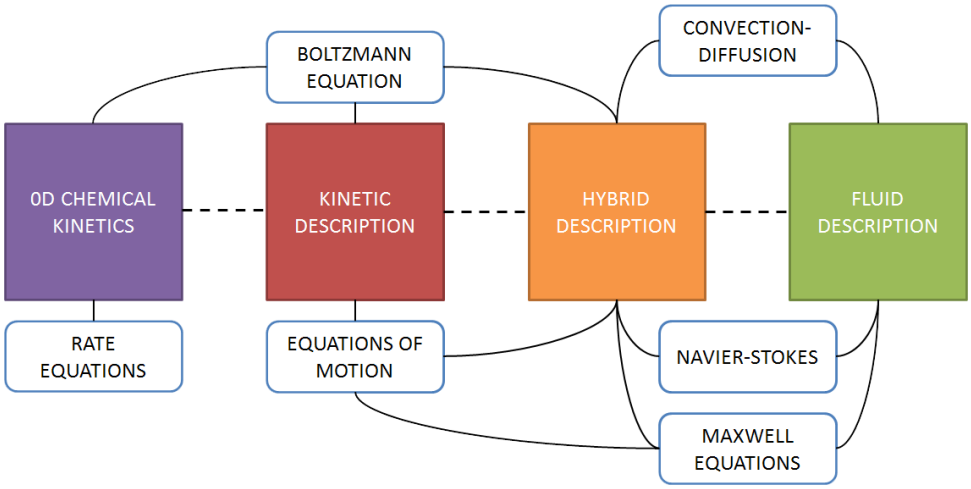

Figure 3.14 Available plasma model descriptions, with the associated equations.

As shown on figure 3.14, the two general concepts of plasma modelling – the kinetic, per-particle description, and the macroscopic, fluid description, share a number of common equations and laws.

3.4.1 The Boltzmann equation

Kinetic simulations consider the position and velocity of each particle in the plasma at the microscopic level. As such, they are the most fundamental way of describing the plasma behaviour, and, the most computationally intensive. The plasma properties are described statistically, either by following the individual behaviour of (super)particles (in a Monte Carlo or particle-in-cell – Monte Carlo approach), or by obtaining the per-particle distribution function via the Boltzmann equation [102]. This distribution function (DF) in a gas is typically defined as:

$$F_a(\boldsymbol{r}, \boldsymbol{v}, t) \tag{3.27}$$

where F_a is the distribution function, $\boldsymbol{r}$ is the particle position, $\boldsymbol{v}$ is the particle velocity, and t is the moment of time. Then, for a given volume:

$$F_a(\boldsymbol{r}, \boldsymbol{v}, t)d\boldsymbol{v} = F_a\big(x, y, z, v_x, v_y, v_z, t\big)dv_x, dv_y, dv_z \tag{3.28}$$

determines the number of particles per unit of volume (1/m^3), in point $\boldsymbol{r}$, at the moment *t*, with velocity components in the ranges $(v_x, v_x + dv_x)$, $(v_y, v_y + dv_y)$, $(v_z, v_z + dv_z)$. In plasmas, the distribution function is described by the Boltzmann equation:

$$\frac{\partial F_a}{\partial t} + \boldsymbol{v} \cdot \nabla_r F_a + \nabla_v \cdot \boldsymbol{a} F_a = \left(\frac{\partial F_a}{\partial t}\right) \tag{3.29}$$

↓	↓	↓	↓
time-dependence of DF	particle position	particle velocity	particle collisions

where F_a stands for the distribution function, $\boldsymbol{v}$ represents the particle velocity, $\boldsymbol{a}$ stands for particle acceleration, and r for the particle position. As a form of measure, the Boltzmann equation is a 6-dimensional, highly non-linear partial differential equation, i.e. solving it by direct methods is extremely difficult. Though exact solutions exist in some cases, practical methods for solving the Boltzmann equations are usually approximate, with the most common ones based on the assumption of an isotropic DF, which is usually accurate for most types of plasma.

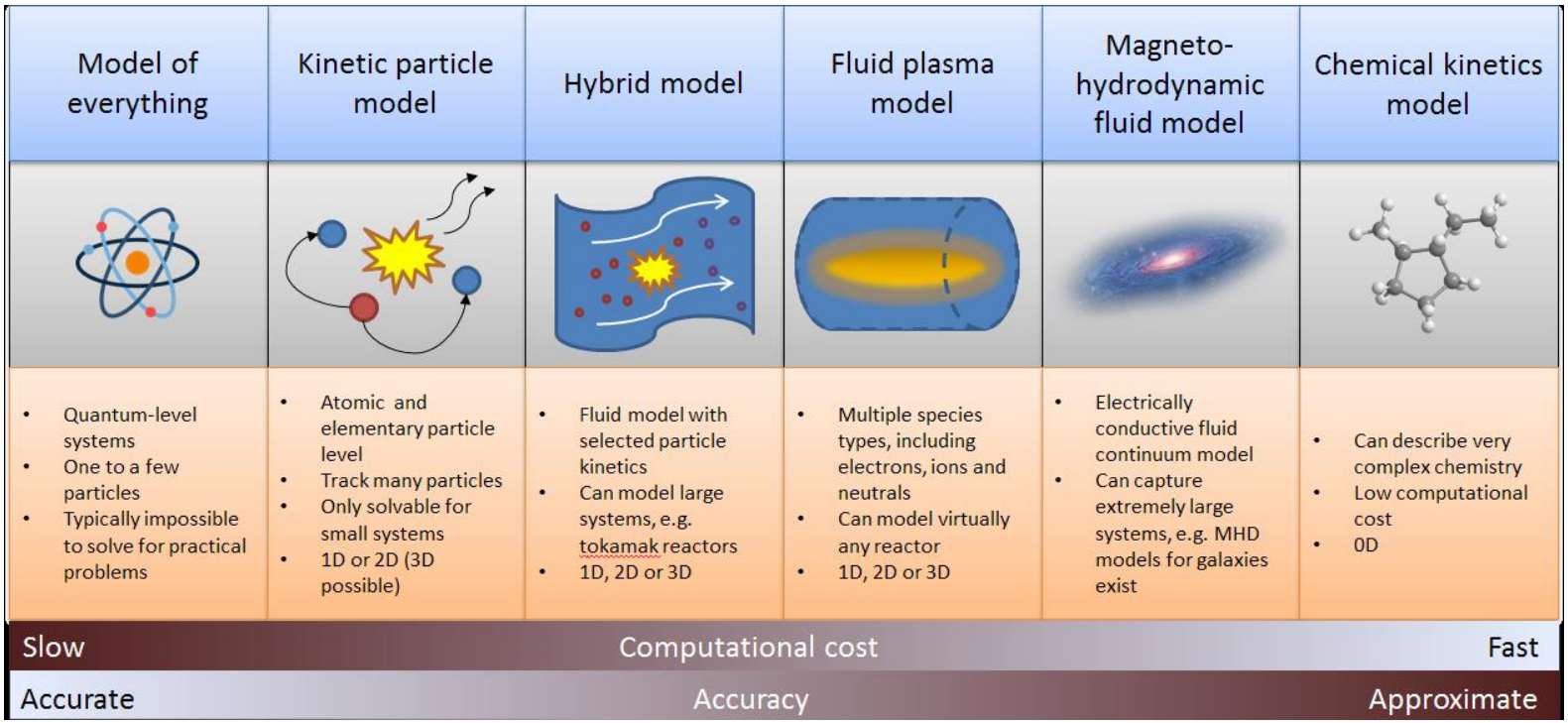

Figure 3.13 A comparison of modelling methods for particle interactions and fluids.

Note that fluid models are derived from the Boltzmann equation. They treat the plasma as a continuous fluid, instead of a group of separate particles. They are based on the first velocity moments of the Boltzmann equation. The velocity moment equations can be obtained by multiplying the Boltzmann equation with a function of the type $a(\boldsymbol{r}, \boldsymbol{v}, t)$, and integrating it over the entire velocity range, i.e. the resulting equations (for different a) are a function of $\boldsymbol{r}$ and t only, which significantly simplifies the calculation. The macroscopic plasma species are then described by their transport coefficients, such as mobility, diffusion coefficient and collision frequency. In the case of a gas flow, the Navier-Stokes (in full or turbulent form) equations are used to compute the gas flow vector, and hence the convection coefficient. The electrodynamics of the model is handled by the Maxwell equations [103]. In problems involving high plasma density with complex chemistry, fluid models are usually the most approachable computational method. Fluid plasma models can include complex plasma chemistry and non-equilibrium processes. Furthermore, fully self-consistent models can be built to replicate experiments, including the simulation of electrical circuits, electromagnetic wave propagation, heat transfer in solids, etc.

Being approximate, fluid plasma models have specific limitations. In addition to the macroscopic-only plasma description, a significant drawback of fluid models is that the EEDF (Electron Energy Distribution Function) is not computed self-consistently within the model, but has to be assumed. Most models assume a Maxwellian or Maxwellian-like EEDF distribution, though methods exist for pre-solving the Boltzmann equation for a non-Maxwellian EEDF [104]. Other physics that cannot be captured by fluid models include plasma waves and structures and small-scale non-equilibrium effects. Some models omit plasma sheaths and cathode electron emission in favour of faster computation.

3.4.2 Solving the Boltzmann equation

In order to construct a working fluid plasma model, the transport coefficients of the species need to be obtained. In addition, the reaction rates for the species production need to be pre-computed and imported in the model. Generally, the transport coefficients are calculated from the collision cross sections, a fundamental data set describing the interactions between the particles in plasma [105]. Cross sections are derived from the ratio of the fluxes of scattered particles through a ring with radius r, and the flux of incident particles within a ring that corresponds to the scattering angle. An example is shown in figure 3.15, where the cross section σ is plotted as a function of the electron energy ε.

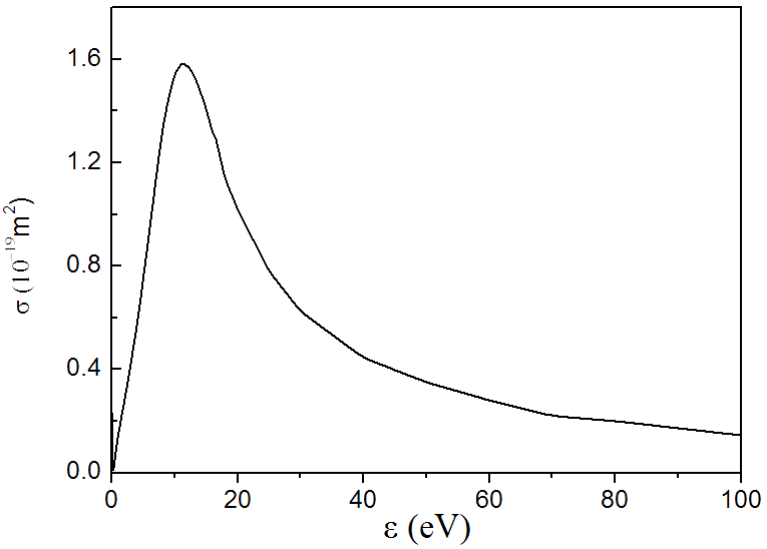

Figure 3.15 An example of an excitation cross section for argon. Obtained from LXCat.

LXCat [106] is an open-access internet resource for sharing electron and ion cross sections, transport parameters, EEDFs and other. The various cross sections used in this work were obtained from this reference.

BOLSIG+ [107] is a freely available program for computer simulation of the Boltzmann equation. It was developed by G. Hagelaar, J-P Boeuf and L. Pitchford at the Laboratoire Plasma et Conversion d'Energie in Toulouse, France. The tool is primarily intended for calculating electron transport properties and reaction rates for fluid plasma models.

The operation principle of BOLSIG+ is straightforward. First, the tool reads the provided cross section collision data. The Boltzmann equation is then solved under the drift-diffusion approximation. Furthermore, the electric field is assumed to be uniform, and there is no spatial dependence of collision probabilities (0D model). A number of parameters can be set-up, such as gas temperature, EEDF type (Maxwellian or non-Maxwellian), the average energy range, number of calculation points, etc. The output data is a file containing electron transport properties and electron impact rate coefficients. The data can be then imported in fluid models.

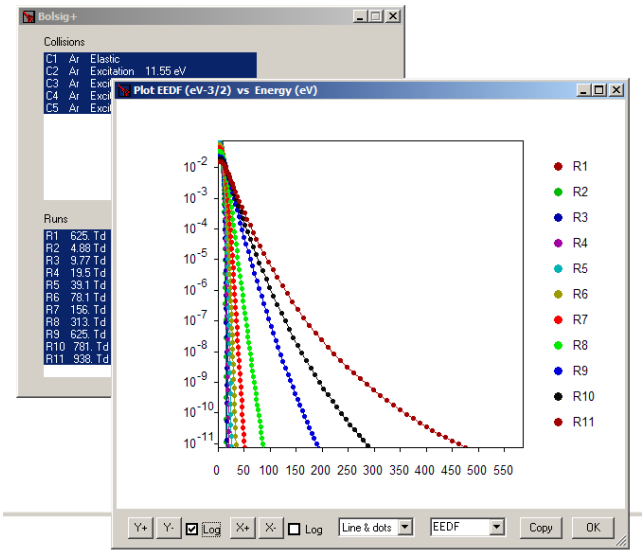

Figure 3.16 An example of the BOLSIG+ workflow.

3.4.3 Building a chemistry set

Chemistry sets define the chemical conditions in plasma for certain discharge conditions. Generally, the particle densities are calculated from the rate of production minus loss of the particles. Electron impact reaction rates can be calculated with BOLSIG+ and imported as functions in the model (see figure 3.17 for a calculated rate coefficient as a function of electron energy, from BOLSIG+).

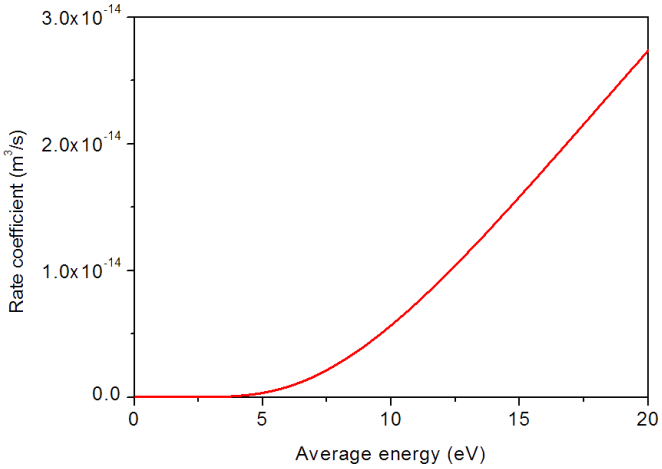

Figure 3.17 An example for an electron impact excitation rate coefficient for argon, as a function of electron energy.

The rates of reactions between heavy species (i.e., neutrals and ions) are calculated from the rate coefficients (usually temperature-dependent, adopted from literature, e.g. [108], [109], multiplied with the densities of the collision partners. Typically, rate coefficient values within a reasonable agreement between authors are sought. Chemical kinetics models are applied to study the detailed multi-body reactions [110], [111], [112]. In the present thesis, chemistry sets for argon and CO_2 plasmas are available at page 178.

3.4.4 Fluid plasma modelling

In the fluid description for plasma, the equations for particle balance take the following general form:

$$\frac{\partial n_A}{\partial t} + \overrightarrow{\nabla_r} \cdot \left(n_A \overline{\vec{v}}\right) = n_A \overline{\upsilon}_{c,production} - n_A \overline{\upsilon}_{c,loss} \tag{3.30}$$

where n_A stands for particle density and $\overline{\vec{v}}$ for average velocity. The terms on the right hand side describes the overall production and loss rates of particles in the system, where $\overline{\upsilon}_c$ stands for momentum transfer collision frequency. In the equation, the particle flux is expressed by:

$$n_A \overline{\vec{v}} = \vec{\Gamma}_A \tag{3.31}$$

The particle balance equation is usually written as:

$$\frac{\partial n_A}{\partial t} + \overrightarrow{\nabla_r} \cdot \vec{\Gamma}_A = R_A \tag{3.32}$$

where R_A stands for the net particle source term, resulting from production and loss processes. In the case of a gas flow, a convection coefficient $\overrightarrow{u_g}$ is added:

$$\frac{\partial n_A}{\partial t} + \overrightarrow{\nabla_r} \cdot \vec{\Gamma}_A + \left(\overrightarrow{u_g} \cdot \nabla\right) n_A = R_A \tag{3.33}$$

Then, under the drift-diffusion approximation, the particle flux for charged species is:

$$\vec{\Gamma}_A = -D_A \nabla n_A + \mu_A n_A \vec{E} \tag{3.34}$$

where D_A represents the diffusion coefficient, μ_A stands for the mobility coefficient, and $\vec{E}$ is the vector of the electric field accelerating the particles.

Fluid plasma models can be solved using numerous different techniques. FEM is the most common method, for its proven reliability. Though many commercial codes and software packages designed for fluid plasma models exist, any FEM or FVM solver that can handle PDEs with good precision can solve the above equations. Some examples of programs able to solve for fluid plasma models are shown below:

Table 3.4 Comparison of plasma simulation codes

Software	Method	Notes	References
Ansys Fluent	FVM	Mainly for CFD	[82]
COMSOL	FEM	Plasma module	[67]
OpenFOAM	FVM	General PDEs only	[83]
STAR-CCM+	FVM		[84]

COMSOL Multiphysics features a capable plasma module designed for fluid plasma problems. Sub-interfaces customized for microwave, ICP, CCP (Capacitively Coupled Plasma) and DC discharges are available, as well as a general drift-diffusion description. Heavy particle interactions can be included, and electrical circuits can be simulated self-consistently. Coupling with heat transfer and fluid flow is also possible. Furthermore, the module includes equilibrium discharge (ED) modelling for problems concerning thermal plasmas, such as plasma torches. By default, the drift-diffusion plasma module solves non-equilibrium plasma models including electron production and balance, as well as the balance equations for ions and excited species. Poisson's equation is solved for the potential distribution. While this is a highly accurate description that works well for most low-pressure problems, atmospheric pressure discharges represent a challenge.

3.4.5 Fluid models for gliding arcs and glow discharges

Modelling of atmospheric pressure gliding arcs with COMSOL has been performed quite successfully within PLASMANT before, though with certain limitations. A fluid plasma model was used for a gliding arc and glow discharge in [113]. The gliding arc characteristics were studied with a quasi-neutral fluid plasma model in [114] , while a quasi-neutral CO_2 plasma model was utilized for a classical gliding arc in [115]. In [99], a gliding arc discharge model was developed using the plasma module in COMSOL 4.3 (see figure 3.18). The problem was reduced to a 2D geometry (in Cartesian and axi-symmetric coordinate systems). Furthermore, the argon plasma chemistry was significantly simplified in order to run the model within the available computational power.

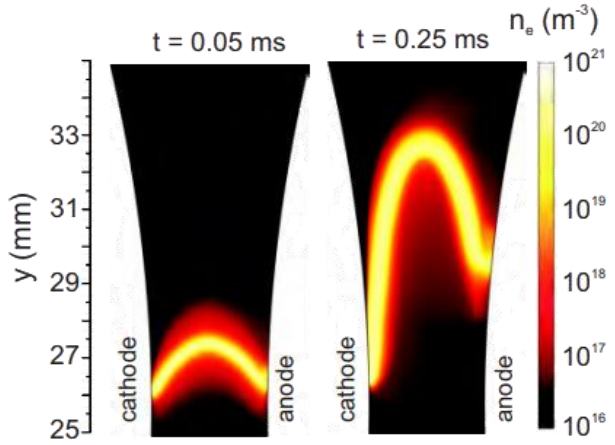

Figure 3.18 A simulated gliding arc in COMSOL, adopted from [99].

The main problem in atmospheric pressure DC discharge modelling is in the high plasma density and strong density gradients near walls and electrodes. The typical number density of electrons in an atmospheric pressure DC discharge is in the range 10^{19}-10^{22} m^{-3}. While this can be handled generally well in the charge-neutral plasma bulk (quasi-neutral region), electron and ion densities near surfaces tend to diverge in the range of a few μm down to the nm range. This effect is illustrated in figures 3.19 and 3.20 below.

The plasma sheath, also called Debye sheath (see figure 3.20), is a region in the plasma with higher concentration of ions than electrons. Hence, instead of being neutral, this region shows a positive space charge. A Debye sheath forms due to the significant differences in the transport properties of ions and electrons.

At barrier surfaces, the faster and lighter electrons deplete much faster than ions, forming a positively charged region.

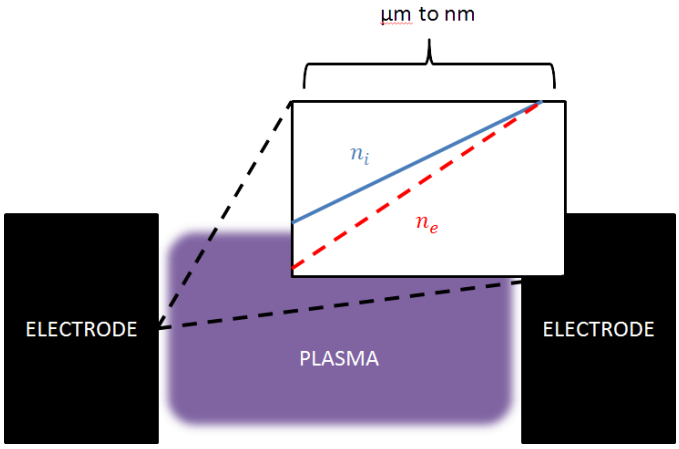

Figure 3.19 A schematic example of ion and electron densities in the plasma sheath.

Typically, plasma sheaths are several Debye lengths thick. The Debye length is:

$$\lambda_D = \sqrt{\frac{\varepsilon_0 k_B / q_e^2}{\frac{n_e}{T_e} + \Sigma_j z_j^2 n_j / T_i}} \tag{3.35}$$

where ε_0 is the permittivity of free space, k_B is the Boltzmann constant, q_e is the electron charge, T_e and T_i are the electron and ion temperature, respectively (in K), n_j is the species density for ions with charge $z_j q_e$, and n_e is the electron density. It is easy to see that at moderate to high plasma density, which is the case of DC atmospheric pressure discharges, this length can be quite short, down to the nm range.

Naturally, this effect increases the computational load of a fluid model, as it needs very fine mesh elements to be resolved. As an example, in [104], a Langmuir probe was simulated, where the plasma sheath was in the order of µm

at the probe surface (see figure 3.21). Consequently, mesh elements in the order of 100 nm were required in this region.

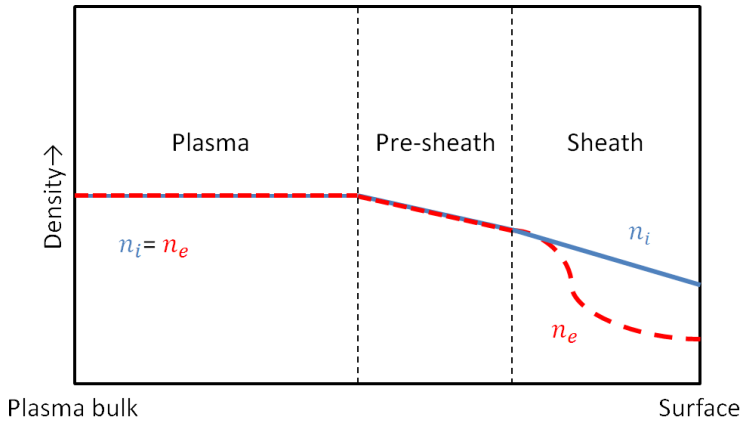

Figure 3.20 Ion and electron densities in a plasma reactor.

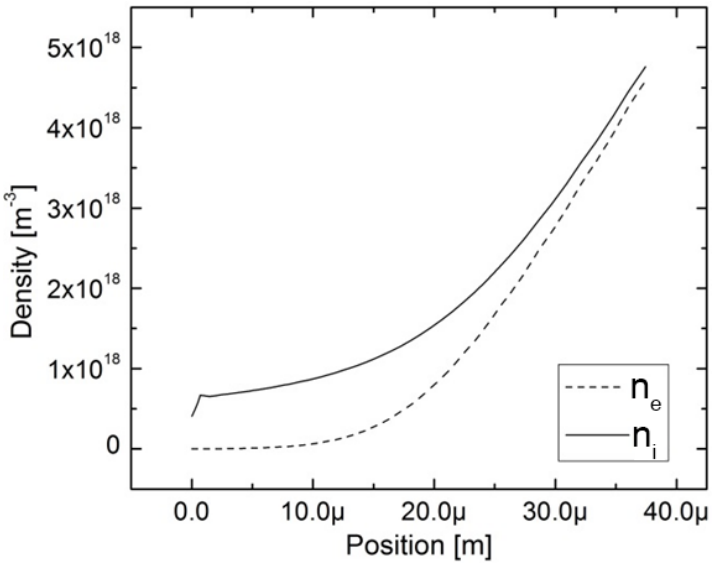

Figure 3.21 Modelled electron and ion density as a function of distance from the surface, for $n_e = 1.98\ 10^{20}\ m^{-3}$ and $T_e = 1$ eV [104].

High mesh density requirements generally render the models unsolvable in 3D, which is needed for the simulating the reverse-vortex gliding arc plasmatron, i.e., the subject of this PhD thesis. Using a more complex chemistry, e.g. CO_2 instead of argon, poses also a significant problem with the full fluid description [116].

For the plasma reactor models developed in this PhD thesis, the focus is on the main plasma bulk, and the plasma sheath is not of high importance, and can be neglected. Typically, the size of the neutral discharge itself is several orders larger than the non-neutral sheath region. Furthermore, micro-scale processes, such as sheath ionization, contribute little to none to plasma-chemical processes, such as CO_2 conversion. The voltage drop over the plasma sheath can also be neglected in most cases, as in atmospheric pressure DC discharges it is typically very low compared to the overall plasma voltage drop. This led to the development of a quasi-neutral (QN) fluid plasma model, which assumes equal electron and ion density throughout the entire, discharge, and hence which does not require to solve the electron balance equation, as well as the Poisson equation [117]. With the assumption of $n_i = n_e$, the plasma sheath formation can be neglected.

3.4.6 The quasi-neutral plasma model

As already explained, the quasi-neutral plasma model is a fluid plasma model with the basic assumption that the ion density (with the sum over all ions) equals the electron density, i.e. $n_i = n_e$. Furthermore, instead of the Poisson equation, the problem is reduced to the charge conservation equation, as shown below. The model is further detailed, and compared to non-quasi-neutral models in [117].

The derivation is done here for argon plasma. Assuming the drift-diffusion approximation, we start with the electron balance equation, which reads:

$$\frac{\partial n_e}{\partial t} + \nabla \cdot \left(-\mu_e n_e \vec{E} - D_e \vec{\nabla} n_e\right) + \left(\overrightarrow{u_g} \cdot \vec{\nabla}\right) n_e = R_e \tag{3.36}$$

where n_e stands for the electron density, μ_e for electron mobility coefficient, D_e for electron diffusion coefficient, $\overrightarrow{u_g}$ for the gas velocity vector, and R_e is the electron production term. The positive ion balance equation reads:

$$\frac{\partial n_i}{\partial t} + \nabla \cdot \left(\mu_i n_i \vec{E} - D_i \vec{\nabla} n_i\right) + \left(\overrightarrow{u_g} \cdot \vec{\nabla}\right) n_i = R_i \tag{3.37}$$

where n_i stands for the ion density, μ_i for ion mobility coefficient, D_i for ion diffusion coefficient, $\overrightarrow{u_g}$ for the gas velocity vector, and R_i is the ion production term. Note the different sign for the ion and electron mobility, as ions are with

positive charge. For convenience, electron and ion fluxes will be written as follows:

$$\left(-\mu_e n_e \vec{E} - D_e \vec{\nabla} n_e\right) = \overrightarrow{G_e} \tag{3.38}$$

where $\overrightarrow{G_e}$ is the flux of electrons.

$$\left(\mu_i n_i \vec{E} - D_i \vec{\nabla} n_i\right) = \overrightarrow{G_i} \tag{3.39}$$

where $\overrightarrow{G_i}$is the flux of positive ions.

Since the production of ions and electrons is assumed to be equal, we subtract equation (3.36) from equation (3.37):

$$\frac{\partial(n_i - n_e)}{\partial t} + \nabla \cdot \left(\overrightarrow{G_i} - \overrightarrow{G_e}\right) + \left(\overrightarrow{u_g} \cdot \vec{\nabla}\right)(n_i - n_e) = R_i - R_e \tag{3.40}$$

We multiply each side of the equation by the elementary electron charge $|q_e|$. Then, the equation reads:

$$|q_e|\frac{\partial(n_i - n_e)}{\partial t} + \nabla \cdot |q_e|\left(\overrightarrow{G_i} - \overrightarrow{G_e}\right) + |q_e|\left(\overrightarrow{u_g} \cdot \vec{\nabla}\right)(n_i - n_e) = 0 \tag{3.41}$$

We can simplify and re-group some parts:

$$|q_e|\left(\overrightarrow{G_i} - \overrightarrow{G_e}\right) = |q_e|\left(\mu_i n_i \vec{E} - D_i \vec{\nabla} n_i - \left(-\mu_e n_e \vec{E} - D_e \vec{\nabla} n_e\right)\right) \tag{3.42}$$

$$= |q_e|\left(\mu_i n_i \vec{E} - D_i \vec{\nabla} n_i + \mu_e n_e \vec{E} + D_e \vec{\nabla} n_e\right) \tag{3.43}$$

$$= |q_e|\left(\mu_i n_i \vec{E} + \mu_e n_e \vec{E} - D_i \vec{\nabla} n_i + D_e \vec{\nabla} n_e\right) \tag{3.44}$$

$$= |q_e|\left(\vec{E}(\mu_i n_i + \mu_e n_e) - D_i \vec{\nabla} n_i + D_e \vec{\nabla} n_e\right) \tag{3.45}$$

The plasma conductivity σ is calculated from the mobility coefficients of the charge carriers:

$$\sigma = |q_e|(\mu_i n_i + \mu_e n_e) \tag{3.46}$$

Taking into account Poisson's equation:

$$\Delta\varphi = -\vec{\nabla} E \tag{3.47}$$

we can rewrite equation (3.41):

$$|q_e| \frac{\partial(n_i - n_e)}{\partial t} + \vec{\nabla}\left[-\sigma\vec{\nabla}\varphi - |q_e|\left(D_i \vec{\nabla} n_i + D_e \vec{\nabla} n_e\right)\right] = 0 \tag{3.48}$$

In the case of ambipolar (quasi-neutral) plasma, the charge density is assumed to be 0. Then, the equation reads:

$$\vec{\nabla} \cdot \left[-\sigma\vec{\nabla}\varphi - |q_e|\left(D_i \vec{\nabla} n_i + D_e \vec{\nabla} n_e\right)\right] = 0 \tag{3.49}$$

and is now the equation of current conservation for quasi-neutral plasma.

In order to derive the balance equations, we follow [118] and [119]. We assume that the thermal diffusion of electrons and ions is negligible:

$$\nabla D_e \nabla n_e \approx D_e \Delta n_e \tag{3.50}$$

$$\nabla D_i \nabla n_i \approx D_i \Delta n_i \tag{3.51}$$

With the assumption of $n_i \approx n_e$, we can denote $n_i = n_e = n_{pl}$ and rewrite equations (3.36) and (3.37) in the following form:

$$\frac{\partial n_{pl}}{\partial t} + \nabla \cdot \left(\vec{E}\left(\mu_i n_{pl}\right) - D_i \vec{\nabla} n_{pl}\right) + \left(\overrightarrow{u_g} \cdot \vec{\nabla}\right) n_{pl} = R_i \tag{3.52}$$

$$\frac{\partial n_{pl}}{\partial t} + \nabla \cdot \left(\vec{E}\left(-\mu_e n_{pl}\right) - D_e \vec{\nabla} n_{pl}\right) + \left(\overrightarrow{u_g} \cdot \vec{\nabla}\right) n_{pl} = R_e \tag{3.53}$$

We can then compare the two equations:

$$\begin{aligned} &\frac{\partial n_{pl}}{\partial t} + \nabla \cdot \left(\vec{E}\left(\mu_i n_{pl}\right) - D_i \vec{\nabla} n_{pl}\right) + \left(\overrightarrow{u_g} \cdot \vec{\nabla}\right) n_{pl} - R_i \\ &\qquad = \frac{\partial n_{pl}}{\partial t} + \nabla \cdot \left(\vec{E}\left(-\mu_e n_{pl}\right) - D_e \vec{\nabla} n_{pl}\right) + \left(\overrightarrow{u_g} \cdot \vec{\nabla}\right) n_{pl} - R_e \end{aligned} \tag{3.54}$$

Most of the terms cancel each other, yielding:

$$\nabla \cdot \left(\vec{E}\left(\mu_i n_{pl}\right) - D_i \vec{\nabla} n_{pl}\right) = \nabla \cdot \left(\vec{E}\left(-\mu_e n_{pl}\right) - D_e \vec{\nabla} n_e\right) \tag{3.55}$$

As already noted, we assume that $n_i = n_e$, and also $\overrightarrow{G_e} = \overrightarrow{G_i}$:

$$\left(\mu_i n_{pl}\right)\vec{E} - D_i \nabla n_{pl} = \left(-\mu_e n_{pl}\right)\vec{E} - D_e \nabla n_{pl} \tag{3.56}$$

$$\left(\mu_i n_{pl}\right)\vec{E} - \left(-\mu_e n_{pl}\right)\vec{E} = D_i \nabla n_{pl} - D_e \nabla n_{pl} \tag{3.57}$$

$$\left(\mu_i n_{pl} + \mu_e n_{pl}\right)\vec{E} = D_i \nabla n_{pl} - D_e \nabla n_{pl} \tag{3.58}$$

$$\left(\mu_i n_{pl} + \mu_e n_{pl}\right)\vec{E} = (D_i - D_e) \nabla n_{pl} \tag{3.59}$$

Therefore, the ambipolar electric field is:

$$\overrightarrow{E_a} = \frac{(D_i - D_e) \nabla n_{pl}}{(\mu_i + \mu_e) n_{pl}} \tag{3.60}$$

We can define the ambipolar diffusion coefficient with the relation:

$$D_a = \frac{D_i - D_e}{(\mu_i + \mu_e)n_{pl}} \tag{3.61}$$

yielding:

$$\overrightarrow{E_a} = D_a \nabla n_{pl} \tag{3.62}$$

We can then re-write the following, replacing $\vec{E}$ by $\overrightarrow{E_a}$::

$$\frac{\partial n_i}{\partial t} + \nabla \cdot \left(\vec{E}(\mu_i n_i) - D_i \vec{\nabla} n_i\right) + \left(\overrightarrow{u_g} \cdot \vec{\nabla}\right) n_i = R_i \tag{3.63}$$

$$\frac{\partial n_i}{\partial t} + \nabla \cdot \left((\mu_i n_i) D_a \nabla n_i - D_i \vec{\nabla} n_i\right) + \left(\overrightarrow{u_g} \cdot \vec{\nabla}\right) n_i = R_i \tag{3.64}$$

$$\frac{\partial n_i}{\partial t} + \nabla \cdot \left(\nabla n_i (\mu_i n_i D_a - D_i)\right) + \left(\overrightarrow{u_g} \cdot \vec{\nabla}\right) n_i = R_i \tag{3.65}$$

We denote:

$$\mu_i n_i D_a - D_i = D_{ai} \tag{3.66}$$

Therefore:

$$\frac{\partial n_i}{\partial t} + \nabla \cdot (\nabla n_i D_{ai}) + \left(\overrightarrow{u_g} \cdot \vec{\nabla}\right) n_i = R_i \tag{3.67}$$

Electron transport properties are typically much higher than the ones of ions:

$$\mu_e \gg \mu_i \tag{3.68}$$

$$D_e \gg D_i \tag{3.69}$$

Therefore, we can assume that:

$$(\mu_i + \mu_e)n_{pl} = \mu_e n_{pl} \tag{3.70}$$

The excited species balance equation requires no further modifications, as it is charge neutral:

$$\frac{\partial n_*}{\partial t} + \nabla \cdot \left(D_* \vec{\nabla} n_*\right) + \left(\overrightarrow{u_g} \cdot \vec{\nabla}\right) n_* = R_* \tag{3.71}$$

The averaged electron energy balance equation reads:

$$\begin{aligned} \frac{\partial n_e \bar{\varepsilon}_e}{\partial t} + \nabla \cdot \left(D_{\varepsilon,e} \vec{\nabla}(n_e \bar{\varepsilon}_e) - \mu_{\varepsilon,e} n_e \bar{\varepsilon}_e \vec{E}\right) + \left(\overrightarrow{u_g} \cdot \vec{\nabla}\right) n_e \bar{\varepsilon}_e \\ = |q_e| \vec{E} \cdot \overrightarrow{G_e} + n_e \Delta \bar{\varepsilon}_e + Q_{bg} \end{aligned} \tag{3.72}$$

In the equation above, the electron energy flux is:

$$\vec{G}_{\varepsilon,e} = D_{\varepsilon,e} \vec{\nabla}(n_e \bar{\varepsilon}_e) - \mu_{\varepsilon,e} n_e \bar{\varepsilon}_e \vec{E} \tag{3.73}$$

where $D_{\varepsilon,e}$ stands for the electron energy diffusion coefficient, $\mu_{\varepsilon,e}$ is the electron energy mobility, and $\vec{E} = \vec{E}_{amb}$, which is already known. In the equation, $|q_e| \vec{E} \cdot \overrightarrow{G_e}$ is the electromagnetic heating term, $n_e \Delta \bar{\varepsilon}_e$ accounts for the averaged electron elastic and inelastic energy losses upon collisions, and Q_{bg} stands for additional background heating, a common modelling approach to reduce the slope of the gradient [99], [120]. The following relations are applied:

$$\mu_{\varepsilon,e} = \frac{5}{3} \mu_e \tag{3.74}$$

$$D_{\varepsilon,e} = \frac{2}{3} \mu_e \bar{\varepsilon}_e \tag{3.75}$$

With the above equations, the species and electron balance equations are complete. For the gas thermal balance, the heat equation is applied:

$$\rho C_p \frac{\partial T_g}{\partial t} + \rho C_p \boldsymbol{u} \cdot \nabla T_g - \nabla \cdot \left(\left(k_g + k_T \right) \nabla T_g \right) = Q \tag{3.76}$$

where Q accounts for heating from elastic and inelastic collisions between the heavy particles and the plasma, i.e. Joule heating.

3.5. Boundary conditions

Boundary conditions are constraint expressions, necessary to obtain a solution for a given differential equation. For instance, in order to solve the Navier-Stokes equations in a given volume, an inlet has to be defined, either with a velocity or pressure constraint, as well as an outlet, and walls (where the velocity is zero). An example is shown in figure 3.22 and the mathematical expressions in table 3.4.

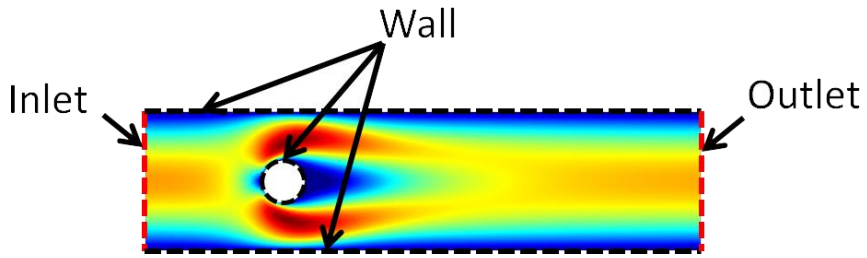

Figure 3.22. Boundary conditions for fluid flows.

Table 3.5. Boundary conditions for flow models

Boundary	Expression	Note
Walls	$\overrightarrow{u_g} = 0$	Zero velocity
Inlet	$\vec{u} = -u_0 \vec{n}$	Velocity
Outlet	$\left[-p\vec{I} + (\mu + \mu_T) \left(\nabla \overrightarrow{u_g} + \left(\nabla \overrightarrow{u_g} \right)^T \right) - \frac{2}{3} (\mu + \mu_T) (\nabla . \overrightarrow{u_g}) \vec{I} - \frac{2}{3} \rho k_T \vec{I} \right] \vec{n} = -\widehat{p_0} \vec{n}$	Pressure

See Navier-Stokes equations (3.3 and 3.4)

On figure 3.23, the main boundary conditions governing plasma models (specific to DC discharges) are shown. The corresponding mathematical expressions can be found in table 3.5, for particle balance equations and heat transfer.

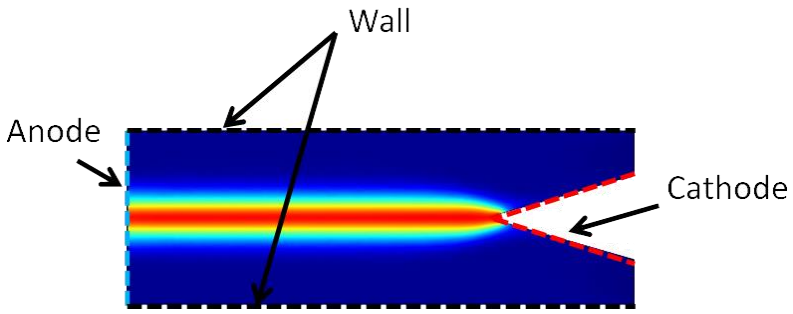

Figure 3.23. Boundary conditions for plasma models.

Table 3.6. Boundary conditions for plasma models

Boundary	Expression	Note
Walls[1]	$-\vec{n}\cdot\left(-D_i\nabla n_i-\mu_i n_i\overrightarrow{E_{amb}}\right)=0$	No flux
Walls[2]	$-\vec{n}\cdot\left(-\mu_{\varepsilon,e}n_e\overrightarrow{E_{amb}}-D_{\varepsilon,e}\nabla(n_e\bar{\varepsilon}_e)\right)=0$	No flux
Walls[3]	$-\vec{n}\cdot(D_*\nabla n_*)=0$	No flux
Walls[4]	$-\vec{n}\cdot\left(-k\nabla T_g\right)=0$	Adiabatic walls
Cathode[5]	U	Voltage
Anode[5]	$0V$	Ground

[1]Ion balance equation (3.37)

[2]Electron energy balance equation (3.72)

[3]Excited species balance equation (3.71)

[4]Heat transfer equation (3.76)

[5]Current conservation equation (3.49)

3.6. Coordinate systems

For a given model, the choice of a coordinate system and dimensionality depends on the problem complexity and accuracy requirements. Some 3D problems are reduced to 2D, which reduces the calculation time by an order of magnitude (required for large chemistry sets). The following coordinate systems were used for the different flow and plasma models in this thesis:

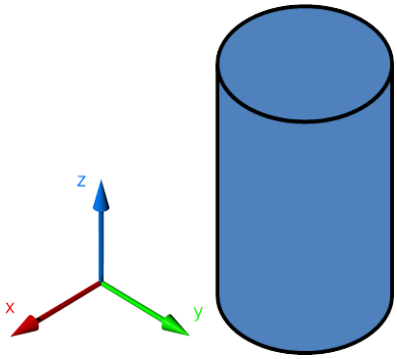

3D Cartesian

$f(x, y, z)$

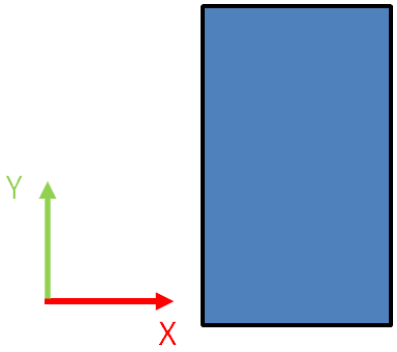

2D Cartesian

$f(x, y)$

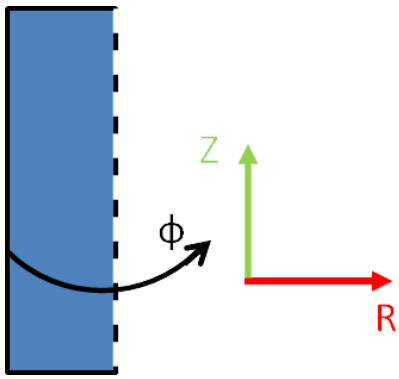

2D Axisymmetric: axial symmetry on dashed line.

$f(r, z, \phi)$

Figure 3.24. 3D, 2D and 2D axi-symmetric coordinate systems.

3.7 Models developed in this thesis

During this work, a large emphasis was put on the development of models that replicate experiments with the highest possible precision. While many studies in computational low-temperature plasma rely on 0D models with a number of assumptions in the time and spatial domains (i.e. plug flow reactor model), here a 1:1 replication was pursued with 2D/3D geometries, precise flow calculations and accounting for adjunct effects, such as the turbulent heat flux.

In Chapter IV, a 3D model of a gliding arc plasma with argon chemistry is developed, and compared with the available literature. The concept of reverse-vortex insulation is demonstrated, capturing the plasma movement and stabilization.

Chapter V is a natural extension of the 3D argon model of Chapter IV, with actual reactor geometry of the gliding arc plasmatron (GAP) available within PLASMANT, and turbulent heat transfer effects. Furthermore, a 2D CO_2 model for this GAP is implemented for a complete reactor analysis.

In Chapter VI, extensive diagnostics are performed for an APGD reactor, and simultaneously, it is simulated using a 2D axi-symmetric argon model. A clear-cut validation of the simulated gas temperature is obtained.

In Chapter VII, the APGD reactor is modelled using a 2D axi-symmetric CO_2 model. Again, a validity check is performed, in this case on the reactor conversion performance. Moreover, based on fluid simulations, reactor improvements are predicted and confirmed by experiments.

Finally, Chapter VIII presents a new vortex flow reactor design, called “dual vortex gliding arc”, commemorating a complete reactor design/simulation method.

CHAPTER IV. A 3D model of a reverse-vortex flow gliding arc reactor

This work is published as:
G Trenchev, St Kolev and A Bogaerts, A 3D model of a reverse vortex flow gliding arc reactor, *Plasma Sources Science and Technology*, **25**-3, 035014, 2016

Abstract

In this Chapter, a gliding arc (GA) plasma reactor with a reverse-vortex flow (RVF) stabilization is modelled by means of a fluid plasma description. The plasma reactor is operating with argon gas at atmospheric pressure. The gas flow is simulated using the k-ε RANS turbulent model. A quasi-neutral fluid plasma model is employed for computing the plasma properties. The plasma arc movement in the reactor is observed, and the results for the gas flow, electrical characteristics, plasma density, electron temperature, and gas temperature are analyzed.

4.1 Model description

The model uses a simplified geometry, which is shown in figure 4.1, along with its finite – element mesh in figure 4.2. A cylinder with a radius of 6 mm and a height of 5 mm represents the plasma chamber. There are 4 tangential gas inlets, each with radius of 0.8 mm, and one axial outlet at the top, with radius of 2.5 mm. All chamber edges are smooth in order to prevent strong velocity gradients and turbulent eddies. This geometry is based on the RVF gliding arc (GA) reactor concept presented in [19].

The gas flow rate ranges from 20 to 50 L/min in the model. The velocity magnitudes go up to 300 m/s inside the reactor, suggesting a highly turbulent gas flow.

As explained in Chapter III (section 3.3), in fluid and gas flows, turbulence stands for rapid oscillations of velocity and pressure, varying over a wide range both in space and time. Contrary to laminar flows, which are quite predictive, turbulent flows are much more chaotic in nature, requiring a greater amount of computing power to be solved numerically.

Gas flow models are usually based on solving the Navier-Stokes equations by means of a discretization mesh [69]. As the flow speed increases, so does the level of turbulence in the flow, resulting in more frequent and denser turbulent oscillating eddies, which require a smaller finite mesh in order to obtain a solution. Such computation is beyond reach, even for modern workstation computer systems. In fact, solving turbulent flows in 3D using the Navier-Stokes equations in their full form still requires supercomputer facilities.

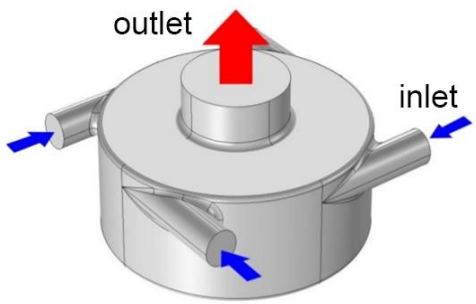

Figure 4.1 RVF gliding arc reactor geometry.

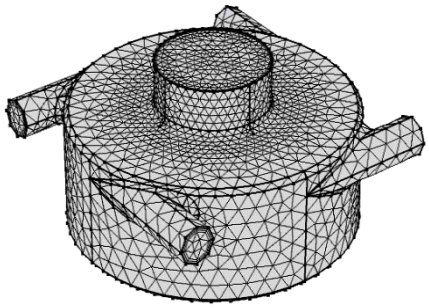

Figure 4.2 RVF gliding arc reactor finite element mesh.

Combined with the plasma model itself, it is clear that this approach would drastically exceed the available computational resources. For this reason, the gas flow is simulated using the so-called k-ε Reynolds-averaged-Navier-Stokes (RANS) turbulent modelling technique, which effectively averages all fluctuating turbulent quantities over time, greatly reducing the computational cost (see details in Chapter III above).

Besides the mass and momentum continuity equations, also the heat equation for the gas thermal balance needs to be solved, which reads as follows:

$$\rho C_p \frac{\partial T_g}{\partial t} + \rho C_p \overrightarrow{u_g} \cdot \nabla T_g - \nabla \cdot \left(k_g \nabla T_g \right) = Q \tag{4.1}$$

where ρ is the gas density, C_p is the heat capacity of the gas, k_g is the temperature-dependent gas thermal conductivity (based on a material look-up table), T_g is the gas temperature and Q accounts for the gas heating due to elastic and inelastic collisions between electrons and heavy particles in the plasma. In order to reduce the computation time, the gas flow model was solved first as a stationary problem and the obtained velocity field and turbulent energy dissipation were used in the plasma model coupled with the gas heating (eq. 4.1). Thus, the model does not consider the hydrodynamic influence of the gliding arc on the gas flow.

The model was computed within its full geometry with nearly 150,000 tetrahedral elements in the complete mesh, with element sizes ranging from 0.3 to 0.7 mm (see figure 4.2). The mesh is denser near the outlet, where the plasma arc is observed.

4.2 Quasi-neutral plasma model

Modelling atmospheric plasmas in 3D is a very challenging task. Often these models consider a discharge at thermal equilibrium, where the gas temperature and electron temperature are equal [121]. However, the GA exhibits a very complicated structure and behavior, including equilibrium and non-equilibrium stages, arc decay and re-ignition, and a complex arc body [122]. A thermal model would not provide the important plasma parameters for the given problem. On the other hand, describing the plasma using a complete fluid model in 3D would

require a very long computational time [99]. In particular, the Debye sheaths formed at the cathode and the anode of the reactor present a significant problem, as they require a very fine finite element mesh (in the order of micrometers) to be solved correctly. For this reason, we have developed a simplified quasi-neutral model, where the ion and electron densities are equal, and thus no Debye sheath can be formed. This approach is explain in detail in Chapter III above, and was also evaluated for a classical GA, with very satisfying results, concluding that the sheath process has no significant influence on the final solution for the arc column [117]. The quasi-neutral model simultaneously solves the equations for the plasma density, electron and gas temperature and electric fields as a function of time (see Chapter III).

The initial streamer stage of the arc is omitted, as it requires additional modelling effort. Instead, an artificial plasma heating function is induced at the initial arc position, creating a temporary plasma channel for the arc to ignite. Once the arc is initiated, the artificial heating is removed, leaving the arc to be sustained only by the electric current flowing through the plasma. The streamer stage of an atmospheric pressure discharge is a very short process in the order of nanoseconds, and should not influence the operating properties of the GA reactor [19].

In figures 4.3 and 4.4, the plasma heating function shape in the reactor and its time dependence are plotted. The function has a maximum at 9.5×10^{-6} s, and is equal to zero after 1.05×10^{-5} s. Applying this artificial plasma heating function does not influence the obtained results. Indeed, numerical tests showed that the arc characteristics after 100 μs do not depend on the initial breakdown process, provided that it is considerably shorter (10 times here) and it does not deposit considerable amount of energy (much lower than the arc energy deposition). The total amount of energy deposited by the artificial heating function amounts to 10^{-6} J, while the actual arc deposits 0.01 J for 100 μs, when the arc is already independent from the heating function.

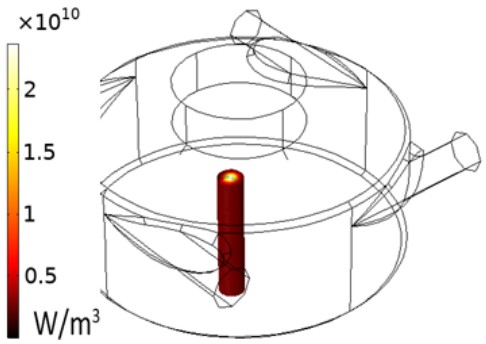

Figure 4.3. Artificial heat function shape – a straight column with a Gaussian distribution of the power density.

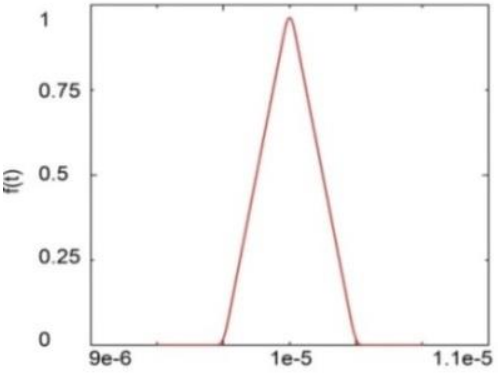

Figure 4.4. Artificial heat function as a function of time.

To further limit the calculation time of the model, the chemistry reaction set is significantly reduced compared to what is mostly used with argon discharge modelling [99]. Only one type of ions and one type of excited species are considered. The mathematical description of the model is based on [123] and [118], and was presented in Chapter III above. The plasma heating and the electron temperature are a result of the applied electric field, but the particle motion due to the electric field is not considered. In addition, no particle flux is permitted at boundary areas. Finally, the reduced set of electron collisions is given in Table 4.1:

Table 4.1. Electron impact reaction set assumed in the model, with the references where the rate coefficients are adopted from.

Reaction	Rate coefficient	Ref.
$\mathbf{e + Ar \rightarrow e + Ar}$	BS[a]	[106]
$\mathbf{e + Ar \rightarrow e + Ar(4s)}$	BS	[106]
$\mathbf{e + Ar(4s) \rightarrow 2e + Ar^+}$	BS	[106]
$\mathbf{Ar^+ + e + Ar \rightarrow Ar + Ar}$	$k\left(m^6/s\right) = 1.5 \times 10^{-40}\left(\frac{T_g}{300}\right)^{-2.5}$ [b]	[99]

[a]Boltzmann solver, [b]T_g in K

4.4 Electrical circuit

The scheme in figure 4.5 represents the electrical circuit of the GA RVF reactor. The bottom boundary (see also figure 4.1) of the reactor is the cathode, connected to a ballast resistor, which in turn is connected to a voltage source supplying 1000 V. The boundary at the top (see also figure 4.1), where the outlet is located, is the anode, or the grounded electrode. Such a configuration represents a flat-type electrode RVF reactor. The current is limited by a ballast resistor (Rb), and a 100 pF capacitor (Cb) forms an RC filtering circuit. The total current for the system is varied by changing the value for the ballast resistor.

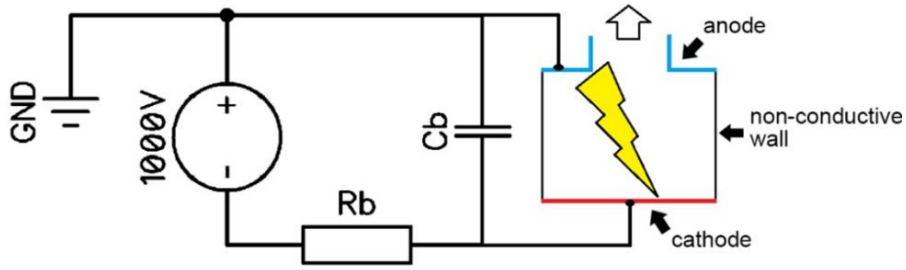

Figure 4.5. Representative electrical scheme of the GA reactor.

4.5 Equations solved in the model

The boundary conditions implemented in the model can be seen in Chapter III, on page 55. The model is structured in several computational interfaces in COMSOL [67], each describing a different physical process, but sharing common variables. The Navier-Stokes equations (3.3, 3.4 in Chapter III) are solved by the Fluid Flow interface. The equations governing particle flux and density (3.36), electron energy balance (3.71), the gas heat balance equation (3.75) and the current conservation equation (3.48) are implemented through the Mathematics interface. Eq. (3.35) is not computed because the electron density is assumed to be equal to the ion density in this quasi-neutral model. The reactor walls do not permit heat conduction, i.e. they act as insulators and their thermal balance is not considered. This is an approximation of the model, which we had to apply, mainly because of computational limitations. The reactor outlet permits convective heat flux only. An additional differential equation solves for the electrical circuit (figure 4.5). As is the case with flows under high rotation, a significant reverse back-flow can be expected at the reactor outlet. In practice, this flow is suppressed by the buoyancy

force caused by the hot gas. However, we do not consider the buoyancy force in the model. Therefore, the back-flow is suppressed in our model. The final solution for the plasma is derived as a multiphysics compilation.

4.6 Results and Discussion

4.6.1 Gas flow

The gas flow is computed as a stationary solution within COMSOL. With 150,000 tetrahedral mesh elements, the velocity streamlines and the pressure gradient are accurate enough for the purpose of the present study.

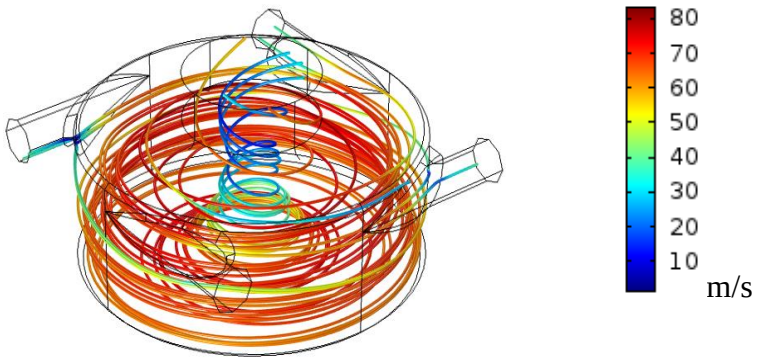

Figure 4.6 Gas velocity streamlines, for a flow rate of 22 L/min.

In figure 4.6, the gas velocity streamlines are plotted in the 3D geometry. Notice the formation of a reverse-vortex in the middle, with lower velocity magnitude, leaving the reactor through the outlet. Figure 4.7 illustrates the values of the velocity in a vertical and horizontal cross section of the reactor. The flow velocity has its maximum value at the midpoint between the side walls and the reactor center. At the center, where the inner reverse-vortex is formed, the velocity is at minimum. Back-flows at the outlet are almost completely suppressed.

As described before, the gas flow coming from the tangential inlets forms a high-velocity peripheral stream along the walls. The tangential inlets essentially act as a swirl generator. As the flow reaches the bottom of the reactor, a new vortex is formed in the reactor center (see figure 4.6). The inner vortex rotates in

the same direction as the outer vortex, but travels in the opposite direction, i.e. in a reverse-vortex. Then the gas enters the reverse vortex area, leaving the reactor through the outlet at a low axial velocity.

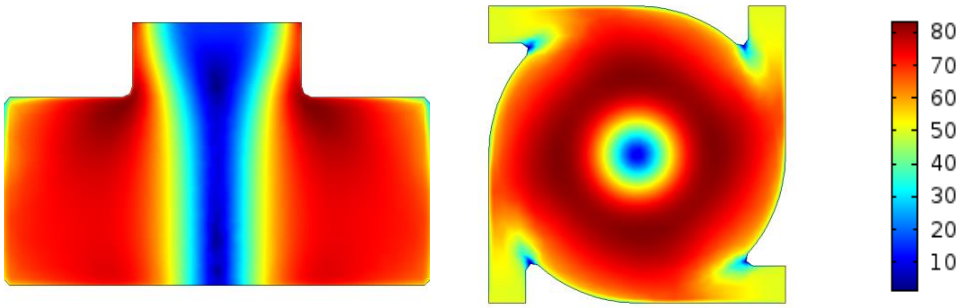

(a) (b) Velocity (m/s)

Figure 4.7. Gas velocity magnitude at a flow rate of 22 L/min (2D cross sections), flow without plasma.
(a) – vertical cross section (reactor center)
(b) – horizontal cross section (tangential inlets midpoint)

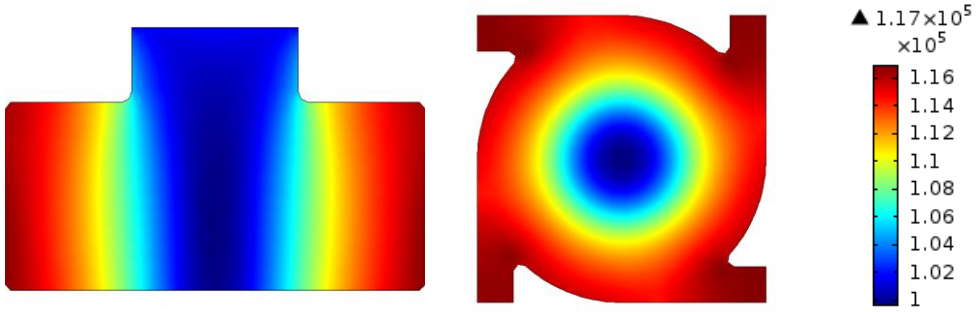

(a) (b) Pressure (Pa)

Figure 4.8. Gas pressure magnitude at a flow rate of 22 L/min (2D cross sections), flow without plasma.
(a) – vertical cross section (reactor center)
(b) – horizontal cross section (tangential inlets midpoint)

The gas becomes slightly pressurized along the side walls (with a pressure increase by about 17%) due to the high flow velocity (see figure 4.8). The inner

vortex remains at relatively constant basic pressure (1 atm). The exit length (see figures 4.7-a and 4.8-a) may raise some questions regarding the correct application of the outlet boundary condition. However, a longer exit length does not influence the results.

It is worth mentioning that the gas dynamics of a vortex flow are usually associated with the phenomenon of temperature separation between the inner and the outer vortex when the pressure drop in the system is significant (several bars). This process is called the Ranque effect, and the device itself is called a Ranque-Hilsch vortex tube [124]. In general, the reverse-vortex in this tube should have a lower temperature (usually about 50 K lower) than the outer peripheral vortex, essentially forming a cooling device without any moving parts. However, the used k-ε RANS description of the flow is not completely adequate for modelling this process. Moreover, the Ranque cooling effect should not significantly affect the plasma properties. Currently, the Ranque effect has no rigorous physical explanation, and is still subject of investigation [124]. Therefore, it is not discussed further, as it is also outside the scope of this study.

4.6.2 Gliding arc properties

The gliding arc current is limited by the ballast resistor in the electrical circuit and the conductivity of the plasma channel. At the finite element mesh settings mentioned above, it takes about 48 hours on an Intel i7-3820 CPU to compute just 300 microseconds, or about 1 revolution for the arc in the reactor. The model calculates up to 1 millisecond. The plasma parameters remain stable over this time frame.

In figure 4.9, the electric potential distribution on a centered cross-section of the reactor is shown at a time of 1 ms, and it is visibly distorted by the plasma arc. Due to the curvature of the outlet edge, the electric field is stronger at the anode, as shown in figure 4.10. The arc ignites and rotates along this edge, as the discharge would normally take place between the points of highest electric field. As also seen in figure 4.10, the electric field is lower at the arc attachment spot due to the flowing electric current.

GA discharges usually operate at a few tens to a few hundreds of volts after arc ignition, depending on the reactor dimensions and power [19], [99], [125]. Figure 4.11 illustrates the calculated voltage drop between the electrodes, as a function of axial position. The voltage is plotted for different gas flow rates. Position z = 0 corresponds to the cathode boundary, while z = 5 mm indicates the position of the anode boundary.

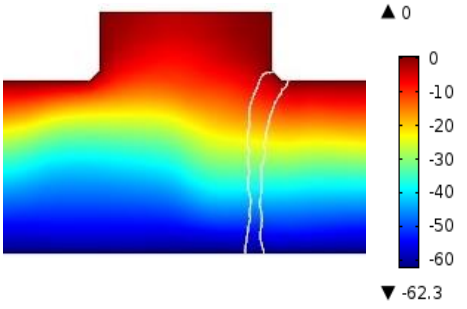

Figure 4.9. Electric potential distribution on a 2D cross-section of the reactor, at a cathode current of 900 mA and flow rate of 22 L/min, t = 200 µs. The arc body is schematically indicated with white lines.

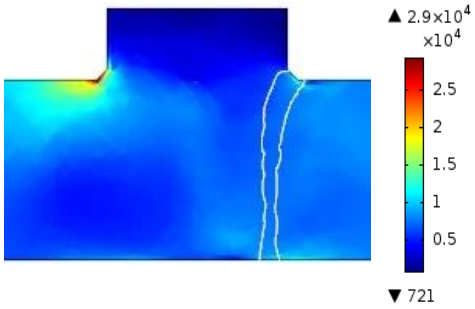

Figure 4.10. Electric field magnitude distribution on a 2D cross-section of the reactor, at a cathode current of 900 mA and flow rate of 22 L/min, t = 200 µs. The arc body is schematically indicated with white lines.

The potential difference between the electrodes after arc ignition (200 µs) at the lowest flow rate of 22 L/min is slightly above 60 V, going up to 120 V as the flow rate increases to 43 L/min. These voltage numbers exclude the sheath regions, as the model describes a quasi-neutral plasma.

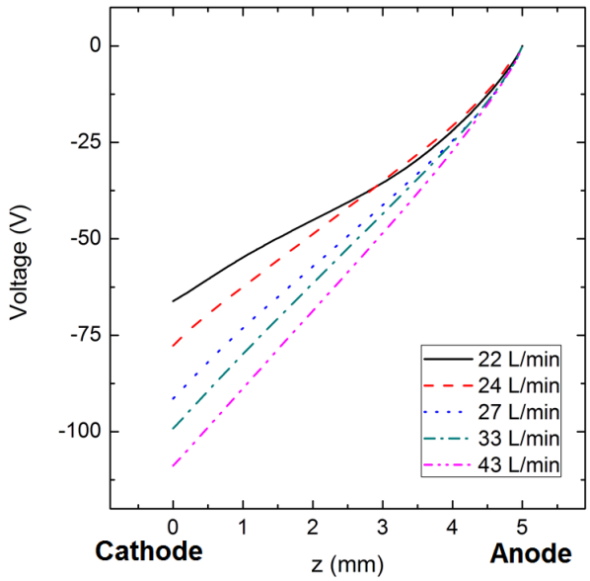

Figure 4.11. Axial plot of potential difference between anode and cathode at different flow rates. Rb = 1000 Ohm, t = 200 µs.

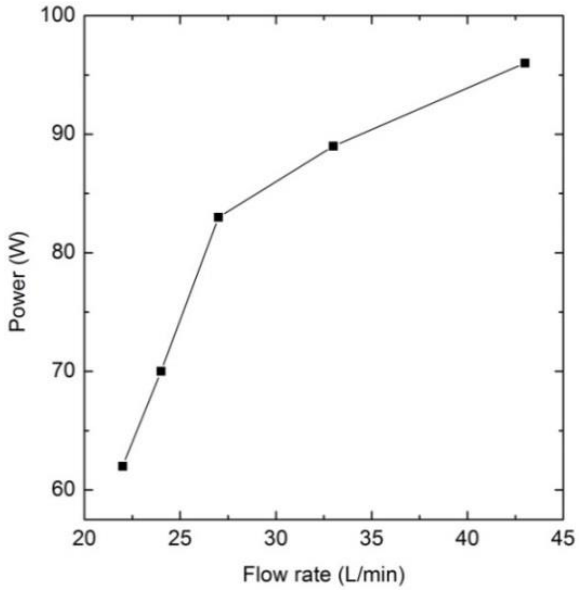

Figure 4.12. Reactor power consumption at different flow rates. Rb = 1000 Ohm, t = 200 μs.

The higher potential difference also leads to higher power consumption in the reactor, as is clear from figure 4.12. The major reason for the arc voltage to increase with higher gas flow rate is the faster gas exchange, which lowers the arc gas temperature and thus increases its electrical resistance. At higher flow rates, the arc is also subjected to an increased convective cooling as a result of the higher turbulence and axial gas flow in the reactor center.

The peak plasma conductivity σ_{pl} at the arc center (see equation 3.45 in Chapter III) ranges between 100 and 150 S/m after arc ignition. As far as the model accuracy allows, it remains relatively constant for different gas flow rates and cathode currents.

In figures 4.13 and 4.14, the cathode current I and the peak arc current density J_{max} (at the arc center) are plotted as a function of ballast resistance and gas flow rate, respectively. The total cathode current drops accordingly with increasing ballast resistance (see figure 4.13), and the peak arc current density ranges between $1x10^6$ and $3x10^6$ A/m^2, which is a typical value for arc and gliding arc discharges [19], [126]. As noted above, higher flow rates cause higher arc electrical resistance, but the total cathode current and the peak arc current density remain nearly unchanged, with values around 900 – 950 mA and $2.5x10^6$ – $4x10^6$ A/m^2, respectively (see figure 4.14). The peak plasma density of the arc itself also remains constant with values in the range of 10^{21} m^{-3} (see section 4.6.3 below). The oscillations in the values for J_{max} could be due to numerical inaccuracies.

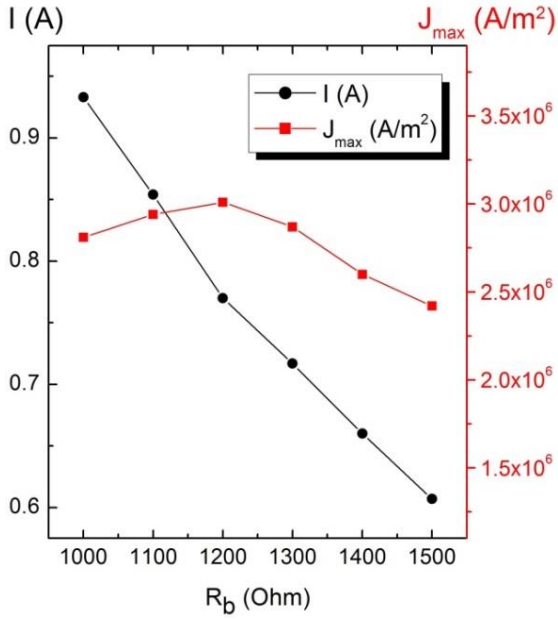

Figure 4.13. Cathode current and plasma arc peak current density vs. ballast resistance, at a flow rate of 22 L/min, t = 200 μs.

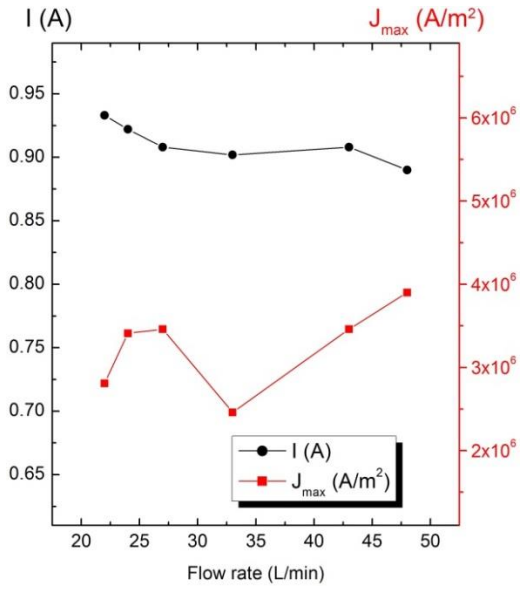

Figure 4.14. Cathode current and plasma arc peak current density vs. flow rate, at a ballast resistance of 1000 Ohm.

4.6.3 Plasma properties

The plasma arc "glides" along the circumference of the outlet, with the gas flow. In figure 4.15, the arc elongation is visualized. The arc ignites as a thin, straight plasma column, and is fully initialized at about 100 μs (figure 4.15a). After 1 complete revolution, which takes about 300 μs at a flow rate of 22 L/min, the arc starts to bend, and slightly elongate, crawling to the outer edge of the reactor. In figure 4.16, the arc movement is visualized, by showing snapshots of the plasma density as isosurfaces, at six different times, viewed from the top of the reactor, including the artificial heating function (first snapshot). The second and last snapshot of figure 4.16 corresponds to figure 4.15a and 4.15b, respectively. The plasma density is in the order of 10^{21} m^{-3}, which is within the expected range for a gliding arc in argon at atmospheric pressure [19], [125], [126]. It remains constant over time, and does not change significantly with flow rate. It is interesting to note that the arc at first tends to glide between the cathode center and the output nozzle edge (anode), where the electric field is slightly higher (see figure 4.10). The arc slowly crawls along the outlet wall, and after several

revolutions, it stabilizes in the reactor center, attached to the outer edge of the outlet, and it remains there, swirling in a quasi-stationary state (figure 4.15b).
As is clear from figure 4.16, the arc gliding process is rather smooth and uninterrupted in our simulations. In reality, the arc movement is much more complex and spontaneous. Two reasons may account for the observed behavior.

First, in the model, the cathode and the anode have perfectly flat, even surfaces. In reality, these surfaces are usually not completely smooth, and feature some microscopic bumps, scratches and lines, which create higher electric fields at certain points, causing the arc erratic behavior. Second, as the fluid flow is turbulent, small oscillations of the flow velocity will bend and deform the arc more significantly in reality. However, these processes are very difficult to study in the present model, as a complex parameterization of the electrode surface would be required, and accordingly, a much finer discretization mesh at these surfaces. Furthermore, a finer mesh and turbulence modelling with a complete Navier-Stokes formulation would also be necessary for the gas in order to describe the turbulent eddies in the flow, and how they affect the arc movement, and shape. This is beyond the scope of the present study.

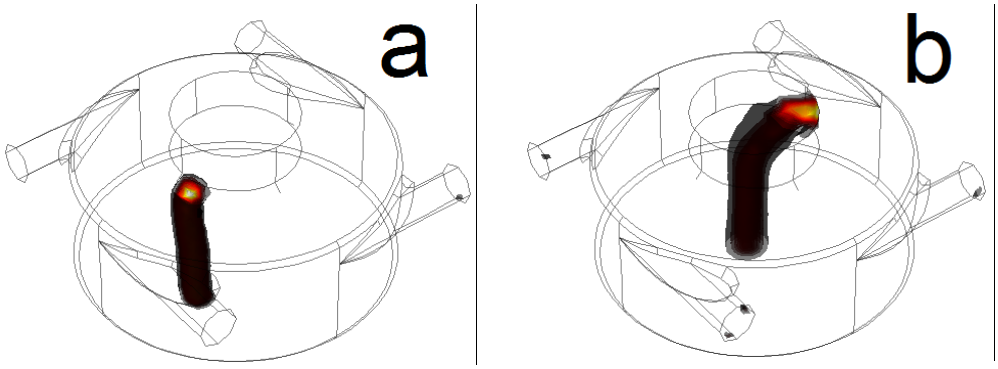

Figure 4.15. Arc evolution over time, view of semi-transparent isosurfaces of plasma density. The arc ignites as a straight plasma column attached to the outlet edge (a). It crawls to the outer edge and stabilizes at the reactor center (b). Gas flow rate - 22 L/min, Rb = 1000 Ohm, current - 930 mA.

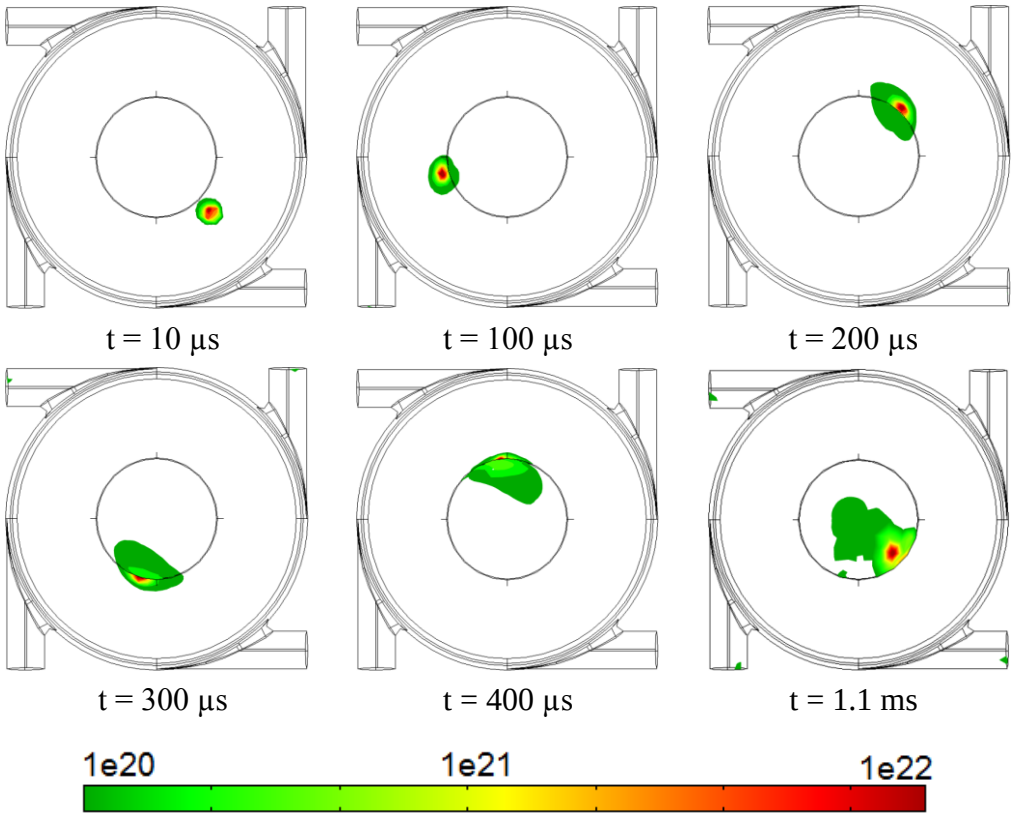

Figure 4.16. Plasma density (in m^{-3}): top view of several semi-transparent isosurfaces (different colour corresponds to different value). The plots are at different timeframes. The flow rate is 22 L/min and the current is 930 mA.

It is difficult to estimate the arc movement speed, as there are many effects that may alter it. First, the arc is attached to the electrodes, and more specifically, to the points with highest reduced electric field (E/n) magnitude, i.e. the sharp edges. Second, the flow velocity differs along the arc axis, and is very low near the electrodes. Third, the change in gas viscosity due to gas temperature may also influence the arc movement. In a real-case scenario, the electrode surface will also affect the arc movement, which would be much more erratic and spontaneous. Furthermore, the flow velocity varies across the arc body at its later development, so not all parts of the arc move with exactly the same velocity as the gas flow. We do not consider the thermal balance for the electrodes (as for the entire walls), which omits effects such as arc "anchoring", again, due to computational limitations.

The spatial distributions of the gas and electron temperature are shown in figure 4.17 and figure 4.18, respectively, in a vertical cut plane through the reactor

center and the arc. As is obvious from figure 4.17, the gas near the side walls of the reactor remains cool (300 K) due to the direction of the flow. The arc spins in the reactor center. Indeed, due to the characteristics of the RVF (figure 4.6), the mass transfer takes place from the walls to the center, effectively insulating the plasma from the sides.

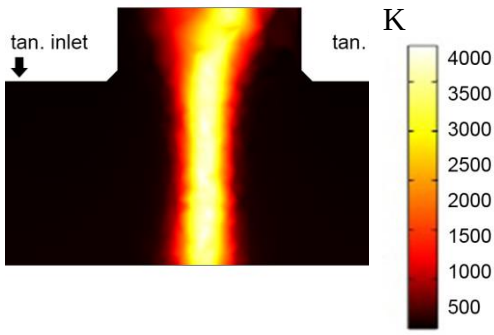

Figure 4.17. Gas temperature distribution in the reactor, for a gas flow rate of 22 L/min and a cathode current of 0.93 A, after 1.5 ms.

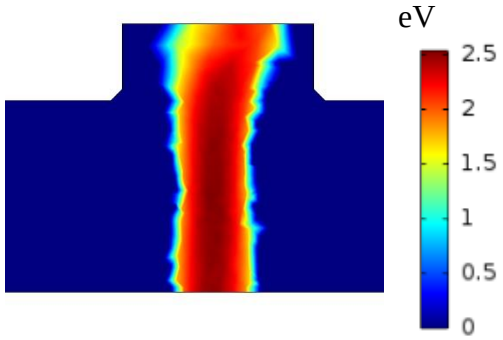

Figure 4.18. Electron temperature distribution in the reactor, for a gas flow rate of 22 L/min and a cathode current of 0.93 A, after 1.5 ms.

As a result, the high temperature gas is confined in the reverse-vortex, and therefore, the plasma thermal insulation is nearly perfect. This is in agreement with earlier studies on the RVF [127]. The maximum gas temperature, in the arc body, is slightly above 4000 K at the given conditions. The electron temperature within the arc body (figure 4.18) is in the order of 2.5 eV, which is rather high for a gliding arc discharge, because in literature values around 1 eV are typically reported [19], [125]. This might be explained by the simplifications, defined in the model.

In figures 4.19 and 4.20, the arc plasma density, the electron temperature and gas temperature are plotted at different values of cathode current and gas flow rate, respectively. For figure 4.19, the results are generated by applying a time-dependent function to the ballast resistor, which increases its value over time. The function is activated after t = 1.1 ms., where the discharge reaches a quasi-stationary state of operation, i.e. the arc characteristics do not change anymore and its rotation is stabilized in the reactor center (see figure 4.15). The resistance value changes with a much slower rate compared to the time for settlement of the

plasma-gas parameters, so the values are the same as if running the model from the beginning, with a fixed resistance value. This approach allows us to obtain continuous results while saving computing time. The plasma density demonstrates a slight change in the given range of conditions, with values in the arc center in the order of $8x10^{20}$ – $2x10^{21}$ m^{-3}. The electron temperature exhibits almost no change, with values of 2.5 – 2.6 eV. The gas temperature clearly rises with increasing cathode current. Furthermore, increasing the flow rate leads to a lower gas temperature in the arc (figure 4.20). This can be explained by the increased mass flow in the reactor.

At flow rates above 45 L/min, the gas temperature becomes relatively low and thus there is no arc contraction, i.e. the plasma channel becomes very wide, filling the whole domain, i.e. it is not an arc anymore. At flow rates below 20 L/min, the gas temperature becomes too high for the simulation, i.e., the finite mesh is unable to handle the strong temperature gradients, and thus, the computation fails. The obtained values for the arc temperature are comparable with some earlier studies on gliding arc discharges, with and without RVF stabilization [125], [126].

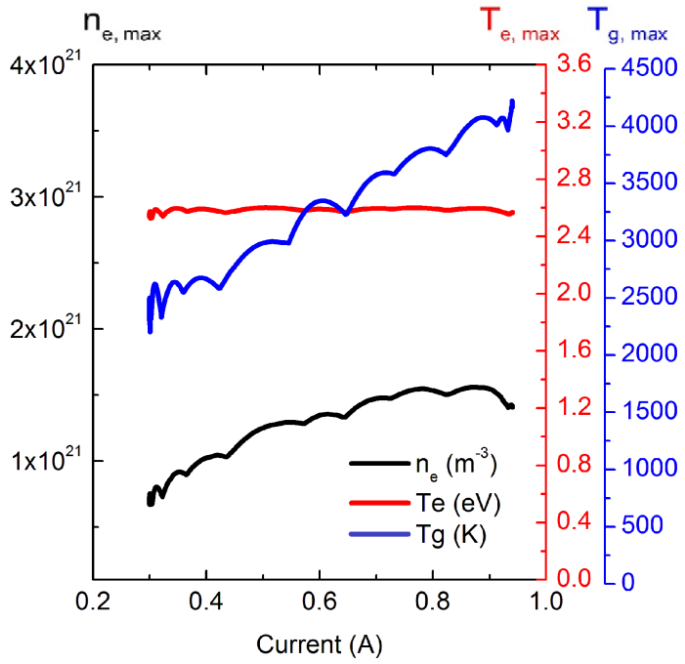

Figure 4.19. Plasma density, electron temperature and gas temperature vs. cathode current, at a gas flow rate of 22 L/min, quasi-stationary state at 1ms.

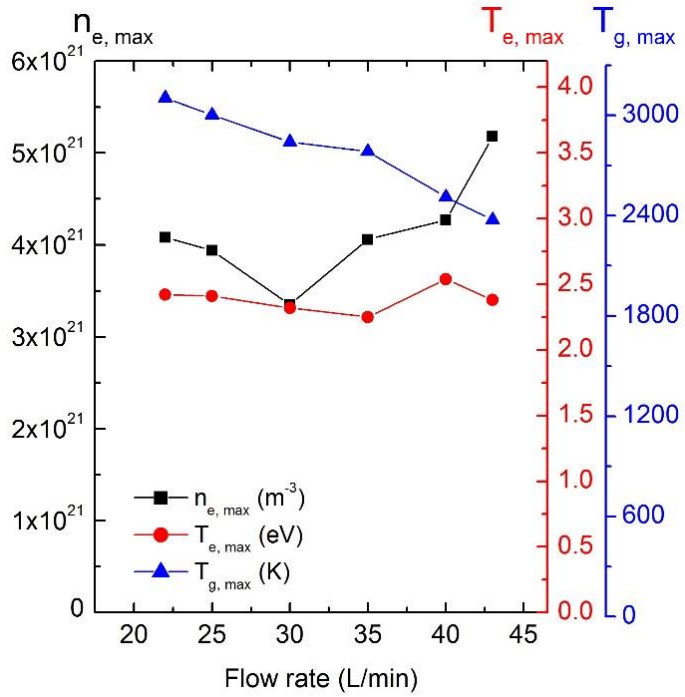

Figure 4.20. Plasma density, electron temperature and gas temperature vs. flow rate, at a cathode current of 900 mA and t = 200 μs.

4.7 Conclusion

In the present Chapter, the physics of a RVF gliding arc reactor is simulated by means of fluid plasma modelling. The properties of the gas flow are obtained using the k-ε RANS turbulent model, and the results correspond well with previous studies on RVF gliding arc reactors. The plasma itself is modelled by means of a quasi-neutral model with a reduced reaction set. The calculated current density corresponds well to the theory and practice of low current atmospheric pressure discharges [19], [125], [126]. The calculated values for plasma density and gas temperature are comparable with experimental and numerical data on gliding arc plasma reactors, with and without RVF stabilization [122], [125], [126]. Indeed, in [125], values were reported for a plasma density of $10^{18} – 10^{19}$ m^{-3}, a gas temperature of 1100 – 2600 K, and an electron temperature of 1 eV for a conventional, lower-current gliding arc reactor operating at 130 mA. In [128], a reverse-vortex was simulated using the RSM (Reynolds stress model) turbulent model with a cylindrical shape to act as a heat source for the reactor. The thermal

insulation behavior was very similar to our case. In [122], plasma densities of 10^{22} – $5x10^{22}$ m^{-3} were reported for a conventional high-power argon gliding arc operating at 68 W, which is very close to the values obtained in the presented model. Certainly, it is not easy to compare different gliding arc setups with different reactor geometries. Our calculated electron temperature is quite high compared to most experimental data for a GA in argon, although it is not dramatically higher, i.e. 1 eV in [125] vs. 2-2.5 eV in our model.

Our calculations also indicate that the arc voltage changes with gas flow rate. The arc gas temperature also depends on the total power deposition (or cathode current) and the flow rate, while the plasma density and electron temperature remain constant after a stable state of the arc is reached. Furthermore, the arc movement is visualized, and although it might not be 100% accurate because of model limitations, it can be concluded that the plasma arc clearly stays well insulated from the side walls due to the gas flow. Thus, the walls are almost perfectly insulated from the plasma, protecting them from the high temperature, and improving the efficiency of the reactor.

The computational time of the model is reasonable, with the stationary study for the gas flow computed within 2 hours, and about 100 μs of the time-dependent plasma model computed within 24 hours on an Intel i7-3820 (4 cores at 3.7 GHz) CPU with 64 GB of RAM.

The model still exhibits some limitations. First, the mesh density of 150,000 elements for the entire model, with element size of 0.3-0.7 mm, should be considered as a lower limit for adequate calculations. However, a denser mesh would simply take too much time to compute for the given time frame. For this reason, the calculated arc shape and arc movement are only approximate. Second, the reaction set is reduced to a minimum, which allows computation of the model without significantly hampering the accuracy. This approach may be suitable for argon, but for other gases envisaged for further investigation, such as CO_2, it would represent a significant problem. Indeed, for the application of CO_2 conversion, a more detailed plasma chemistry set would have to be incorporated, dramatically increasing the calculation time [61], [111], [129]. Third, the quasi-neutral assumption of the model leaves out the possibility to study the Debye sheaths at the boundary areas and the electrodes, which makes the model reliable only with respect to the properties of the plasma column. Other methods for refining, such as adaptive mesh generation were explored, but the resulting computation time was too long.

The lack of concrete experimental and other simulation data for RVF gliding arc reactors makes it difficult to validate our model. This reactor type is relatively new, and is only recently gaining interest in the fields of plasma gas conversion, plasma fuel enhancement, and plasma surface processing. We hope that more experimental data will become available, allowing us to better validate our model.

Finally, the reactor shape does not correspond to the features of a real device, but only to a simplified description of a reverse-vortex tube [19], again, for the sake of optimizing the computation time. However, in the next Chapter, we apply the model to a real RVF GA setup, used within our group PLASMANT. Nevertheless, the present study proves that problems, which are essentially 3D in nature, are now within the grasp of modern plasma modelling techniques.

CHAPTER V. CO_2 Conversion in a Gliding Arc Plasmatron: Multi-Dimensional Modelling for Improved Efficiency

This work is published as:
G Trenchev, St Kolev, W Wang, M Ramakers and A Bogaerts, CO_2 Conversion in a Gliding Arc Plasmatron: Multidimensional Modeling for Improved Efficiency, *J. Phys. Chem C*, **121**, 24470-24479, 2017

Abstract

The gliding arc plasmatron (GAP) is a highly efficient atmospheric plasma source, which is very promising for CO_2 conversion applications. To understand its operation principles and to improve its application, we present here comprehensive modelling results, obtained by means of computational fluid dynamics simulations and plasma modelling. Due to the complexity of the CO_2 plasma, a full 3D plasma model would not be computationally feasible. Therefore, we combine a 3D turbulent gas flow model with a 2D plasma and gas heating model in order to calculate the plasma parameters and CO_2 conversion characteristics. In addition, a complete 3D gas flow and plasma model with simplified argon chemistry is used to evaluate the gliding arc evolution in space and time. The calculated values are compared with experimental data from literature as much as possible, in order to validate the model. The insights obtained in this study are very helpful for improving the application of CO_2 conversion, as they allow us to identify the limiting factors in the performance, based on which solutions can be provided on how to further improve the capabilities of CO_2 conversion in the GAP.

5.1 Model description

5.1.1 Reactor geometry

The gliding arc plasmatron (GAP) modelled in this work is based on the exact design, used experimentally [59], and is shown in figure 5.1. This design was developed by Rabinovich and co-workers at Drexel University [64]. It consists of a small RVF cylindrical chamber with two opposing cylindrical electrodes insulated with Teflon. This headpiece is typically mounted on a large tube, which is used to attach measurement instruments, such as a gas chromatograph and temperature sensors (see figure 5.1(a)), but it can also be detached from this tube, and operated in open design, so that the arc movement can be visualized (see figure 5.1(b)).

The RVF GAP module is quite versatile and it offers different configurations, as both the cathode cap and the outlet anode are interchangeable for different flow configurations and outlet diameters. In the model, we only consider the internal structure, which can be seen in figure 5.2.

The reactor has 6 tangential inlets with a diameter of 1.6 mm and an axial outlet with a diameter of 7.08 mm. The cathode (outlined in red, figure 5.2(b)) is where the high voltage is applied. In the experimental reactor, the entire side wall is at cathode potential, and the initial discharge gap is the narrow area between the anode surface and this cathode sidewall (see "Gap", figure 5.2(b)).

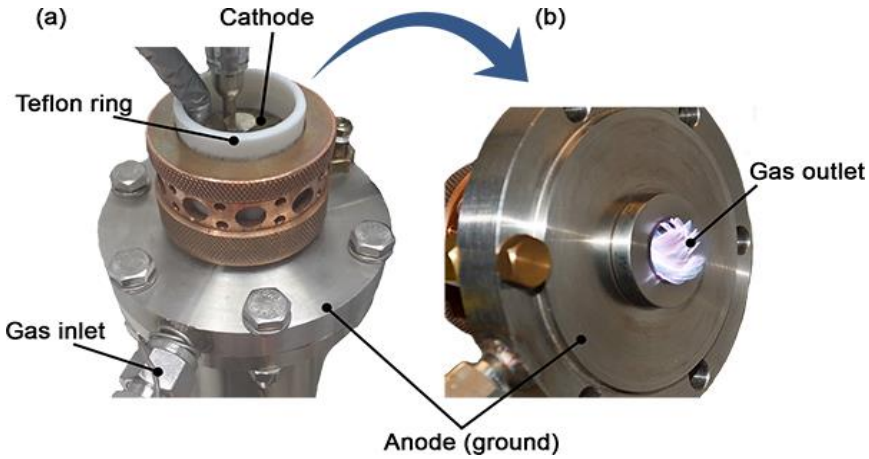

Figure 5.1. Photograph of the gliding arc plasmatron mounted on the gas tube (a) and detached, rotated 90^o operating in free-air (b). The white Teflon insulator is visible – it is a sealing ring that encloses the cathode and acts as an electrical separator with the anode. It is not featured in the model, as it is an external entity with respect to the modelling geometry.

However, in the plasma model, we consider only the back-end boundary as a cathode (red area, figure 5.2(b)), in order to avoid plasma density and electron temperature errors at the sharp geometry edge near the "gap". Both cases were evaluated, and no difference was found in the plasma parameters. Indeed, once the arc is stabilized in the centre, it is not in contact with the side walls, and the entire electrical current flows through the respective boundary where the arc is attached, i.e., the cathode cap in figure 5.2.

5.1.2 Gas flow model

The gas flow is simulated in the entire internal 3D reactor geometry. The typical experimental flow rates are around 20 L/min, which corresponds to rather high internal flow speeds, in the range of 50-150 m/s. This will lead to strong turbulent oscillations, and if the modelling would be performed using the classical Navier-Stokes equations with direct numerical simulation (DNS), this would yield excessively long calculation times, for which supercomputers are required [69], [120]. However, small-scale turbulent effects are out of scope of this study, as most of the computing power is dedicated to the actual plasma model.

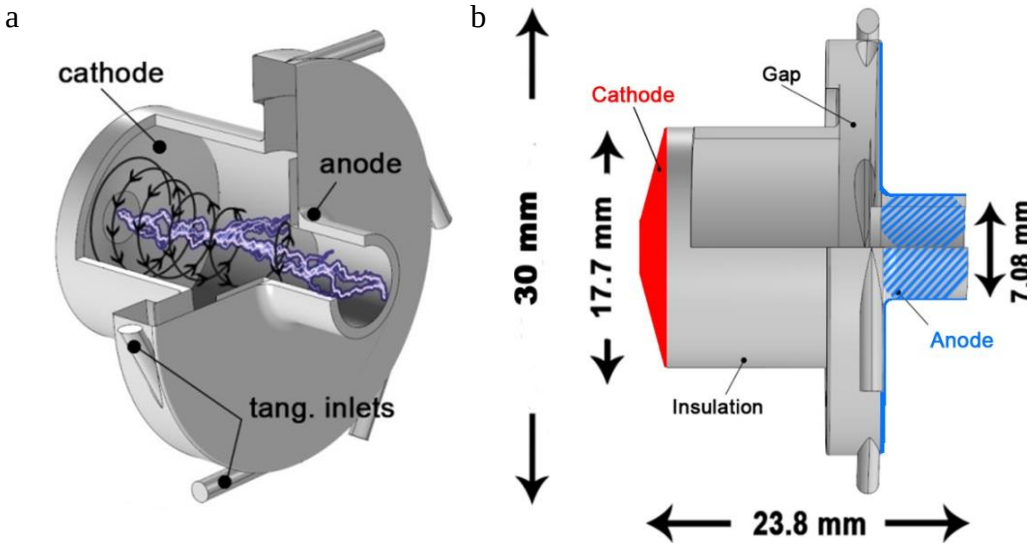

Figure 5.2. Internal structure of the reactor used for the model, with artistic representation of the arc. The reverse-vortex is indicated with black arrow lines (a). Side view of the internal structure (b). The domain length is 23.8mm, the swirl generator has a diameter of 30 mm. "Insulation" stands for a non-conductive boundary. The cathode is indicated in red and the anode in blue (striped).

For this reason, we use a RANS (Reynolds-Averaged-Navier-Stokes) turbulent model, which significantly reduces the computational requirements by averaging turbulence over time (see details in Chapter III). Nevertheless, the model is still accurate enough for the purpose of this study. We use the Shear Stress Tensor (SST) model, which excels over most common turbulent models, like the *k-ε* model [94] (see again details in Chapter III). This more advanced model solves the flow near the reactor walls more accurately, and is more precise with turbulent variables, such as the turbulent viscosity, which affects the heat transfer. More importantly, the turbulent heat transfer is also included in the new model (see Chapter III). Note that in Chapter IV, we used a *k-ε* turbulent model to predict the flow field, and the turbulent heat transfer was not included, but we will demonstrate here that it has a crucial effect on the gas temperature. The turbulent heat transfer model is based on the Kays-Crawford model [67], [96] (see details in Chapter III). The model inputs, such as gas flow rate and arc current, are adopted from our experiments [59], in order to provide a solid ground for discussion and investigation.

In a gas medium, the temperature is determined by the gas thermal balance equation including a heat source. As explained in Chapter III, the equation is denoted as follows:

$$\rho C_p \frac{\partial T_g}{\partial t} + \rho C_p \overrightarrow{u_g} \cdot \nabla T_g - \nabla \cdot \left(\left(k_g + k_T \right) \nabla T_g \right) = Q \tag{5.1}$$

where C_p is the specific heat capacity of the gas, k_g is the temperature-dependent gas thermal conductivity (based on a material look-up table), k_T is the turbulent heat conductivity of the fluid, T_g is the gas temperature and Q accounts for the gas heating due to elastic and inelastic collisions between electrons and heavy particles in the plasma.

The Kays-Crawford model [67], [96] accounts for the resulting turbulent heat flux. It is solved for the turbulent Prandtl number, which is the ratio of the momentum eddy diffusivity and heat transfer eddy diffusivity. In this way, turbulence acts as an enhancement to the gas thermal conductivity through intense eddy mixing, resulting in a higher effective value for heat conduction for the conditions of the considered discharge, i.e. heat transfer is dominated by turbulent effects. See Chapter III for additional details.

5.1.2 2D and 3D plasma models

The 3D plasma model is based on the simplified argon chemistry, presented in Chapter IV, in order to keep the computation time reasonable. This model was proven to be reasonably accurate, and comparable with more complex chemistry models [99]. It is a fluid plasma model, built upon the assumption of a quasi-neutral plasma, i.e. ion and electron densities are equal [117] (see details in Chapter III). The following equation is solved for the ion density:

$$\frac{\partial n_i}{\partial t} + \nabla.\left(-D_i \nabla n_i + \mu_i n_i \overrightarrow{E_{amb}}\right) + \left(\vec{u}_g.\nabla\right) n_i = R_i \tag{5.2}$$

where n_i stands for the ion density, μ_i stands for the ion mobility, $\overrightarrow{E_{amb}}$ is the ambipolar electric field, $\vec{u}_g$ is the gas flow velocity vector, D_i is the ion diffusion coefficient, and R_i stands for the ion production and loss rates due to chemical reactions. The electron density n_e is derived from the quasi-neutrality condition, which in this case is $n_e = n_i$ since only a single type of ion is considered in the model. Besides the above balance equation, a balance equation is solved for the Ar excited atoms, as well as for the average electron energy.

The plasma chemistry in CO_2 gas is much more complex. We present here an already reduced reaction set, adopted from [130] – further reduction would lead to significant loss of accuracy for the given conditions. The chemistry set involves 40 species (see table 5.1), 24 electron impact reactions, 19 ion reactions, as well as 7 vibrational transfer reactions. We put specific attention to the CO_2 vibrational levels, as they are stated to play an important role in energy-efficient CO_2 conversion in a GA [130], [131]. Details about the vibrational levels included in our model can be found in [61], [111], [132].

Table 5.1. Overview of the CO_2 plasma species included in the model

Ground state neutrals	**CO_2, CO, C, O_2, O**
Charged species	e, CO_2^+, O_2^+, CO_3^-, O_2^-, O^-
Excited species	CO_2 (25 vibrational states, 1 electronic excitation state), O_2 (3 vibrational states)

With this CO_2 chemistry, the computation time would be too long for a 3D model, as much more PDEs (Partial Differential Equations) need to be solved for the particle balances. Furthermore, the complexity of the reactions increases the mesh requirements, as the density gradients for some of the species tend to be very strong. Thus, the model cannot work with the same settings as the 3D argon model. Therefore, we use a simplified 2D cut-off of the geometry. The flow pattern is directly interpolated into the 2D plane (see figure 5.3) through interpolation functions in COMSOL. The cut-off is essentially a plane of the 3D geometry, conserving all remaining geometrical features.

As can be seen in figure 5.3, the 2D cut-plane of the reactor is used as modelling entity, removing the swirl generator (tangential inlets), as no discharge takes place there. Accordingly, a fine 2D mesh is generated with 10,000 triangular elements and boundary layers. Thus, the red boundary becomes cathode and the blue – anode (see figure 5.3(b)), as in figure 5.2. The 3D flow vectors for "x" and "z" directions are translated to "x" and "y" directions in the 2D model. The "z" direction becomes just the length of the modelling plane, and holds no gradients. This is the major limitation of the 2D approach: since the tangential motion (i.e. motion in the "z" plane) is not accounted for, the essential vortex pattern of the plasma cannot be captured. The flow pattern only features the sideways motion (from reactor periphery to centre), and the outflow through the outlet (see figure 5.4(b) below). This is done by the use of interpolation tables within COMSOL. With the same approach, the data for the turbulent heat conductivity is moved from the 3D to the 2D model.

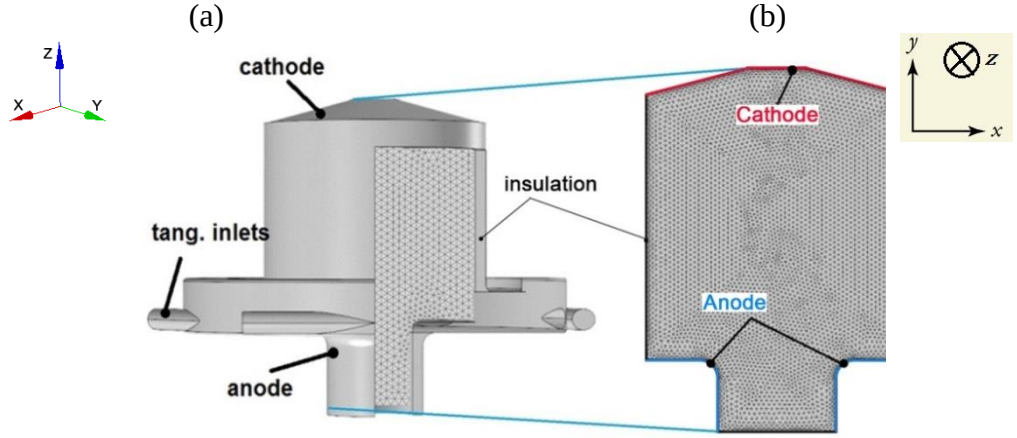

Figure 5.3. 3D reactor geometry (a) and the interpolated modeling plane in 2D (b), with indication of the computational mesh. See coordinate systems on the left (3D) and on the right (2D).

5.2 Results and Discussion

5.2.1 Gas flow patterns

The 3D gas flow stream lines, calculated with the SST model in argon gas, are presented in figure 5.4. In figure 5.4(a), the stream line plot clearly depicts the formation of a reverse-vortex flow. The gas is forced into a tangential motion from the swirl generator (tangential inlets) and continues this trend through the reactor towards the closed cathode side at the end (= back of figure 5.4(a)), after which it moves in the opposite direction, in a smaller inner vortex towards the outlet. The details of the flow direction in a 2D plane of the reactor can be observed more clearly in figure 5.4(b), showing that the flow, when entering the reactor, first moves close to the sidewalls towards the top (= closed end of the reactor, i.e. cathode). Then, it returns and travels to the outlet in the opposite direction, forming a reverse-directed spiral, i.e. the reverse-vortex flow. The initial outer vortex takes place close to the walls, due to the high inlet stream and moves at a high velocity (around 30-40 m/s). The inner reverse-vortex has a much lower velocity, which decreases towards the centre, and it exits the reactor with a velocity magnitude around 20 m/s. This can be observed by the colour scale in figure 5.4.

A defining characteristic of the RVF is that the mass transfer takes place from the sides of the reactor to its centre. This can be clearly seen by looking at the flow vectors in figure 5.4(b) – the gas is transferred from the reactor periphery to the centre, and it leaves the reactor through the outlet. The plasma reacts directly to this mechanism, as it is a part of the gas. In other words, when the gas stream is forced to the centre, the plasma channel will also move to the centre (due to convection; see convection term in equations 1 and 2), and it will stay in this position as long as the gas keeps it stabilized. In this way, not only the plasma is effectively stabilized in the centre, but also the mass transfer is directed towards the centre from all directions – meaning that the walls are thermally insulated from the hot plasma arc column.

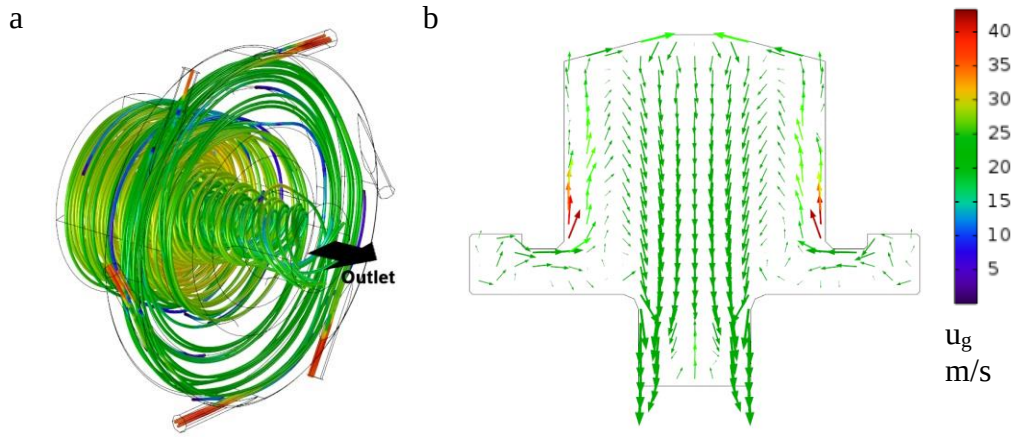

Figure 5.4. Stream line plot in 3D (a) and arrow surface plot in 2D (b) of the gas flow pattern, for an inlet gas flow rate of 22 L/min. The color scale at the right indicates the gas velocities in m/s, and applies to both (a) and (b). Important note: the total velocity magnitude of all 3 vector components is expressed in the color scale, in order to match the ranges of (a) and (b). However, in (b), the arrows represent only the axial and transverse directions, as the tangential motion (a) cannot be depicted in 2D.

The fact that no heat is lost to the reactor walls or other parts of the reactor means that more power is consumed by the discharge, i.e. the plasma generation is more effective. Furthermore, keeping the walls insulated (cold) is also beneficial for the reactor materials itself. These results are consistent with the behaviour shown in Chapter IV and in other works on reverse-vortex flows [19], [64], [127].

5.2.2 Argon plasma models

The obtained flow data in 3D is used directly as a stationary initial condition for the plasma model. The flow velocity is used in the convection term in the species balance equations (see Chapter III), while the obtained values for turbulent heat conductivity are used as effective thermal conductivity in equation 3.23 of Chapter III.

In figure 5.5(a), we illustrate the calculated plasma density, for an arc current of 240 mA, after a computation time of 5.3 ms, when the arc is stabilized in the centre of the reactor. The plasma density is around 10^{20} m^{-3}. This value of

10^{20}-10^{21} m^{-3} is typical for GA plasmas at atmospheric pressure [19], [125]. The peak value does not change significantly during arc stabilization.

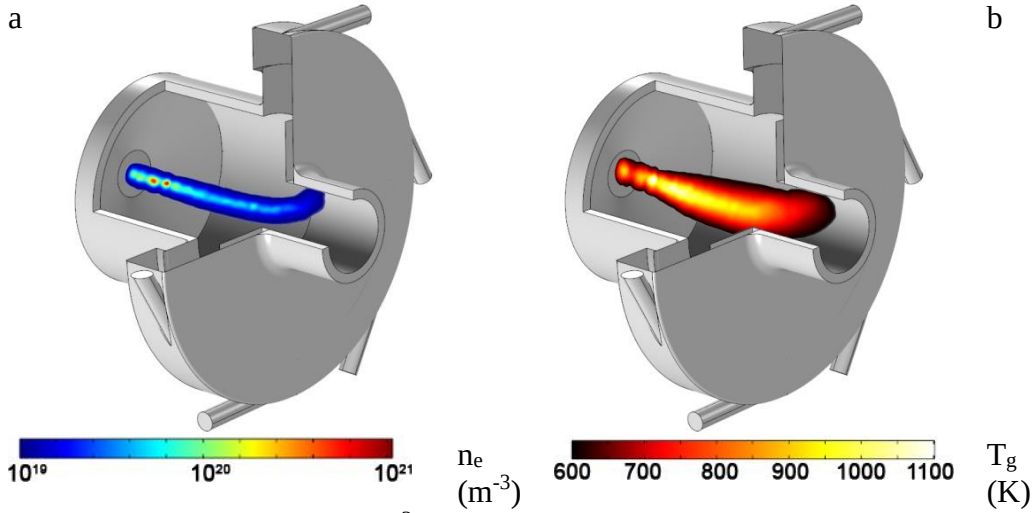

Figure 5.5. Plasma density [m^{-3}] (a), and gas temperature [K] (b), in the stabilized arc, depicted as iso-surface plots after 5.3 ms of computation time, for 240 mA of arc current and a gas flow rate of 22 L/min.

The calculated gas temperature (figure 5.5(b)) at the same arc current of 240 mA is around 600-700 K at the sides of the arc, and it reaches 900-1100 K at the centre, with a maximum of about 1100 K close to the cathode end, where the arc is slightly more contracted and the plasma density also reaches its maximum (see figure 5.5(a)). These values are much lower than in those obtained in Chapter IV, which is due to the inclusion of turbulent heat transfer (see section 3.3.5). The effective heat conductivity (see equation 3.25 of Chapter III) is now a combination of the gas thermal conductivity (0.016 W/m.K for argon at atmospheric pressure) and the computed turbulent heat conductivity, which accounts for heat transfer caused by the rapid turbulent oscillations in the flow. The computed value in the model is around 1-1.5 W/m.K (see below), hence around 100 times higher than the value for the gas thermal conductivity, which was used in our previous model of Chapter IV. This explains why the gas temperature is now much lower, and more realistic. Indeed, taking into account the turbulent heat conductivity leads to a more distributed energy transfer in the gas, and thus, a lower maximum gas temperature [133].

In order to demonstrate this effect in more detail, we show in figure 5.6 the gas temperature in a 2D plot, calculated for the same conditions as in figure 5.6, both without and with including the turbulent heat conductivity. It is obvious that

the temperature reaches a maximum value of 2400 K in the case without turbulent heat conductivity. Furthermore, the thermal profile of the arc column is now much narrower, i.e., with a diameter of only 2 mm (figure 5.6(a)) vs 3-4 mm in figure 5.6(b) because of the lower heat conductivity of the gas medium. This clearly illustrates the important role of turbulent heat conductivity in the GAP.

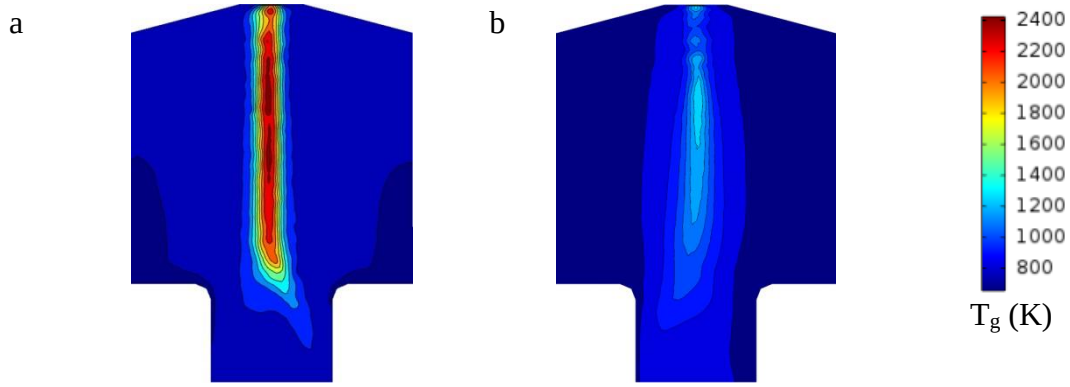

Figure 5.6. Gas temperature in the 3D argon model, without (a) and with (b) turbulent heat transfer, for the same conditions as in figure 5.5. Gas inlets are omitted in the 2D projection.

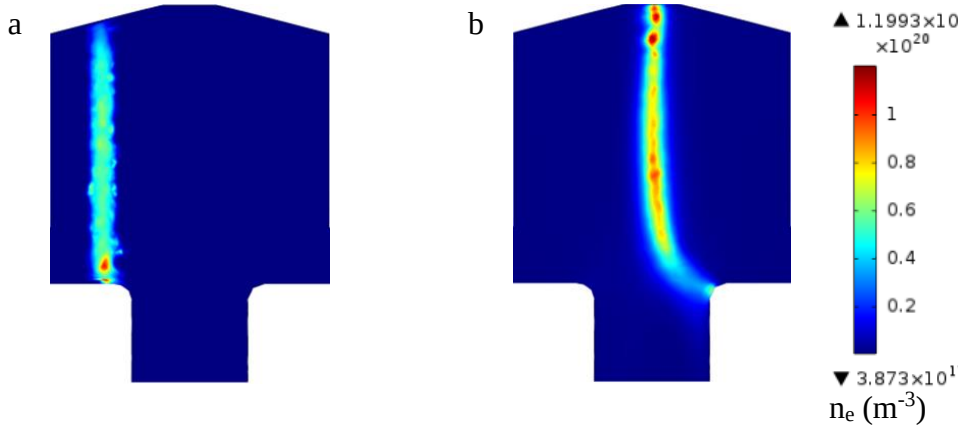

Figure 5.7 Arc position at 0.1 ms (a) and 5.3 ms (b), for the same conditions as in figure 5.5. Gas inlets are omitted in the 2D projection.

As the turbulent heat conductivity is anisotropic (see below), the arc temperature shows areas with higher and lower temperature, particularly in the area close to the cathode (figure 5.5(b)). In addition, the higher heat conductivity leads to a wider thermal profile of the arc, as clearly shown in figure 5.6. This

effect has consequences for the plasma density as well (figure 5.5(a)), i.e. gas turbulence has an influence on the entire arc structure.
In figure 5.7, the time-evolution of the arc position is illustrated in a 2D plane. The arc ignites at the periphery of the reactor (figure 5.7(a)) and gradually revolves in a spiral motion to the reactor centre (figure 5.7(b)). Then, it elongates towards the outlet and keeps rotating in a semi-stationary state (note the elongation in figure 5.7). Note that the complex arc body cannot be completely depicted by a 2D cross-section, as it is bent in all 3 directions. This process can be observed further in figure 5.8, presenting the top-view of the arc rotation. The arc body becomes a straight column, but hook-shaped at the anode end. The revolution period is approximately 0.7 ms. We have also performed high-speed photography experiments of the arc rotation in our experimental reactor, showing a similar behaviour and rotational speed [134].

While the argon model provides valuable information of the discharge formation, the main purpose of this work is to model the GAP operating in CO_2. A complex CO_2 chemistry would yield excessive calculation times if using a 3D model. Hence, we need to develop this model in 2D. However, a 2D model raises some questions about its accuracy for describing the GAP. As mentioned, the first and most obvious difference is that there would be no gradients of plasma density or temperature in the "z" direction with respect to the modelling surface (refer to figure 5.3).

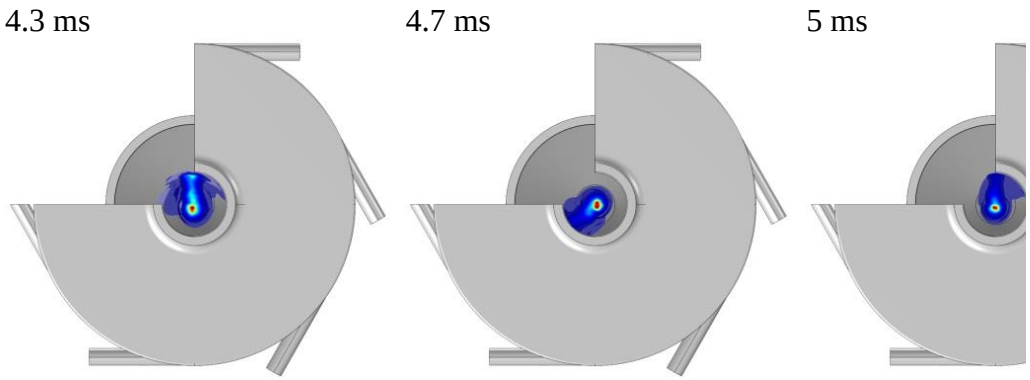

Figure 5.8. Arc position after stabilization in the reactor centre, at 4.3, 4.7 and 5 ms (corresponding to one full rotation), for the same conditions as in figure 5.5, illustrating how the rotating arc is attached at the anode end. A part of the anode body (at the top left) is removed, as done in figure 5.5 above, to illustrate the inner part of the reactor.

Second, the total arc current cannot be expressed in amperes, as there is no surface to integrate the current density upon – the cathode and anode boundaries are 1D lines. Therefore, the arc current can be expressed in A/m only. In addition, some convective cooling, coming from the tangential gas stream around the arc, is inevitably omitted too.

To assess the effect of using a 2D model, we first developed the 2D model for argon, and we compared it with the 3D argon model results, before applying the 2D model for CO_2. In figure 5.9, the effective heat conductivity for argon is moved from the 3D (a) to the 2D (b) model.

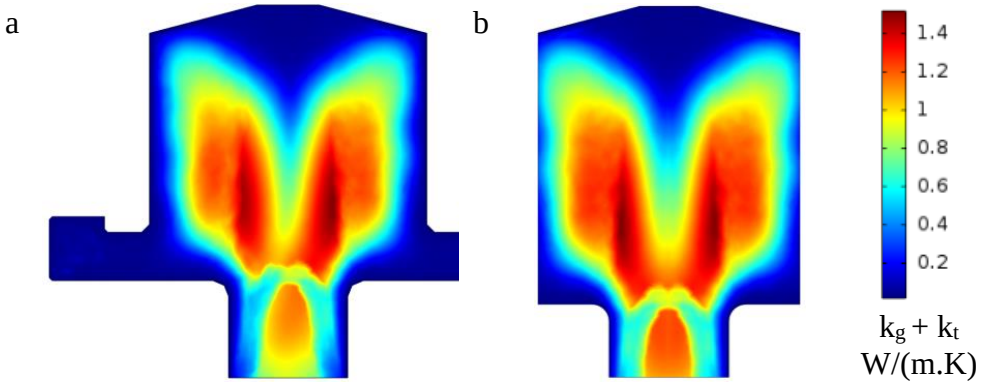

Figure 5.9. Effective heat conductivity (gas + turbulent) for argon in 3D (a) and interpolated in 2D (b).

Assuming that the arc has a cylindrical (or "wire") shape (judging from the 3D results), the total current in the 2D model can be approximated as follows. We assume that the current density in the "z" direction has the same distribution as in the "y" direction, i.e. the arc is symmetric. In this way, the current is obtained by integrating the current density over the arc region ($I = \int \sigma E 2\pi r dr$). This method has already been applied in [114] with satisfactory results.

In figure 5.10, we show the results from the 2D argon model at the same conditions as in figure 5.5, in order to compare with the 3D model results for model verification. Note that the geometry is a bit more simplified, neglecting the inlets and focusing only on the cylindrical reactor. At an estimated arc current of 240 mA (or current density in the 2D plane of 100 A/m), the plasma density calculated with the 2D model is in the same order of magnitude as in the 3D model, with $2x10^{20}$ m^{-3} in the arc centre (cf. figure 5.10(a) and figure 5.5(a)).

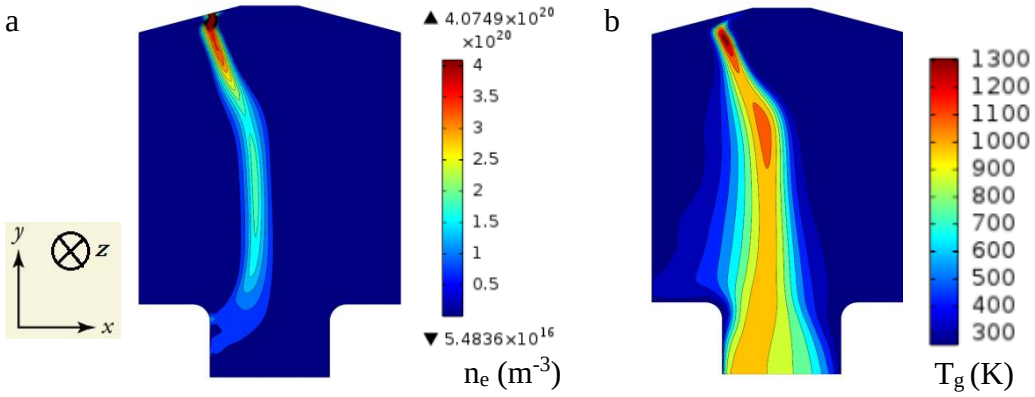

Figure 5.10. Plasma density (a) and gas temperature (b) in the 2D argon model, for the same conditions as in figure 5.5.

The gas temperature shows rather good agreement with the 3D model (i.e., 1300 K vs 1100 K in 3D; cf. figure 5.10(b) and figure 5.5(b)). Of course the lack of convection cooling around the arc has an influence. In [114] the difference between the 3D and 2D model results is lower, because the gas movement was dominantly in the same direction as the arc movement. The local increase of density and temperature at the top portion of the arc is visible in both the 2D and 3D model results, and is due to a local drop in turbulent conductivity (see figure 5.9). In general, from the good agreement between the 3D and 2D model results for argon, we can conclude that the 2D model provides a realistic picture of the GAP, and can also be used to describe the GAP in CO_2. These results are presented in the next section.

5.2.3 CO_2 plasma model

The CO_2 model is a combination of a 3D gas flow model and a 2D plasma model. For the CO_2 turbulent heat conductivity, an additional 3D computation is carried out, for CO_2 gas. This was done in order to account for the specific aspects of turbulence in the CO_2 gas. While the flow field for CO_2 is not significantly different from that of argon, the resulting turbulent heat conductivity is much higher (4-5 W/(m.K)), due to the higher turbulent viscosity. Because of this, the plasma in CO_2 is subject to even more intense turbulent cooling. The turbulent

heat conductivity and the flow field for CO_2 were included in the 2D CO_2 model in the same manner as described in section 5.2.2 - by using interpolation tables. The CO_2 model provides the same type of data as presented above for argon, but major differences in the actual results are to be expected due to some fundamental differences between argon and CO_2 plasmas. First, the different plasma chemistry leads to different excitation levels and power requirements. Therefore, the CO_2 plasma density (figure 5.11(a)) is about an order of magnitude lower when compared to argon at similar conditions, i.e., with a maximum of $4x10^{19}$ m^{-3} in the arc centre vs $4x10^{20}$ m^{-3} for argon (see figure 5.10(a)). Similar reporting for GA plasma can be found in other works. Indeed, in [125], diagnostics were carried out on a classical air GA plasma, showing values for the plasma density of 10^{18}-10^{19} m^{-3} and for the vibrational temperature of 2600 ± 300 K in the non-equilibrium zone. A gas temperature of up to 4000 K was measured in [135], reporting a similar plasma density as well, i.e., 10^{18}-10^{20} m^{-3}, for an arc discharge with CO_2. In [136], a vibrational temperature of 3500 K is reported for air plasma.

The reason for this difference in plasma density is because the applied power is also distributed to vibrational excitation and dissociation of the molecules in the case of CO_2, besides ionization and electronic excitation, which are the only possible inelastic electron-induced processes in argon. In other words, the CO_2 gas requires much more power to reach the same level of ionization in comparison with argon. The different plasma chemistry will alter the results even further.

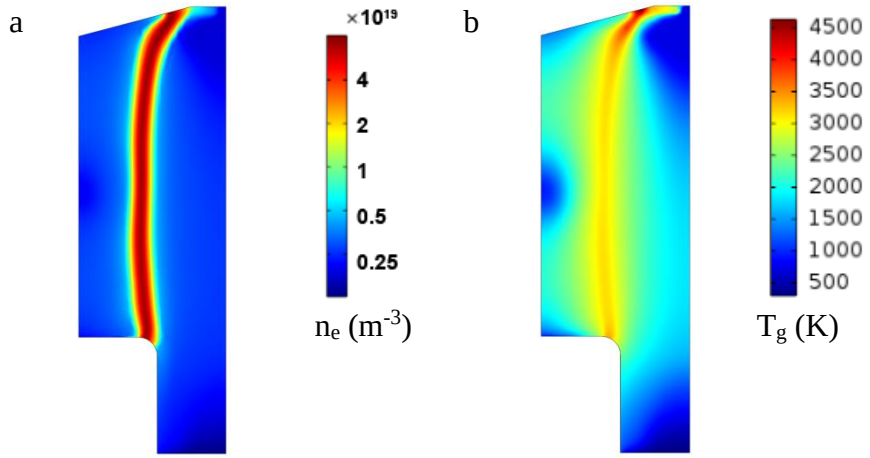

Figure 5.11. Plasma density (a) and gas temperature (b) at 100 A/m of current density in the CO_2 model, a gas flow rate of 22 L/min, and after a calculation time of 1 ms. The estimated total current is 240 mA.

The numerous collisional reactions in the CO_2 plasma contribute more to the gas heating, and result in a much higher value for the gas temperature (see figure 5.11(b)). Furthermore, vibrational excitation, and subsequent vibrational-translational relaxation, which is an important gas heating mechanism in CO_2, is absent in argon. In the case of CO_2, the arc centre, which is subjected to intense turbulent cooling, is characterized by a gas temperature of 3100 K (figure 5.11(b)), while in the arc ends, where it is attached to the electrodes, an even higher value (4500 K) is reached, due to the lower turbulent heat conductivity in these areas. This behaviour is similar to the 3D argon model results, where the arc temperature is also non-uniform, due to the influence of the anisotropic heat conductivity, but the values in argon are much lower (cf. figure 5.11(b) and 5.5(b)).

It needs to be mentioned that the gas temperature value of 4500 K in the CO_2 model near the electrodes is actually quite high. The boundary condition for the reactor walls and electrodes is adiabatic in this model, i.e. no heat transfer can take place at these entities (see details in Chapter III). This leads to an overestimation of the arc temperature near the electrodes. In a real-case scenario (classical or RVF GA), the electrodes are large pieces of metal, often connected to additional metal tubes for gas exhaust (see figure 5.1) or a physical support. In such case, the heat will be distributed to the rest of the system. In addition, it has to be taken into consideration that this is the temperature of the plasma itself, which density is far lower than the density of steel, for example. This means that the total heat transfer to the electrodes will be rather low, and therefore well absorbed by the metal structure, without raising its temperature to the melting point. On the other hand, normal wear (i.e. microscopic melt points), especially on the cathode, occurs in our experiments due to the thermionic emission. So the gas temperature near the electrodes is to be viewed with caution, as it might be overestimated. Modelling a more detailed interaction between the arc and the electrodes is not possible at this point.

When taking the electrodes into consideration, another important remark needs to be given. The reactor operates in the “arc” regime of a DC atmospheric discharge. This means that the cathode surface features a hot (a few thousand degrees K) spot, which is a source of thermal electron emission and strong black-body radiation. When measuring the total power input in the reactor, it has to be considered that a significant amount of it goes into cathode heating. Its amount will depend on a number of conditions. A sharp-edged electrode would promote a higher electric field and stronger emission (see results of the electric field in

Chapter IV), but will also heat up and even melt, depending on the total current. The actual size and shape of the electrode, and the properties of the metal (heat conductivity) will have an impact on the heat distribution and hence power draw. Last but not least, the work function of the particular metal used for the cathode can influence the conditions of forming a cathode spot. For this reason, when comparing electrical characteristics, it has to be mentioned that the cathode spot formation is not featured in the model.

Note that the arc in figure 5.11 is not stabilized in the reactor centre yet, because the results are plotted at a time of 1 ms. However, at this time, the steady-state values of plasma density and gas temperature are reached already, as was demonstrated in Chapter IV, i.e. they would not change as the arc advances further into the reactor centre. The reason that the arc is not shown in the centre here is due to the fact that the centre-line of the modelling plane holds a boundary condition that does not permit flux, i.e. with the arc at this position, the model would provide invalid results, as the boundary condition "no flux" will not permit the plasma in the centre. For this reason, the arc is modelled only until it is still near the sidewall (corresponding to 1 ms of modelling time).

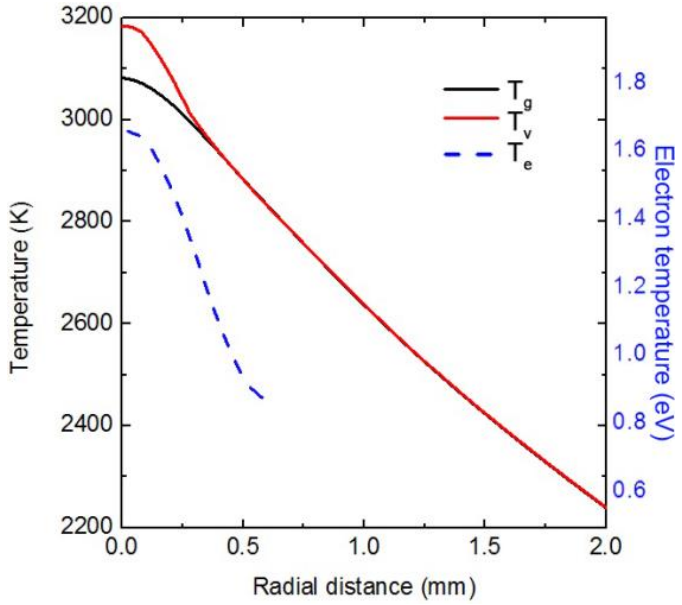

Figure 5.12. Gas (translational) temperature and vibrational temperature (determined from the first vibrational level) (in K; left axis), and electron temperature (in eV; right axis), in the arc, as a function of radial position from the arc centre, for the same conditions as in figure 5.11.

Figure 5.12 illustrates the electron temperature, gas temperature and the vibrational temperature, determined from the first vibrational level of CO_2, as a function of radial position from the arc centre, for the same conditions as in figure 5.11, at y = 15 mm, time = 1 ms.

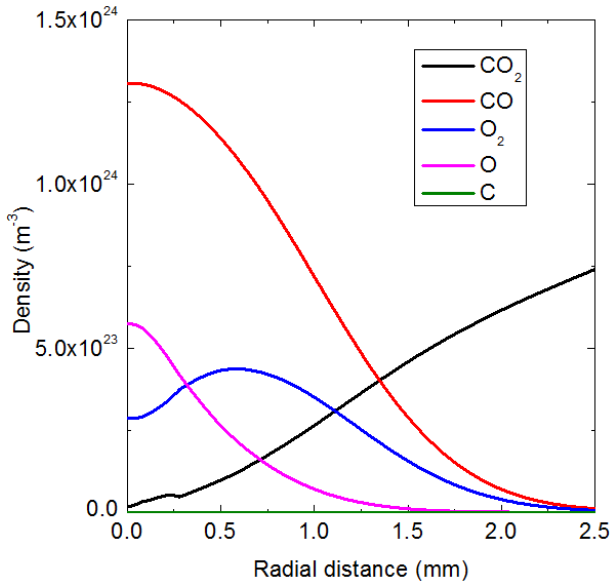

Figure 5.13. Number density of the various neutral species in the arc, as a function of radial position from the arc centre.

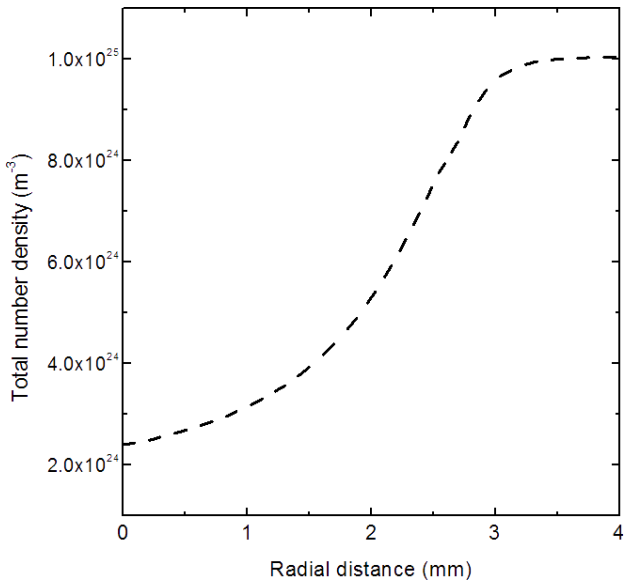

Figure 5.14. Total number density of all species, as a function of radial position from arc centre.

The electron temperature reaches a maximum of 1.6 eV in the arc centre, and drops to lower values after 0.5 mm distance, in correspondence with experimental data from literature for a GA in air [125]. As expected, this value is lower than the calculation result in argon (i.e. 2.5-2.6 eV; see Chapter IV). The electron temperature is plotted up to 0.5 mm only, in order to omit the background heating temperature. The electron temperature value is much higher than the gas temperature and vibrational temperature (i.e., 1.6 eV or 18500 K, vs ca. 3000 K), indicating the non-equilibrium character of the GAP, and explaining why it is very suitable for CO_2 conversion, as the electrons are energetic enough to activate the gas by ionization, excitation and dissociation. The gas temperature shows a less steep drop as a function of radial position, due to the high turbulent thermal conductivity. The difference between gas temperature and vibrational temperature is only around 100 K in the arc centre, and both temperatures even become equal to each other after 0.25 mm from the centre. This difference between vibrational temperature and gas temperature is lower than what was calculated in [130]. The reason for this difference is the higher current density, and thus energy input of the discharge, at the conditions under study. The fact that the vibrational temperature is so similar to the gas temperature indicates that the vibrational distribution function (VDF) of CO_2 is close to thermal, and that the higher vibrational levels of CO_2 are not really overpopulated, which would be needed for energy-efficient CO_2 conversion. Thus, although CO_2 conversion proceeds already in an energy-efficient way in a GAP [64], [59], our model calculations reveal that the energy efficiency could be further improved when the vibrational kinetics could be further exploited.

Figure 5.13 presents the number density of different neutral species in the plasma region, as a function of position from the arc centre, for the same conditions as in figure 5.11. The conversion of CO_2 into CO (and O/O_2) is evident: The neutral CO_2 density shows a clear drop in the arc centre, down to 10^{22} m^{-3} in the periphery of the arc, and even below in the arc centre, indicating almost complete conversion. Clearly, apart from CO_2 splitting upon electron impact collisions, a significant thermal conversion takes place. This can also be deduced from the obtained gas temperature: the thermal conversion can reach 70% with a gas temperature above 3000 K [17]. High gas temperatures actually contribute well to the overall conversion. This complete conversion is, however, only limited to a very narrow arc region, while the rest of the CO_2 gas travelling through the reactor is not being converted (or only to a limited extent, due to thermal conversion when it comes in close contact with the arc). Moreover, it is of crucial

importance how the gas approaches the discharge zone: molecules moving axially with respect to the arc will be exposed to the plasma for a longer time period, in comparison to molecules entering from the sides or swirling around in the vortex. Therefore, the overall CO_2 conversion in the GAP will be significantly more limited, i.e., we measured values in the order of 5-10% [59]. Overall, the problem can be viewed as a two-phase gas mixing process, where a (virtually) untreated gas mixes with a chemically active discharge.

Thus, while the RVF configuration causes the discharge to be stabilized in the centre of the reactor, and forces the gas to travel axially with respect to the plasma arc, not all the gas passes through the discharge zone: a significant amount still leaves the reactor without being in touch with the plasma. In fact, this amount varies across the discharge itself: the arc becomes wider near the reactor outlet, resulting from a combination of flow effects, gas expansion and heat conductivity. The gas velocity magnitude is much higher at the outlet walls than in the central arc itself (see figure 5.4). Also, the flow velocity varies across the arc length, which complicates the estimation further. In order to gain some insight in the problem, the flow rate of gas through the arc body is evaluated. In figure 5.15, the flow velocity is integrated over the arc cross-section, yielding the flow rate at several positions in the axial direction, i.e., along the arc length – from the cathode surface to the outlet. Notice that the flow rate varies across the entire arc body, ranging from 0.3 to 5 L/min.

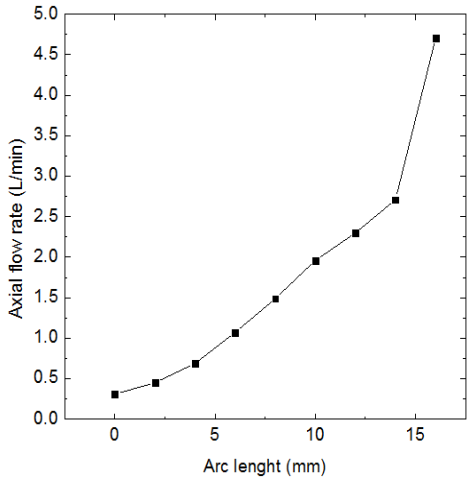

Figure 5.15. Axial flow rate through the arc cross-section for the same conditions as in figure 11. Inlet flow rate: 22 L/min.

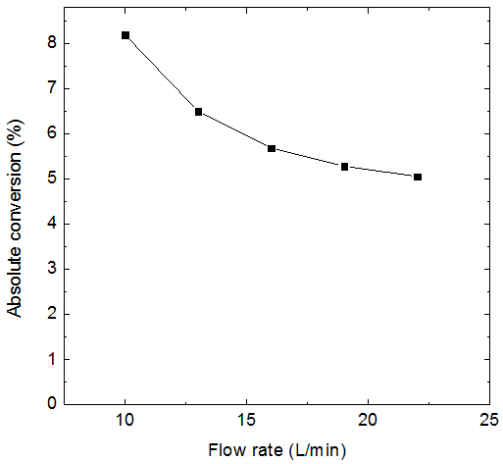

Figure 5.16. Measured absolute conversion of CO_2 at different flow rates, for reactor power of 500 W, adopted from [59].

In figure 5.14, the total number density of all species is plotted as a function of radial distance to the arc centre, showing the inverse relationship with the gas temperature, following the ideal gas law.

Averaging the values in figure 5.15 gives an average flow rate through the arc body of 1.74 L/min. From figure 5.13 we can assume 100% conversion within the arc itself, so we can conclude that the actual conversion would correspond to the percentage of flow moving through the arc. It should be noted that this is an ideal case, with extremely fast quenching, in order to avoid the recombination of CO and O/O_2 back to CO_2. Comparing the average flow rate of 1.74 L/min passing through the arc body to the total gas flow rate of 22 L/min at the inlet indicates that 8% of the gas is forced axially through the arc and is completely converted. This corresponds well with the experimental values of the CO_2 conversion obtained in our GAP, which tend to be between 5% and 8% (see figure 5.16) [59]. The values below 8% are explained because in reality some recombination of CO and O/O_2 back into CO_2 will take place as well (i.e., non-ideal case; see above). It is clear that a longer arc would increase the discharge flow capacity and yield better results. Increasing the total input flow rate would increase the arc throughput as well, but on the other hand, the residence time for the molecules will drop, lowering the overall conversion, as can be observed from figure 5.15.

Another way of improvement would be to increase the turbulent mixing and conductivity, which would lower the gas temperature. By doing so, the reverse reaction, i.e., the three-body recombination reaction of CO with O into CO_2, can be avoided to some extent, improving the net conversion and the energy efficiency. Note that this three-body reverse reaction of CO + O + M is one of the predominant reactions for CO_2 formation, along with $O_2 + CO \rightarrow CO_2$ [130]. Moreover, a lower gas temperature will cause less vibrational-translational relaxation, which is an effective loss mechanism for the higher vibrational levels. Hence, this lower temperature will allow to better exploit the vibrational kinetics through an overpopulation of the higher vibrational levels, which are crucial for energy efficient CO_2 conversion. On the other hand, a higher temperature also gives rise to thermal conversion, which contributes to the overall conversion, but it will not be able to pass the thermal equilibrium limit. The latter should be possible by the non-thermal conversion induced by electrons and the vibrational CO_2 levels, which is the strength of plasma-based CO_2 conversion [17]. It has indeed been shown before that the gas temperature plays a key role in the energy efficiency for CO_2 conversion in so-called warm plasmas, such as GA discharges and microwave plasmas, and in general, lower temperatures yield a more energy

efficient conversion [137]. Therefore, the discharge temperature control is of utmost importance for the reactor efficiency.

Increasing the turbulent mixing, to lower the gas temperature, can be achieved by increasing the flow rate or changing the characteristic dimensions of the reactor (i.e. inlet/outlet diameter, reactor body size, etc.). In addition, the total arc power has a clear influence on the gas temperature, but in practice its adjustment range is limited due to the power source and the arc regime specifics (i.e. the arc plasma requires a high current and results in a rather low discharge voltage, in comparison with a glow regime, for instance) [59].

5.3 Conclusion

In this Chapter, we present a very first model for a RVF GA reactor for CO_2 conversion. Due to the high computational cost, the study is composed by separate 3D and 2D models - a 3D argon gas flow and 3D argon plasma model, as well as a 3D CO_2 gas flow and 2D CO_2 plasma model. The 3D argon model operates with a simplified chemistry set for argon, and is focused on the gas dynamics, the arc movement, and the basic plasma characteristics of a GA in RVF configuration, such as plasma density and temperature. The calculated plasma density and gas temperature in argon are around 10^{20} m^{-3} and 1100 K, respectively, and these values are comparable to the available literature [19], [125], [127]. We also clearly demonstrate the arc rotation and stabilization mechanism through elaborate 3D observations. This work is a substantial improvement of Chapter IV due to the usage of a realistic (and not just a conceptual) geometry, the total arc current lying within the experimental range, and especially the turbulent heat transfer calculation.

The insulation mechanism is clear: the RVF reactor forces the mass flow from the walls in the direction to the arc, i.e. the walls can only receive minor heating by radiation from the arc, but not through convection or conduction. The major effect of the turbulent heat transfer on the calculated gas temperature is demonstrated, by comparing with calculation results where this was not yet included. The high flow turbulence in the reactor leads to intense heat exchange due to rapid turbulent oscillations. The effect is dominant for the arc cooling – the turbulent gas thermal conductivity for the given conditions is almost 100 times higher than the gas thermal conductivity. This leads to a much wider thermal profile of the arc, a difference in arc contraction, and a significantly lower gas temperature. As far as we know, this effect has not been demonstrated so far in low-temperature arc plasma models.

Applying the model to a CO_2 plasma indicates that the CO_2 conversion is partially through electron impact activation and partially thermal. Indeed, the gas

temperature is around 3000 K, hence a factor 3 higher than in argon, because of the more collisional plasma and in particular by the gas heating due to vibrational excitation of CO_2, following by vibrational-translational relaxation. Our model also shows that, in spite of the high gas temperature, the arc is not in thermal equilibrium, in agreement with other works [125], [135], [136] as the electron temperature is still a factor 6 higher than the gas temperature. However, the vibrational temperature is quite close to the gas temperature, and we believe that the energy efficiency of CO_2 conversion in the RVF GAP, although being very promising already (~ 30-35%, [59]) can be further improved if the non-equilibrium character of the vibrational distribution function can be further exploited. Effects of the turbulent cooling may have a significant impact on this property, because vibrational-translational relaxation, which is the major loss mechanism for the higher vibrational levels, will be reduced at lower temperature. That is the reason why we stress its importance in this Chapter. A lot of emphasis in this Chapter is put on the argon models in 2D and 3D, while the main object of interest is the CO_2 plasma. There is a good reason for this – argon and CO_2 plasmas are fundamentally different. They feature different plasma properties, gas temperature and discharge structure. As the CO_2 plasma model is within reach only in 2D models, there is no way to predict whether it will retain the same properties in 3D. For this reason, the approach of "downgrading" a 3D argon model into 2D, and comparing them, was used to validate the accuracy of the method: as the difference between the 3D and 2D argon models is acceptable, we therefore conclude that the 2D CO_2 model provides data with a reasonable accuracy. In this way, we have extracted the most of the currently available methods, and their limitations.

Finally, we also calculated the densities of the CO_2 splitting products, i.e., mainly CO, O_2 and O, and we demonstrated that the CO_2 conversion in the centre of the arc is virtually 100%. The reason that the overall CO_2 conversion is so much lower in our experiments is because only a limited fraction of the gas passes through the actual discharge. We evaluated the overall conversion through detailed analysis of the flow configuration, predicting that the gas flow through the arc is only about 8 % of the total gas flow at the inlet. This means that the overall conversion is also limited to (at maximum) 8 %, which is in excellent agreement with our experimental findings.

While these models can already provide a lot of important information, they still lack some specific features. First, the electrode surface is not accounted for. As mentioned, microscopic bumps and scratches on the electrodes cause a local increase of the electric field, and thus attract the arcs. In reality, the arc movement is much more random, while the model shows a smooth transition of the arc position. Also, the adiabatic boundary condition for the electrodes is an approximation of the model. This has been already discussed in previous Chapter. The lack of description for the electrode heat balance omits the ability of the

model to perform calculations for thermionic emission on the cathode "hot spots", or emission zones. Furthermore, the 3D-2D CO_2 approach also has its limitations: with the arc being a plane instead of a "string", there is no easy way to measure what portion of the gas mixes with the discharge and can be converted. The gas cannot swirl around the arc, bend it in a spiral shape, or flow around it, as it would do in the 3D model and the experiments. Therefore, for predicting the fraction of gas passing through the arc, we used the insights obtained from the argon 3D model.

In summary, the study presented here makes the most out of the available plasma modelling methods. A complete 3D quasi-neutral model for argon plasma describes the arc motion in detail and incorporates advanced turbulence modelling for turbulent heat transfer. A CO_2 model, which uses a combined approach – flow and turbulence calculations in 3D and plasma model calculation in 2D, describes the complex plasma chemistry, and its impact on CO_2 conversion. With this foundation, the path is clear: we have a clear definition of the arc shape and its movement, its plasma parameters in CO_2 gas, and its conversion rate, based on which we plan to develop in the future a complete computational study of the conversion and energy efficiency, involving more complex flow modelling, featuring particle tracing.

CHAPTER VI. Modelling and diagnostics of an atmospheric pressure glow discharge

This work is presented as:
G Trenchev, M Vasiljevic, A Nikiforov, St Kolev, P Awakowicz, N Bibinov and A Bogaerts., "Poster: Model of an atmospheric pressure glow discharge," *VEIT, Sozopol, Bulg.*, 2017.

Abstract

The atmospheric pressure glow discharge (APGD) with gas flow is a robust non-thermal DC plasma source with a variety of applications. One of its main qualities is that it sustains a glow-like regime, which keeps the gas temperature relatively low, while still providing a moderately dense plasma. In order to gain insight into its operation and characteristics, we analyse a pin-to-mesh APGD by means of optical emission spectroscopy in an Ar/N_2 gas mixture, and we further investigate it through computer modelling. A very good agreement is reached between modelling and experiments.

6.1. APGD experimental setup

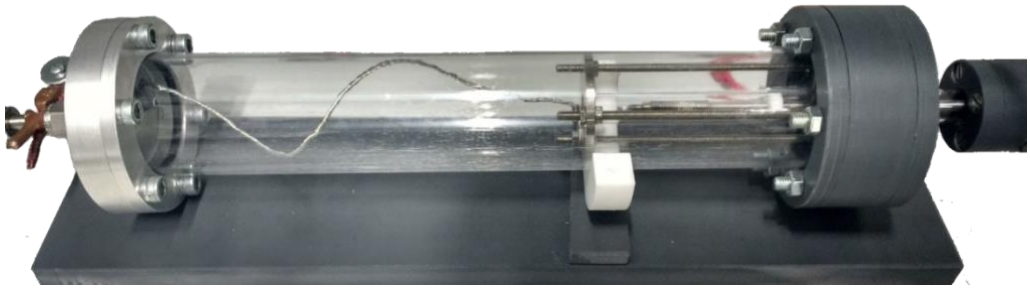

Figure 6.1. Photograph of the APGD reactor. The metal plate holding the anode mesh is mounted on 3 metal pins. The small internal tube is in the reactor center, where the cathode pin is also visible.

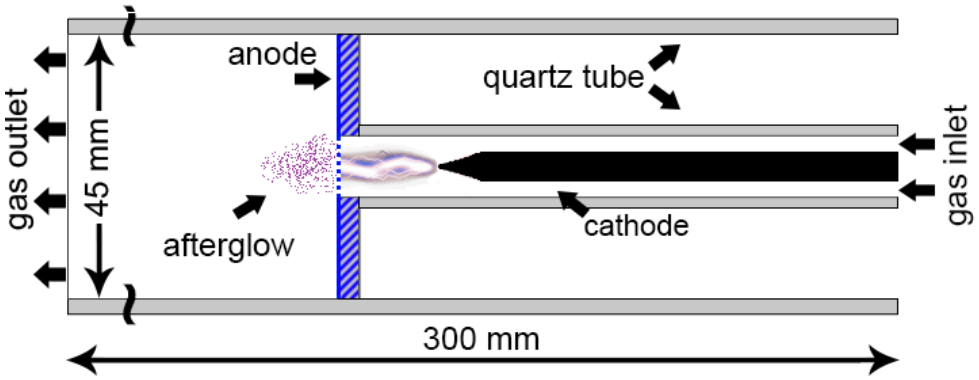

Figure 6.2. Schematic of the reactor design, with artistic representation of the discharge and the afterglow. The external tube has a length of 300 mm and internal diameter of 45 mm; the small tube internal diameter is 10 mm and its length is 100 mm. The gas enters the reactor axially, inside the smaller tube and flowing around the cathode pin, which has a diameter of 5 mm and adjustable length of 78 mm.

The APGD consists of an outer quartz tube with length of 300 mm and internal diameter of 45 mm, which houses the electrodes and the internal gas guide tube. The smaller internal tube (also made of quartz) holds the cathode pin and guides the gas flow to the anode mesh (see figures 6.1 and 6.2). The anode mesh is mounted on a metal plate at the end of the internal tube. The distance between both electrodes can be varied with an adjustment screw.

The distance between the cathode pin (black) and the anode plate and mesh (blue, dotted/striped in figure 6.2) is set to 16 mm in this work. The gas flow inlet

is indicated on the right, and the gas travels axially with respect to the cathode pin. An outlet is mounted on the end of the reactor (left), acting as a gas exhaust.

A high voltage power supply, supplying up to 30 kV at 40 mA with a negative output is used. A 300 kΩ ballast resistor limits the electric current. The flow of argon/nitrogen gas mixture is adjusted by a MKS mass flow controller. The total flow rate of the gas mixture is 10 L/min. The discharge current in our experiments is varied between 5 and 10 mA.

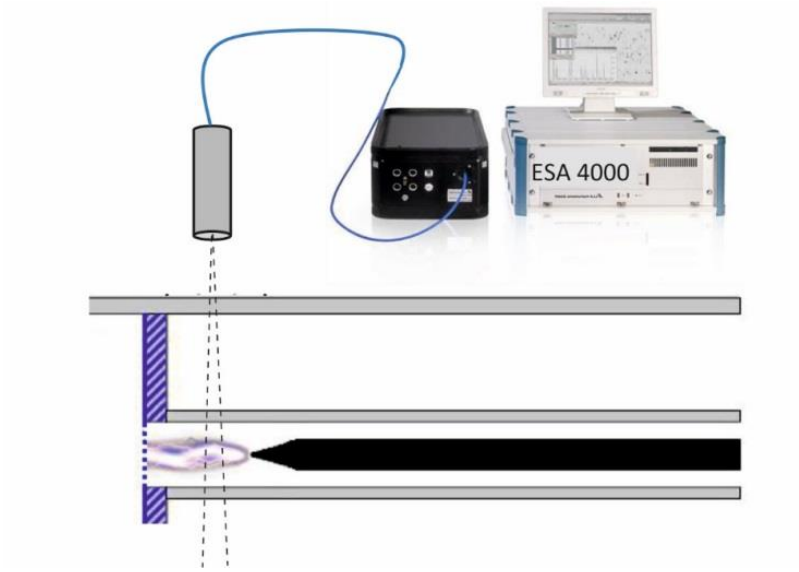

Figure 6.3. Experimental set-up for the OES diagnostics of the APGD. An aperture that ends an optical fiber connected to Echelle spectrometer is placed at the distance of 50 mm from the axis of APGD plasma source (see figure 6.3). The total apex angle of acceptance cone of the optical fiber with the aperture amounts to 1.5°.

For the purpose of OES (optical emission spectroscopy) discharge characterization, we collaborated with the group of Prof. Awakowicz at Ruhr-Universität Bochum, which has a relatively and absolutely calibrated broad-band spectrometer Echelle "ESA-4000". This spectrometer has a high resolution of 15 pm up to 60 pm and a broad wavelength range from 200 to 800 nm. The spectral resolution is sufficient for separation of the rotational lines in the measured emission spectrum of nitrogen molecular ions. The spectrometer is calibrated

using deuterium and tungsten ribbon lamps as secondary light source standards. Figure 6.3 illustrates the system configuration for the OES diagnostics.

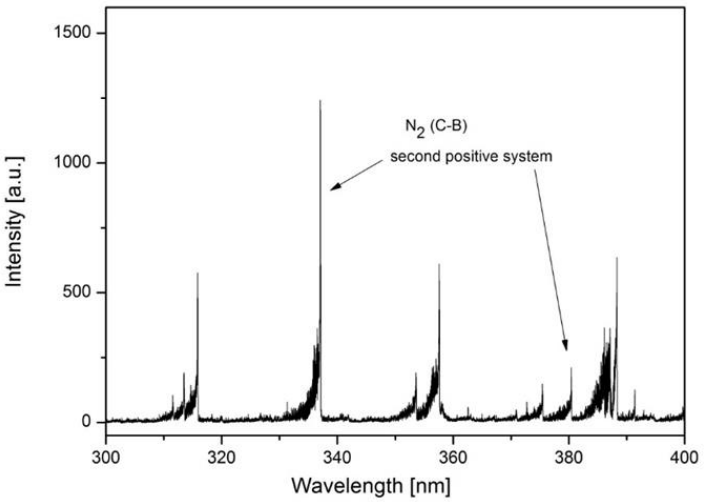

Figure 6.4. Sample spectrum, measured in APGD at 7.5 mA with Ar/N_2 0.95/0.05 gas mixture. Two nitrogen molecular bands, namely N_2(C-B,0-0) at 337.1 nm and N_2(C-B,0-2) at 380.5 nm, are used to determine the gas temperature.

The gas temperature in the active plasma zone of the APGD is determined by analysis of the rotational structure of the nitrogen molecular bands in the second positive system, namely the 0–0 and 0-2 vibrational band of N_2(C–B) emission (see figure 6.4). We determine the rotational temperature T_r (equal to the translational temperature) of neutral molecular nitrogen by means of the corresponding Boltzmann plot (equation 6.1), in assumption of thermal equilibrium populations:

$$\ln\left(\frac{I_{N'N''}}{\nu^3_{N'N''''}S_{N'N''}g_{N'}}\right) = -\frac{B_{\nu'}N'(N'+1)hc}{kT_r} \tag{6.1}$$

where $I_{N'N''}$ is the intensity of the rotational line of the non-resolved fine structure, N is the rotational angular momentum quantum number, excluding electron and nuclear spin, $\nu_{N'N''}$ is the frequency of the radiation, $S_{N'N''}$ is the appropriate Hönl–London factor, $g_{N'}$ is the degeneracy of the upper rotational level, $B_{v'}$ is the molecular rotational constant for the upper vibrational level, h is Planck's constant

and c is the speed of light. Because of enough long lifetime in plasma and frequently collisions under atmospheric pressure conditions, the rotational and translational degrees of freedom of the nitrogen molecule in ground state are in equilibrium. The rotational distribution is changed only slightly by electron impact excitation. Therefore, the rotational distribution of excited $N_2(C)$ and ground $N_2(X)$ states are similar and the rotational temperature of the former is equal to the gas temperature. The second positive system of nitrogen can be excited in argon/nitrogen mixture also by collisions with argon metastables. The rotational distribution of the N(C) state excited in this process differs strongly from the rotational distribution at high gas temperature. But because of effective rotational relaxation under atmospheric pressure conditions in argon/nitrogen mixture, an equilibrium between the rotational and translational degrees of freedom is achieved before emissions of the photons [138]. Therefore, the rotational temperature determined using the second positive system on molecular nitrogen in argon/nitrogen mixture under atmospheric pressure conditions is very similar to the gas temperature. The obtained results for the gas temperature will be presented in section 6.4.

6.2. APGD modeling

The APGD model is developed by means of COMSOL Multiphysics [67]. The gas flow model involves solving the Navier-Stokes equations for a stationary solution (see details in Chapter III). Subsequently, the gas flow data is used as a direct input for the plasma model, which consists of 8 partial differential equations (PDEs), i.e., 5 PDEs for species balance, 1 gas heat transfer equation, 1 equation for the electric potential distribution, and an ordinary differential equation describing the external circuit of the discharge. As mentioned, the argon plasma chemistry is based on [99], [113] assuming a quasi-neutral plasma [117], i.e. the wall sheaths are neglected and excluded from the simulation. We have employed this method in previous Chapters, concluding that, if focusing on the properties of the plasma column, it provides the same results as a non-quasineutral model, which has much stronger computational requirements (and leads to problematic model meshing). The model is in 2D, assuming cylindrical symmetry, which saves computation time (the reactor geometry, in figures 6.1 and 6.2, is very suitable for such approach).

The gas flow is computed using the laminar flow interface in COMSOL Multiphysics. This interface allows for computing the Navier-Stokes equations in

their full form. The following equations are computed, here shown in cylindrical (axi-symmetric) coordinates:

$$\frac{1}{r}\frac{\partial(r\boldsymbol{u}_r)}{\partial r}+\frac{\partial \boldsymbol{u}_z}{\partial z}=0 \tag{6.2}$$

$$\frac{\partial \boldsymbol{u}_r}{\partial t}+\boldsymbol{u}_r\frac{\partial \boldsymbol{u}_r}{\partial r}+\boldsymbol{u}_z\frac{\partial \boldsymbol{u}_r}{\partial z}=-\frac{1}{\rho}\frac{\partial p}{\partial r}+\frac{\mu}{\rho}\left\{-\frac{\boldsymbol{u}_r}{r^2}+\frac{1}{r}\frac{\partial}{\partial r}\left(r\frac{\partial \boldsymbol{u}_r}{\partial r}\right)+\frac{\partial^2 \boldsymbol{u}_r}{\partial z^2}\right\}+f_r \tag{6.3}$$

$$\frac{\partial \boldsymbol{u}_z}{\partial t}+\boldsymbol{u}_r\frac{\partial \boldsymbol{u}_z}{\partial r}+\boldsymbol{u}_z\frac{\partial \boldsymbol{u}_z}{\partial z}=-\frac{1}{\rho}\frac{\partial p}{\partial z}+\frac{\mu}{\rho}\left\{\frac{1}{r}\frac{\partial}{\partial r}\left(r\frac{\partial \boldsymbol{u}_z}{\partial r}\right)+\frac{\partial^2 \boldsymbol{u}_z}{\partial z^2}\right\}+f_z \tag{6.4}$$

where ρ stands for the gas density, $\boldsymbol{u}_{r,z}$ is the respective gas flow velocity vector, p is the gas pressure, μ is the dynamic viscosity of the fluid, and $f_{r,z}$ stands for the body force vector. The boundary conditions are identical to the ones used in Chapter IV.

The fluid plasma model is built upon the assumption of a quasi-neutral plasma, i.e. ion and electron densities are equal (see details in Chapter III). The model is constructed using the Math module in COMSOL. The following equation is solved for the ion density:

$$\frac{\partial n_i}{\partial t}+\nabla.\left(-D_i\nabla n_i+\mu_i n_i\overrightarrow{E_{amb}}\right)+\left(\vec{u}_g.\nabla\right)n_i=R_i \tag{6.5}$$

where n_i stands for the ion density, μ_i stands for the ion mobility, $\overrightarrow{E_{amb}}$ is the ambipolar electric field, $\vec{u}_g$ is the gas flow velocity vector, D_i is the ion diffusion coefficient, and R_i stands for the ion production and loss rates due to chemical reactions. The electron density n_e is derived from the quasi-neutrality condition, which in this case is $n_e = n_i$.

In the model, the following species are considered: Ar – argon atoms, Ar^+ – argon ions, Ar_2^+– argon molecular ions, Ar(4s) – all 4s levels considered as a single lumped excitation level, Ar(4p) – all 4p levels considered as a single lumped excitation level, and Ar_2^* – excited molecules. The reactions are presented in tables 6.1 and 6.2, with the according source data. As the model is quasi-neutral, the electron balance equation is not computed, as the electron density is the same as the total ion density. The full reaction set can be seen in [113].

The discharge current is calculated from a discharge control circuit featuring a ballast resistor, depicted in figure 6.5.

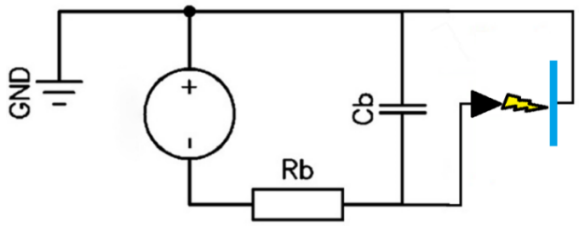

Figure 6.5. Electrical scheme of the model with cathode (black) and anode (blue).

In figure 6.5, the ballast resistor limits the discharge, and it can be set in accordance with the desired current. The capacitor Cb (100pF) serves for reducing the voltage spikes. The electrodes are depicted in balck (cathode pin) and blue (anode). In the model, the above schematic is handled by an ordinary differential equation (ODE) from the Math module in COMSOL.

6.3. Results and Discussion

In figure 6.6, the gas flow pattern obtained from the model is presented. This is the direct result from solving the Navier-Stokes equations. The flow rate of 10 L/m is achieved by imposing 2.5 m/s for the inlet boundary velocity. As the simulation indicates, the gas flow velocity reaches 3.5 m/s in between the cathode pin and the quartz tube, as well as in a narrow region close to the tube wall, while the flow velocity in the center of the tube is only around 1 m/s or even lower near the cathode pin. Furthermore, the gas flow is laminar for the given flow rates.

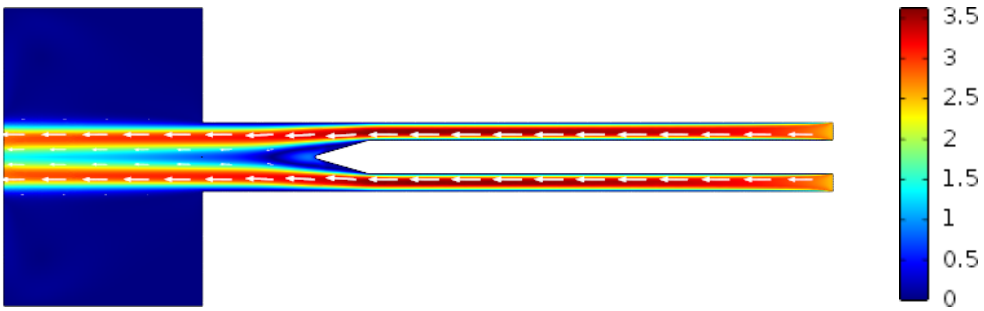

Figure 6.6. Gas flow pattern and velocity at a flow rate of 10 L/min. The flow direction is indicated with white arrows, while the velocity is represented by the color scale at the right of the figure.

In figure 6.7, we illustrate the calculated plasma density. A peak density of $7.5x10^{19}$ m^{-3} is reached at the tip of the cathode, which is to be expected, as the electric field is the strongest there. The rest of the discharge shows a rather uniform decaying distribution with density in the range of $10^{18} – 10^{19}$ m^{-3}, which is typical for DC glow regimes [19]. In [139], similar values were reported for an atmospheric pressure plasma jet operating in argon. In [140], a similar plasma density (10^{14} cm^{-3}) was reported for an argon plasma jet.

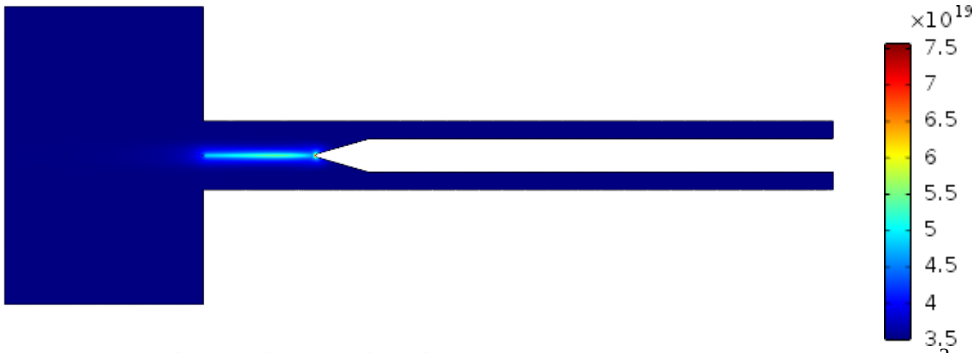

Figure 6.7. Plasma density distribution at 10 mA, 10 L/min. (m^{-3})

At the given conditions of 10 mA discharge current and 10 L/min of gas flow rate, the gas temperature reaches over 1300 K near the cathode pin, as can be seen in figure 6.8. A hot discharge plume can be observed, propagating beyond the anode mesh. This is a direct result from the flow convection (see figure 6.6).

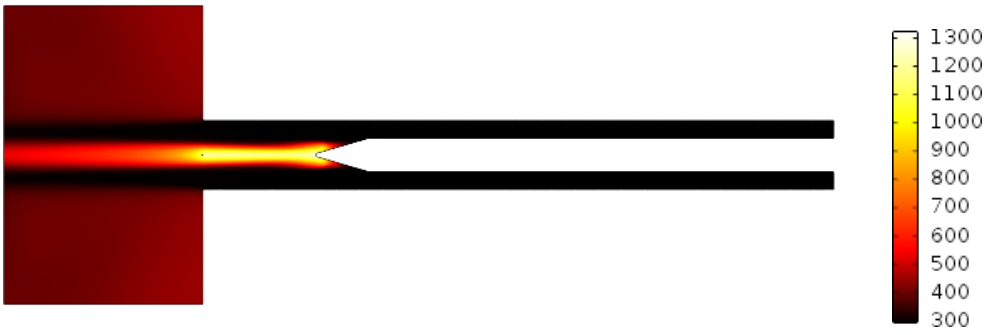

Figure 6.8. Gas temperature distribution at 10 mA, 10 L/min. (K)

The potential distribution is plotted in figure 6.9. The cathode voltage is at -250 V, defined with respect to the grounded anode (mesh and plate). Voltage drops of a few hundred volts are typical for argon DC discharges. It is important to note that due to the quasi-neutral assumption in the model (see Chapter III), the

Poisson equation is not solved, and the plasma sheaths cannot be resolved, i.e. the calculated voltage drop is typically lower than in experiments.

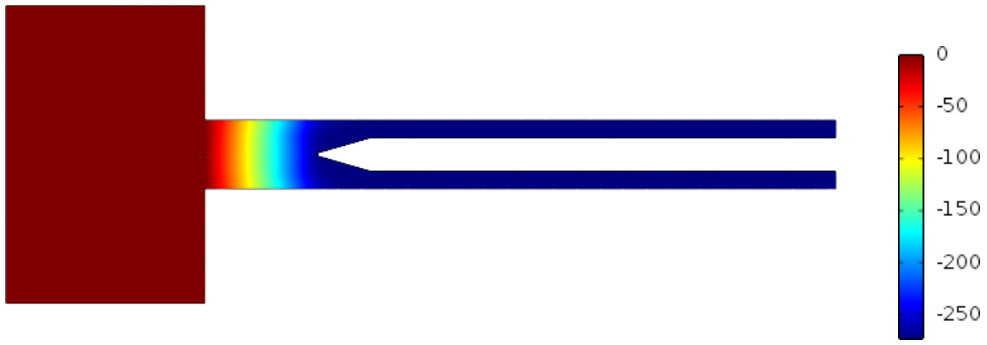

Figure 6.9. Potential distribution at 10 mA, 10 L/min. (V)

In figure 6.10 we present the electron temperature in the discharge. The peak value of about 2.6 eV is rather high for such type of discharge (though well within typical limits [19]). The electron temperature off-axis is around 2 eV or lower, while it drops to 0.6-1 eV in the afterglow region, which is logical, as there is no electric field in this region. Further comparison can be made with similar studies on low-temperature argon plasma sources. In [53], an electron temperature of up to 3.9 eV was reported for an atmospheric pressure plasma jet. Another study of an RF argon plasma jet yielded electron temperature of 2-3 eV [140].

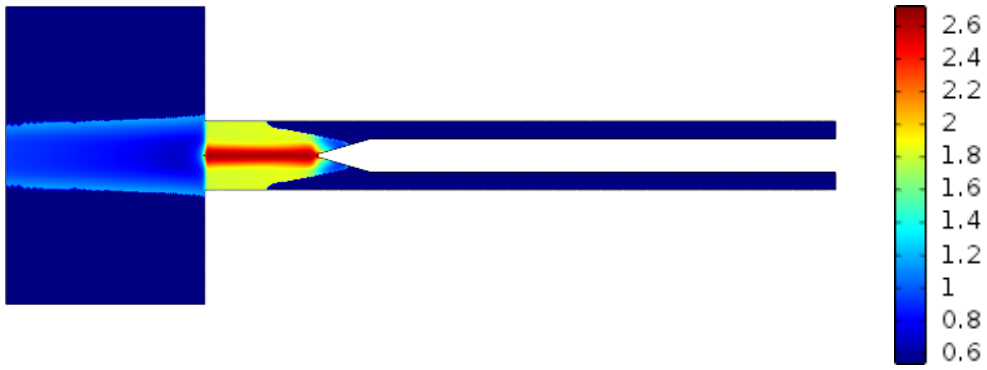

Figure 6.10. Electron temperature distribution at 10 mA, 10 L/min. (eV)

We performed calculations for different values of the electric current, and the results are illustrated in Figures 6.11 and 6.12 for the various plasma parameters investigated, taken at a position z = 7 mm from the cathode tip, i.e. the position

of the OES lens. As seen in figure 6.11, the plasma density and gas temperature increase almost linearly with current. While 10 mA yields a gas temperature of nearly 1300 K and a plasma density of about $5x10^{19}$ m^{-3} (see also figures 6.7 and 6.8), at 5 mA, the gas temperature is only about 1000 K. This might be more beneficial for energy-efficient gas conversion [116]. In figure 6.12, it can be seen that the total voltage across the discharge decreases at higher current. This is to be expected, because of the higher plasma conductivity, yielding a lower total resistance and thus voltage drop. The reduced electric field strength follows nearly the same trend, determined by a combination of the effects of gas expansion due to heat and potential drop.

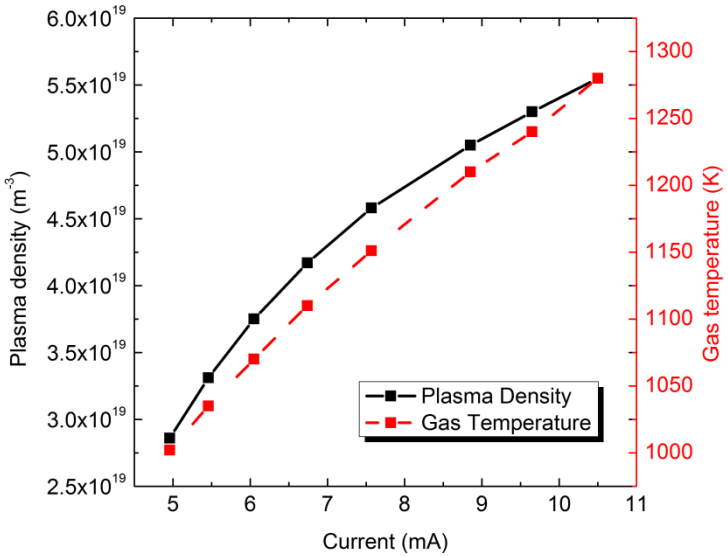

Figure 6.11. Plasma density and gas temperature at different discharge currents.

In figure 6.13, we plot the gas and electron temperature as a function of radial distance from the central axis, at 8 mm from the cathode pin. The gas temperature exhibits a steep slope from 1250 K down to 273 K, demonstrating that the hot plasma region has a radius of about 1 mm. Naturally, this distribution is shaped by the effects of flow convection, gas expansion and plasma species decay. The electron temperature behavior is very similar, decreasing from 2.5 eV in the center to about 1.4 eV in the outer region, which arises from the stabilizing background heating in the model.

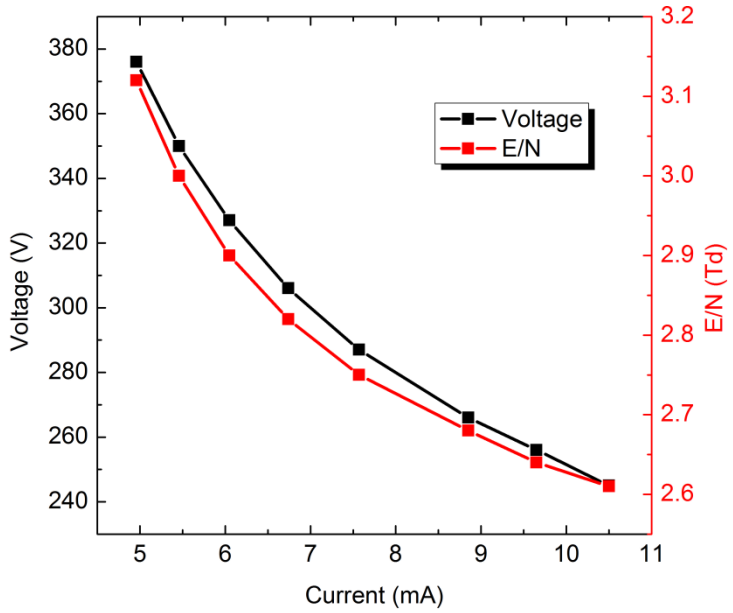

Figure 6.12. Total voltage drop and reduced electric field at different discharge currents.

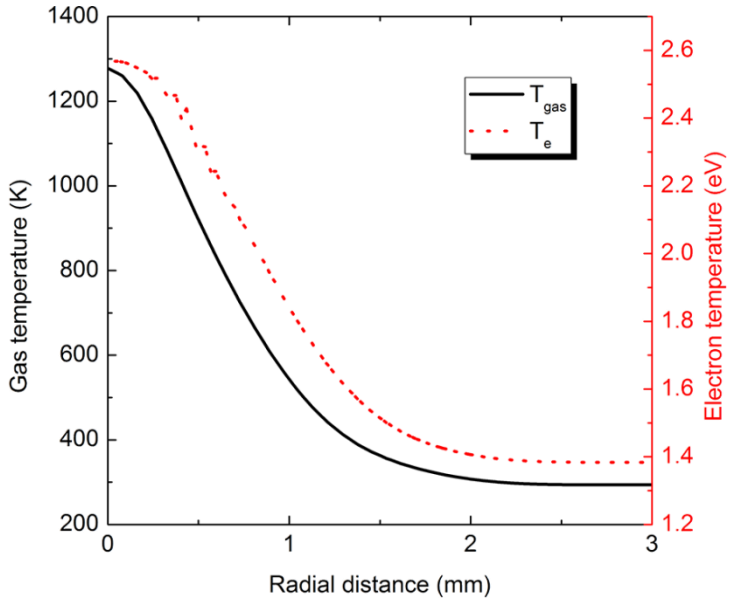

Figure 6.13. Gas and electron temperature as a function of radial distance from the discharge center, at 7 mm from the cathode pin, for 10 mA and 10 L/min.

Figure 6.14 presents the densities of the various plasma species in the discharge, as a function of radial distance from the central axis. The Ar^+ ions are dominant, with a density of about $5x10^{19}$ m^{-3}. The molecular ions Ar_2^+ reach a maximum density of $3x10^{18}$ m^{-3}, while the excited Ar atoms, i.e., Ar(4s) and Ar(4p), have maximum densities of about $2x10^{18}$ m^{-3} and $5x10^{17}$ m^{-3}.

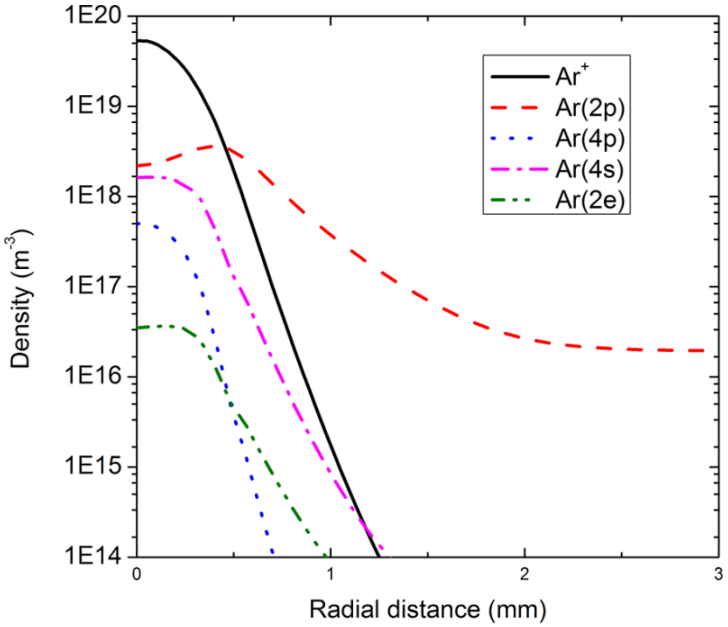

Figure 6.14. Species number density as a function of radial distance from the discharge center, at 7 mm from the cathode pin, for 10 mA and 10 L/min.

Although the Ar(4s) atoms have a maximum density close to that of the Ar_2^+ ions, they exhibit a much narrower distribution, i.e. corresponding to less species in the discharge volume. Finally, the Ar_2^* excited molecules are characterized by a maximum density of $3x10^{16}$ m^{-3} in the discharge center.

On figures 6.15 and 6.16, the axial distributions of the gas temperature and plasma density are shown. On figure 6.15, starting from the 0 point (cathode pin), we see a maximum gas temperature of nearly 1400 K (at 10 mA), with a gradual drop to 1300 K along the discharge. This value remains relatively constant across the discharge until the anode plate, which is marked by a sharp drop in gas temperature, as the gas is no longer subjected to heating beyond this point. This behavior is also observed at lower currents.

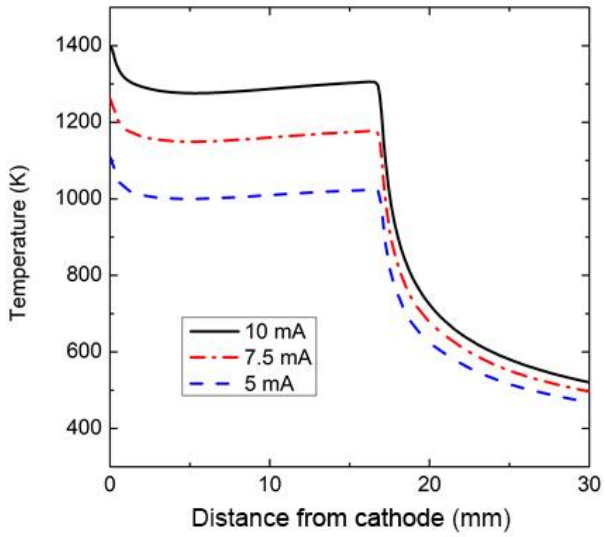

Figure 6.15. Axial distribution of the gas temperature, for 3 different current values. 0 mm matches the cathode pin.

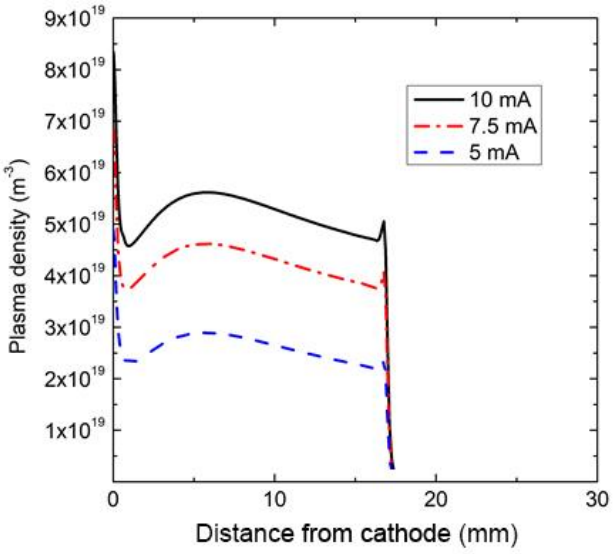

Figure 6.16. Axial distribution of the plasma density, for 3 different current values. 0 mm matches the cathode pin.

Looking at figure 6.16, we see a similar picture: a maximum value of the plasma density is reached at the cathode pin, followed by a relatively constant

value in the discharge. The drop at the anode is very abrupt, and this is easy to understand: the lack of electric field beyond the anode means that no plasma is produced.

In figure 6.17 the model results for the gas temperature are compared with the experimental values obtained using two bands, namely N_2(C-B, 0-0) at λ= 337.1 nm and N_2(C-B, 0-2) at λ= 380.5 nm. As it was shown before, the radial distribution of the gas temperature is approximately constant for the entire active APGD volume.

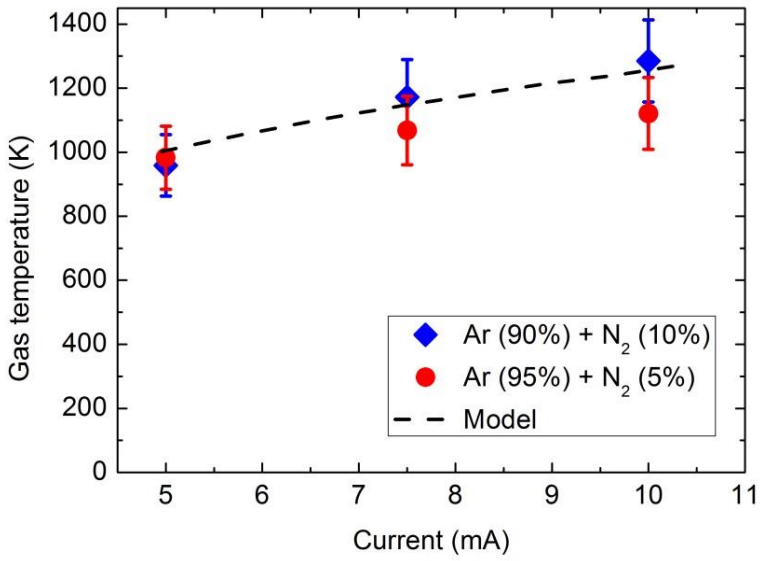

Figure 6.17. The averaged gas temperature in APGD, both simulated and measured in Ar/N_2 gas mixture using OES. The inaccuracy of the gas temperature determination using OES amounts in this study to 10% (shown by the error bars in the figure).

Therefore, spatially non-resolved measurements of the gas temperature can be compared to the simulated averaged values. Two modes of nitrogen mixing were employed – with 5% and 10% of total N_2 in the gas input. The simulated and measured values of gas temperature in the APGD are very similar. The inaccuracy of the gas temperature determination using OES amounts in this study to 10%. The measured values are very similar to the gas temperature determined in the near-cathode layer in an atmospheric pressure DC plasma jet in nitrogen flow [141].

6.4. Conclusion

We investigated an APGD by means of a 2D fluid plasma model for argon and OES measurements with low N_2 admixture. The calculated gas flow pattern, as well as the 2D distributions of gas temperature, plasma density, electron temperature, electric potential and reduced electric field, are plotted in order to visually characterize the discharge. The calculated gas temperature was found in reasonable agreement with the experimental data for different values of the electric current. This serves as an experimental validation of the plasma model, which confirms its applicability for atmospheric DC discharges. Of course, the main difference between the model and the experiments is the presence of N_2 admixture, which is not accounted for in the model. However, the N_2 contents were kept low, for the sake of comparison with the model. According to the results, a 5% N_2 mixture appears to be the minimum amount required for sufficient band emission, because the noise floor is already quite high. The opposite approach on further improving the agreement – by adding N_2 in the model chemistry – might be viable as well, but it will introduce more chemical reactions, thus increasing the computation time (apart from the need of developing and validating the chemistry set). Furthermore, while the experimental data matches the model in gas temperature, it is unclear whether this is the case for other plasma parameters, such as species density and electron temperature, which could not be obtained experimentally due to practical limitations. Nevertheless, this work is a valuable addition to the knowledge base for APGD, a promising plasma source with numerous possible applications. In the next Chapter, the APGD will be exploited for CO_2 conversion.

CHAPTER VII. Atmospheric pressure glow discharge for CO_2 conversion: Model-based exploration of the optimum reactor configuration

This work is published as:

G Trenchev, A Nikiforov, W Wang, St Kolev and A Bogaerts, Atmospheric pressure glow discharge for CO_2 conversion: Model-based exploration of the optimum reactor configuration, *Chemical Engineering Journal*, **362**, 830-841, 2019

Abstract.

We investigate the performance of an atmospheric pressure glow discharge (APGD) reactor for CO_2 conversion in three different configurations, through experiments and simulations. The first (basic) configuration utilizes the well-known pin-to-plate design, as also studied in previous Chapter, which offers a limited conversion. The second configuration improves the reactor performance by employing a vortex-flow generator. The third, "confined" configuration is a complete re-design of the reactor, which encloses the discharge in a limited volume, significantly surpassing the conversion rate of the other two designs. The plasma properties are investigated using an advanced plasma model.

7.1 Experimental setup

The APGD is powered by a high voltage Technix DC power supply, capable of supplying up to 30 kV at 40 mA, regulated to 0.05 % accuracy, with a negative output. A 300 kΩ ballast resistor limits the electric current and sustains the discharge in the glow mode. The flow of CO_2 gas is adjusted by a Bronkhorst mass flow controller. The discharge current in our experiments is varied between 20 and 30 mA. The treated gas is measured by a GAS CompactGC gas-chromatograph (GC; Interscience). The gas composition is captured by the thermal conductivity detector (TCD-B channel) of the GC. A Molsieve 5A and Rt-Q-Bond column were used to separate O_2 and CO. A back-flush configuration for the CO_2 gas protects the 5A column from poisoning. Figure 7.1 presents the entire experimental setup.

The CO_2 conversion is obtained by the following formula:

$$X_{CO_2}[\%] = \frac{n_{CO_2(in)} - n_{CO_2(out)}}{n_{CO_2(in)}} \times 100\% \qquad (7.1)$$

where $nCO_{2(in)}$ is the CO_2 concentration without plasma, and $nCO_{2(out)}$ is the CO_2 concentration after plasma treatment. Note that we only measured CO_2 and O_2 as products. In principle, there can also be some O_3 production, but it is considered negligible here, due to the high temperature. We always performed three consecutive measurements, to obtain an average value and standard deviation.

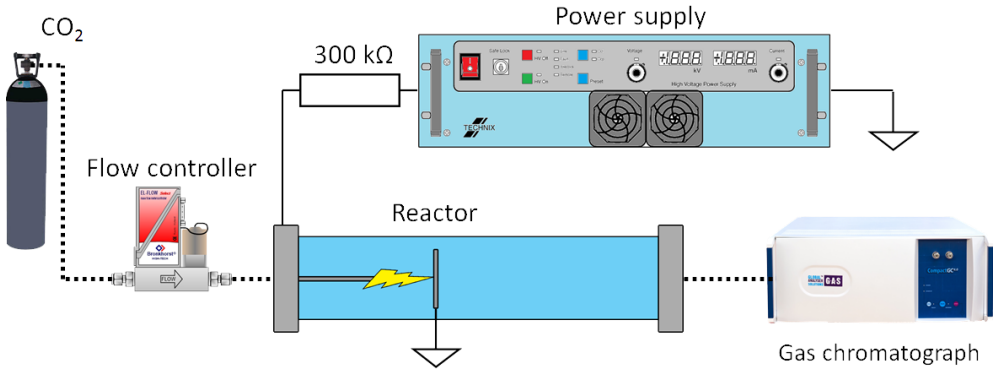

Figure 7.1. Experimental set-up. Dotted lines represent gas connections, full lines represent electrical connections. The CO_2 gas is at 99.5 vol% purity, supplied by Air Liquide.

The specific energy input (SEI), which is an important parameter to determine the energy efficiency, is defined as:

$$SEI[kJ\ L^{-1}] = \frac{Plasma\ power\ [kW]}{Flow\ rate\ [\frac{L}{min}]} \times 60\ \frac{s}{min} \quad (7.2)$$

where the flow rate is defined as standard litres per minute (L/min) and the power (P) is the product of voltage (U) and current (I), i.e. P = U*I, as measured on the power supply indicators, subtracting the power loss in the ballast resistor. The energy efficiency is then defined as:

$$\eta[\%] = \frac{\Delta H_R[kJ\ mol^{-1}] \times X_{CO_2}[\%]}{SEI[kJ\ L^{-1}] \times 22.4\ L\ mol^{-1}} \quad (7.3)$$

where ΔH_R is the reaction enthalpy for CO_2 splitting at standard conditions (279.8 kJ mol^{-1}).

7.2 Different AGPD reactor configurations: design improvement based on gas fluid dynamics simulations

7.2.1 Basic APGD

The main body of the APGD reactor consists of an outer quartz tube with total length of 300 mm and internal diameter of 45 mm (see previous Chapter, as well as figure 7.2). An internal quartz tube, with a diameter of 10 mm and length of 100 mm contains the cathode pin. The cathode faces an anode plate, which is mounted on three metal pins inside the main tube, but the discharge takes place only in the internal quartz tube. The gas enters the reactor axially, inside the smaller tube, and flows around the cathode pin, which has a diameter of 5 mm and adjustable length of 78 mm. The electrodes are made of stainless steel (Therma 310S), which is heat and corrosion resistant, and with a tungsten tip on the cathode. We performed experiments for an inter-electrode (i.e., pin-to-plate) distance of 18 mm. A larger distance would require a higher applied voltage, but the latter did not allow stable plasma due to the high temperature of the cathode tip (see section 7.3).

We should mention that this discharge is specifically called “atmospheric pressure glow discharge” (APGD), but it does not look like a typical low pressure glow discharge in terms of appearance, since it is a constricted discharge and not a diffusive plasma, filling a significant part of the reactor. However, we certainly

see distinctive characteristics of a glow discharge, with a large potential drop between the electrodes (several kV), at low current (in the order of mA). For example, an arc discharge would display a low potential drop (few hundred V), and a high current (1A and above) with much higher plasma density. Further reference about this APGD, including some photos of the discharge, albeit in N_2, can be found in ref. [142].

These experiments turned out that the basic APGD design yields a limited CO_2 conversion (see section 7.3), and for this reason, we developed two modified configurations, as will be explained in the next sections.

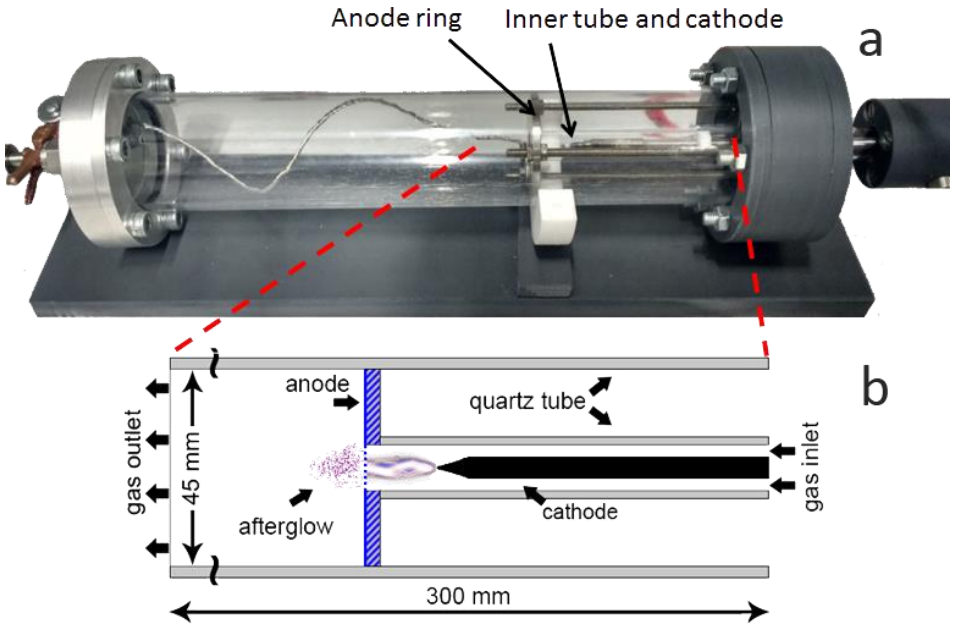

Figure 7.2. Photograph (a) and schematic diagram (b) of the APGD reactor. The metal plate holding the anode mesh is mounted on three metal pins. The small internal quartz tube is in the reactor center, where the cathode pin is also visible. The schematic diagram (b) clearly shows the pin-to-plate reactor design, with artistic representation of the discharge and the afterglow.

7.2.2 Vortex-flow APGD

The vortex-flow APGD makes use of a swirl-flow generating brass ring mounted on the cathode pin (made of stainless steel with tungsten tip, the same as in the basic configuration). The ring has eight holes, oriented in such a direction so that they guide the gas flow to the cathode tip, while also rotating in a vortex (see figure 7.3).

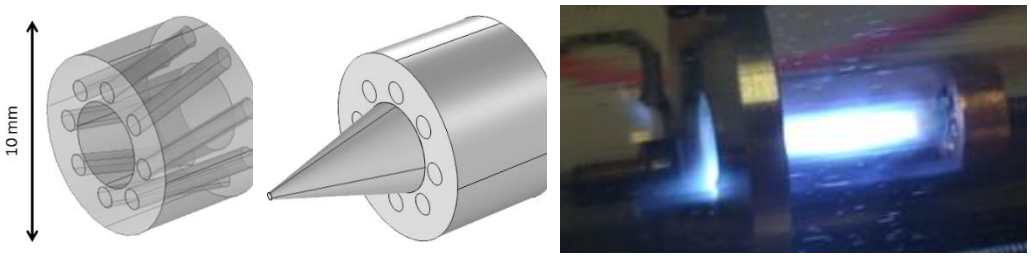

a b c

Figure 7.3. Vortex generating brass ring, transparent view showing the inclined holes (a), positioned on the cathode tip (b), and in operation (c).

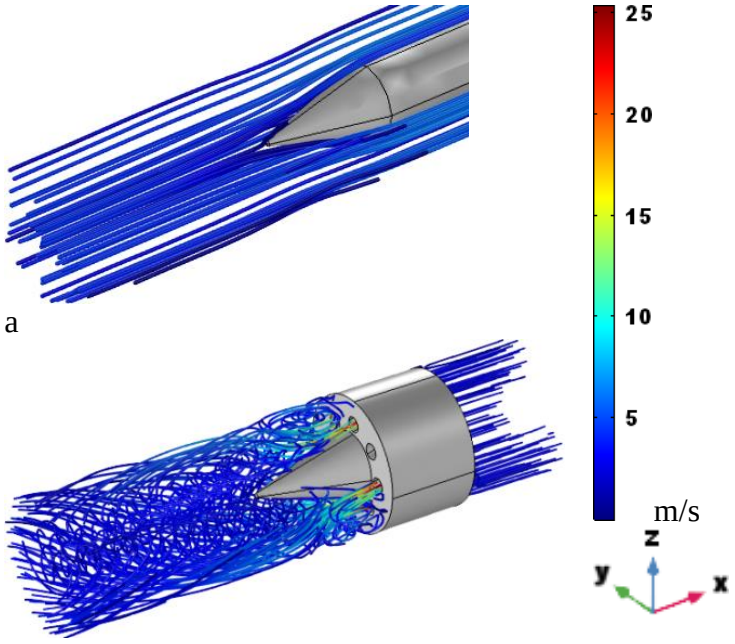

a

b

Figure 7.4. Design process of the vortex-flow APGD through gas fluid dynamics simulations. The basic configuration (a) with no vortex generator shows typical laminar flow lines. Configuration (b), with an inclination of the vortex-generating tubes of 13^{O}, shows complex rotating flow patterns.

The idea behind it is to (1) slow down the axial gas flow velocity, and increase the residence time of the gas molecules in the plasma, (2) force the gas to the actual discharge zone so that a larger fraction of gas passes the plasma, and (3) lower the gas temperature through increased flow turbulence, as well as cool

down the cathode itself, as the brass ring acts as a radiator. The latter will allow to use a larger power input, which will lead to a higher conversion (see section7.3), and in addition, a lower gas temperature is beneficial for energy-efficient CO_2 dissociation through the vibrational pathway (see Introduction, [17], [19], [61], [62], [137], [143]).

This design was first investigated by gas fluid dynamics simulations, to find out the optimum configuration, such as the inclination angle of the holes. These simulations are based on solving the Navier-Stokes flow equations (see Chapter III).

As can be seen from figure 7.4(a), without a vortex generator, the gas flow is almost laminar, while a complex rotating flow pattern is observed in the vortex configuration (figure 7.4(b)). The vortex flow rate through the discharge area was evaluated by integrating the magnitude of the radial and tangential components of the gas flow vector (y and z) over a plane covering the discharge area (a circle with diameter of 2 mm), and the results are shown in figure 7.5, as a function of inclination angle of the holes. The flow rate passing through the discharge area reaches a maximum at 13° inclination angle. Larger inclination angles were not feasible, due to obstruction with the cathode pin. Hence, we selected the 13° inclination angle as the vortex-flow design for production, as we want to reach maximum vortex-flow development.

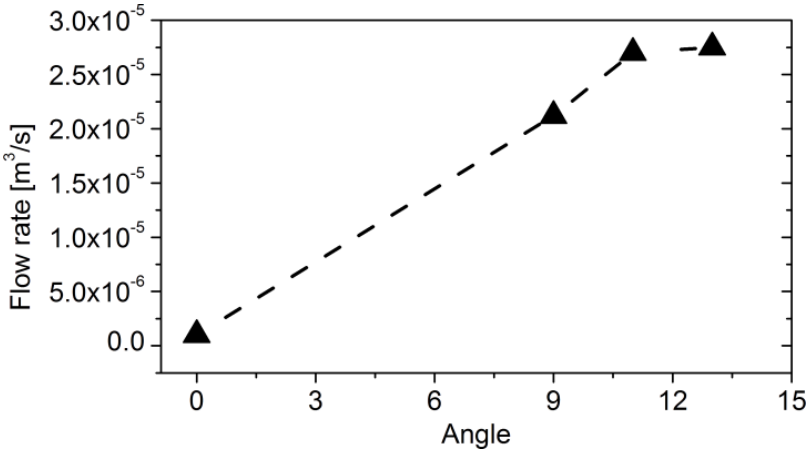

Figure 7.5. Dot product (magnitude) of the tangential and radial flow vectors passing through the discharge area, as a function of inclination angle of the eight holes in the vortex-flow APGD configuration.

We performed experiments for an inter-electrode distance of 18 mm, as in the case of the basic APGD design, but also for a larger distance of 22 mm, which allows a higher power deposition, and thus higher CO_2 conversion (see section

7.3). In contrast to the basic APGD design, the vortex-flow design indeed allowed for a longer inter-electrode distance without melting of the cathode tip, due to the vortex gas flow (see section 7.3 below).

7.2.3 Confined APGD

The third configuration of the APGD is based on the assumption that still only a limited part of the gas actually flows through the discharge zone. This is clearly the main limitation in GA plasmas, as demonstrated by the fluid dynamics simulations for a gliding arc plasmatron (GAP) (see Chapters IV and V above), and it is also observed from the model for the previous two APGD designs in our current work (see further). As a solution, we have encapsulated the entire discharge in a narrow ceramic tube. The tube channel matches the discharge dimensions, as obtained from our plasma model calculation (see section 7.4 below), i.e. no gas can pass through without being activated by the plasma.

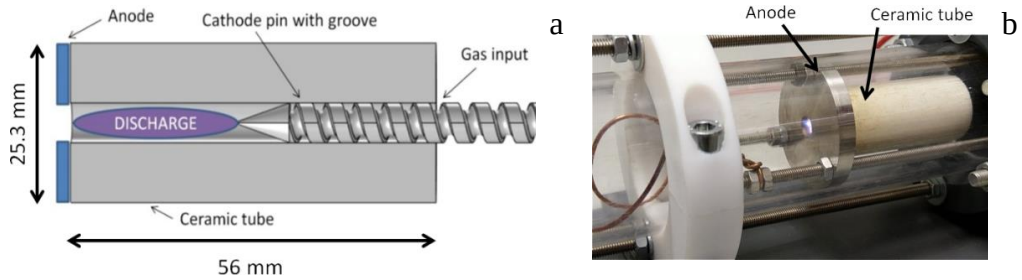

Figure 7.6. Schematic diagram of the "confined" APGD, illustrating the internal configuration of the device (a). Photograph of the reactor in operation (b).

Figure 7.6 illustrates this so-called "confined" configuration of the APGD. The high-temperature ceramic tube with inner radius of 2.5 mm seals tightly with the grooved cathode pin after heat expansion. The entire cathode is made from steel Therma 310S. The gas is delivered to the groove with the same inner quartz tube (with a diameter of 10 mm) as shown in figure 7.2. In this way, the groove acts as a small channel for the gas, conducting flow at high velocity. The distance between the tip of the cathode and the anode plate was again 22 mm, like in the vortex-flow design. With this configuration, two important properties are obtained: a simple, reliable design for confining the discharge, and an effective cooling for the cathode pin, which will allow using higher power input in the plasma. Indeed, even with a steel cathode, 30 mA of current at a flow rate of 1

L/min is possible without melting due the active cooling from the high gas flow velocity along the grooves.

Based on the average axial gas flow velocity for all three reactor configurations, we estimate the gas residence time in the discharge zone to be 10 ms, 13 ms and 50 ms for the basic, vortex and confined setups, respectively. The gas temperature is around 2500K in the discharge centre, and 437K average in the reactor volume (see further details in the modelling section).

7.3 CO_2 conversion performance

We present here the results for the CO_2 conversion and energy efficiency in the three different configurations, for three different values of electric current. The CO_2 conversion is evaluated by means of gas chromatography.

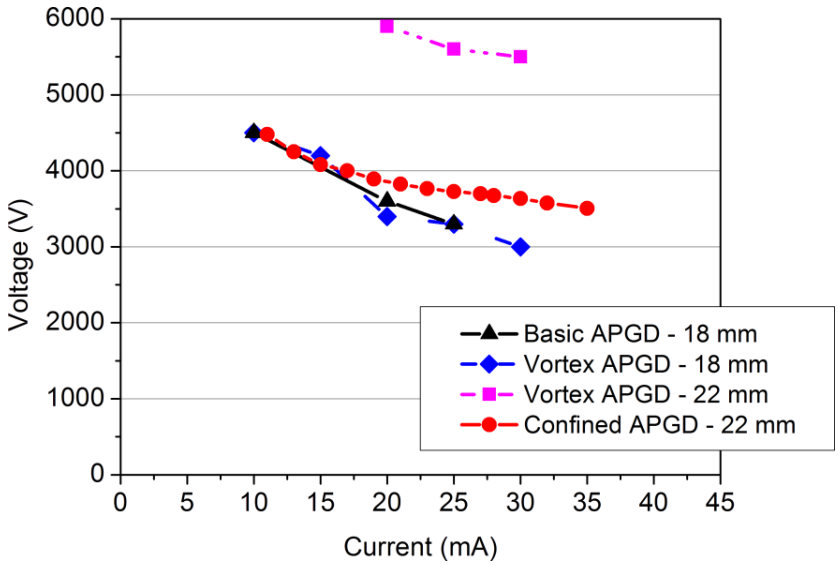

Figure 7.7. V-I (voltage vs. current) characteristic of the three APGD variants, indicating also the cathode-anode distance.

A vital assessment of the actual discharge regime is its current-voltage characteristic. Figure 7.7 presents the measured voltage as a function of the fixed current source for the three different configurations, each within its operation limits. As can be seen from the graph, the voltage drop between the electrodes tends to remain fairly high, but is decreasing steadily with higher current. A glow-to-arc transition would be marked by a sudden voltage peak, followed by a rapid drop. The "confined" APGD was even tested up to 35 mA, with no signs of arcing,

which assures that the reactor operates in the glow regime. As it is shown on the graph, the minimum operating current for the 18 mm APGD is 10 mA (11 mA for the confined variant). Below this value, discharge self-pulsing would occur.

Figure 7.8(a) shows that the basic APGD yields a conversion around 3.5-4.5 %, for an inter-electrode distance of 18 mm. As mentioned in section 7.2.1 above, a longer inter-electrode distance would naturally increase the required potential drop over the discharge, and hence the specific energy input (SEI), and thus the CO_2 conversion, as the latter typically rises with SEI (although at the expense of the energy efficiency) [17]. However, the basic APGD is unable to sustain a stable plasma at higher voltage, or current above 25 mA, due to the critically high temperature (at the melting point) of the cathode tip.

This problem is solved with the vortex-flow APGD: as it acts as a radiator to the cathode, it allows for higher power input. This is beneficial for the CO_2 conversion. Figure 7.8 indeed illustrates that the vortex-flow APGD can reach higher current and power (30 mA and more than 160 W vs. 90 W for the basic design), and can also be operated at longer inter-electrode distance (22 mm). Thus, it is not surprising that the high SEI of the vortex-flow configuration with 22 mm inter-electrode distance and 30 mA current yields a higher CO_2 conversion, i.e., around 8.3 %.

Finally, the confined APGD allows us to reach a CO_2 conversion up to 12.5 % at 30 mA. This is a significant improvement compared to both the basic and vortex-flow APGD configurations. At 20 and 25 mA, an enhancement factor of around 3 is obtained compared to the basic design, and around 2 with respect to the vortex-flow design. At 30 mA, an enhancement of a factor 1.5 is obtained with respect to the vortex-flow design, while the basic design was not stable at 30 mA, due to a too high cathode temperature, with the risk of cathode melting.

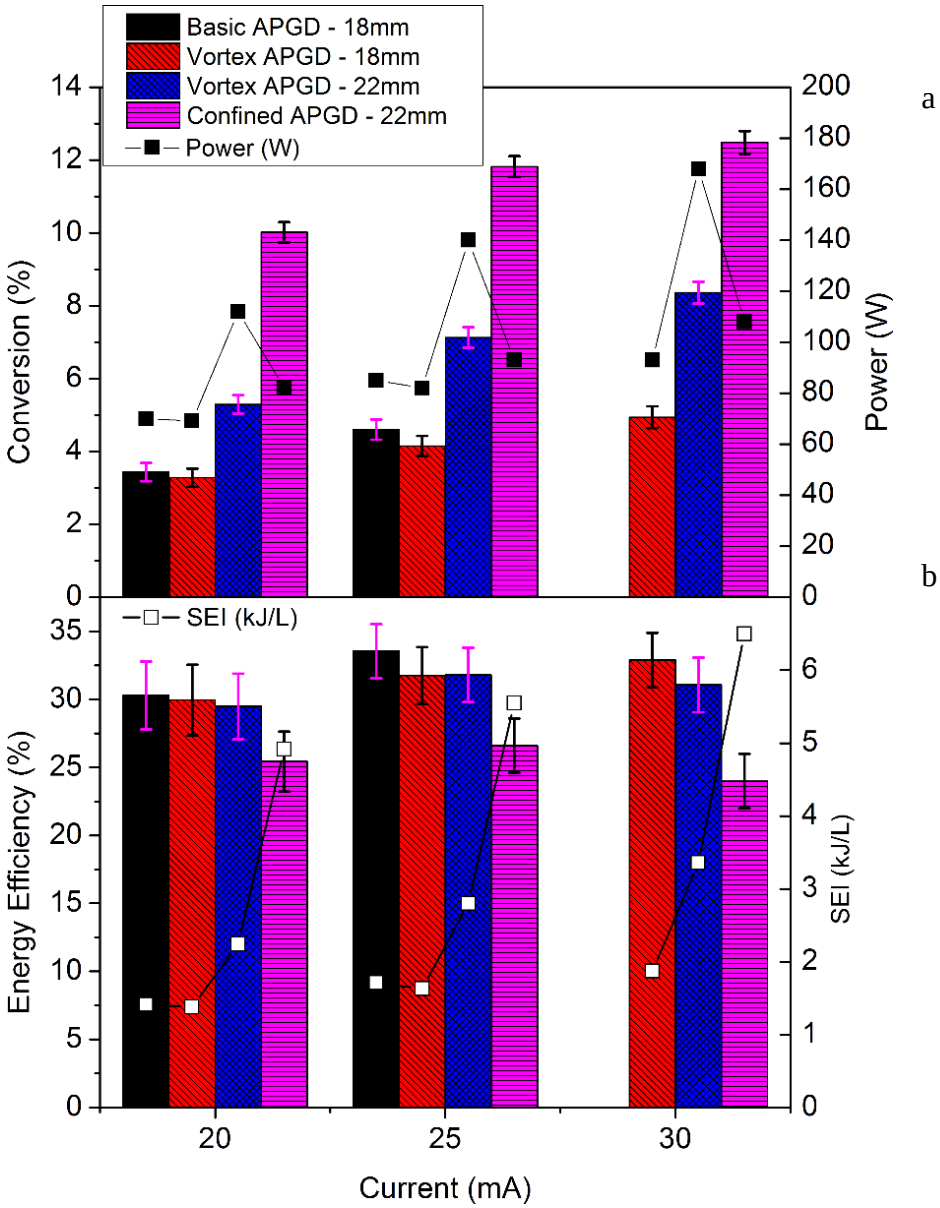

Figure 7.8. CO_2 conversion (a) and corresponding energy efficiency (b), for the basic, vortex-flow (with two different inter-electrode distances) and confined APGD, for three different values of discharge current. The flow rate is 3 L/min in the basic and vortex-flow design, while it is 1 L/min in the confined design. The power input and SEI for the different cases are plotted as well, with the corresponding values indicated in the right y-axis of (a) and (b), respectively. The error bars are quantified from the basic accuracy of the instruments, and the number of measurements per data point (3), using standard formulas.

The main reason for this higher conversion is the fact that a larger fraction of gas passes through the active plasma, as the plasma fills up the entire discharge region (see figure 7.6). In addition, the high SEI (6.48 kJ/L at 30 mA, compared to 3.36 kJ/L in the vortex-flow design, for 22 mm inter-electrode distance; see figure 7.8(b); right y-axis) also explains the higher conversion. Indeed, as mentioned above, the specific design of the confined APGD allows for efficient cathode cooling, and thus enables this configuration to operate at high power input (above 100 W) with a low flow rate (1 L/min).

However, this higher conversion comes at the price of a lower energy efficiency, as illustrated in figure 7.8(b). The energy efficiency is nearly 30 % for the basic and vortex-flow designs at 20 mA, and even above 30 % at 25 and 30 mA, while it drops to 25 % at 20 mA, 26.5 % at 25 mA and 24 % at 30 mA, for the confined APGD. Two main factors contribute to this efficiency loss. First, the plasma is in direct contact with the walls (see figure 7.6), which means that energetic electrons and ions will lose energy and transfer heat upon impact with the ceramic walls. Indeed, we observed that the ceramic piece heats up significantly (over 100 ^{o}C), despite being relatively non-conductive to heat. The second reason is that at high SEI, the discharge is closer to thermal equilibrium, which will inherently lower the energy efficiency, as the most energy-efficient vibrational-induced dissociation pathway is not fully explored [17]. In general, we can conclude from figure 7.8(a) that the conversion does not rise to the same extent as the SEI, for both the vortex-flow design and especially the confined design, and this explains the slight drop in the energy efficiency (see figure 7.8(b)), because the latter is defined by both the conversion and SEI (see eq. 7.3 in section 7.1 above). Nevertheless, the drop in energy efficiency compared to the basic and vortex-flow designs is at maximum only around 20 %, which is clearly lower than the enhancement factors observed for the conversion, so we may conclude that the confined design overall yields the best results.

In figure 7.9, we compare our results with the best results obtained in various types of plasma reactors from literature. The figure is adopted from [17], with our data points added. It is clear that the APGD does not provide "record values", both in terms of conversion and energy efficiency, but still performs rather well, significantly surpassing DBDs in energy efficiency, and achieving a higher conversion than most GA reactors. Note that the best results presented in figure 7.9 were obtained with microwave (MW) and RF discharges, but these record values were reported in the 1980's and could not yet be reproduced since then. Moreover, they were obtained at reduced pressure, where it is easier to reach thermal non-equilibrium, and thus higher and more energy-efficient CO_2 conversion [17], [19]. However, the reduced pressure operation requires vacuum equipment, which is less convenient for industrial exploitation, and it presents an additional cost, not included in the energy efficiency shown in figure 7.9. At present, atmospheric pressure reactors seem to be unable to reach a CO_2

conversion above 20 % with reasonable energy efficiency. The APGD, particularly in the "confined" configuration, gets closer to this boundary, with a conversion of 12.5 % and corresponding energy efficiency around 25 %.

As no other atmospheric DC plasma reactor seems to offer such a combination of CO_2 conversion and energy efficiency, we believe that the confined APGD is quite promising for practical applications, also in view of its simple design, although further improvements will be needed to make it competitive with other emerging technologies. Indeed, the energy efficiency is still below the efficiency target, as defined in [17]. Nevertheless, the latter was defined for pure CO_2 conversion, while the results are typically better for the combined conversion of CO_2 and CH_4 (dry reforming of methane, DRM) [17]. In future work, we plan to investigate the performance of our APGD for DRM, and we also plan to develop further improved designs, based on computer modeling. Finally, it is worth to mention that our results are clearly above the thermal equilibrium limit, which is also indicated in figure 7.9. This illustrates that the CO_2 conversion in our APGD is due to non-equilibrium plasma processes, and not just due to thermal conversion, as will be discussed below.

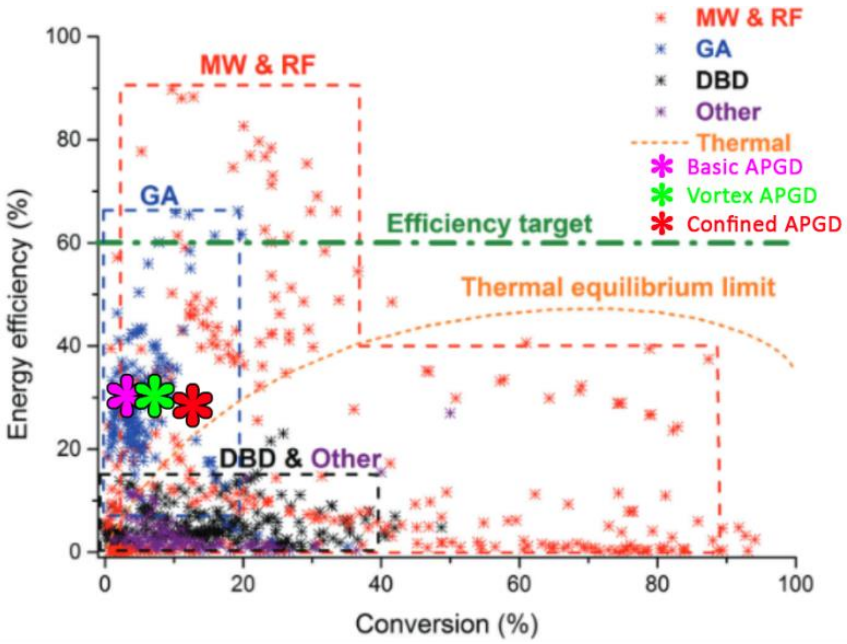

Figure 7.9. Comparison of our results, in terms of energy efficiency vs CO_2 conversion, with data collected from literature for CO_2 conversion by different plasma reactors, adopted from [17]. In addition, also the energy efficiency target and thermal equilibrium limit are presented (see text).

7.4 Non-equilibrium plasma-induced CO_2 conversion: Insights from plasma modelling

In this Chapter, we present three different APGD configurations, which demonstrate a difference in conversion performance (see previous section). The basic APGD shows quite low conversion around 4.5 %, which is limited by the low power handling ability of the reactor. The vortex-flow APGD allows a larger inter-electrode distance, and thus raising the power input (hence, SEI) by 50%. Therefore, it reaches a conversion up to 8.3 %. Finally, the confined APGD reaches a conversion of 12.5 %, because it can handle a further increase in SEI, and especially because it allows all gas to pass through the plasma. These configurations were developed based on gas fluid dynamics calculations, as explained in section 7.2, but a gas flow analysis alone is insufficient to explaining the behavior of the plasma and the underlying mechanisms for the higher CO_2 conversion. Therefore, we investigate here the nature of the discharge through detailed plasma fluid dynamics modeling.

We developed a fluid dynamics model, very similar to the model presented in Chapters IV and V for a GAP. It is based on solving the Navier-Stokes equations to obtain the gas flow pattern, while the plasma model is based on the drift-diffusion approximation, and it assumes quasi-neutral plasma [117] (see details in Chapter III). As the CO_2 plasma chemistry is too extensive for a 3D geometry [116], we have to limit ourselves to a 2D model. For this reason, the model can only be applied to the basic design, as the latter is characterized by a laminar flow with a pin-to-plate configuration, which is cylindrically symmetrical (figure 7.2), allowing to use a 2D axi-symmetric approach. Indeed, the vortex motion originating from the two other designs cannot be properly described in 2D, but based on our previous experience [117], we believe that the present model is sufficient to predict the plasma behavior, and to elucidate the underlying mechanisms (and limitations) of the CO_2 conversion. Detailed information on the modelling method, is available in Chapter III. The plasma species considered in the model are listed in table 7.1.

Table 7.1. CO_2 plasma species included in the model

Ground state neutrals	CO_2, CO, C, O_2, O
Charged species	e, CO_2^+, O_2^+, CO_3^-, O_2^-, O^-
Excited species	CO_2 (25 vibrational states*, 1 electronic excitation state), O_2 (3 vibrational states)

*Combined in three groups, following the level lumping method of [130], [144]

Figure 7.10 describes the boundary setup in the plasma model geometry. This is a small excerpt of the entire reactor, covering only the parts with actual plasma. As mentioned above, an axially symmetric approach is used, i.e. with cylindrical coordinate system.

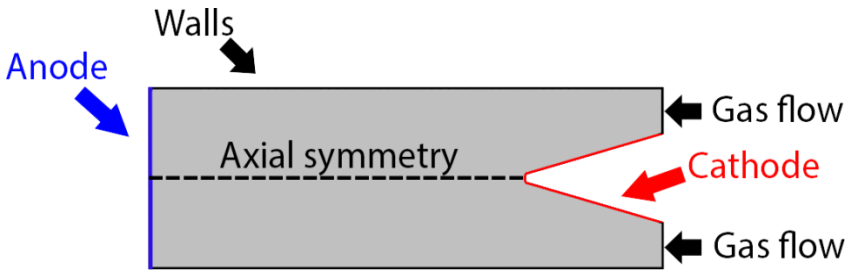

Figure 7.10. Schematic illustration of the boundary conditions in the plasma model

First, to assess the model capabilities, we compare in figure 7.11 the measured and calculated CO_2 conversion and energy efficiency as a function of discharge current for the basic APGD design. The conversion in the model is obtained by integrating the species density over the reactor output, while the energy efficiency is derived from the conversion, power and flow rate; see equations (7.2) and (7.3). Note that the calculation results also contain a data point at 22.5 mA. A higher current (e.g., 30 mA) leads to model instability, consistent with the experiments.

The calculated and measured conversions and energy efficiencies are both in quite good agreement, showing that the model presents a realistic picture of the plasma characteristics affecting the CO_2 conversion (see below). While the calculated conversion is slightly underestimated, the energy efficiency is somewhat overestimated, and this can be explained by the model approximations. Indeed, we use a quasi-neutral model, in which the plasma sheath, i.e. the cathode layer, is not explicitly included. Hence, the voltage drop across the sheath is not accounted for. As a result, the model predicts a lower overall voltage drop across the discharge. Indeed, while the experimental voltage drop is 5.6 kV (at 25 mA, 22 mm), the calculated value (also at 25 mA) is only 4.2 kV. Hence, this is 25% lower than in the experiments. Since the power input is calculated as the product of voltage and current, it is also underestimated by 25 %, explaining why the calculated energy efficiency is somewhat higher than the measured values in figure 7.11. However, we want to stress that our model is fully self-consistent across all parameters, with only the current as primary input, and self-consistently calculating the power from the voltage drop, so this comparison gives a thorough assessment of the real predicting capabilities of our model.

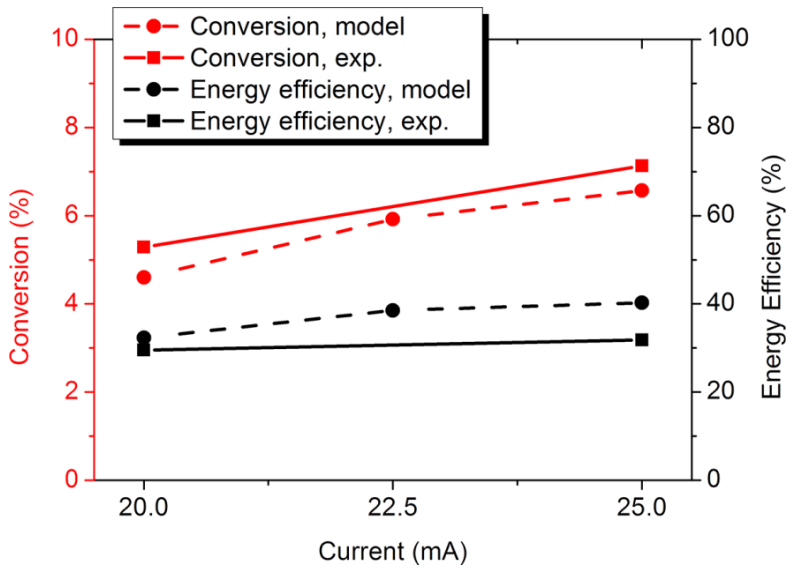

Figure 7.11. Comparison of calculated and measured CO_2 conversion and energy efficiency as a function of discharge current, for the basic APGD design.

As our model yields a reasonable agreement with measured conversion and energy efficiency, we believe it presents a realistic picture of the plasma characteristics affecting the CO_2 conversion. This includes the gas temperature, the electron density and temperature, the vibrational temperature, the electric field, the species densities and the reaction mechanisms responsible for the CO_2 conversion. Thus, we will now present these characteristics, to better understand the underlying mechanisms of CO_2 conversion in the APGD.

Figure 7.12 illustrates a gradient-mapped photograph of the basic APGD reactor in operation (a), as well as the temperature profile obtained from the model (b). The close relation between the measured plasma luminosity (a) and the calculated gas temperature (b) is very obvious. The peak gas temperature (at the cathode tip) reaches 2600 K, but the value remains fairly uniform around 2400-2500 K along the discharge axis. In [145], an APGD in air was investigated by means of spectroscopy, measuring a rotational temperature of up to 2000 K. Hence, our calculated value is slightly higher, which can be explained by the differences in reactor design. In addition, it would be better to compare with a CO_2 plasma, but such data are not available. Indeed, measuring the rotational temperature in CO_2 plasma is very difficult without add-in gases (typically N_2), which affects the overall accuracy.

When we compare the calculated gas temperature in this APGD with values obtained in GA plasmas, we can conclude that similar values are reached in a classical GA. For instance, in [125] a gas temperature of 2600 K was measured for a classical GA in air. However, in a gliding arc plasmatron (GAP), we calculated a much higher gas temperature (around 3000 K) for CO_2 (see Chapter

V), and in [66] the measured value in N_2 was reported to be even 5500 K. Hence, the gas temperature in the APGD seems to be significantly lower than in a GAP. This is beneficial for efficient CO_2 conversion, because (i) it might give less vibrational-translation relaxation losses, and (ii) the recombination reaction of CO + O_2 → CO_2 + O becomes less important at lower temperatures (with a rate constant of $1.28 \times 10^{-12} \exp(-12800/T_{gas})$, see page 185).

Figure 7.12(c) illustrates the calculated electron density profile (also called plasma density). Obviously, the maximum electron density (around $2x10^{18}$ m^{-3}) is at the cathode tip, due to the electric field enhancement in this region (see below).

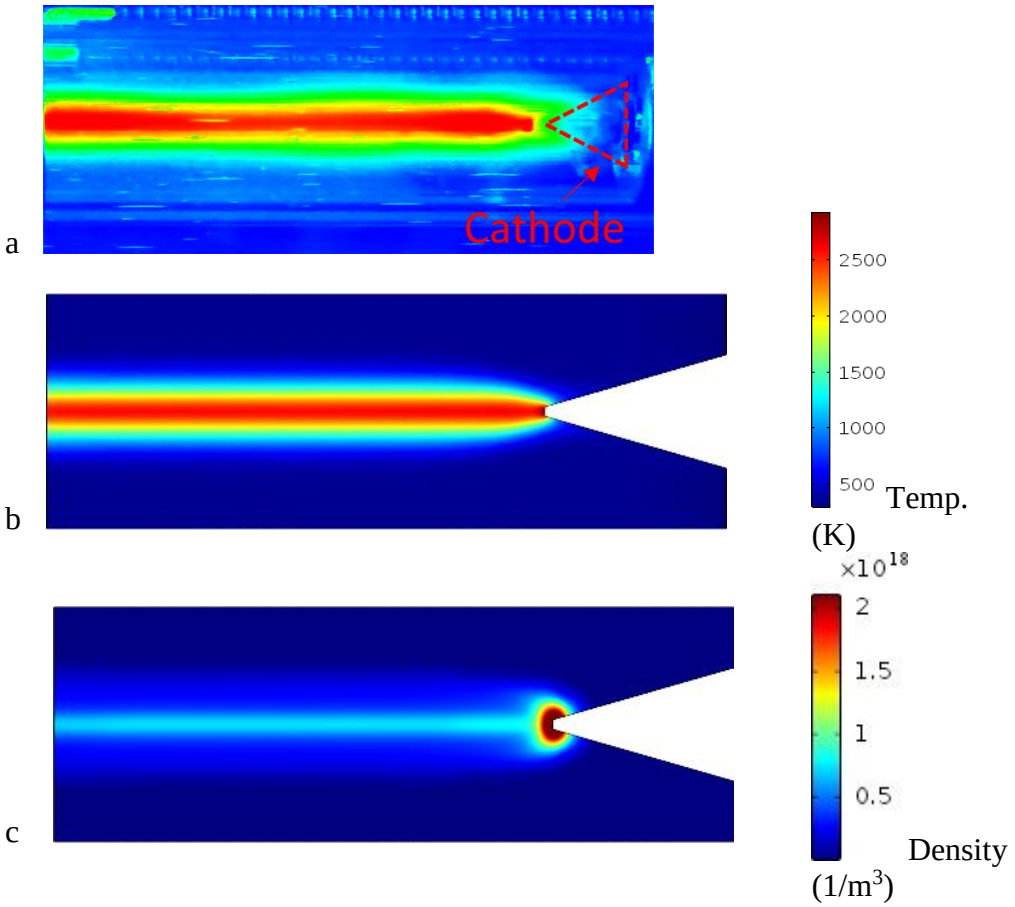

Figure 7.12. Gradient-mapped photograph of the basic APGD, illustrating the measured plasma luminosity (in arbitrary units) (a), the calculated gas temperature profile (b), and electron (or plasma) density (c) at 25 mA and 3 L/min.

A plasma density in the order of 10^{18} m^{-3} has also been reported for APGDs in literature, i.e., 10^{18} for an APGD in N_2 [146], and around $5x10^{18}$ m^{-3} for an APGD in helium [147]. It is clear from figure 7.12(c) that the plasma is concentrated near the cathode tip, and hence, the discharge does not fill the entire reactor volume. Thus, a significant amount of gas will pass between the plasma and the walls, being untreated by the plasma, hence confirming our conclusions made in section 7.3 above. As already explained in section 7.2, this is the reason we developed the confined APGD configuration (figure 7.6 above), which fully encapsulates the discharge in the reactor volume.

Figure 7.13(a) shows that the electron temperature in the discharge is about an order of magnitude higher than the gas temperature (i.e. 1.9 eV or 20,000 K vs. 2500 K), which means that the plasma is in thermal non-equilibrium. For comparison, in [148] an electron temperature of 1.4 eV was reported for a low-current (10 mA) APGD in N_2. Hence, the electrons have sufficient energy to activate the CO_2 molecules by electron-impact vibrational excitation, leading to CO_2 splitting. At the cathode tip, the electron temperature reaches 3 eV in a very small region, due to the enhanced electric field at the sharp edge. Although this is a very small, localized region, it could have some impact on the overall CO_2 dissociation through high-energy electron impact electronic excitation. However, the region of high-energy electrons is relatively small (see figure 7.13(a)), which explains why this process plays a minor role in the CO_2 dissociation (see below).

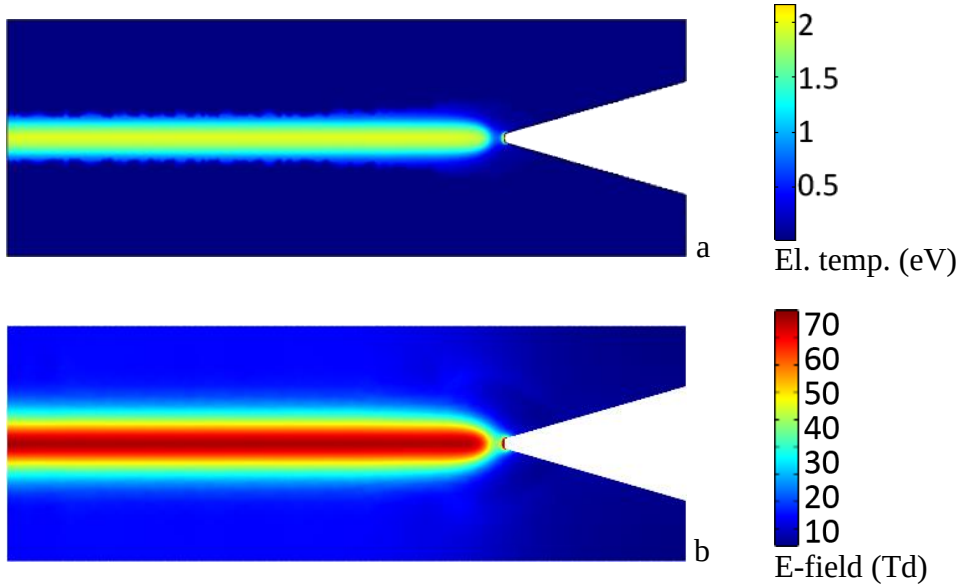

Figure 7.13. Calculated electron temperature profile (a) and reduced electric field profile (b), at 25 mA and 3 L/min.

In figure 7.13(b), we plot the calculated electric field profile in the reactor. It is depicted as reduced electric field, i.e., electric field divided by gas number density, expressed in units of Td (1 Td = 10^{-21} V m^2). This is done because the reduced electric field is a very important parameter to characterize the CO_2 conversion ability of gas discharge plasmas [17], [19]. Indeed, reduced electric field values below 100 Td (typical for MW and GA plasmas) are known to give rise to electron temperatures (around 1-2 eV) most suitable for vibrational excitation, which is the most energy-efficient CO_2 dissociation pathway, while values above 100-200 Td (characteristic for DBD plasmas) mainly result in electronic excitation-dissociation and ionization, due to the higher electron temperatures produced [19]. It is clear that the APGD gives rise to a reduced electric field around 60 Td in the discharge center, which is thus very beneficial for vibrational excitation due to the produced electron temperature of 1.5 – 2 eV (see figure 7.13(a)), explaining the good energy efficiency reached in our experiments (see figure 7.8(b) above). A small area around the cathode tip shows a higher value, above 100 Td, which produces the high electron temperature in figure 7.13(a). These values are in agreement with [141], [149], for a direct current plasma jet at atmospheric pressure.

Table 7.2. Main CO_2 splitting and formation reactions, and their relative contributions to the total splitting and formation, integrated over the entire plasma volume, at 25 mA and 3 L/min.

CO_2 splitting		Relative contribution (%)
1.	$O + CO_{2(vib)} \rightarrow CO + O_2$	74.4
2.	$e^- + CO_{2(vib)} \rightarrow e^- + CO + O$	9.79
3.	$O + CO_{2(gr)} \rightarrow CO + O_2$	9.5
4.	$M + CO_{2(vib)} \rightarrow CO + O + M$	3.74
5.	$e^- + CO_{2(gr)} \rightarrow e^- + CO + O$	2.23

CO_2 formation		Relative contribution (%)
1.	$CO + O_2 \rightarrow CO_2 + O$	90.72
2.	$CO + O + M \rightarrow CO_2 + O$	9.14
3.	$CO + O^- \rightarrow CO_2 + e^-$	0.14

Figure 7.14 illustrates the neutral species densities in the plasma, as a function of axial position along the discharge center (a) and radial position, at an axial position of 11 mm from the cathode tip (b). In (a), 0 mm corresponds to the cathode tip and 18 mm is the position of the anode. Along the discharge axis, CO is the main plasma species: its density is up to a factor 3 higher than the CO_2 density. This indicates a quite high (~75%) conversion in the center, while it drops

rapidly beyond 1 mm from the discharge center (see figure 7.14(b)). The O_2 and O atom densities are also a direct result from the CO_2 dissociation. Upon a splitting reaction, naturally an O atom will be produced, which can further recombine into O_2.

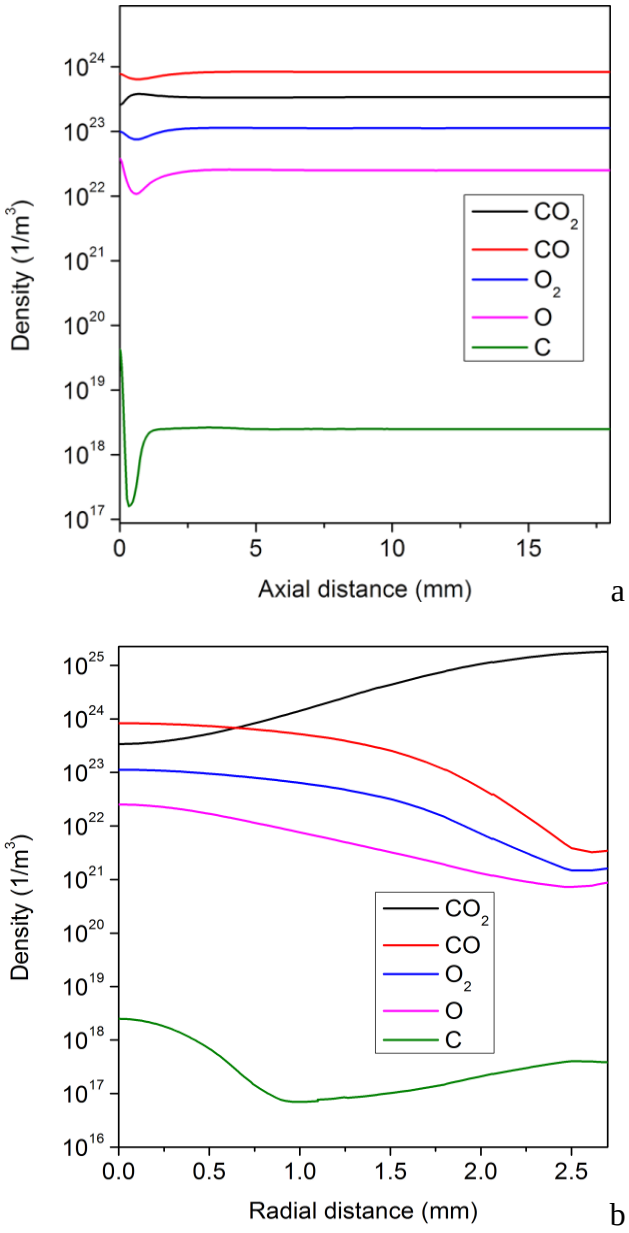

Figure 7.14. Axial density distribution, at the discharge center (a), and radial density distribution at an axial position of 11 mm from the cathode tip (b), of the neutral species in the plasma, at 25 mA and 3 L/min.

In Table 7.2, we present the relative contributions of the CO_2 splitting and formation reactions, integrated over the discharge volume. The reason that we present the individual splitting and formation reactions, and not just the net reactions, is that separate CO_2 splitting reactions (i.e., for the CO_2 molecules in vibrational levels and ground state: reactions 1 and 3, and reactions 2 and 5) yield common products, so we cannot simply subtract the formation reactions from the splitting reactions to obtain the net reactions. However, in this way, it looks like 84% of the CO_2 splitting is upon collision with an O atom (with either CO_2 in the vibrational levels or in the ground state), but this accounts only for the forward (splitting) reaction, and not for the reverse reaction, hence it does not represent the net splitting. When looking at the net contribution, this reaction contributes for less than 50%, because the reverse reaction is also very important (90%, cf. Table 7.2). Indeed, the net contribution of this reaction cannot be more than 50%, because the O atoms must first be created from another CO_2 splitting reaction (e.g., reaction 2, 4 or 5 in Table 7.2).

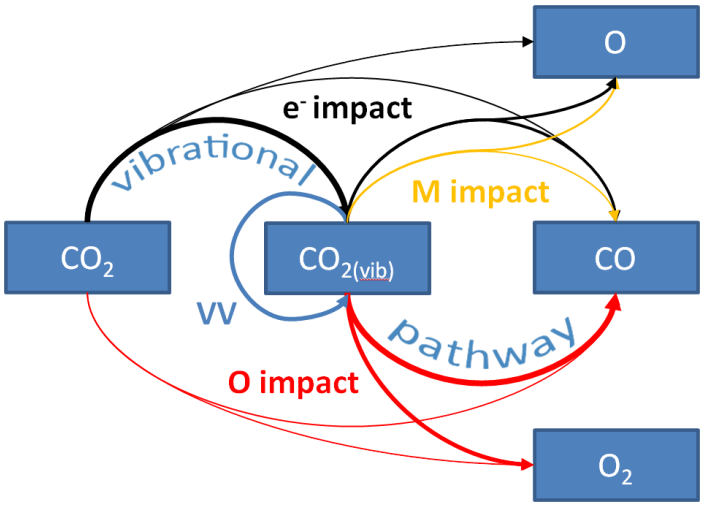

Figure 7.15. Reaction scheme of the main CO_2 splitting mechanisms. The main dissociation process is the so-called "vibrational pathway", starting from electron impact vibrational excitation of the CO_2 ground-state molecules, followed by gradually populating the higher vibrational levels through vibrational-vibrational (VV) relaxation collisions, which are then dissociated into CO and O_2 upon impact of O atoms. The dissociation upon O atom impact can also occur from the CO_2 ground-state molecules. In addition, electron impact dissociation, both from CO_2 vibrational levels and ground-state molecules, also contributes to CO_2 splitting, as well as the dissociation upon impact by any molecule in the plasma (M).

The main CO_2 splitting mechanism is the collision of O atoms with vibrationally excited CO_2 molecules, with a relative contribution of 74 %. This process is of course initiated by electron impact vibrational excitation of ground-state CO_2 molecules, followed by so-called ladder climbing by vibrational-vibrational relaxation collisions, gradually populating the higher CO_2 vibrational levels, i.e. the so-called "vibrational pathway", as illustrated in Figure 7.15.

The same process also occurs for CO_2 ground-state molecules, with a relative contribution of 9.5%. Besides, electron impact dissociation upon collision with both vibrationally excited and ground-state CO_2 molecules also contributes for about 9.8% and 2.2%, respectively, to the total splitting process. Note that the contribution of electron impact dissociation from the ground state is mainly due to the energetic electrons close to the cathode tip, and because this process is only important in a small region, it explains the low relative importance of this process. Finally, dissociation upon reaction with any other neutral species in the plasma (mainly molecules: M) contributes for 3.7% to the total conversion, again mainly from the CO_2 vibrational levels. Hence, when summing up the splitting reactions upon collision with O atoms or electrons (or other molecules M), with either CO_2 ground-state or vibrational levels, we see that the vibrational levels contribute for about 88 % to the CO_2 splitting in the discharge volume, while the ground-state molecules contribute for about 12 %. This demonstrates the important role of the CO_2 vibrational levels in the CO_2 splitting process in the APGD reactor.

When comparing to the mechanisms of CO_2 splitting in a GA plasma, we can see some similarities, but also some differences. Indeed, for a transient AC GA, model calculations predicted a relative contribution of 66 % and 19 %, for dissociation upon impact of O atoms and electrons with vibrationally excited CO_2, respectively [130]. On the other hand, in the quasi-stationary regime, characteristic for a DC GA, the contributions of these two processes were predicted to be 43% and 40%, respectively, pointing towards very similar contributions for both O atom and electron impact dissociation of the CO_2 vibrational levels [130]. While the APGD can also be interpreted as a quasi-stationary discharge (given that it is also a DC plasma), it is important to note that the model used in [130] was only a 1D model. In [115] a 2D CO_2 model was developed for a classical GA, and the contribution of splitting upon impact of O atoms with vibrationally excited CO_2 molecules was also found to be dominant here (80%), while the same process with ground-state CO_2 contributed for 9.2%, hence very similar to our APGD results. Electron impact dissociation was found to be somewhat less important, while the splitting of CO_2 upon collision with other molecules (M) was higher (7.3% for the vibrational levels). This difference can be attributed to the different type of plasma, different reactor volume and the iterative nature of the classical GA. On the other hand, a 0D modelling study on a GA for CO_2 conversion predicted that electron impact dissociation of vibrationally excited CO_2 was much more pronounced (61-67%), while the

splitting upon impact with O atoms contributed only for 7-10% [131]. This can be attributed to the much lower gas temperature assumed as input in this 0D model, i.e., around 1200 K, promoting the electron impact reactions above thermal (neutral) reactions. In [137], a modeling study of a microwave discharge for CO_2 conversion in a wide range of conditions indeed revealed that the dissociation upon impact with O atoms and any molecules (M) becomes more important at higher power deposition (promoting the vibrational excitation) and temperature (promoting neutral (thermal) dissociation reactions above electron reactions). Our simulation results for the gas temperature (figure 7.12(b)) show that the temperature in the APGD is indeed high enough to promote the dissociation reactions upon impact by O atoms.

It is clear that vibrational excitation of CO_2 acts as an effective leverage to the overall CO_2 conversion, and this explains the good energy efficiency obtained in our experiments. However, as can be noted from figure 7.12, the CO_2 conversion only occurs in a small region of the reactor, i.e., along the discharge center, which limits the overall CO_2 conversion, as also seen in our experiments. Indeed, a significant fraction of the gas does not pass through the plasma region, and this was the reason why we developed the confined APGD design, to make sure that all gas will be activated by the plasma, yielding a higher overall conversion.

To elucidate which CO_2 vibrational levels contribute most to the CO_2 splitting, i.e., rather the higher or lower levels, we plot in figure 7.16 the vibrational distribution function (VDF) at the discharge center, at an axial position of 11 mm from the cathode tip, for three different values of electric current. It is clear that the VDF exhibits a Boltzmann distribution, dictated by the gas temperature. Indeed, the dashed line indicates a Boltzmann distribution at a temperature of 2500 K, and it largely coincides with the calculated VDFs. The vibrational temperature is typically obtained from the ratio of the first vibrational level and the ground state:

$$T_{v1} = \frac{E_{v1}}{k \ln\left(\mathrm{nCO}_{2(v1)}/\mathrm{nCO}_{2(gr)}\right)} \tag{7.4}$$

where E_{v1}/k is the energy of the first vibrational state and $nCO_{2(v1)}$, $nCO_{2(gr)}$ stand for the densities of vibrationally excited and ground-state CO_2 molecules, respectively. In figure 7.17, we plot both the vibrational and translational (gas) temperature as a function of radial position, and it is obvious that they are almost identical. They are both around 2500 K along the discharge center (see also figure 7.12(b) above), but they gradually drop to room temperature near the walls. The fact that they are almost equal indicates that the VDF of CO_2 is close to thermal,

as is indeed obvious from figure 7.16. This means that the higher vibrational levels are less populated and only the lower vibrational levels of CO_2 actually contribute to the CO_2 conversion. Although the energy efficiency in our experiments is quite good already, it could be further improved if the higher CO_2 vibrational levels could be overpopulated compared to a Boltzmann distribution. This overpopulation is typically realized by vibrational-vibrational (VV) relaxation, as mentioned above, but it is counteracted by vibrational-translational (VT) relaxation, which depopulates the vibrational levels. The latter process becomes more important at high gas temperature. Hence, we believe that a further improvement of the energy efficiency would only be possible if we can let the APGD operate at much lower temperature, i.e., below ca. 1000 K. It was indeed demonstrated by Berthelot and Bogaerts [137] that a non-thermal VDF, with a significant overpopulation of the higher vibrational levels, could only be realized at high power density, while at the same time low gas temperature, but the latter is not easy to realize at atmospheric pressure [61]. This represents a fundamental challenge for developing atmospheric pressure sources for CO_2 splitting. In future work we will aim to develop a further improved APGD design that can operate at high power density, but at the same time at lower gas temperature.

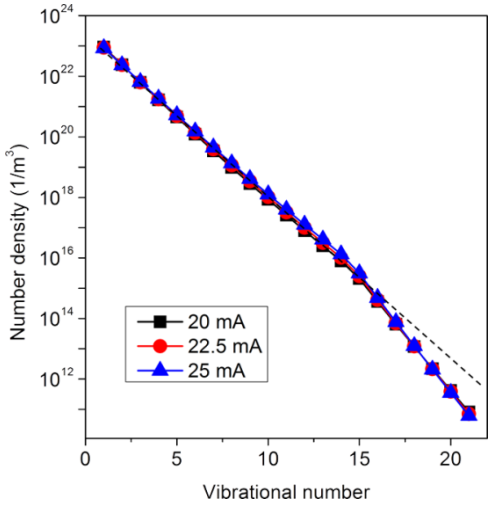

Figure 7.16. Vibrational distribution function (VDF) of CO_2, at the discharge center (axial position of 11 mm from the cathode tip), at 3 L/min and three different electrical currents. A Boltzmann distribution at 2500 K is also plotted for comparison (dashed line).

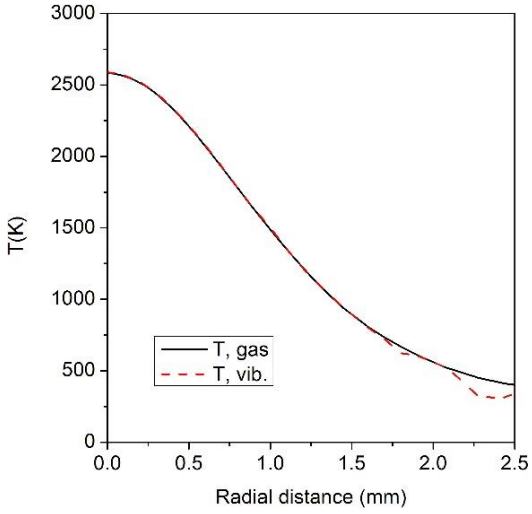

Figure 7.17. Radial distribution of the gas and vibrational temperature at an axial position of 11 mm from the cathode tip, at 3 L/min and 25 mA.

7.5 Conclusion

In this Chapter, we thoroughly investigated the potential of an APGD reactor for CO_2 conversion, by a combination of experiments and modeling. In the experiments we explored two different reactor improvements with the aid of gas fluid dynamics simulations. In addition, we also developed a fluid plasma model to obtain a better insight in the underlying mechanisms in the plasma, and in the way they affect the performance of the APGD for efficient CO_2 conversion. The basic APGD design shows limited overall CO_2 conversion, which can be explained from the model, because the plasma is only created in a limited region of the reactor, i.e., around the central axis. The calculated conversion inside the plasma region is around 75%, but as a significant fraction of the gas does not pass through this plasma region, the overall conversion is limited to 4.5 %. The energy efficiency is fairly good (around 30 %), but the model indicates that it could be further improved, because the calculated VDF exhibits a Boltzmann distribution, dictated by the gas temperature. This is due to the significant role of VT relaxation, depopulating the vibrational levels, which is especially important at high gas temperature. Thus, the energy efficiency could be further improved if the higher vibrational levels could be overpopulated, which should be realized by a higher power density, but at the same time reducing the gas temperature.

We therefore proposed some reactor modifications. The vortex-flow AGPD effectively lowers the cathode temperature, and thus allows for operation at higher power, which leads to a higher conversion of about 8 %. However, because of the higher power, the gas temperature is still high, limiting the energy efficiency due to a thermal VDF. In addition, still only a limited gas fraction passes through the discharge.

The confined APGD addresses this issue by making use of a ceramic tube with a smaller inner radius of 2.5 mm that fits precisely with the cathode pin. A spiral groove is carved on the pin, guiding the gas into the tube, which acts as effective cooling for the cathode pin, preventing it from melting, and thus also allowing us to use higher power. The plasma region is indeed limited to a radius of 2.5 mm or less, as predicted by the model, so using this ceramic tube with small inner radius makes sure that the plasma fills the entire reactor, and all the gas passes through the active plasma. This gives rise to a higher conversion of 12.5 %. However, because the plasma now fills up the entire reactor, it is in contact with the walls, leading to loss of plasma species, as well as heat loss to the walls. For this reason, the energy efficiency is somewhat lower than in the vortex-flow APGD, i.e., around 26 %. Nevertheless, the enhancement in conversion is much more significant, i.e., a factor 3 compared to the basic APGD design and a factor 1.5-2 compared to the vortex-flow design. This makes the confined APGD reactor the more cost-effective option for CO_2 conversion.

The plasma model, besides explaining the limited CO_2 conversion in the basic (and vortex-flow) APGD configuration due to the limited fraction of gas passing through the plasma, as well as the limits in energy efficiency due to a thermal VDF, also provides very useful information on other plasma characteristics in the APGD. The calculated electron (or plasma) density of 10^{18} m^{-3} is in reasonable agreement with experimental observations in an APGD (albeit operating at somewhat other conditions and gases, as no experimental data for CO_2 are available in literature). The calculated gas temperature is around 2500 K, which is comparable to measured values in an APGD in air [145], but somewhat lower than in a GAP, where we calculated values of 3000 K for CO_2 (see Chapter V) and even up to 5500 K were measured for N_2 [66]. This means that the thermal dissociation processes for CO_2 conversion are somewhat lower in the APGD, although still quite significant. Indeed, the vibrational temperature is equal to the gas temperature, and the VDF follows a Boltzmann distribution. The vibrational levels contribute most to the CO_2 splitting, i.e., 88% of the dissociation occurs from the vibrational levels (mainly from the lower levels), while 12% originates from the CO_2 ground state. Indeed, due to the high electric field near the cathode tip, high-energy electrons contribute to the CO_2 splitting with a somewhat larger contribution than in the GAP. However, electron impact dissociation (through electronic excitation) is not the most energy efficient process, so it would be better if we could further exploit the vibrational dissociation pathway by overpopulation of the higher vibrational levels. Nevertheless, the discharge is clearly in non-equilibrium, with the gas temperature being almost 10 times lower than the electron temperature, which was calculated at around 1.9 eV. In addition, the reduced electric field is calculated to be around 60 Td in the discharge center, indicating optimum conditions to maximize the vibrational excitation. Hence, we believe the APGD is a very promising plasma source for CO_2 splitting, especially in the confined configuration, but future efforts should focus on increasing the power density, but at the same time lowering the gas temperature, and thus further promoting the vibrational pathway, to further enhance the CO_2 conversion and energy efficiency. Furthermore, as the gas temperature outside the plasma region is still fairly high, we might expect some contribution from the gas phase chemistry in this region to the CO_2 conversion as well, but this is not yet taken into account in our models. We plan to account for this in our future work, when further finetuning/optimizing the reactor design.

In addition, we plan to further improve our plasma fluid dynamics model, to be able to account for effects that are currently neglected, but which might be important for the reactor design optimization. Indeed, the model would have more predictive power if we could implement a coupled heat transfer and fluid dynamics model, to estimate the cooling power and the inlet gas temperature, as the latter might be important to suppress vibrational-translational relaxations. A fully coupled flow simulation + plasma model is, however, not yet feasible at this

stage. Indeed, the Navier-Stokes equations for the flow simulation are solved in 3D, but for the plasma model, we take only the 2D cut-plane of the reactor, because a 3D model including the complete CO_2 chemistry would be prohibitively slow. Therefore, any radial or vortex flow is omitted in the plasma model and the flow vectors are adopted as stationary solution from the 3D model. If we want to make a coupled study, we have to include the flow as time-dependent, and compute it together with the plasma equations, which are also time-dependent. This could slow down the computations by a factor 10, and it is even no guarantee to reach a stable solution. In addition, the solution might not be accurate anymore: the flow would react to the plasma (i.e. due to expansion and buoyance force), but the system would be incomplete without the third vector. Another, simpler approach would be to include a heat zone (instead of plasma) in the flow. However, this raises more questions than answers. Indeed, our aim is to cool down the cathode, but it is not yet clear how much heat is actually produced there. The cathode heats up due to several different and complex mechanisms, including Joule heating, thermionic emission, ion bombardment, and heating from back-scattered electrons. Hence, in order to obtain a proper solution, we would need an accurate cathode spot description, which is a major challenge due to the huge number of reactions and species included in the model. In the confined APGD configuration, the situation would become even more complex, because also the plasma-surface interactions between the plasma and the walls would need to be accounted for. All these effects are outside the scope of our present study, but we plan to study them in our future work. Nevertheless, the present model is already very useful to understand reactor design modifications.

Hence, in spite of the fact that our model could be further improved, we showed in this paper that, using modelling as a main driving force, we could design and test improved APGD configurations, which is more time and cost effective than tedious trial-and-error experiments. In addition, the support from plasma modeling presents a significant advancement in our understanding of the underlying plasma mechanisms of CO_2 conversion in the APGD.

CHAPTER VIII. Dual-vortex plasmatron – a novel plasma reactor for gas conversion applications

Abstract

Atmospheric pressure gliding arc discharges are gaining increasing interest for gas conversion applications, due to their simplicity and high energy efficiency. However, they are characterized by some specific drawbacks, such as non-uniform gas treatment, limiting the conversion, as well as high temperature cathode spot development and severe electrode degradation. In this Chapter, a dual-vortex plasmatron is presented – a gliding arc reactor with innovative electrode configuration that seeks to solve these problems as an all-in package.

The design aims to improve the conversion capability of the GA reactor by elongating the arc in two directions, to increase the residence time of the gas inside the arc, and to actively cool the cathode spot by rotation of the arc and gas convection. A fluid non-thermal plasma model is developed to study the arc behaviour in the reactor. A reactor prototype has been built and tested, showing equivalent conversion performance compared to the existing reverse-vortex GA reactors.

8.1. Concept and design

Reverse-vortex stabilization is a known method for gaseous flame and plasma stabilization [19], [127], [128]. It has been practically implemented for a GA reactor, for gas conversion applications [59], [64]. As shown in figure 8.1 (a), it essentially considers a tubular vessel, where tangential inlets are mounted on the same side as a larger, axial outlet. As shown in the figure, this forms a tangential flow that creeps along the reactor walls, and upon reaching the bottom, it forms an inner vortex (in red) with a smaller radius, travelling in the opposite direction (hence reverse-vortex). In simple terms, mass flow is directed from the walls to the reactor centre, which effectively insulates the walls from convective heating. The number of inlets may differ (e.g. 1-6) (see also Chapters IV and V, where 4 and 6 inlets were considered). Furthermore, the outlet diameter can vary, but generally it should be significantly smaller than the diameter of the reactor itself, to avoid that the gas, when entering the reactor, can immediately escape without traveling through the entire arc.

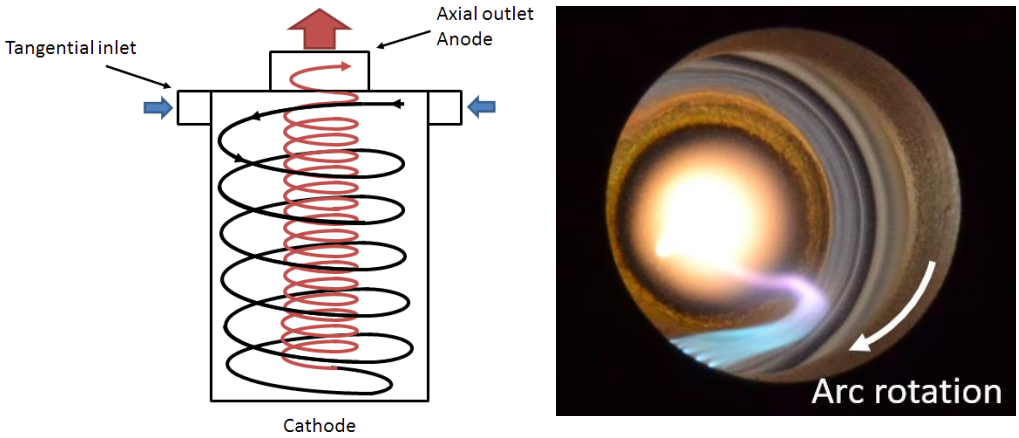

Figure 8.1. Reverse-vortex flow stabilization concept (a) and internal view of a reverse-vortex flow stabilized gliding arc (b).

In figure 8.1 (b), a reverse-vortex flow stabilized gliding arc reactor is demonstrated with a fast-shutter photograph of the arc. The bright cathode spot is very obvious, emitting strong black-body radiation. The cathode spot is a source of intense heat and thermionic emission, bringing the arc closer towards thermal equilibrium ($T_i \approx T_e$). This hampers the energy efficiency for CO_2 conversion, as it dissociates the molecules thermally rather than through the more efficient vibrational pathway [17], [21]. The effect of heat insulation of the gliding arc in

a reverse-vortex flow has been shown through modelling, as demonstrated in Chapters IV and V. With no doubt, the arc is indeed forced in the reactor centre [116], [134]. This configuration, however, leaves the cathode spot almost static on the cathode cap, as can be verified on the photograph above. Clearly, the gliding arc is manifested in different stages: the area closest to the cathode spot is most thermal, while closer to the anode the arc cools down. Some difference in light emission can be spotted in figure 8.1 (b), and variations in plasma density and temperature have been captured through modelling, though without cathode spot description (see Chapters IV and V). Due to the intense arc contraction, the discharge is rather thin (see figure 8.1(b)), which was also verified in simulations (Chapters IV and V above) and experiments [134]. The discharge radius is typically no more than 2 mm. This means that only a limited portion of the gas actually passes through the plasma region and can be converted, while the rest leaves the reactor untreated. In addition, the maximum power capability of the reactor is limited by its ability to elongate the arc – whose maximum length is practically the distance between cathode and anode. The arc diminishes shortly after the anode, as is visible in figure 8.1(b).

The new dual-vortex plasmatron concept, presented in this Chapter, is shown in figure 8.2. A single tangential inlet, creating a high flow velocity, is attached to an electrically insulating piece (Teflon, ceramic or equivalent). Two hollow electrodes with conical shape are attached to the opposing sides, forming a symmetric vessel. The gas travels tangentially inside the reactor, forming two symmetric vortices. The two outlets have a small radius with respect to the main chamber radius, in order to facilitate high speed rotational flow at the outlet edge, and hence rotate and cool down the cathode spot.

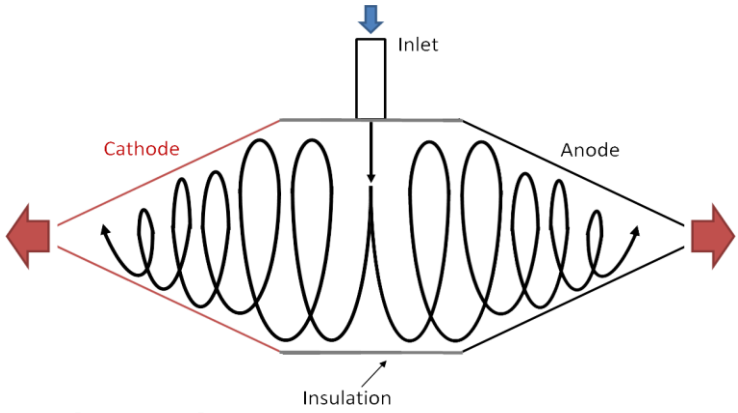

Figure 8.2. Dual vortex plasmatron - concept

The practical realisation was carried out with CNC machining at the University of Antwerp. The electrodes are made of stainless steel 316, and the insulation layer is made of Teflon. The six bolts that hold the construction together are also non-conductive (figure 8.3). Non-conductive domains are depicted in blue in figure 8.3-a.

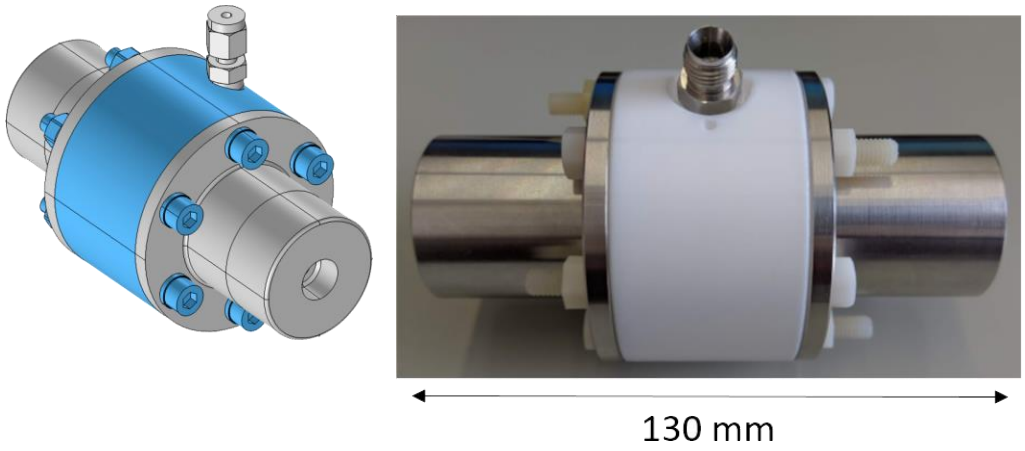

a b

Figure 8.3. 3D CAD model of the dual-vortex plasmatron (a), and the machined unit (b).

The produced reactor is 130 mm long when assembled. One tangential inlet with ¼" NPT thread insert acts as tangential inlet. The inlet internal diameter is 2 mm for high gas flow velocity. The two outlets are terminated with ¼" NPT threads for steel tube insertion.

The internal structure of the reactor can be viewed in detail in figure 8.4. A stepped insert in the Teflon flange ensures correct placement and distancing for the electrodes. The arc ignition gap (start-up gap) is 2 mm long, and it also contains the single tangential inlet (see figure 8.4). The conical cavities in the electrodes are 44 mm long (each), with a large diameter of 24 mm and small diameter of 6.35 mm. As the arc ignites at the start-up gap (shortest distance between the electrodes), it is rapidly elongated by the fast tangential gas flow coming from the inlet. Gradually, it is extended sideways, in both directions towards the two outlets, forming a long discharge of about 90 mm length.

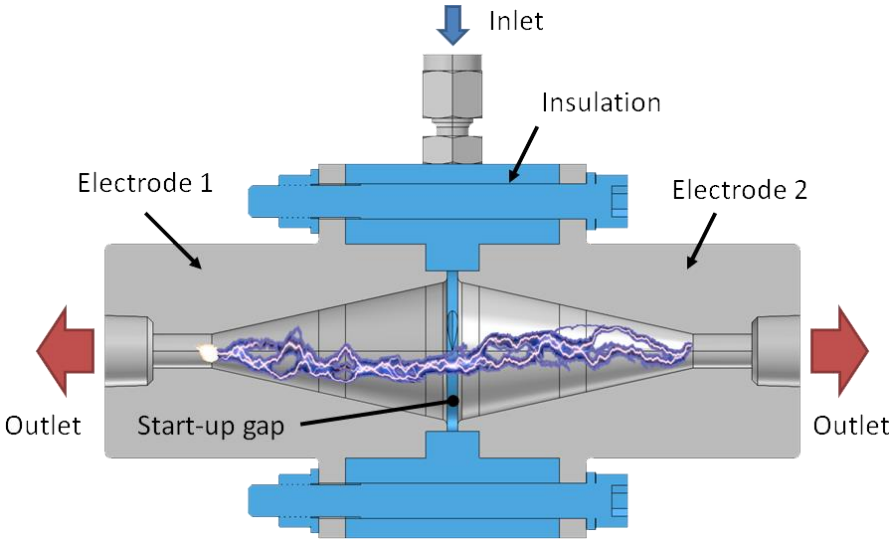

Figure 8.4. Half cut-off side view of the dual-vortex plasmatron, with artistic representation of the arc discharge.

Electrodes 1 and 2 are completely identical, and neither is defined as cathode or anode – this only depends on the power supply polarity. Operating with AC power supply is indeed also possible. The start-up voltage was predicted to be around 6 kV using Paschen curves, and is actually around 6.5 kV in the practical experiment. The electrode edges are filleted in order to prevent hot spot formations. Flow rates of 5 to 30 L/min are permitted (the main limiting factors are the pressure on the tangential inlet and the cooling rate of the reactor).

8.2. Model description

In order to characterize the flow in the reactor, a turbulent flow model is employed within COMSOL Multiphysics [67]. The Navier-Stokes equations are again solved for the mass and momentum conservation:

$$\nabla \cdot \boldsymbol{P} + f = \rho \frac{\partial \boldsymbol{u}}{\partial t} + \rho(\boldsymbol{u} \cdot \nabla)\boldsymbol{u} \tag{8.1}$$

$$\frac{\partial \rho}{\partial t} + \nabla \cdot (\rho \boldsymbol{u}) = 0 \tag{8.2}$$

Where $\boldsymbol{P}$ stands for the Cauchy stress tensor, f represents the fluid body force, ρ stands for fluid density and $\boldsymbol{u}$ is the gas flow vector. The turbulence description follows the k-epsilon model (see Chapter III).

The plasma model is again based on the drift-diffusion quasi-neutral fluid model, as also explained in detail in Chapter III. The following equation is solved for the species balance:

$$\frac{\partial n_i}{\partial t} + \nabla.\left(-D_i \nabla n_i + \mu_i n_i \overrightarrow{E_{amb}}\right) + (\boldsymbol{u}.\nabla) n_i = R_i \tag{8.3}$$

A limited reaction set is used for argon 3D plasma modelling, as in Chapter IV.

8.3. Experimental setup

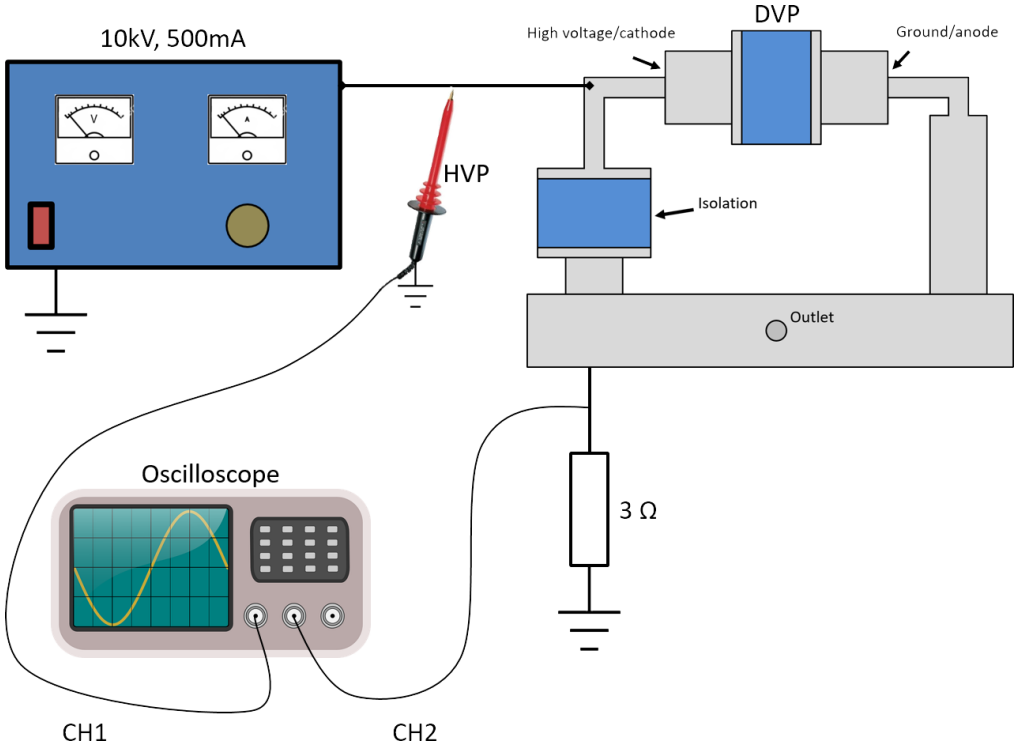

Figure 8.5. Electrical configuration of the experiment.

The electrical configuration of the experiment is shown in figure 8.5. A high voltage, switch-mode DC power supply capable of 10kV and 500mA, is connected to the dual-vortex plasmatron (DVP). The DVP is mounted on a mixing console, which connects the two outlets into one, where one side is isolated by an

additional Teflon piece (with a gap of 40 mm). The voltage signal is picked up with a high voltage probe (HVP) with a 1:1000 ratio. The current signal is acquired with a 3Ω shunt resistor. A Keysight DSO-X 1102A 100MHz oscilloscope is used. The power is calculated using the relation:

$$P = U \times I \tag{8.4}$$

where P is the electrical power, U is the voltage and I is the current.

The gas composition is measured using an Interscience Compact gas-chromatograph (GC) equipped with a TCD detector (see Chapter VII), and an Interscience Trace GC 1310, also utilizing the TCD detector. A Bronkhorst El-Flow Select mass flow controller handles the gas input.

8.4. Results and Discussion

A stationary solver (PARDISO) was used to calculate the gas flow velocity vector for three different flow rates – 6.6, 10 and 20 L/min. The results are represented using streamlines following the velocity vector, with a colour expression showing the total velocity magnitude.

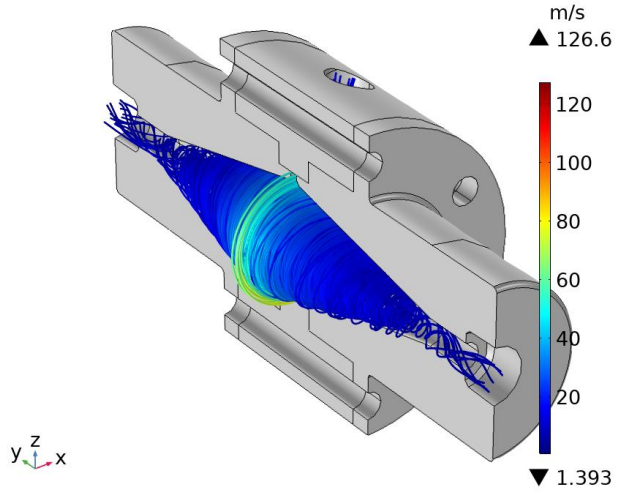

Figure 8.6. Gas flow velocity streamlines at a flow rate of 10 L/min (m/s). Half-cut 3D view.

Figure 8.6 illustrates the gas flow velocity profile. A high velocity at the start-up gap of over 100 m/s is observed. As intended, the rotational motion is

preserved towards the outlets of the reactor. The velocity magnitude in the main gas bulk is in the order of 10-40 m/s. The vortex development is symmetric. Figure 8.7 shows a detail of the flow profile near one of the outlets. Normally, a cathode (or anode) spot attachment would occur in this region, on the outlet edge. In the present design, however, the high rotational velocity of the flow will rotate the cathode (or anode) spot along the outlet edge, which will reduce the heating and damage of the electrode.

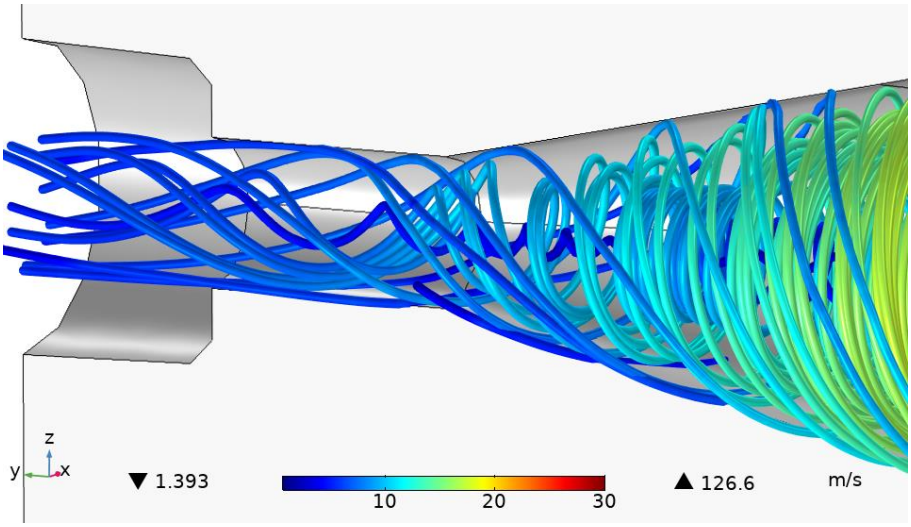

Figure 8.7. Detail of the gas flow velocity streamlines at the electrode end: the high rotational speed will rotate the cathode spot, to limit the heating and damage of the electrode. Flow rate: 10 L/min.

In figure 8.8, the gas flow profiles are plotted with arrows for three different flow rates of 6.6, 10 and 20 L/min. The colour indicates the magnitude of the axial velocity component (on the y-axis). The flow is essentially separated into forward flowing (positive values, i.e. green to red) and backward flowing (negative values, i.e. green to blue). We can then distinguish the presence of a secondary reverse-vortex in the gas flow for all three cases. At low flow rate (6.6 L/min), this reverse vortex is somewhat weakly pronounced, with backward velocity of around 1 m/s. At 10 L/min, the reverse vortex travels backwards at about 2 m/s. At high flow rate (20 L/min), the reverse vortex is very pronounced, with backward velocity of up to 4 m/s. The surrounding forward vortex (with forward velocity) travels much faster at 6 m/s and higher. This means that in addition to the unique flow configuration, the dual-vortex reactor also shows reverse-vortex behaviour to

some extent. The reverse-vortex flow has been discussed before as a very effective method for plasma stabilization and insulation [19], [120], as demonstrated both by experiments [59], [135] and modelling (see Chapters IV and V). Generally, the reverse-vortex flow contributes well to efficiently sustaining the plasma by insulating it from the reactor walls and thus preventing heat losses. It also improves the gas mixing, and lowers the gas temperature through intense turbulent heat transport (see Chapter V).

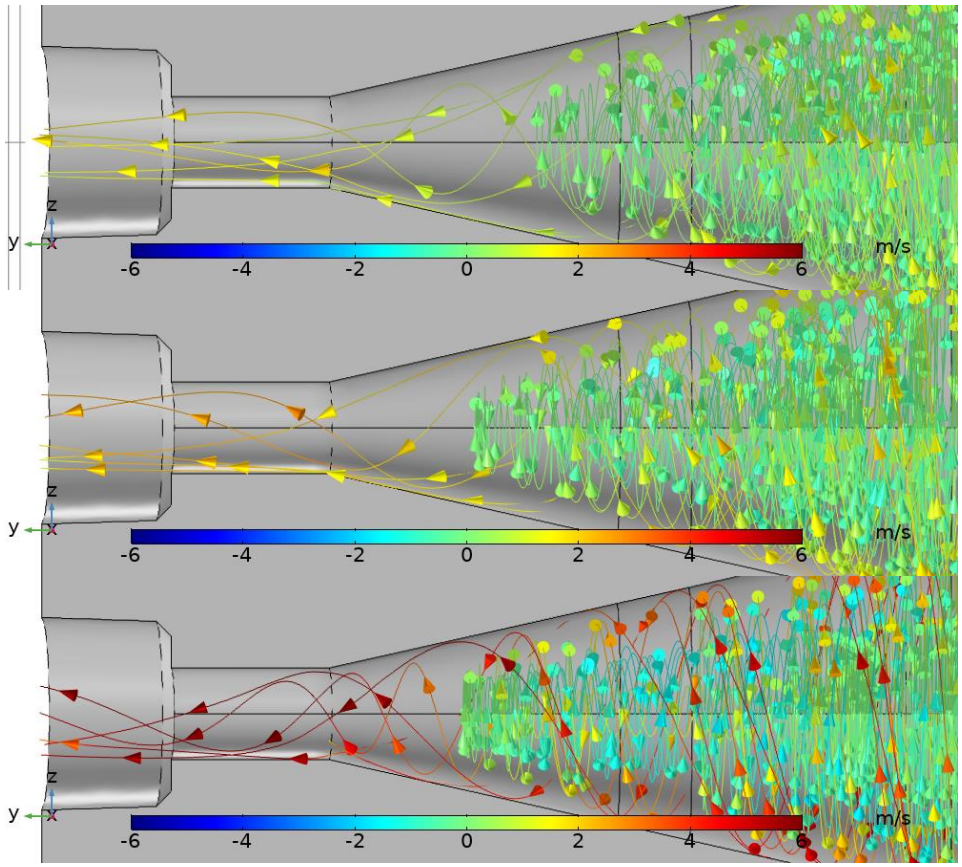

Figure 8.8. Gas flow velocity streamlines near one of the electrode ends, at three different flow rates. The colour indicates the axial flow velocity (along the y-axis).

The plasma modelling was carried out in two stages – for initial discharge conditions at arc ignition, and for a quasi-stationary discharge. It was already shown in Chapter IV that the arc glides into a quasi-stationary "stabilized" state

with little axial rotation after a certain amount of time, which depends on the reactor design and flow rate. In Chapter IV this state was achieved after 1 ms for a conceptual RVF GA reactor geometry, while in Chapter V a stationary state was achieved after 5 ms for the actual RVF GAP reactor geometry. Generally, as the model does not include complex features as arc re-ignition and spot attachments (see Chapter III), the gliding process is smooth with relatively small changes in the plasma parameters. For this reason, only the initial and final (steady-state) stage of the arc are shown here, for the sake of a reasonable computation time. Naturally, the streamer stage of the arc is omitted through a short time-dependent artificial heating function.

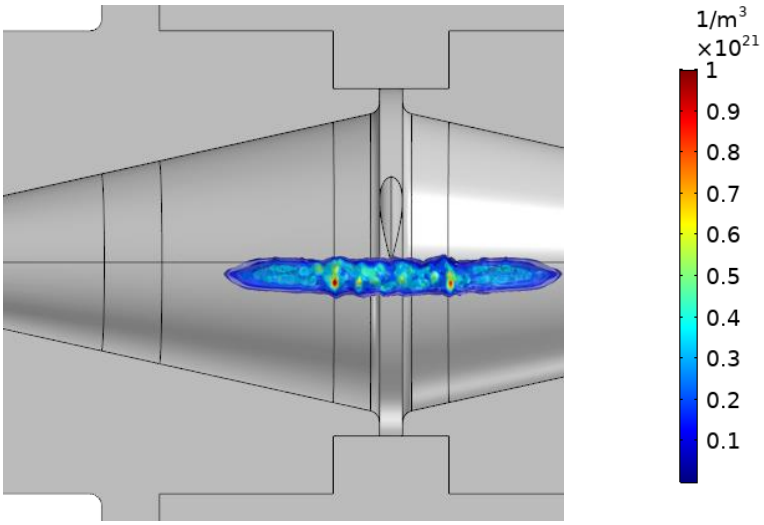

Figure 8.9. Plasma density for the initial arc stage at 11 μs, at 460 mA arc current and 10 L/min gas flow rate.

Figure 8.9 depicts the arc development just in front of the tangential inlet inside the reactor. This is the initial stage of the plasma, indicating a short, straight column gliding at the shortest distance between the two electrodes (see figure 8.4). For this computation, the full internal body of the reactor was modelled, with 490,000 mesh elements, which severely prohibits longer computation times, i.e. until further arc extension. Still, the arc electrode attachment and gliding could be observed from the calculations. The plasma density is in the range of 10^{20} m^{-3}, which is typical for gliding arcs in argon [120], [125], [150] (see also Chapters IV and V).

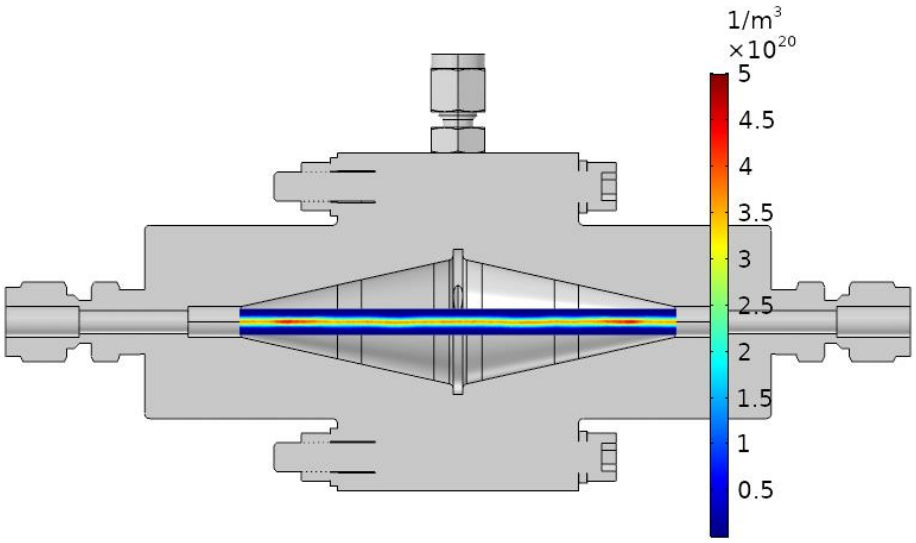

8.10. Arc position in the reactor, plasma density plot at 10 L/min.

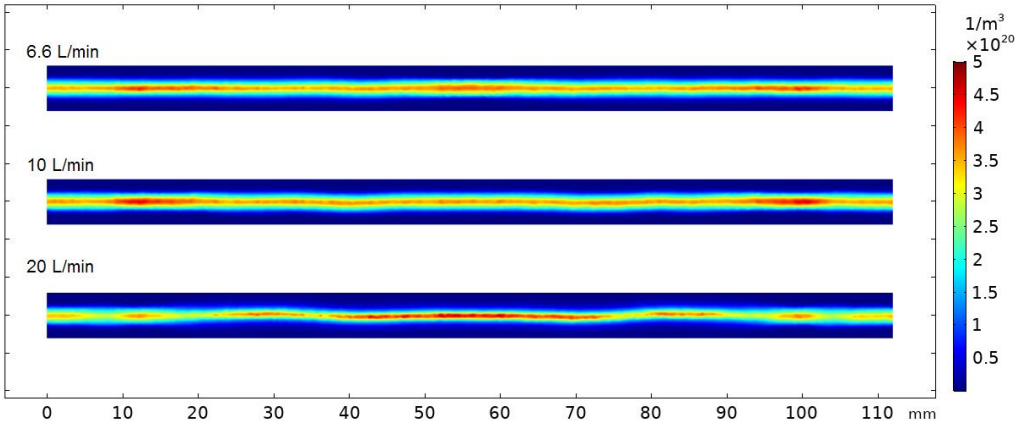

Figure 8.11. Plasma density at steady-state, for three different flow rates, at 460 mA.

Figure 8.10 and 8.11 illustrate the fully elongated state of the arc, i.e. stabilized in the reactor centre, for three different flow rates. Similarly to Chapter IV and V, no significant change in the plasma density is observed. However, a closer looks reveals some peculiarities. At the highest flow rate (20 L/min), the arc demonstrates some bending, as a result of the spiral-like flow profile. Furthermore, the plasma density in the centre is slightly higher (around $5x10^{20}$ m^{-3}) than at the low flow rate of 6.6 L/min, due to the stronger convection coefficient. We observed a non-homogenous arc structure in Chapter V as well.

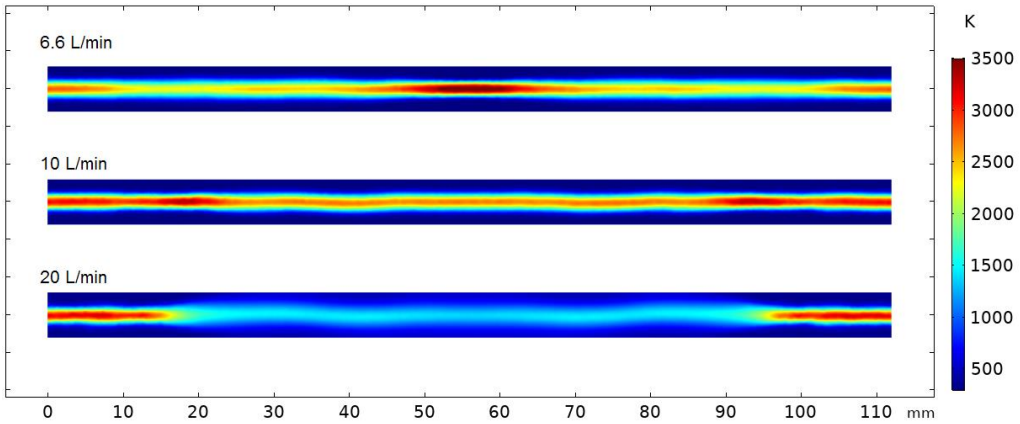

Figure 8.12. Plasma gas temperature at steady-state, for three different flow rates, at 460 mA.

Figure 8.12 depicts the gas temperature. At 6.6 L/min, the gas temperature reaches 3500 K in the centre of the arc, cooling down to about 2000 K towards the sides, but rising again to 3000 K near the electrodes. At 10 L/min, the temperature is more homogeneous along the arc length, with values around 2800-3000 K, and slightly lower in the center. A striking difference can be observed at the high flow rate of 20 L/min. A large portion of the arc (between 20 and 90 mm; see the scale in figure 8.12) is rapidly cooled to 1500 K and below. This effect is attributed to turbulent heat transfer [96], [116], but the development of a reverse-vortex (figure 8.7) leads to additional heat transfer. The calculated temperatures are comparable to earlier studies for a classical gliding arc [99], [125].

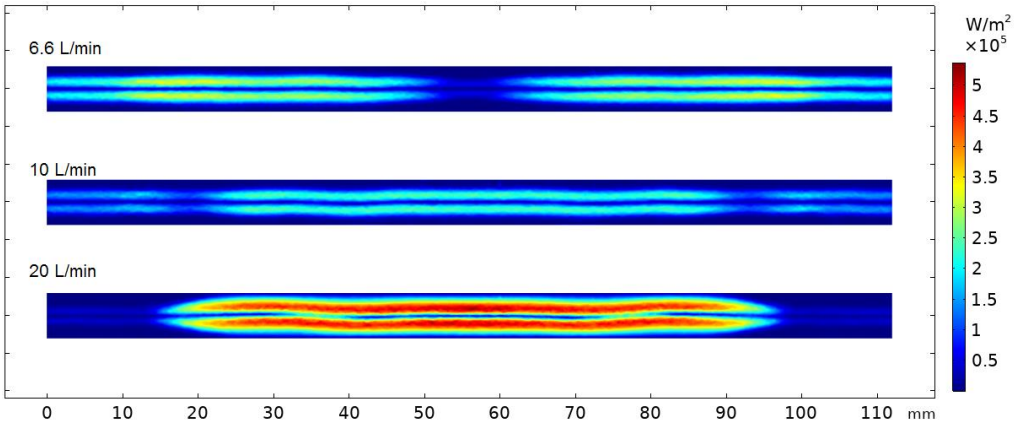

Figure 8.13. Turbulent heat flux magnitude around the plasma, for three different flow rates, at 460 mA.

In figure 8.13, the reason for the significantly lower temperature at the highest flow rate is clear: the turbulent heat transfer has the maximum intensity at the areas of low gas temperature indicated in figure 8.12. Interestingly, the turbulent heat transfer seems completely different for different gas flow rates. At a flow rate of 6.6 L/min, two heat exchange zones can be observed at 10-30 and 80-100 mm (see length scale in figure 8.13), while the turbulent heat exchange in the centre is very low, as confirmed by the maximum temperature in figure 8.12. At 10 L/min, the turbulent heat exchange zones spread from the discharge centre, but with a rather low magnitude (around $2x10^5$ W/m^2), which explains the homogenous temperature distribution for 10 L/min, shown in figure 8.12. At 20 L/min, the highly turbulent zones are clearly visible (see figure 8.13), which explains the pronounced drop in temperature.

A constant electron temperature of about 2.5 eV is predicted for the three different flow rates, as is evident from figure 8.14. This is similar to Chapter IV, where we also found that the electron temperature was rather independent of the gas temperature and flow rate. At 20 L/min, the electron temperature exhibits a broader profile in the radial direction, which can be explained with the lower arc contraction at low gas temperatures.

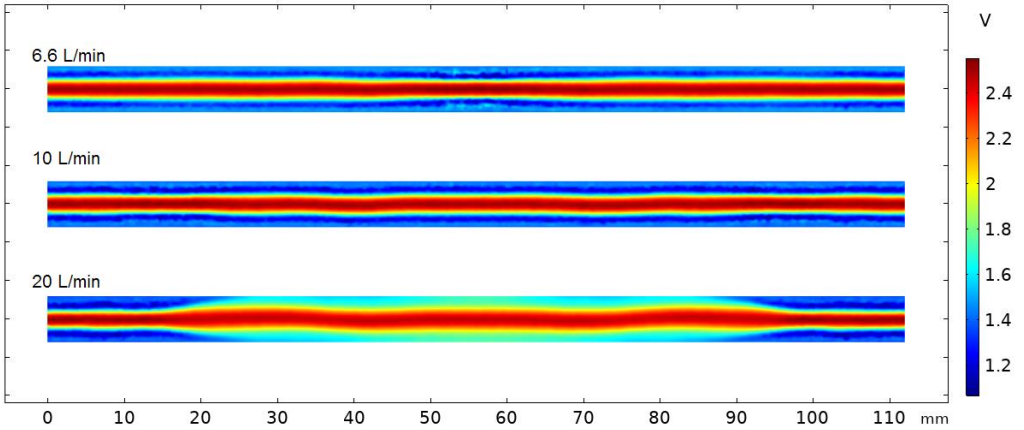

Figure 8.14. Electron temperature, for three different flow rates, at 460 mA.

Lower gas temperatures are preferable overall, as they increase the non-equilibrium of the discharge, and promote the more efficient vibrational CO_2 dissociation [21]. In the case of the reverse-vortex flow GAP [59], a gas temperature of 3000 K was calculated for CO_2 plasma (see Chapter V), and 5500

K was measured experimentally with N_2 [66]. These values are too high for (energy efficient) vibrational-induced CO_2 conversion [17], [19], [60], but they point towards mainly thermal conversion. The demonstrated turbulent cooling capability of the dual-vortex plasmatron indicates potential for high energy efficiency and high power handling, which can improve the overall conversion, if also the fraction of gas passing through the arc is enhanced.

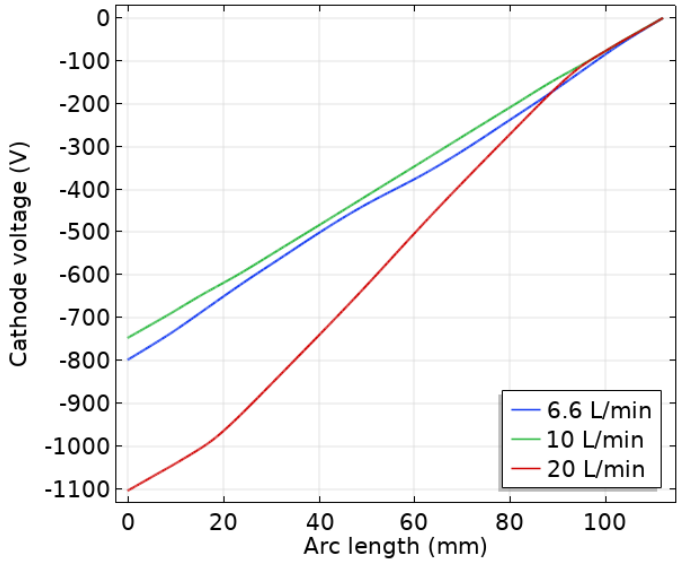

Figure 8.15. Cathode voltage drop at different flow rates.

Figure 8.15 plots the voltage drop across the discharge centre. The two lower flow rates yield a similar voltage drop of around 750-800 V. At 20 L/min, the voltage drop increases significantly to around 1100 V, indicating a lower plasma conductivity. Indeed, the volume-averaged plasma conductivity in the case of 6.6 and 10 L/min is 7.22 and 7.91 S/m, respectively, while in the case of 20 L/min, it is 4.78 S/m. This is to be expected from the intensive arc cooling, leading to a lower gas temperature and a drop in plasma density in certain arc areas (see figures 8.12 and 8.13). While no direct plasma parameters are illustrated here, this result might be interesting for experiments, as it can be implied that the sudden increase in the turbulent heat flux can be detected though measuring the voltage drop across the plasma.

In order to assess the vortex-driven plasma insulation from the walls, a static artificial heat source term is introduced in the computational reactor volume. This

source term is defined by two analytical functions (Gaussian distribution for the x and z coordinates, and a rectangular function for the y coordinate). Integrating the power density of the obtained 3D distribution equals 1000 W, the predicted maximum power capability of the reactor. The same flow field vector, as shown in figure 8.7 for 20 L/min, is used to drive the convectional heat flux. The artificial heat source is shown in figure 8.16.

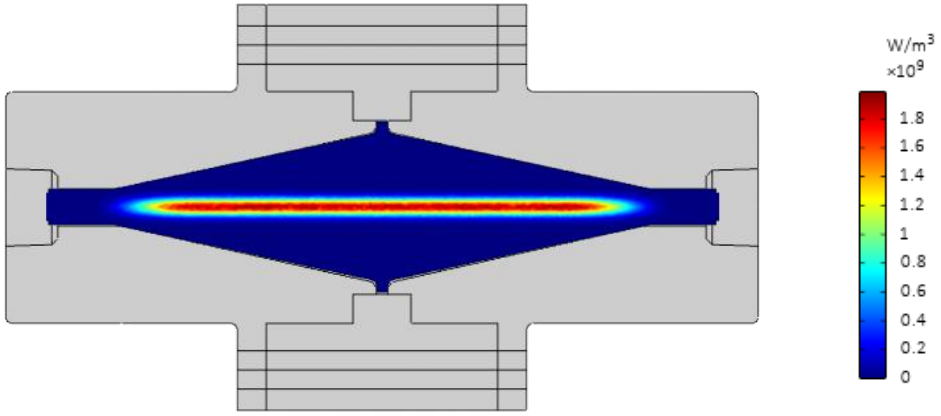

Figure 8.16. Artificial heat source power density in the dual-vortex plasmatron.

A stationary solver is used to solve the heat transfer equation. As such, the presented solution reflects the steady-state of the reactor, which would normally be reached after a considerable amount of time (minutes). Such time scale is currently out of reach with an actual plasma model, where, despite the simplifications, just 1ms of simulation time takes about 50 hours to compute.

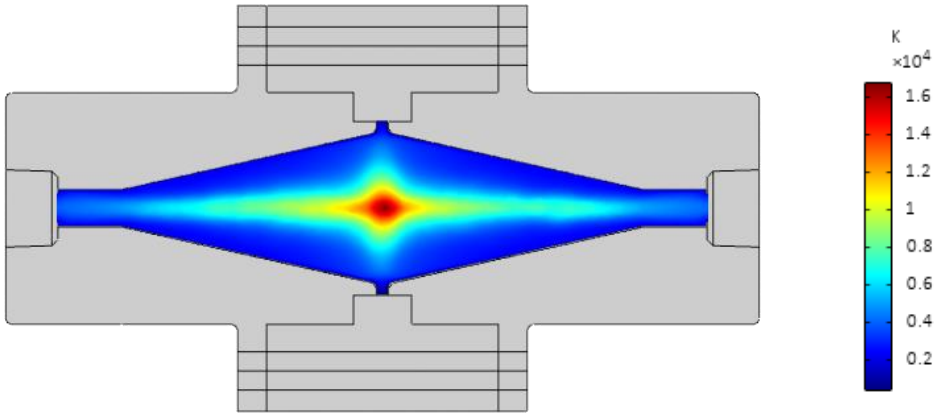

Figure 8.17. Stationary temperature distribution in the dual-vortex plasmatron at 20 L/min.

Figure 8.17 illustrates the steady-state temperature distribution. It should be noted that this simulation does not take into account any chemical reactions or turbulent heat flux, as it focuses on the convective heat transfer only. Integrating the normal convective heat fluence (irradiance of a surface) over the reactor walls equals 82 W, while the integrated fluence over the reactor outlets equals 2070 W, meaning that only a negligible portion of the reactor power is lost through convective wall heating. The integrated conductive fluence through the walls and the outlets is even more negligible, with values of 0.007 W and 2.6×10^{-5} W, respectively, due to the low thermal conductivity of the CO_2 gas.

8.5. Experimental results

Figure 8.18 illustrates the oscilloscope waveform taken from the setup. The figure shows repetitive arc behavior (normal gliding arc), with some variation in the peak voltage/current values, which is again typical for a gliding arc. The voltage peaks to around 6.5 kV, which is the ignition point. The current peaks at around 1 A. The period between the pulses is around 5 μs, which equals to 200 kHz repetition rate. Note that this might be influenced by the switching frequency of the power supply itself.

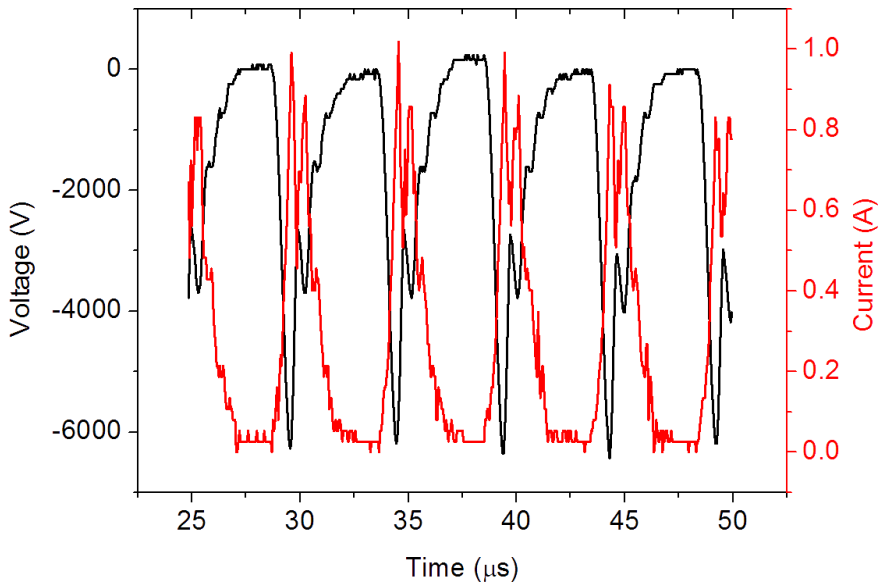

Figure 8.18. Oscilloscope waveform of the discharge. Conditions: 10 L/min, 332 mA average current.

At the pulse edges, slight ripples are visible, indicating an inductive load. This might be caused by the arc and the power supply cables combined. The average power from the obtained signal equals 460 W at 10 L/min, which is lower than for the reverse-vortex gliding arc (GAP) system in [59], [66], [134].

The volt-amp characteristic (with average values) of the is shown in figure 8.19. The minimum current to sustain a discharge was found to be 150 mA. Up to 200 mA, a slow increase of the voltage was observed. A sudden peak in the voltage appears at 240 mA, probably indicating a glow-to-arc transition (see Chapter II). While this is certainly an interesting phenomenon, the low accuracy of the power supply current regulation limits the number of data points that can be obtained for a more detailed study.

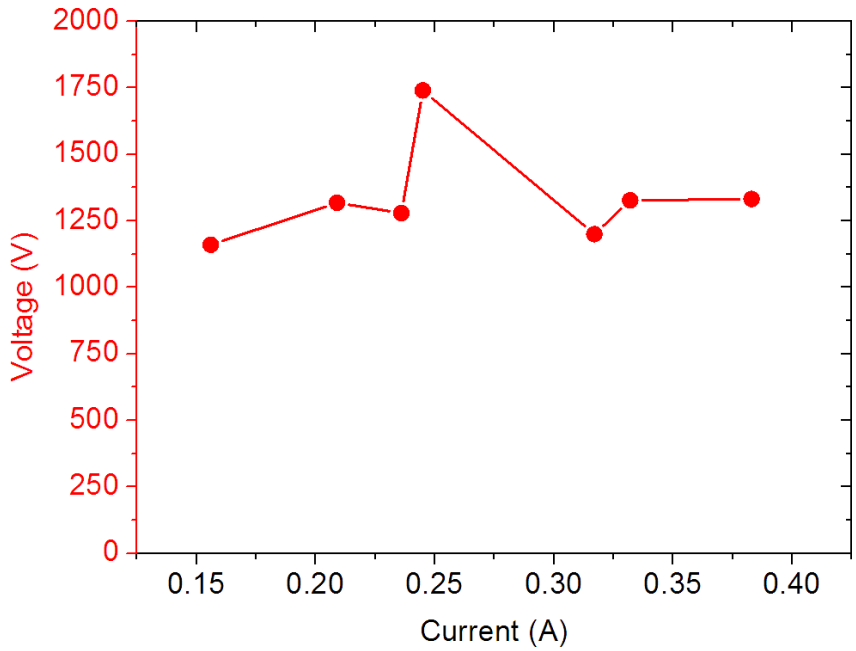

Figure 8.19. Volt-amp characteristic of the dual-vortex plasmatron at 10 L/min.

The given setup demonstrates unstable behavior. The power supply is unable to supply enough current to sustain the arc above flow rates of 12.5 L/min. At 10 L/min, it is generally more stable, with reliable arc ignition and sustainment. At 15 L/min, the discharge could not be sustained long enough for reliable gas chromatography measurements. Lower flow rates (5 and 7.5 L/min were tested) do not provide enough cooling for the reactor electrodes. This allows a limited working bracket for the reactor flow rate. For this reason, the results for the conversion and energy efficiency are shown as a function of the SEI (specific energy input) in figure 8.20.

Two flow rates are used, 10 and 12.5 L/min (which were proven stable). At 10 L/min and 446 W of power, a CO_2 conversion of 9.5% is obtained. The conversion drops to 7.2% at 12.5 L/min (SEI = 2.19 kJ/mol), though a relatively high energy efficiency of 38% is still maintained. This might be related to the discharge temperature: at lower temperature, the thermal conversion in the discharge is proportionally lower [17], [60].

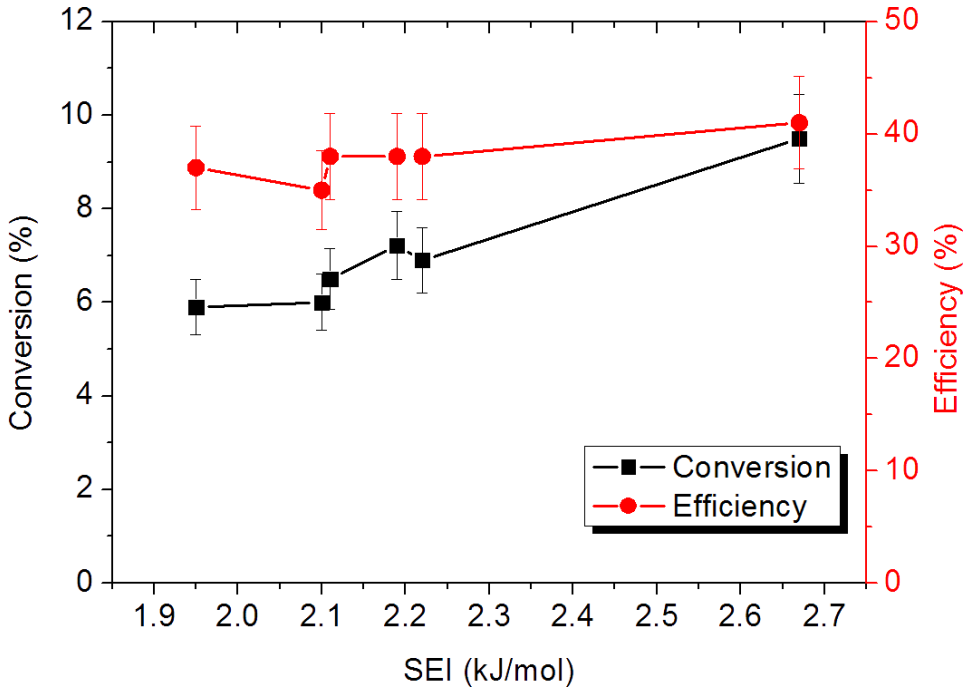

Figure 8.20. CO_2 conversion and energy efficiency for the dual-vortex plasmatron, as a function of SEI. No stable discharge was obtained between 2.2 and 2.7 kJ/mol. Lower SEI values than 1.95 kJ/mol did not yield a sufficiently stable (for gas chromatography) discharge either, as the arc would break up frequently due to low current. Values higher than 2.7 kJ/mol did not provide sufficient cooling for the electrodes and the reactor body.

The results are comparable to [151], where a conversion of 8% was achieved at the same flow rate using a gliding arc plasmatron (GAP), though at higher power. The power is varied: at lower discharge current, the SEI can be brought to around 2 kJ/mol (with power of 350W), with conversion around 6%. The energy efficiency in this case is still high – around 38%. At SEI of 2.65 kJ/mol, the highest point for the energy efficiency is 41%, which is higher than

what was obtained in [151] and [60]. In the future, we want to further exploit the capabilities of the DVP, because theoretically it shows good potential, but it is currently limited by the power supply available in our lab.

8.6. Conclusion

In this work, a completely new reactor concept was designed from scratch, based on computer simulations. The reactor was extensively investigated using fluid flow, heat transfer and plasma models. The simulation results are compared with relevant literature, with good agreements.

The performance of the dual-vortex plasmatron was tested for CO_2 conversion. The first results, although limited by the power supply, are encouraging: a good energy efficiency (up to 41%) is measured at a flow rate of 10 L/min. This shows that the reactor is capable of utilizing the vibrational excitation of CO_2 molecules to some extent, for energy efficient conversion.

Electrode degradation is something that needs to be checked on the long-term. Currently, no observable pitting in the reactor electrodes was present, which is a good sign for the reactor reliability.

The main obstacle towards using the full potential of the reactor, is the power supply unit. As the rotating plasma is a highly reactive load, the strain on the power supply caused by reflected power is very high, and higher flow rates resulted in discharge instabilities. Possibly, a high-current AC power supply could solve this problem. We plan to build such a power supply in the future. Further developments might include a de Laval nozzle [152] for rapid flow quenching at the outlets.

CHAPTER IX. Power supply considerations

In this last Chapter, we want to focus briefly on the power supplies for DC plasma reactors. Indeed, the power supply is one of the most important aspects in any plasma source design, and, as experiments in our group PLASMANT taught us in previous years, it is often most problematic component for reaching a stable discharge. In the case of atmospheric DC plasmas, such as glow and gliding arc discharges, high-voltage power supplies are almost universally required. While the theoretical background typically dictates to adjust the high voltage supply according to gap distance, pressure and gas, and to set the desired current via internal resistance [153], some specific properties, particularly in gliding arc discharges, can remain overlooked.

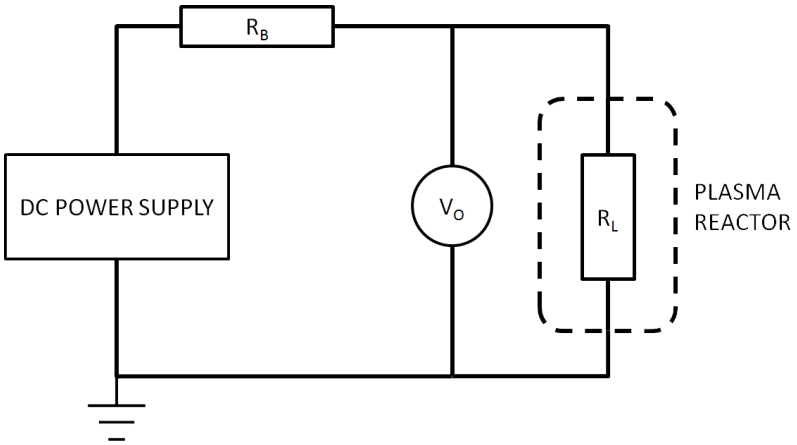

Figure 9.1. Theoretical circuit for a DC plasma reactor set-up.

In figure 9.1, the ballast resistor R_B limits the supply current for the discharge. Typically, high-density DC discharges have a very high electrical conductivity (see Chapter IV), which means that with a voltage-source power supply, the total circuit current will rise uncontrollably, until it is limited by the supply power capability or its internal output resistance. In most cases, especially for non-equilibrium discharges, a limiting ballast resistor in the range 1 – 50 kΩ is used. Then, the power (W) delivery in the circuit (in the plasma load R_L) can be calculated as:

$$P_L = I^2 \cdot R_L \tag{9.1}$$

The load resistance of the plasma column (R_L) is not known in advance, and is highly non-linear. For instance, the total resistance of the plasma in Chapter IV was around 70 Ω, with plasma column conductivity in the range 100-150 S/m. In [59], the measured plasma power was in the range 500-600 W, with average voltage around 1000 V, which means an average arc resistance of around 2 kΩ. However, this resistance is not static, and can rapidly change, as the arc glides along the electrodes. Furthermore, the gliding arc exhibits numerous re-attachments and re-ignitions [134], which act as a fast on-off switch for the load resistance. Essentially, the circuit breaks at random intervals.

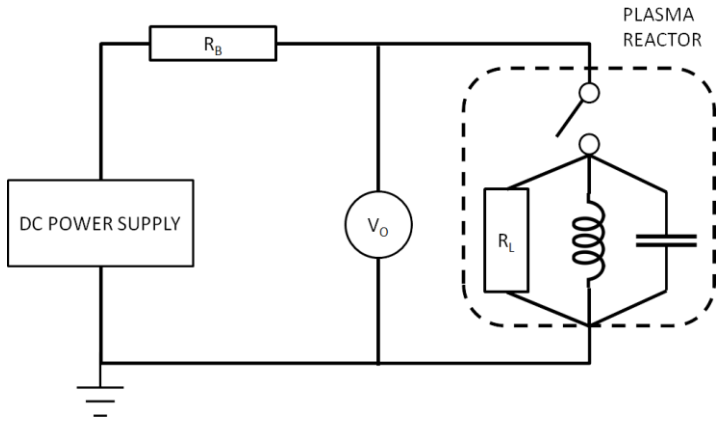

Figure 9.2. A closer-to-reality DC plasma reactor circuit

The plasma column itself does not behave as a simple resistor. It shows some inductive behaviour, as well as certain capacitance, especially in fast-rotating setups [59]. Furthermore, the inter-electrode gap represents an air capacitor between the arc break-up intervals. This leads to figure 9.2, where a more detailed, although still quite optimistic circuit is shown. A group of RLC (resistance-inductance-capacitance) parameters can describe the presence of a sustained arc in an electrical circuit. Note that none of these parameters is static, as they change rapidly with the plasma state. For instance, a re-ignition process might be initiated by local electric field enhancement caused by a rough electrode surface. A local arc break-up or back-breakdown can take place at any position, and is further enhanced by the presence of flow turbulence [134]. For this reason, the gliding arc can be referred to as a highly reactive electrical load with varying

impedance. In comparison to a purely resistive load, in which the entire power input is dissipated by the load itself, the reactive load reflects a certain amount of this power back to the power source [154].

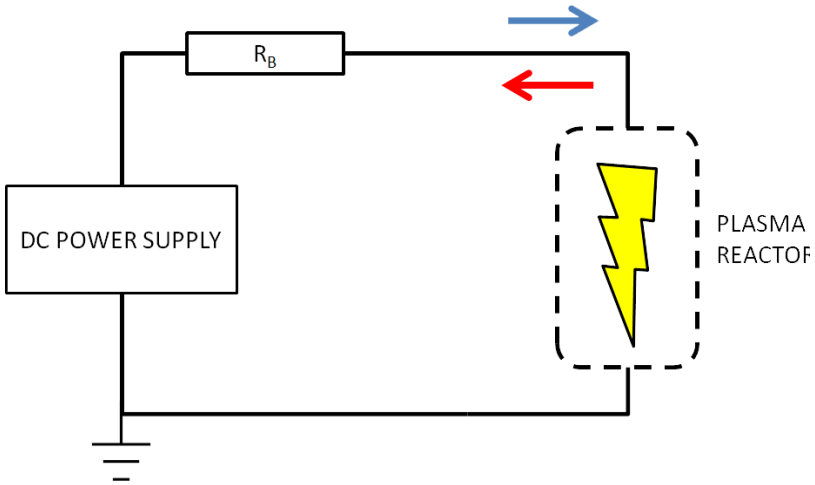

Figure 9.3. Power is pushed by the power supply (blue arrow), but partially reflected back (red arrow).

A parallel can be made with the reflected power in an unmatched transmission line [154]. Being a fundamental problem in audio and RF electronics, the impedance matching between the power source and the load is of crucial importance for ensuring that the full power will be effectively distributed into the load itself [155]. To alleviate this, matching networks and transmission lines are used in RF engineering. However, these concepts are based on known load impedance. It has been shown that for gliding arc discharges, this impedance is not static and typically varies rapidly by a factor of 2 [156]. Meanwhile, most high-voltage power supplies are designed around a purely resistive load. The reflected power surge negatively affects the driving and filtering stages, from considerable wear to a complete failure.

During various experiments, high-voltage power supply failures were experienced in the PLASMANT group in the previous years, some of which are depicted in figures 9.4, 9.5 and 9.6. Currently, power supplies are a major concern for new DC plasma setups. Typically, surges of reflected power overload the filtering or protection stage of the power supply.

In one instance, the output stage of a switch-mode unit was overheated until its output resistor cracked (see figure 9.4). Despite its low value of 22 Ω and high

power rating (240 W), it overheated due to its inductance, as the resistor is of the wire-wound type. In addition, the overcurrent protection (OCP) was frequently triggered by the low impedance of the ignition stage of the gliding arc. For a gliding arc typically working at 500 mA, the start-up current can be higher than 4A. The particular unit was modified with a much more relaxed OCP and less output filtering to make it suitable for gliding arcs.

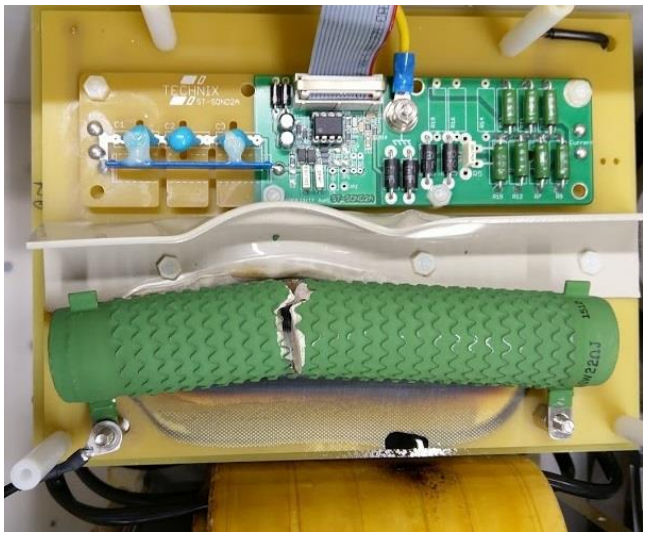

Figure 9.4. Wire-wound output resistor on a switching-mode high voltage power supply at PLASMANT.

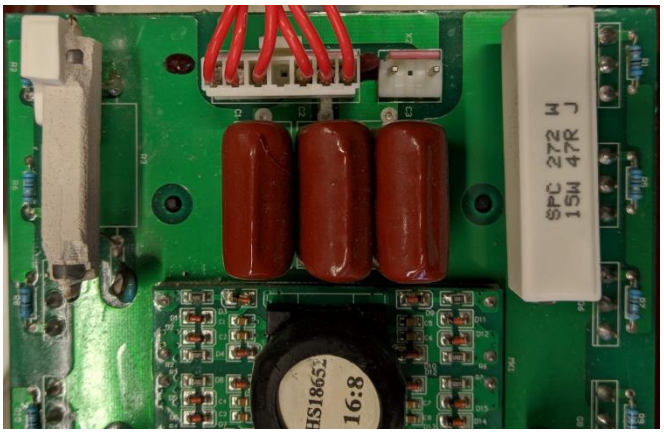

Figure 9.5. Broken power resistor (on the left) in the driving stage of a switch-mode power supply for the reverse-vortex flow gliding arc plasmatron (GAP) at PLASMANT.

In another example (figure 9.5), a purpose-built switching DC unit for gliding arc got half of its driving stage broken after several source resistors failed. As with most high-voltage, high-current power supply designs, a zero-voltage switching circuit in the driver stage is used. Sudden changes in the load impedance seem to put the components through severe stress (especially inductive wire-wound resistors), leading to partial or complete damage. In the example in figure 9.4, the power supply resumed normal operation after replacing several resistors and capacitors.

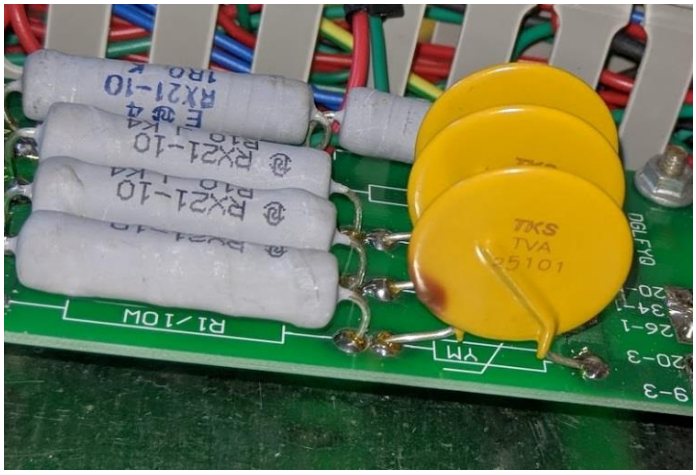

Figure 9.6. Broken protective element (varistor, right) in a linear power supply for a rotating gliding arc reactor at PLASMANT.

In a third instance, a large linear high-voltage DC power supply capable of 500 mA at 10 kV had a protective element broken (see figure 9.6) after a gliding arc was initiated without sufficient ballast resistance. The varistor covers the over-voltage protection of the current-regulating transistor stage. Over-voltage was reached when the repetitive on-off switching of the gliding arc induced high voltage in the output filtering (featuring an inductance coil) of the power supply. The lack of sufficient ballast resistance allowed for high current spikes. The unit returned to normal operation after replacing the varistor.

In figure 9.7, the voltage and current of a rotating gliding arc are shown. On channel 1 (yellow), the voltage is measured using a 1:1000 high voltage probe. On channel 2, a 3-Ohm shunt resistor is used to track the arc current. The current

signal shows a highly oscillating behaviour (ringing), indicating an inductive load.

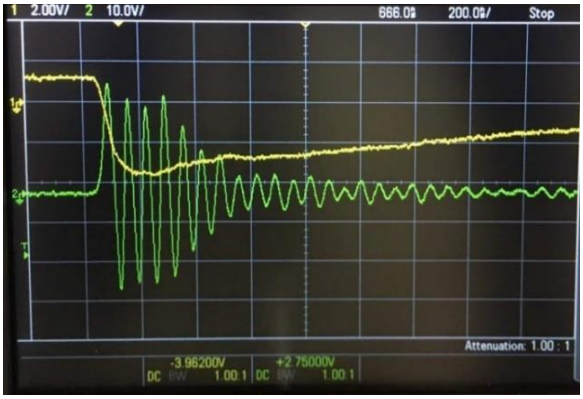

Figure 9.7. Oscilloscope recording of a linear DC power supply-driven rotating gliding arc.

The inductive part of the load is comprised of the cable inductance, and inductive filtering elements, and the inductance of the arc itself. Furthermore, stray capacitance, cable capacitance, and the capacitance of the dielectric insulation between the electrodes can contribute to the overall load impedance, as already shown in figure 9.2. Unfortunately, there is no universal answer on how to accommodate any high voltage power supply for work with a gliding arc. One solution is to use a high value ballast resistor:

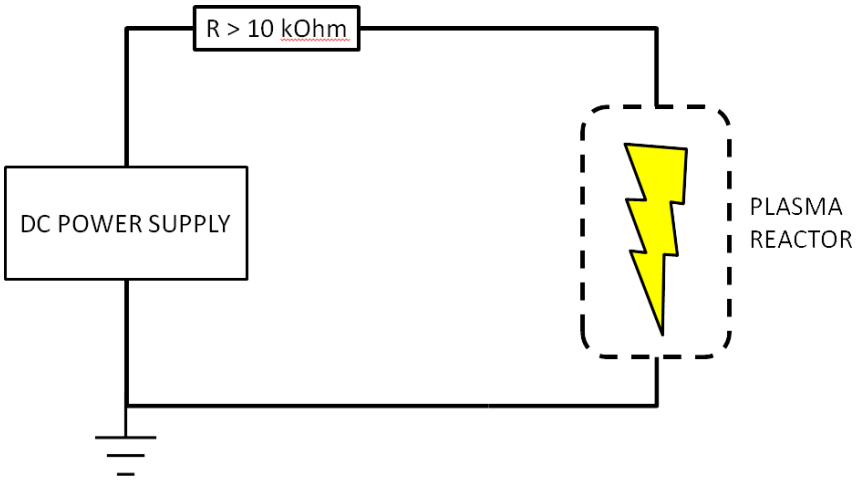

Figure 9.8. Resistor-adjusted DC plasma reactor circuit. Heat losses in the resistor equal to $P = I^2R$

The value of the resistor is typically around 10 kΩ and above, thus, a large amount of power is wasted through Joule heating. In this way, the power supply essentially becomes a current source.

Another way to introduce some sort of power supply protection, is to include a series inductance in the circuit (figure 9.9) instead of a high-value resistor.

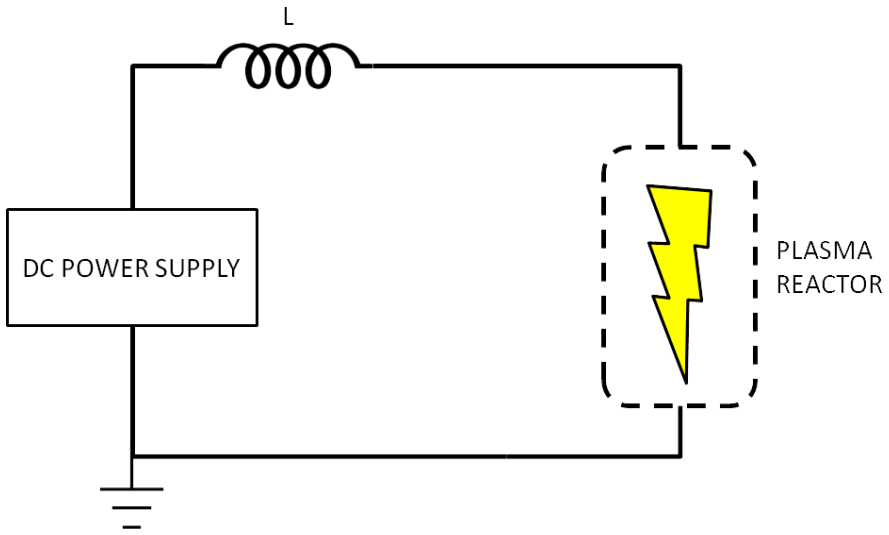

Figure 9.9. Inductance-adjusted DC plasma reactor circuit.

Contrary to what can be expected by adding inductive load (i.e. the inductance coil), a high-value inductance (significantly higher than the inductance of the cables) close to the reactor can resist to rapid changes in the circuit voltage, therefore providing some relief for the power supply output. However, this largely depends on the switching frequency of the arc, and needs to be tested extensively with different inductance values.

The third way to efficiently drive DC arcs, is to use a purpose-built power supply output stage. A general rule is to use as little as output filtering as possible (none is even better), and devise a robust driving circuit. In figure 9.11, an example of a high-voltage stage of a switching DC power supply is shown. The concept of zero-voltage resonant switching (ZVS) means that the active components (N-channel MOSFETS, 4xIRFP250N in the figure) are switched only when the voltage across is zero or close to zero. In this way, the heat losses in the switching elements are reduced to a minimum. The unit is powered by a

low-voltage, high current switching power supply (24 V DC). The MOSFET transistors drive a high current (~50 A) through a fly-back transformer with a high winding ratio (typically 1:1000). It is possible to parallel more transistors for higher current output. High AC voltage is produced on the output and rectified with a diode bridge. An array of high-voltage diodes can be used, i.e. RHRP8120 type or similar. The 100 pF output capacitor represents the cable stray capacitance. A simulation result in LTspice [157] is shown on figure 9.10. In the case of [59], [134], a comparable DC power supply was used, with no output filtering at the diode bridge.

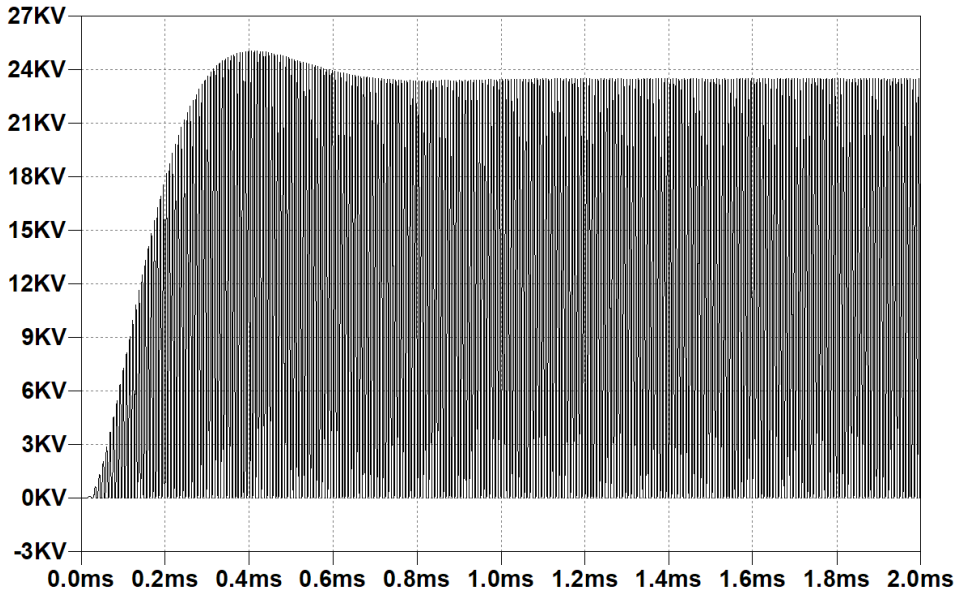

Figure 9.10. Output voltage of the switching power supply, simulated in LTspice.

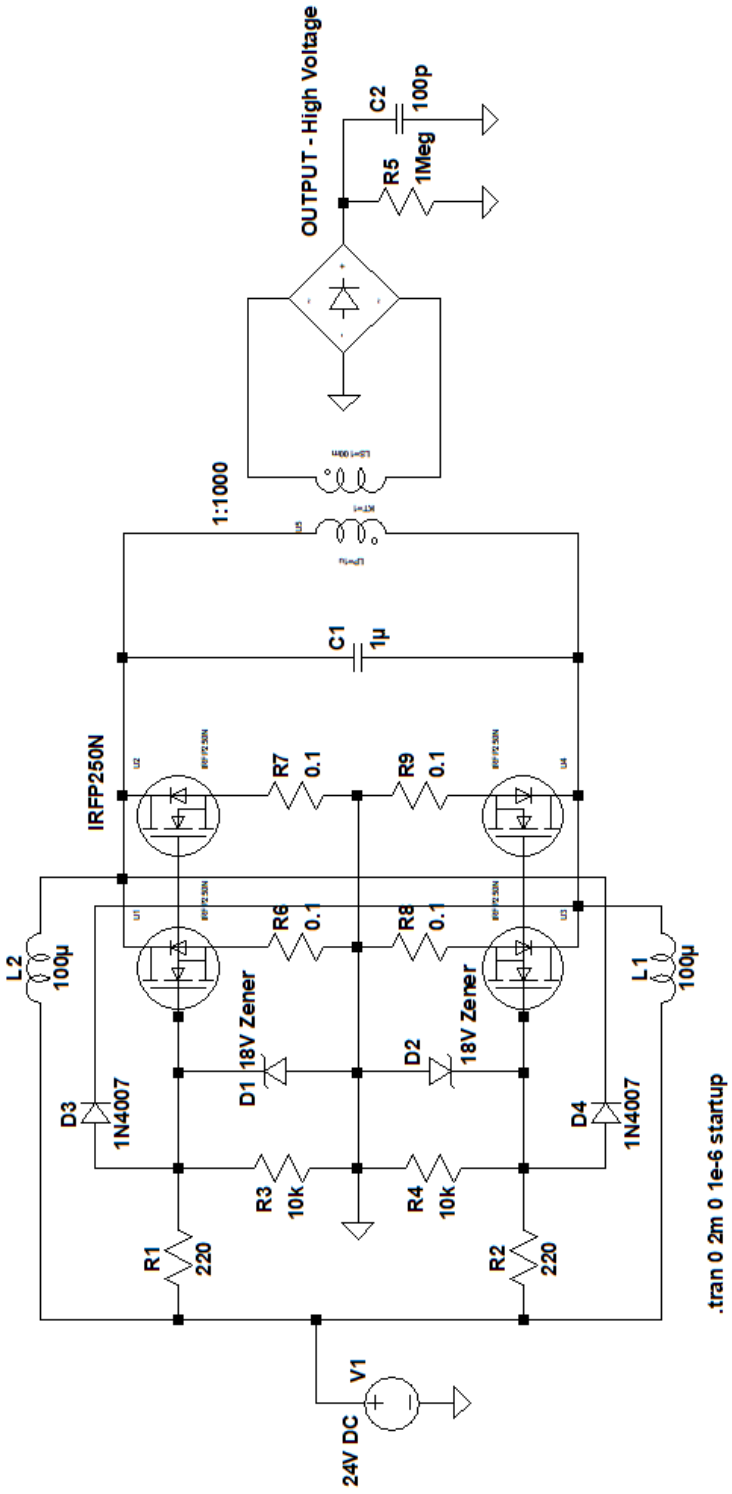

Figure 9.11. Schematic example of a quad-transistor ZVS resonant power supply, simulated in LTspice.

In summary, our recommendations for the power supply of GA reactors are as follows:

- Use less capacitive filtering on the output
- Build robust ZVS driving stages (for switching units)
- Use high output resistance (current source)
- Use series inductance if necessary and/or applicable
- Build/include relaxed overcurrent/overvoltage protection
- Avoid wire-wound resistors on the power delivery path
- Combinations of the above are almost always better

Over the years, we have acquired unique hands-on experience with high voltage sources at the PLASMANT research group. Translating this into actual decisions would be to also focus on AC (instead of DC) sources in the future, as they tend to be more robust and efficient. Certainly, DC sources should still be kept as relevant, but for less reactive loads, such as the APGD reactor. An important step in the future will be to introduce SPICE-based electronics modelling for plasma discharges.

Summary and Future Outlook

Summary

"There are no facts, only interpretations."

Friedrich Nietzsche

The purpose of computational modelling is not to merely replicate the results of an experiment – any linear system can be adjusted to do this. Instead, computational modelling combines the known basic physical relations into a greater understanding of complex processes. As such, its aim is to extend the parametric range, to expand the area of observation, and to granulate the intricate details that an ordinary experimental measurement can miss.

In this thesis, the fundamental knowledge of fluid dynamics, electrodynamics, particle physics and chemistry is combined into the broader picture of plasma modelling. Though it is not seamless, this merge provides interesting insights, not only of the given physical phenomena, but also of what is possible through simulations today.

Chapter I concisely describes the main purpose of this work. The climate change due to greenhouse emissions is, and will be, one of the main challenges of the 21st century. Plasma-based gas conversion, although still in an early stage, might be a promising answer to this demand. With the increasing adoption of simulation-based engineering, it is evident that computer modelling will be indispensable towards novel, efficient plasma-based gas conversion systems.

In Chapter II, the topic of plasma science, with an emphasis on DC discharges, is introduced. An overview of various atmospheric pressure plasma sources is given, with a deeper discussion on the main subjects of this thesis – the DC glow and arc discharge.

Chapter III thoroughly describes the existing modelling techniques for plasmas and fluids. Moreover, this part of the thesis serves as a compact plasma modelling "handbook", with examples, model derivations, and relevant literature.

In Chapter IV, the model-based journey towards efficient plasma-based CO_2 conversion begins with one of the first 3D models of low-temperature gliding arcs in COMSOL. A novel concept is explored: the reverse-vortex flow plasma stabilization. As it is an inherently 3D problem, a reduced chemistry quasi-neutral model is developed, and calculated in a full 3D geometry. The arc rotation is

observed, and the plasma parameters are compared with literature, showing good agreement. The insulation principle of the reverse-vortex flow is shown in the simulation, confirming theory and experiments.

In Chapter V, the 3D plasma model is extended to the real, 1:1 geometry of an actual gliding arc plasmatron (GAP) featuring reverse-vortex flow stabilization. The full rotation and stabilization process of the plasma arc are observed. Furthermore, a new model complication is introduced: the turbulent heat transfer. The calculations show that a significant amount of turbulence is developed in the reverse-vortex flow plasmatron, leading to an intense energy transfer. It is indicated that the turbulence is crucial for the gas temperature in the plasma, and hence, the importance of the chemical reactions. This effect is further explored in a CO_2 model with complex chemistry. Taking advantage of the flexibility of COMSOL Multiphysics, the flow field and turbulent heat conductivity in CO_2 gas are calculated in 3D, and interpolated in a 2D CO_2 model. It is clearly shown how turbulence can directly affect the CO_2 dissociation rate and therefore, reactor efficiency.

Chapter VI extends the study into the experimental field. A new, promising candidate for plasma-based CO_2 conversion – the APGD reactor, is put under investigation. A more fundamental approach is taken, with optical emission diagnostics performed by P. Awakowitz and N. Bibinov. The quasi-neutral plasma model developed within this thesis is compared with the experimental results, showing excellent agreement for the gas temperature.

This model validation paves the way for further simulations, carried out in Chapter VII, where model-based reactor modifications for the APGD are explored. A high conversion ability is achieved, with 50% improvement with respect to the basic APGD design and to the reverse-vortex flow gliding arc plasmatron discussed in Chapter 5. Furthermore, the plasma chemistry is analysed in detail by means of a CO_2 plasma model. This Chapter thus shows the capabilities of model-based reactor engineering for plasma-based CO_2 conversion.

Chapter VIII is the pinnacle of this thesis. Bridging the obtained knowledge, a novel dual-vortex plasmatron is designed and engineered from scratch, and subsequently tested in practice. First data from the experiments show convincing values with conversion in the range of 6-9.5% and energy efficiency of up to 41%. However, more tests with a more capable power supply will be needed to further improve its performance and reliability.

Finally, Chapter IX discusses some issues and provides guidelines for high-voltage power supplies for DC (gliding arc) discharges. The problems are discussed with some case examples of the group PLASMANT.

In short, the most important outcomes of this work can be summarized as follows:

- 3D modelling of atmospheric pressure plasmas is within reach for common computational tools and methods. The 3D argon plasma model is in good agreement with experiments from literature.
- The reverse-vortex flow is an elegant method for plasma stabilization, and an efficiency boost for gas conversion in gliding arc discharges.
- The turbulent heat flux effect is crucial for determining the gas temperature in a plasma subject to turbulence, and therefore also for the plasma chemistry.
- The CO_2 plasma modelling of the reverse-vortex flow gliding arc plasmatron reactor reveals a high gas temperature, and mostly thermal CO_2 dissociation. Turbulent heat flux enhancement might improve the performance, in terms of either reducing the gas temperature, thus creating more non-equilibrium conditions between vibrational and gas temperature, or enhancing the fraction of gas passing through the arc plasma, or a combination of both.
- The APGD reactor demonstrates a better overall performance in CO_2 conversion in comparison with GA, with less strain on the power supply.
- The confined APGD reactor has higher conversion ability than the basic APGD design, but clearly demonstrates the need for plasma insulation from the walls.
- A set of modelling methods was developed, allowing for model-based reactor engineering.
- A novel dual-vortex GA reactor was developed from scratch, showing promising first results for CO_2 conversion.

Perspectives and future outlook

Plasma modelling has a lot to offer, not only to researchers in the field, but also to fluid analysts, particle physicists, chemical engineers and many others. As it entangles several scientific fields in a unique way, its solutions break ground for many further advancements.

Although the models presented in this thesis are suffering from long computation times, a newer generation of computers will allow the use of finer spatial and time discretisation, which will offer an even more in-depth analysis of the processes in plasma. For instance, the influence of small-scale turbulence effects might then be studied in greater detail, and averaging turbulence models might be replaced by the LES and DNS methods. Furthermore, chemistry sets of higher complexity might be used. The flexibility of COMSOL or equivalent software might be used to add cathode spot effects, plasma-electrode interactions, and many other effects. More specifically, studies on plasma-based gas conversion might be extended significantly, especially in the time domain, where the time-dependant performance of a plasma reactor might be simulated precisely.

For a more direct evaluation of the reactor conversion performance, particle tracing can be used, as it was already mentioned in the conclusion of Chapter V. This method has already been developed and successfully applied in the Master thesis by Matthijs Lasure at the University of Antwerp [158].

Samenvatting

Samenvatting

Het doel van een rekenmodel is niet louter om de resultaten van een experiment te repliceren – elk lineair systeem kan namelijk aangepast worden om dit te doen. In plaats daarvan, combineert een rekenmodel de gekende fysieke basisrelaties in een groter bewustzijn van gecompliceerde processen. Zodoende, is hun doel om het parametrische bereik uit te breiden, om het domein van de observatie uit te breiden, en om de ingewikkelde details te vormen die een gewone experimentele meting kan missen.

In deze thesis, de fundamentele kennis van de vloeistofdynamiek, elektrodynamica, deeltjesfysica en chemie is gecombineerd in een breder beeld van plasmamodelering. Hoewel het niet naadloos is, biedt deze samenvoeging interessante inzichten, niet alleen van de gegeven fysieke verschijnselen, maar ook van wat mogelijk is door middel van simulaties vandaag.

Hoofdstuk I beschrijft beknopt het hoofddoel van dit werk. De klimaatverandering als gevolg van de uitstoot van broeikasgassen is en zal één van de belangrijkste uitdagingen van de 21^{e} eeuw zijn. Op plasma gebaseerde gasconversie, hoewel nog in een vroeg stadium, is misschien een veelbelovend antwoord op deze vraag. Met de toenemende adaptatie van simulatie-gebaseerde engineering/ontwikkelingen, is modellering onmisbaar voor nieuwe, efficiënte Plasma-gebaseerde gasconversiesystemen.

In hoofdstuk II wordt het onderwerp plasmawetenschap, met de nadruk op DC-ontlading, geïntroduceerd. Een overzicht van verschillende plasmabronnen van atmosferische druk wordt weergegeven, met een diepere discussie over de belangrijkste onderwerpen van deze thesis – de DC gloei en vlamboog ontlading.

Hoofdstuk III beschrijft diepgaand de bestaande modelleertechnieken voor plasma en vloeistoffen. Bovendien dient dit deel van de thesis als een compacte plasmamodellering handboek met voorbeelden, afgeleide modellen, en belangrijke literatuur.

In hoofdstuk IV, de op modellen gebaseerde reis naar efficiënte CO_2-omzetting op basis van plasma begint met een van de eerste 3D-modellen van zweefbogen met lage temperatuur in COMSOL. Een nieuw concept wordt verkend: de plasmastabilisatie in de omgekeerde vortexstroom. Omdat het een probleem inherent aan 3D is, wordt een quasi-neutraal model met verminderde chemie ontwikkeld en berekend in een volledige 3D-geometrie. De boogrotatie wordt geobserveerd en de plasmaparameters worden vergeleken met de literatuur, dewelke trouwens een goede overeenkomst vertonen. Het isolatieprincipe van de

omgekeerde vortexstroom wordt in de simulatie getoond, hetgeen de theorie en experimenten bevestigen.

In Hoofdstuk V wordt het 3D-plasmamodel uitgebreid naar de echte 1: 1-geometrie van een echte zweefboog Plasmatron (GAP) met omgekeerde vortexstromingsstabilisatie. Het volledige rotatie- en stabilisatieproces van de plasmaboog wordt waargenomen. Verder wordt een nieuwe modelcomplicatie geïntroduceerd: de turbulente warmteoverdracht. De berekeningen tonen aan dat er een aanzienlijke hoeveelheid turbulentie is ontwikkeld in de reverse-vortex flow plasmatron, wat leidt tot een intense energieoverdracht. Er wordt aangetoond dat de turbulentie cruciaal is voor de gastemperatuur in het plasma en daarmee het belang van de chemische reacties. Dit effect wordt verder onderzocht in een CO_2-model met complexe chemie. Door gebruik te maken van de flexibiliteit van COMSOL Multiphysics, worden het stromingsveld en de turbulente warmtegeleidbaarheid in CO_2-gas berekend in 3D en geïnterpoleerd in een 2D CO_2-model. Er wordt duidelijk aangetoond hoe turbulentie de CO_2-dissociatiesnelheid en daardoor de efficiëntie van de reactor rechtstreeks kan beïnvloeden.

Hoofdstuk VI breidt het onderzoek uit naar het experimentele veld. Er wordt een nieuwe, veelbelovende kandidaat voor plasma-gebaseerde CO_2-conversie, meer bepaald de APGD-reactor, onderzocht. Hier volgen we een meer fundamentele benadering, met optische emissiediagnostiek uitgevoerd door P. Awakowitz en N. Bibinov. Het quasi-neutrale plasmamodel, ontwikkeld in dit proefschrift wordt vergeleken met de experimentele resultaten. Deze vergelijking toont een uitstekende overeenkomst voor de gastemperatuur.

Deze modelvalidatie baant de weg voor verdere simulaties, uitgevoerd in Hoofdstuk VII, waar model-gebaseerde reactoraanpassingen voor de APGD worden onderzocht. Een hoge conversiecapaciteit wordt bereikt, met een verbetering van 50% ten opzichte van het basisontwerp van APGD en de omgekeerde vortex zweefboog plasmatron besproken in hoofdstuk 5. Bovendien wordt de plasmachemie in detail geanalyseerd met behulp van een CO_2-plasmamodel. Dit hoofdstuk toont dus de mogelijkheden van modelgebaseerde reactortechnologie voor CO_2-omzetting op basis van plasma.

Hoofdstuk VIII is het hoogtepunt van dit proefschrift. Het overbrugt de verkregen kennis. Een nieuwe dual-vortex plasmatron is helemaal opnieuw ontworpen, ontwikkeld en vervolgens in de praktijk getest. Eerste gegevens van de experimenten tonen overtuigende waarden met conversie in het bereik van

6-9% en energie-efficiëntie tot 41% . Er zijn echter meer tests nodig om de prestaties verder te verbeteren in de toekomst.

Ten slotte bespreekt hoofdstuk IX enkele problemen en biedt het richtlijnen voor hoogspanningsvoedingen voor DC-ontladingen (glijvonken). De problemen worden besproken met enkele voorbeelden uit de PLASMANT-groep.

Kortom, de belangrijkste resultaten van dit werk kunnen als volgt worden samengevat:

- 3D-modellering van atmosferische druk plasma's is binnen handbereik voor algemene computationele hulpmiddelen en methoden. Het 3D-argon-plasmamodel is in goede overeenstemming met experimenten uit de literatuur.
- De omgekeerde vortexstroom is een elegante methode voor plasmastabilisatie en een efficiëntieverhoging voor gasomzetting bij zweefboogontladingen.
- Het turbulente warmtefluxeffect is cruciaal voor het bepalen van de gastemperatuur in een plasma dat onderhevig is aan turbulentie, en daarom ook voor de plasmachemie.
- De CO_2-plasmamodellering van de reverse-vortex flow gliding arc plasmatron reactor onthult een hoge gastemperatuur en meestal thermische CO_2-dissociatie. Turbulente warmtefluxversterking zou de prestaties kunnen verbeteren, in termen van hetzij verlaging van de gastemperatuur, waardoor meer niet-evenwichtsomstandigheden worden gecreëerd tussen vibratie- en gastemperatuur, of het verbeteren van de fractie gas die door het boogplasma gaat, of een combinatie van beide.
- De APGD-reactor laat een betere algehele prestatie zien in CO_2-conversie in vergelijking met de reverse-vortex GA, met minder belasting van de voeding.
- De ingesloten APGD-reactor heeft een hoger conversievermogen dan het basis APGD-ontwerp, maar toont duidelijk de noodzaak aan voor plasma-isolatie van de wanden.
- Er is een set modelleringsmethoden ontwikkeld, die modelgebaseerde reactortechniek mogelijk maakt.
- Een nieuwe dual-vortex GA-reactor werd vanaf nul ontwikkeld, met veelbelovende eerste resultaten voor CO_2-omzetting.

Curriculum vitae

Personal details

Name: Georgi Lazarov Trenchev
Date and place of birth: 9th May 1990, Bansko, Bulgaria
E-mail: georgi.trenchev@uantwerpen.be ; gltrenchev@abv.bg

Education

2014 - present: PhD candidate at the University of Antwerp, Chemistry Department, PLASMANT research group, supervisor: prof. Annemie Bogaerts

2013 - 2014: MSc Communications and Physical Electronics, Faculty of Physics, Sofia University "St. Kliment Ohridski"

2009 - 2013: BSc Engineering Physics, Faculty of Physics, Sofia University "St. Kliment Ohridski"

Grants and awards

2015: Research Foundation Flanders (FWO) PhD Fellowship
2012: Texas Instruments Analog Design Contest – TOP 20 award

Research interests

Plasma Physics, Fluid Dynamics, Electronics, Applied Electrodynamics

Supervised students

2019: Matthijs Lasure, MS Chemistry, University of Antwerp
Thesis: Turbulence improvement of a reverse vortex flow gliding arc reactor for CO_2 conversion

List of publications

As first author

1. G Trenchev, A. Bogaerts, Dual-vortex plasmatron: a novel plasma reactor for gas conversion applications, *in preparation*

2. G. Trenchev, A. Nikiforov, W. Wang, St. Kolev and A. Bogaerts, Atmospheric pressure glow discharge for CO_2 conversion: Model-based exploration of the optimum reactor configuration, *Chemical Engineering Journal,* **362**:830-841, 2019

3. G. Trenchev, St. Kolev, W. Wang, M. Ramakers and A. Bogaerts, CO_2 Conversion in a Gliding Arc Plasmatron: Multi-Dimensional Modelling for Improved Efficiency, *J. Phys. Chem. C*, **121**-39, 2017

4. G. Trenchev, St. Kolev and Zh. Kiss'ovski, Modeling a Langmuir probe in atmospheric pressure plasma at different EEDFs, *Plasma Sources Sci. Technol.,* **26**, 055013, 2017

5. G. Trenchev, St. Kolev and A. Bogaerts, A 3D model of a reverse vortex flow gliding arc reactor, *Plasma Sources Sci. Technol.* **25**, 035014, 2016

6. G. Trenchev, Zh. Kiss'ovski, Simulation of Plasma Filled Hemispherical Cavity as Dielectric Resonator Antenna, *Journal of Physics: Conf. Series*, **768**-1, 2016

As co-author

1. T. Paunska, G. Trenchev, A. Bogaerts, St. Kolev, A 2D model of a gliding arc discharge for CO_2 conversion, AIP Conference Proceedings, **2075**:1, 2019

2. A. Bogaerts, R. Snoeckx, G. Trenchev and W. Wang, Modeling for Better Understanding of Plasma-based CO_2 conversion, book chapter in: *Plasma Chemistry and Gas Conversion*, Intech Open, 2018

3. A. Bogaerts, A. Berthelot, S. Heijkers, S Kolev, R. Snoeckx, S. Sun, G Trenchev, K. V. Laer, W. Wang, CO_2 conversion by plasma technology: Insights from modeling the plasma chemistry and plasma reactor design, *Plasma Sources Sci. Technol.*, **26**-6, 2017

4. M. Ramakers, J. A. Medrano, G. Trenchev, F. Gallucci and A. Bogaerts, Revealing the arc dynamics in a Gliding Arc Plasmatron: A better insight to improve CO_2 conversion, *Plasma Sources Sci. Technol.*, **26**-12, 2017

5. M. Ramakers, G. Trenchev, S. Heijkers, W. Wang and A. Bogaerts, Gliding Arc Plasmatron: Providing an Alternative Method for Carbon Dioxide Conversion, *ChemSusChem*, **10**-12, 2642–2652, 2017

6. St. Kolev, S. Sun, G. Trenchev and A. Bogaerts, Quasi-Neutral Modeling of Gliding Arc Plasmas, *Plasma Processes and Polymers*, **14**, 4-5, 2017

List of conference contributions

1. ISPC 24, Naples, Italy, June 2019, Talk: Atmospheric pressure glow discharge for CO_2 conversion: model-based design improvement

2. IWSSPP 8, Kiten, Bulgaria, June 2018, Talk: Atmospheric pressure glow discharge for CO_2 conversion: modelling and experiments

3. VEIT 20, Sozopol, Bulgaria, October 2017, Poster: Model of an atmospheric pressure glow discharge

4. ISPC 23, Montreal, Canada, July 2017, Poster: Modelling a reverse-vortex flow gliding arc plasmatron for CO_2 conversion

5. ESCAMPIG 23, Bratislava, Slovakia, July 2016, Talk: 3D Model of a reverse-vortex gliding arc plasmatron

6. IWSSPP 7, Kiten, Bulgaria, June 2016, Talk: 3D Model of a reverse-vortex gliding arc plasmatron

7. BPS Scientific Meeting, Gent, Belgium, May 2016, Talk: 3D Model of a reverse-vortex flow gliding arc plasmatron

8. ISPC 22, Antwerp, Belgium, July 2015, Poster: Modelling a reverse-vortex flow gliding arc plasma reactor in 3D

9. IWSSPP 2014, Kiten, Bulgaria, June 2014, Poster: Simulation of plasma filled hemispherical cavity as dielectric resonator antenna

Reaction sets for the plasma models used in this work

Table A1. Reaction set for the 3D Ar models

Reaction		Rate coefficient (k)	Ref.
1.	e + Ar → e + Ar	BS	[106]
2.	e + Ar → e + Ar(4s)	BS	[106]
3.	e + Ar(4s) → 2e + Ar^+	BS	[106]
4.	Ar^+ + e + Ar → Ar + Ar	$1.5 \times 10^{-40} \left(\frac{T_g}{300}\right)^{-2.5}$	[159]

BS = Boltzmann solver [107]

Table A2. Reaction set for the 2D Ar models

Reaction		Rate coefficient (k)	Ref.
1.	e + Ar → e + Ar	BS	[106]
2.	e + Ar → e + Ar(4s)	BS	[106]
3.	e + Ar → e + Ar(4p)	BS	[106]
4.	e + Ar → e + Ar(4d)	BS	[106]
5.	e + Ar → 2e + Ar^+	BS	[106]
6.	e + Ar(4s) → e + Ar(4p)	BS	[160]
7.	e + Ar(4s) → 2e + Ar^+	BS	[161]
8.	e + Ar(4p) → 2e + Ar^+	BS	[161]
9.	e + Ar(4s) → e + Ar	BS, DB	[106]
10.	e + Ar(4p) → e + Ar	BS, DB	[106]
11.	e + Ar(4p) → e + Ar(4s)	BS, DB	[160]
12.	Ar^+ + 2e → Ar + e	$8.75 \times 10^{-39} T_e^{-4.5}\ (eV)$	[25]
13.	Ar^+ + e + Ar → Ar + Ar	$1.5 \times 10^{-40} \left(T_g(K)/300\right)^{-2.5}$	[159]
14.	Ar_2^+ + e → Ar^+ + Ar + e	$1.11 \times 10^{-12} exp\left(-\frac{2.94 - 3\left(T_g(eV) - 0.026\right)}{T_e(eV)}\right)$	[162]
15.	Ar_2^+ + e → Ar^+ + Ar(4s)	$1.04 \times 10^{-12} \left(300/T_e(K)\right)^{0.67} \frac{1 - exp\left(-418/T_g(K)\right)}{1 - 0.31 exp\left(-418/T_g(K)\right)}$	[163], [164]
16.	Ar_2^* + e → Ar_2^+ + 2e	$9 \times 10^{-14} \left(T_e(eV)\right)^{0.7} exp\left(-3.66/T_e(eV)\right)$	[165]
17.	Ar_2^* + e → Ar + Ar + e	1×10^{-15}	[165]
18.	Ar(4s) + Ar(4s) → Ar_2^+ + e	$\frac{1}{2} 6.3 \times 10^{-16} \left(T_g(K)/300\right)^{0.5}$	[166]
19.	Ar(4s) + Ar(4s) → Ar^+ + Ar + e	$1.62 \times 10^{-16} \left(T_g(K)\right)^{0.5}$	[167]
20.	Ar(4s) + Ar(4p) → Ar^+ + Ar + e	$1.62 \times 10^{-16} \left(T_g(K)\right)^{0.5}$	[167]
21.	Ar(4p) + Ar(4p) → Ar^+ + Ar + e	$1.62 \times 10^{-16} \left(T_g(K)\right)^{0.5}$	[167]
22.	Ar(4p) + Ar → Ar(4s) + Ar	5×10^{-18}	[110]
23.	Ar^+ + 2Ar → Ar_2^+ + Ar	$2.5 \times 10^{-43} \left(T_g(K)/300\right)^{-3/2}$	[110]
24.	Ar_2^+ + Ar → Ar^+ + 2Ar	$\frac{6.06 \times 10^{-12}}{T_g(K)} exp\left(-\frac{1.51 \times 10^4}{T_g(K)}\right)$	[162]

25.	$Ar(4s) + 2Ar \rightarrow Ar_2^+ + Ar$	3.3×10^{-44}	[165]
26.	$Ar(4p) + 2Ar \rightarrow Ar_2^+ + Ar$	2.5×10^{-44}	[110]
27.	$Ar_2^* + Ar_2^* \rightarrow Ar_2^* + 2Ar + e$	$5 \times 10^{-16}\left(T_g(K)/300\right)^{0.5}$	[110]
28.	$Ar_2^* + Ar(4s) \rightarrow Ar_2^+ + Ar + e$	$6 \times 10^{-16}\left(T_g(K)/300\right)^{0.5}$	[110]
29.	$Ar(4s) \rightarrow Ar + h\nu$	$\nu_c(s^{-1}) = g_{eff} \times 3.145 \times 10^8$	[167]
30.	$Ar(4p) \rightarrow Ar(4s) + h\nu$	$\nu_c(s^{-1}) = 4.4 \times 10^7$	[167]
31.	$Ar_2^* \rightarrow 2Ar + h\nu$	$\nu_c(s^{-1}) = 6 \times 10^7$	[165]

The rate coefficients are in ($m^3 \cdot s^{-1}$) or ($m^6 \cdot s^{-1}$) for the two-body and three-body reactions, respectively. DB = detailed balance [168]. $g_{eff} = (1.15/\pi)\left(\lambda_{4s}/(6H)\right)$ where $\lambda_{4s} = 105.7\ nm$ and H is a characteristic dimension of the reactor.

Table A3. Reaction set for the 2D CO_2 models [130]

Process	Reaction	Rate coefficient
Elastic collision[a]	$e + CO_2 \rightarrow e + CO_2$	EEDF
Ionization[a]	$e + CO_2 \rightarrow e + e + CO_2^+$	EEDF
Dissociative attachment[b]	$e + CO_2 \rightarrow O^- + CO$	EEDF
Dissociation[b, d]	$e + CO_2 \rightarrow e + CO + O$	EEDF
Electronic excitation[a]	$e + CO_2 \rightarrow e + CO_2e1$	EEDF
Vibrational excitation	$e + CO_2 \rightarrow e + CO_2v_a$	EEDF
Vibrational excitation	$e + CO_2 \rightarrow e + CO_2v_b$	EEDF
Vibrational excitation	$e + CO_2 \rightarrow e + CO_2v_c$	EEDF
Vibrational excitation	$e + CO_2 \rightarrow e + CO_2v_d$	EEDF
Vibrational excitation	$e + CO_2 \rightarrow e + CO_2v_i$ (i = 1-21)	EEDF
Elastic collision	$e + CO \rightarrow e + CO$	EEDF
Dissociation	$e + CO \rightarrow e + C + O$	EEDF
Dissociative attachment	$e + CO \rightarrow C + O^-$	EEDF
Elastic collision[a]	$e + O_2 \rightarrow e + O_2$	EEDF
Dissociation[b]	$e + O_2 \rightarrow e + O + O$	EEDF
Ionization[a]	$e + O_2 \rightarrow e + e + O_2^+$	EEDF
Dissociative attachment[b]	$e + O_2 \rightarrow O + O^-$	EEDF
Attachment[a]	$e + O_2 + M \rightarrow M + O_2^-$	EEDF
Vibrational excitation	$e + O_2 \rightarrow e + O_2v_{1,2,3}$	EEDF
Attachment	$e + O + M \rightarrow M + O^-$	1×10^{-31}
Electron–ion recombination	$e + CO_2^+ \rightarrow CO + O$	$2 \times 10^{-5}{T_e}^{-0.5}/T_g$
Electron–ion recombination	$e + CO_2^+ \rightarrow C + O_2$	$3.94 \times 10^{-7}{T_e}^{-0.4}$
Electron–ion recombination	$e + O_2^+ + M \rightarrow O_2 + M$	1×10^{-26}
Electron–ion recombination	$e + O_2^+ \rightarrow O + O$	$6 \times 10^{-7}{T_e}^{-0.5}{T_g}^{-0.5}$

[a]Same cross section used for reactions of CO_2v_i, and idem for O_2v_i.

[b]Cross section also used for reactions of CO_2vi, and for O_2v_i, but modified by lowering the energy threshold by the excited state energy.

[c]Cross section also used for reactions of CO_2vi, but scaled and shifted in energy using Fridman's approximation [19].

[d]Dissociation through electron impact excitation with 7.0 eV threshold.

Process	Reaction	Rate coefficient
Recombination	$O^- + CO_2 + M \rightarrow CO_3^- + M$	9.0×10^{-29}
Electron detachment	$O^- + CO \rightarrow CO_2 + e$	5.5×10^{-10}
Electron detachment	$CO_3^- + CO \rightarrow 2CO_2 + e$	5.0×10^{-13}
Recombination	$CO_3^- + CO_2^+ \rightarrow 2CO_2 + O$	5.0×10^{-7}
Electron detachment	$O^- + M \rightarrow e + O + M$	4.0×10^{-12}
Electron detachment	$O^- + O \rightarrow e + O_2$	2.3×10^{-10}
Charge transfer	$O_2^- + O \rightarrow O^- + O_2$	3.3×10^{-10}
Electron detachment	$O_2^- + O_2 \rightarrow O_2 + O_2 + e$	2.18×10^{-18}
Electron detachment	$O_2^- + M \rightarrow O_2 + M + e$	$2.70 \times 10^{-10}(T_g/300)^{0.5}\exp(-5590/T_g)$
Charge transfer	$O + CO_3^- \rightarrow CO_2 + O_2^-$	8.0×10^{-11}
Recombination	$O_2^- + CO_2^+ \rightarrow CO + O_2 + O$	6.0×10^{-7}
Charge transfer	$O_2 + CO_2^+ \rightarrow CO_2 + O_2^+$	5.3×10^{-11}
Charge transfer	$O + CO_2^+ \rightarrow CO + O_2^+$	1.64×10^{-10}
Recombination	$O_2^+ + CO_3^- \rightarrow CO_2 + O_2 + O$	3.0×10^{-7}
Recombination	$O_2^+ + O_2^- \rightarrow O_2 + O_2$	2.0×10^{-7}
Recombination	$O_2^+ + O_2^- \rightarrow O_2 + O + O$	4.2×10^{-7}
Recombination	$O_2^+ + O_2^- + M \rightarrow O_2 + O_2 + M$	2.0×10^{-25}
Recombination	$O_2^+ + O^- \rightarrow O_2 + O$	1.0×10^{-7}
Recombination	$O_2^+ + O_2^- \rightarrow O_2 + O + O$	2.6×10^{-8}

M represents any neutral species taken into account in the model. The same rate coefficient is used for every species. The rate coefficients are in ($cm^3 \cdot s^{-1}$) or ($cm^6 \cdot s^{-1}$) for the two-body and three-body reactions, respectively.

Process	Reaction	Rate coefficient
VT relax[a]	$CO_2v_{a,\,b,\,c,\,d} + M \rightarrow CO_2 + M$	$7.14 \times 10^{-8} exp\left(-177/T_g^{-1/3} + 451/T_g^{-2/3}\right)$
VT relax[a, b]	$CO_2v_1 + M \rightarrow CO_2v_a + M$	$0.43 exp\left(-407/T_g^{-1/3} + 824/T_g^{-2/3}\right)$
VT relax[, b]	$CO_2v_1 + M \rightarrow CO_2v_b + M$	$0.86 exp\left(-404/T_g^{-1/3} + 1096/T_g^{-2/3}\right)$
VT relax[a, b]	$CO_2v_1 + M \rightarrow CO_2v_c + M$	$1.43 \times 10^{-5} exp\left(-252/T_g^{-1/3} + 685/T_g^{-2/3}\right)$
VV relax	$CO_2v_i + CO_2 \rightarrow CO_2v_{i-1} + CO_2v_{a,\,b}$ *(i ≥ 2)*	$2.13 \times 10^{-5} exp\left(-242/T_g^{-1/3} + 633/T_g^{-2/3}\right)$
VV relax[c]	$CO_2v_i + CO_2v_j \rightarrow CO_2v_{i-1} + CO_2v_{j+1}$ *(20 ≥ j ≥ 0), (21 ≥ i ≥ 1)*	$1.80 \times 10^{-11} exp\left(24.7/T_g^{-\frac{1}{3}} - 65.7/T_g^{-2/3}\right)$
VV relax[a, c]	$O_2v_i + M \rightarrow O_2v_{i-1} + M$, *(i = 1, 2, 3)*	$7.99 \times 10^{-5} exp\left(-320/T_g^{-1/3} + 615/T_g^{-2/3}\right)$

[a]*M* represents any neutral species taken into account in the model. The same rate coefficient is used for every species.

[b]These reactions are also taken into account for v_i (i > 1), but then they are not considered separately, and the rate coefficient is then taken as the sum of (i), (ii) and (iii), leading to level $CO2v_{i-1}$, because for the higher levels, no individual symmetric mode levels are included in the model. See Kozák and Bogaerts [111] for more information.

[c]v_0 means the ground state of CO_2 or O_2. The rate coefficients are in ($cm^3 \cdot s^{-1}$) and T_g is in K. The rate coefficients are given for the reaction between ground state and first vibrational level, and they are scaled for the higher transitions.

VT: Vibrational – Translational; VV: Vibrational – Vibrational

Process	**Reaction**	**Rate coefficient**
Neutral reaction	$CO_2 + M \rightarrow CO + O + M$	$4.39 \times 10^{-7}\exp(-65000/T_g)$
Neutral reaction	$CO_2 + O \rightarrow CO + O_2$	$7.77 \times 10^{-12}\exp(-16600/T_g)$
Neutral reaction	$CO + O + M \rightarrow CO_2 + M$	$8.20 \times 10^{-34}\exp(-1560/T_g)$
Neutral reaction	$CO + O_2 \rightarrow CO_2 + M$	$1.28 \times 10^{-12}\exp(-12800/T_g)$
Neutral reaction	$CO_2 + C \rightarrow CO + CO$	1.00×10^{-15}
Neutral reaction	$O_2 + C \rightarrow CO + O$	3.00×10^{-11}
Neutral reaction	$CO + M \rightarrow C + O + M$	$1.52 \times 10^{-4}\exp(T_g/298)^{-3.1}\exp(-12800/T_g)$
Neutral reaction	$C + O + M \rightarrow CO + M$	$2.14 \times 10^{-29}\exp(T_g/300)^{-3.08}\exp(-2114/T_g)$
Neutral reaction	$O + O + M \rightarrow O2 + M$	$1.27 \times 10^{-32}\exp(T_g/300)^{-1}\exp(-170/T_g)$

The rate coefficients are in ($cm^3 \cdot s^{-1}$) or ($cm^6 \cdot s^{-1}$) for the two-body and three-body reactions, respectively. T_g is in K. Reaction set based on [130] and [144].

References

[1] G. Clark, "The Industrial Revolution," in *Handbook of Economic Growth*, vol. **2**, North Holland, 2014, pp. 217–262.

[2] G. Marland, T. A. Boden, and R. J. Andres, *Global, Regional, and National CO_2 Emissions. In Trends: A Compendium of Data on Global Change*. 2005.

[3] Y. Sampei and M. Aoyagi-Usui, "Mass-media coverage, its influence on public awareness of climate-change issues, and implications for Japan's national campaign to reduce greenhouse gas emissions," *Glob. Environ. Chang.*, vol. **19**, p. 203, 2009.

[4] European commision, "2020 Climate and Energy Package," *European Commision.eu*, 2016. [Online]. Available: http://ec.europa.eu/clima/policies/strategies/2020_en.

[5] J. Khan and M. H. Arsalan, "Solar power technologies for sustainable electricity generation - A review," *Renew. Sustain. Energy Rev.*, vol. **55**, pp. 414–425, 2016.

[6] M. E. Khodayar, S. D. Manshadi, H. Wu, and J. Lin, "Multiple Period Ramping Processes in Day-Ahead Electricity Markets," *IEEE Trans. Sustain. Energy*, vol. **7**, no. 4, pp. 1634–1645, 2016.

[7] D. O. Akinyele and R. K. Rayudu, "Review of energy storage technologies for sustainable power networks," *Sustain. Energy Technol. Assessments*, vol. **8**, pp. 74–91, 2014.

[8] G. Ning and B. Popov, "Cycle Life Modeling of Lithium-Ion Batteries," *J. Electrochem. Soc.*, vol. **151**, p. A1584, 2004.

[9] Panasonic, "Overview of lithium ion batteries." 2011.

[10] B. E. Conway, *Electrochemical Supercapacitors*, 1st ed. Springer-Verlag Berlin Heidelberg, 1999.

[11] S. D. Garvey and A. Pimm, "Compressed Air Energy Storage," in *Storing Energy: With Special Reference to Renewable Energy Sources*, 2016.

[12] B. Kantharaj, S. Garvey, and A. Pimm, "Compressed air energy storage with liquid air capacity extension," *Appl. Energy*, vol. **157**, pp. 152–164, 2015.

[13] S. Rehman, L. M. Al-Hadhrami, and M. M. Alam, "Pumped hydro energy storage system: A technological review," *Renew. Sustain. Energy Rev.*, vol. **44**, pp. 586–598, 2015.

[14] B. Steffen, "Prospects for pumped-hydro storage in Germany," *Energy Policy*, 2012.

[15] B. Bolund, H. Bernhoff, and M. Leijon, "Flywheel energy and power storage systems," *Renew. Sustain. Energy Rev.*, vol. **11**, no. 2, pp. 235–258, 2007.

[16] M. W. Chase, *NIST-JANAF Thermochemical Tables*, 4th ed. Washington, US: American Institute of Physics, 1998.

[17] R. Snoeckx and A. Bogaerts, "Plasma technology-a novel solution for CO_2 conversion?," *Chem. Soc. Rev.*, vol. **46**, no. 19, pp. 5805–5863, 2017.

[18] A. Bogaerts, T. Kozák, K. Van Laer, and R. Snoeckx, "Plasma-based conversion of CO2: Current status and future challenges," *Faraday Discuss.*, vol. **183**, pp. 217–232, 2015.

[19] A. Fridman, *Plasma chemistry*, 1st ed., vol. **1**. New York: Cambridge University

Press, 2008.
[20] R. I. Asisov, A. A. Fridman, V. K. Jivotov, E. G. Krasheninnikov, B. I. Patrushev, B. V. Potapkin, "Conference contribution," in *5th International Symposium on Plasma Chemistry*, 1983, vol. **1**, p. 52.
[21] R. J. Azizov *et al.*, "The nonequilibrium plasmachemical process of decomposition of CO_2 in a supersonic SHF discharge," *Sov. Phys. Dokl.*, vol. **28**, pp. 567–569, 1983.
[22] S. C. Roy, O. K. Varghese, M. Paulose, and C. A. Grimes, "Toward solar fuels: Photocatalytic conversion of carbon dioxide to hydrocarbons," *ACS Nano*, vol. **4**, no. 3, pp. 1259–1278, 2010.
[23] T. Estermann, M. Newborough, and M. Sterner, "Power-to-gas systems for absorbing excess solar power in electricity distribution networks," *Int. J. Hydrogen Energy*, vol. **41**, no. 32, pp. 13950–13959, 2016.
[24] M. E. Dry, "The Fischer-Tropsch process: 1950-2000," *Catal. Today*, vol. **71**, no. 3–4, pp. 227–241, 2002.
[25] Y. Raizer, *Gas Discharge Physics*. Berlin, Germany: Springer-Verlag Berlin Heidelberg, 1991.
[26] H. Fritz, "Das Polarlicht," vol. **1**, no. 1, p. 1, 1881.
[27] S. Eliezer and Y. Eliezer, *The Fourth State of Matter: An Introduction to Plasma Science*, 2nd ed. Bristol and Philadelphia: CRC Press, 2001.
[28] M. Madau, "Edited version of Image:Lightning over Oradea Romania 2.jpg., Public Domain." [Online]. Available: https://commons.wikimedia.org/w/index.php?curid=5322846.
[29] J. Strang, "The Aurora Borealis, or Northern Lights, shines above Bear Lake," 2005. [Online]. Available: https://commons.wikimedia.org/wiki/File:Aurora_Borealis_and_Australis_Poster.jpg#/media/File:Polarlicht_2.jpg.
[30] ESA, "Large and small stars in harmonious coexistence," *heic0607a*, 2006. [Online]. Available: https://www.spacetelescope.org/images/heic0607a/.
[31] F. Massines, N. Gherardi, N. Naudé, and P. Ségur, "Glow and Townsend dielectric barrier discharge in various atmosphere," *Plasma Phys. Control. Fusion*, vol. **47**, no. 12 B, p. B577, 2005.
[32] L. Tonks and I. Langmuir, "A general theory of the plasma of an arc," *Phys. Rev.*, vol. **34**, no. 6, pp. 876–922, 1929.
[33] U. Kogelschatz, "Atmospheric-pressure plasma technology," *Plasma Phys. Control. Fusion*, vol. **46**, no. 12 B, p. 006, 2004.
[34] S. K. Pankaj *et al.*, "Applications of cold plasma technology in food packaging," *Trends Food Sci. Technol.*, vol. **35**, no. 1, pp. 5–17, 2014.
[35] M. G. Kong *et al.*, "Plasma medicine: An introductory review," *New J. Phys.*, vol. **11**, p. 115012, 2009.
[36] N. N. Misra, O. Schlüter, and P. J. Cullen, "Plasma in Food and Agriculture," in *Cold Plasma in Food and Agriculture: Fundamentals and Applications*, Academic Press, 2016, pp. 1–16.
[37] C. Llewellyn Smith and D. Ward, "Fusion," *Energy Policy*, vol. **36**, no. 12, pp. 4331–4334, 2008.
[38] M. H. Anderson, J. R. Ensher, M. R. Matthews, C. E. Wieman, and E. A.

Cornell, “Observation of Bose-Einstein condensation in a dilute atomic vapor,” *Science (80-.).*, vol. **269**, no. 5221, pp. 198–201, 1995.

[39] H. Bohr and H. B. Nielsen, “Hadron production from a boiling quark soup. A thermodynamical quark model predicting particle ratios in hadronic collisions,” *Nucl. Physics, Sect. B*, vol. **128**, no. 2, pp. 275–293, 1977.

[40] H. S. Uhm, Y. C. Hong, and D. H. Shin, “A microwave plasma torch and its applications,” *Plasma Sources Sci. Technol.*, vol. **15**, no. 2, 2006.

[41] Y. A. Lebedev, “Microwave discharges: generation and diagnostics,” *J. Phys. Conf. Ser.*, vol. **257**, p. 012016, 2010.

[42] V. A. F. N. Kniseley, “Inductively coupled plasmas,” *Anal. Chem.*, vol. **46**, no. 13, p. 1155A, 1974.

[43] R. Rezaaiyaan, G. M. Hieftje, H. Anderson, H. Kaiser, and B. Meddings, “Design and Construction of a Low-Flow, Low-Power Torch for Inductively Coupled Plasma Spectrometry,” *Appl. Spectrosc.*, vol. **36**, pp. 627–631, 1982.

[44] H. Jansen, H. Gardeniers, M. de Boer, M. Elwenspoek, and J. Fluitman, “A survey on the reactive ion etching of silicon in microtechnology,” *J. Micromechanics Microengineering*, vol. **6**, no. 1, pp. 14–28, 1996.

[45] U. Kogelschatz, “Dielectric-barrier discharges: Their History, Discharge Physics, and Industrial Applications,” *Plasma Chem. Plasma Process.*, vol. **23**, no. 1, pp. 1–46, 2003.

[46] M. Nagatsu, K. Sugiyama, I. Motrescu, M. Ciolan, A. Ogino, and N. Kawamura, “Surface modification of fluorine contained resins using an elongated parallel plate electrode type dielectric barrier discharge device,” *J. Photopolym. Sci. Technol.*, vol. **31**, no. 3, pp. 379–383, 2018.

[47] A. Bogaerts, E. Neyts, R. Gijbels, and J. Van der Mullen, “Gas discharge plasmas and their applications,” *Spectrochim. Acta - Part B At. Spectrosc.*, vol. **57**, no. 4, pp. 609–658, 2002.

[48] Z. Donkó, P. Hartmann, and K. Kutasi, “On the reliability of low-pressure dc glow discharge modelling,” *Plasma Sources Sci. Technol.*, vol. **15**, no. 2, pp. 178–186, 2006.

[49] S. R. and S. M. Engel A V, “On the glow discharge at high pressure,” *Z. Phys.*, vol. **85**, no. 144, 1933.

[50] D. Staack, B. Farouk, A. Gutsol, and A. Fridman, “DC normal glow discharges in atmospheric pressure atomic and molecular gases,” *Plasma Sources Sci. Technol.*, vol. **17**, no. 2, p. 13, 2008.

[51] M. Laroussi and T. Akan, “Arc-free atmospheric pressure cold plasma jets: A review,” *Plasma Process. Polym.*, vol. **4**, no. 9, pp. 777–788, 2007.

[52] B. L. Sands, B. N. Ganguly, and K. Tachibana, “A streamer-like atmospheric pressure plasma jet,” *Appl. Phys. Lett.*, vol. **92**, no. 15, p. 151503, 2008.

[53] A. Schmidt-Bleker, J. Winter, A. Bösel, S. Reuter, and K. D. Weltmann, “On the plasma chemistry of a cold atmospheric argon plasma jet with shielding gas device,” *Plasma Sources Sci. Technol.*, vol. **25**, no. 1, p. 015005, 2015.

[54] A. Bogaerts and R. Gijbels, “Mathematical description of a direct current glow discharge in argon,” University of Antwerp, 1996.

[55] E. L. Murphy and R. H. Good, “Thermionic Emission, Field Emission, and the Transition Region,” *Phys. Rev.*, vol. **102**, no. 6, pp. 1464–1473, 1956.

[56] T. Ohji and T. W. Eagar, “Infrared radiation from an arc plasma and its application to plasma diagnostics,” *Plasma Chem. Plasma Process.*, vol. **12**, no. 4, pp. 403–419, 1992.
[57] R. Pothiraja, N. Bibinov, and P. Awakowicz, “Pulsed corona plasma source characterization for film deposition on the inner surface of tubes,” *J. Phys. D. Appl. Phys.*, vol. **43**, no. 49, p. 495201, 2010.
[58] A. Bogaerts *et al.*, “CO_2 conversion by plasma technology: Insights from modeling the plasma chemistry and plasma reactor design,” *Plasma Sources Sci. Technol.*, vol. **26**, no. 6, 2017.
[59] M. Ramakers, G. Trenchev, S. Heijkers, W. Wang, and A. Bogaerts, “Gliding Arc Plasmatron: Providing an Alternative Method for Carbon Dioxide Conversion,” *ChemSusChem*, vol. **10**, no. 12, 2017.
[60] G. Trenchev, A. Nikiforov, W. Wang, S. Kolev, and A. Bogaerts, “Atmospheric pressure glow discharge for CO_2 conversion: Model-based exploration of the optimum reactor configuration,” *Chem. Eng. J.*, vol. **362**, pp. 830–841, 2019.
[61] T. Kozák and A. Bogaerts, “Evaluation of the energy efficiency of CO_2 conversion in microwave discharges using a reaction kinetics model,” *Plasma Sources Sci. Technol.*, vol. **24**, no. 1, p. 015024, 2015.
[62] W. Bongers *et al.*, “Plasma-driven dissociation of CO_2 for fuel synthesis,” *Plasma Process. Polym.*, vol. **14**, no. 6, p. 126, 2017.
[63] Y. Uytdenhouwen, S. Van Alphen, I. Michielsen, V. Meynen, P. Cool, and A. Bogaerts, “A packed-bed DBD micro plasma reactor for CO_2 dissociation: Does size matter?,” *Chem. Eng. J.*, vol. **348**, p. 557, 2018.
[64] T. Nunnally, K. Gutsol, A. Rabinovich, A. Fridman, A. Gutsol, and A. Kemoun, “Dissociation of CO_2 in a low current gliding arc plasmatron,” *J. Phys. D. Appl. Phys.*, vol. **44**, no. 27, p. 274009, 2011.
[65] S. Heijkers, L. M. Martini, G. Dilecce, P. Tosi, and A. Bogaerts, “Nanosecond Pulsed Discharge for CO_2 Conversion: Kinetic Modeling to Elucidate the Chemistry and Improve the Performance,” *J. Phys. Chem. C*, vol. **123**, no. 19, pp. 12104–12116, 2019.
[66] S. Gröger *et al.*, “Characterization of a nitrogen gliding arc plasmatron using optical emission spectroscopy and high-speed camera,” *J. Phys. D. Appl. Phys.*, vol. **52**, no. 6, p. 1361, 2019.
[67] J. O. Wilkes, “Introduction to COMSOL Multiphysics (Formerly , FEMLAB),” *Manual*, 2009. [Online]. Available: http://cdn.comsol.com/documentation/5.1.0.145/IntroductionToCOMSOLMultiphysics.pdf.
[68] B. R. Hunt, R. L. Lipsman, and J. M. Rosenberg, *A Guide to MATLAB*. Cambridge: Cambridge University Press, 2012.
[69] J. H. Ferziger and M. Perić, *Computational Methods for Fluid Dynamics*, 3rd ed. Berlin: Springer, 2012.
[70] B. Kirby and B. Kirby, “Stokes Flow,” in *Micro- and Nanoscale Fluid Mechanics*, Cambridge: Cambridge University Press, 2012, pp. 178–198.
[71] O. C. & User:Kraaiennest, “Flow patterns around a sphere at very low Reynolds numbers,” 2014. [Online]. Available: https://commons.wikimedia.org/wiki/File:Flow_patterns_around_a_sphere_at_v

ery_low_Reynolds_numbers.svg.
[72] C. R. Doering, “The 3D Navier-Stokes Problem,” *Annu. Rev. Fluid Mech.*, vol. **41**, no. 1, pp. 109–128, 2009.
[73] S. H. Hollingdale and H. H. Goldstine, *The Computer from Pascal to von Neumann*, vol. **57**, no. 401. US: Princeton University Press, 2007.
[74] J. L. Hess and A. M. O. Smith, “Calculation of potential flow about arbitrary bodies,” *Prog. Aerosp. Sci.*, vol. **8**, no. C, pp. 1–138, 1967.
[75] D. B. Jack Steehler, “Understanding Moore’s law: four decades of innovation,” *Choice Rev. Online*, vol. **44**, no. 11, pp. 44-6278-44–6278, 2013.
[76] R. C. and L. ERICKSON, “PAN AIR - A higher order panel method for predicting subsonic or supersonic linear potential flows about arbitrary configurations,” in *14th Fluid and Plasma Dynamics Conference*, 1981, p. 1255.
[77] H. YOUNGREN, E. BOUCHARD, R. COOPERSMITH, and L. MIRANDA, “Comparison of panel method formulations and its influence on the development of QUADPAN, an advanced low-order method,” in *Applied Aerodynamics Conference*, 2013, p. 1827.
[78] D. L. Ashby, “Potential Flow Theory and Operation Guzde for the Panel Code PMARC,” *NASA Technical Memorandum*. 1991.
[79] A. Placzek, A.; Sigrist, J.-F.; Hamdouni, “Numerical simulation of an oscillating cylinder in a cross-flow at low Reynolds number: Forced and free oscillations,” *Comput. Fluids*, vol. **38**, pp. 80–100, 2009.
[80] M. D. F. Moukalled , L. Mangani, *The Finite Volume Method in Computational Fluid Dynamics: An Advanced Introduction with OpenFOAM® and Matlab (Fluid Mechanics and Its Applications)*, 1st ed. Berlin, Germany: Springer, 2015.
[81] O. C. Zienkiewicz and R. L. Taylor, *The finite element method. Fifth edition*, 5th ed., vol. **79**, no. 2. Butterworth-Heinemann, 2002.
[82] Inc. ANSYS, “ANSYS FLUENT Theory Guide,” *Release 18.2*, 2013.
[83] OpenFOAM, “OpenFOAM - The Open Source CFD Toolbox - User Guide,” 2014.
[84] S. W. Van Haren, “Testing DNS capability of OpenFOAM and STAR-CCM + (MSc Thesis),” Delft University of Technology, 2011.
[85] “SIMSCALE,” *Simulation software reinvented for the web*. [Online]. Available: https://www.simscale.com.
[86] Autodesk, “Autodesk Inventor.” [Online]. Available: https://www.autodesk.com/products/inventor/overview.
[87] S. Chen and G. D. Doolen, “Lattice Boltzmann Method for Fluid Flows,” *Annu. Rev. Fluid Mech.*, vol. **30**, no. 1, pp. 329–364, 2002.
[88] C. Groton, “PCU Virginia (SSN 774) returns to the General Dynamics Electric Boat shipyard,” 2004. [Online]. Available: https://en.wikipedia.org/wiki/Virginia-class_submarine#/media/File:US_Navy_040730-N-1234E-002_PCU_Virginia_(SSN_774)_returns_to_the_General_Dynamics_Electric_Boat_shipyard.jpg.
[89] A. J. Smits, B. J. McKeon, and I. Marusic, “High–Reynolds Number Wall Turbulence,” *Annu. Rev. Fluid Mech.*, vol. **43**, no. 1, pp. 353–375, 2011.

[90] A. N. Kolmogorov, “A refinement of previous hypotheses concerning the local structure of turbulence in a viscous incompressible fluid at high Reynolds number,” *J. Fluid Mech.*, vol. **13**, no. 1, pp. 82–85, 1962.
[91] D. Nagel, “Stanford U Solves Fluid Dynamics Problem with 1.5 Million-Core Supercomputer,” 2013. [Online]. Available: https://campustechnology.com/articles/2013/01/29/stanford-u-solves-fluid-dynamics-problem-with-1.5-million-core-supercomputer.aspx.
[92] W. Rodi, “Comparison of LES and RANS calculations of the flow around bluff bodies,” *J. Wind Eng. Ind. Aerodyn.*, vol. **69**–**71**, pp. 55–75, 1997.
[93] B. Mohammadi and O. Pironneau, *Analysis of the K-Epsilon Turbulence Model*, 1st ed. New York: Wiley, 1994.
[94] F. Menter, M. Kuntz, and R. Langtry, “Ten Years of Industrial Experience with the SST Turbulence Model,” *Heat Mass Transf.*, vol. **4**, p. 625, 2003.
[95] P. Sagaut, *Large Eddy Simulation for Incompressible Flows – An Introduction*, vol. **73**, no. 5. Berlin: Springer-Verlag Berlin Heidelberg, 2001.
[96] B. Weigand, J. R. Ferguson, and M. E. Crawford, “An extended Kays and Crawford turbulent Prandtl number model,” *Int. J. Heat Mass Transf.*, vol. **40**, no. 17, pp. 4191–4196, 1997.
[97] S. Pancheshnyi, B. Eismann, G. Hagelaar, and L. Pitchford, “ZDPlasKin: a new tool for plasmachemical simulations,” in *The 11th International Symposium on High pressure, Low Temperature Plasma Chemistry*, 2008.
[98] D. Winske, L. Yin, N. Omidi, H. Karimabadi, and K. Quest, “Hybrid Simulation Codes: Past, Present and Future—A Tutorial,” *Sp. Plasma Simul.*, pp. 136–165, 2007.
[99] S. Kolev and A. Bogaerts, “A 2D model for a gliding arc discharge,” *Plasma Sources Sci. Technol.*, vol. **24**, no. 1, p. 015025, 2015.
[100] E. N. Parker, “9. Magnetohydrodynamics,” in *Conversations on Electric and Magnetic Fields in the Cosmos*, 1st ed., US: Princeton University Press, 2019, pp. 92–122.
[101] Y. Zhou, W. H. Matthaeus, and P. Dmitruk, “Colloquium: Magnetohydrodynamic turbulence and time scales in astrophysical and space plasmas,” *Rev. Mod. Phys.*, vol. **76**, no. 4, pp. 1015–1035, 2004.
[102] L. Desvillettes and C. Mouhot, “Stability and uniqueness for the spatially homogeneous boltzmann equation with long-range interactions,” *Arch. Ration. Mech. Anal.*, vol. **193**, no. 2, pp. 227–253, 2009.
[103] D. Fleisch, *A Student’s Guide to Maxwell’s Equations*. Cambridge: Cambridge University Press, 2012.
[104] G. Trenchev, S. Kolev, and Z. Kiss’Ovski, “Modeling a Langmuir probe in atmospheric pressure plasma at different EEDFs,” *Plasma Sources Sci. Technol.*, vol. **26**, no. 5, p. 055013, 2017.
[105] A. Bogaerts, W. Wang, A. Berthelot, and V. Guerra, “Modeling plasma-based CO_2 conversion: Crucial role of the dissociation cross section,” *Plasma Sources Sci. Technol.*, vol. **25**, no. 5, p. 055016, 2016.
[106] L. C. Pitchford *et al.*, “LXCat: an Open-Access, Web-Based Platform for Data Needed for Modeling Low Temperature Plasmas,” *Plasma Process. Polym.*, vol. **14**, no. 1–2, p. 2, 2017.

[107] G. J. M. Hagelaar, “Brief documentation of BOLSIG+ version 07/2015,” 2015. [Online]. Available: http://home.zcu.cz/~kozakt/MPPL/literatura/BolsigDoc0715.pdf. [Accessed: 18-Jul-2019].
[108] D. L. Baulch *et al.*, “Evaluated Kinetic Data for Combustion Modelling,” *J. Phys. Chem. Ref. Data*, vol. **21**, no. 3, pp. 411–734, 1992.
[109] F. Westley, J. T. Herron, and R. J. Cvetanovic, *Compilation of chemical kinetic data for combustion chemistry :* Washington, US: U.S. Department of Commerce, 1987.
[110] S. K. Lam, D. Zheng, A. Lo, A. Dem’yanov, and A. P. Napartovich, “Kinetics of Ar2* in high-pressure pure argon,” *J. Phys. D. Appl. Phys.*, vol. **33**, no. 3, pp. 242–251, 2000.
[111] T. Kozàk and A. Bogaerts, “Splitting of CO_2 by vibrational excitation in non-equilibrium plasmas: A reaction kinetics model,” *Plasma Sources Sci. Technol.*, vol. **23**, no. 4, p. 045004, 2014.
[112] T. Silva *et al.*, “Kinetic study of low-temperature CO_2 plasmas under non-equilibrium conditions. I. Relaxation of vibrational energy,” *Plasma Sources Sci. Technol.*, vol. **27**, no. 1, 2018.
[113] S. Kolev and A. Bogaerts, “Similarities and differences between gliding glow and gliding arc discharges,” *Plasma Sources Sci. Technol.*, vol. **24**, no. 6, p. 065023, 2015.
[114] S. R. Sun, S. Kolev, H. X. Wang, and A. Bogaerts, “Coupled gas flow-plasma model for a gliding arc: Investigations of the back-breakdown phenomenon and its effect on the gliding arc characteristics,” *Plasma Sources Sci. Technol.*, vol. **26**, no. 1, p. 015003, 2017.
[115] W. Wang, D. Mei, X. Tu, and A. Bogaerts, “Gliding arc plasma for CO_2 conversion: Better insights by a combined experimental and modelling approach,” *Chem. Eng. J.*, vol. **330**, pp. 11–25, 2017.
[116] G. Trenchev, S. Kolev, W. Wang, M. Ramakers, and A. Bogaerts, “CO_2 conversion in a gliding Arc plasmatron: Multidimensional modeling for improved efficiency,” *J. Phys. Chem. C*, vol. **121**, no. 39, p. 24470, 2017.
[117] S. Kolev, S. Sun, G. Trenchev, W. Wang, H. Wang, and A. Bogaerts, “Quasi-Neutral Modeling of Gliding Arc Plasmas,” *Plasma Process. Polym.*, vol. **14**, no. 4–5, 2017.
[118] P. Rosenau and E. Türkel, “Ambipolar diffusion in a multi-species medium,” *Phys. Scr.*, vol. **31**, no. 3, pp. 207–209, 1985.
[119] J. D. Ramshaw and C. H. Chang, “Ambipolar diffusion in two-temperature multicomponent plasmas,” *Plasma Chem. Plasma Process.*, vol. **13**, no. 3, pp. 489–498, 1993.
[120] G. Trenchev, S. Kolev, and A. Bogaerts, “A 3D model of a reverse vortex flow gliding arc reactor,” *Plasma Sources Sci. Technol.*, vol. **25**, no. 3, 2016.
[121] A. Gleizes, J. J. Gonzalez, and P. Freton, “Thermal plasma modelling,” *J. Phys. D. Appl. Phys.*, vol. **38**, no. 9, p. R153, 2005.
[122] X. Tu, H. J. Gallon, and J. C. Whitehead, “Electrical and optical diagnostics of atmospheric pressure argon gliding arc plasma jet,” in *30th ICPIG*, 2011.
[123] B. Parent, M. N. Shneider, and S. O. Macheret, “Sheath governing equations in

computational weakly-ionized plasmadynamics," *J. Comput. Phys.*, vol. **232**, no. 1, pp. 234–251, 2013.
[124] A. F. Gutsol, "The Ranque effect," *Uspekhi Fiz. Nauk*, vol. **167**, no. 6, p. 665, 2008.
[125] A. Czernichowski, "Spectral and electrical diagnostics of gliding arc," *Acta Phys. Pol. A*, vol. **89**, no. 5--6, pp. 595–603, 1996.
[126] G. Elaragi, "Discharge Characteristics of Gliding Arc Plasma Reactor With Argon/Nitrogen," *J. Adv. Phys.*, vol. **7**, no. 1, pp. 1316–1323, 2015.
[127] A. Gutsol and J. A. Bakken, "A new vortex method of plasma insulation and explanation of the Ranque effect," *J. Phys. D. Appl. Phys.*, vol. **31**, no. 6, pp. 704–711, 1998.
[128] C. S. Kalra, Y. I. Cho, A. Gutsol, A. Fridman, and T. S. Rufael, "Gliding arc in tornado using a reverse vortex flow," *Rev. Sci. Instrum.*, vol. **76**, no. 2, p. 025110, 2005.
[129] R. Snoeckx, R. Aerts, X. Tu, and A. Bogaerts, "Plasma-based dry reforming: A computational study ranging from the nanoseconds to seconds time scale," *J. Phys. Chem. C*, vol. **117**, no. 10, pp. 4957–4970, 2013.
[130] W. Wang, A. Berthelot, S. Kolev, X. Tu, and A. Bogaerts, "CO_2 conversion in a gliding arc plasma: 1D cylindrical discharge model," *Plasma Sources Sci. Technol.*, vol. **25**, no. 6, p. 065012, 2016.
[131] S. R. Sun, H. X. Wang, D. H. Mei, X. Tu, and A. Bogaerts, "CO_2 conversion in a gliding arc plasma: Performance improvement based on chemical reaction modeling," *J. CO_2 Util.*, vol. **17**, pp. 220–234, 2017.
[132] A. Berthelot, A.; Bogaerts, "Modeling of plasma-based CO_2 conversion: lumping of the vibrational levels," *Plasma Sources Sci. Technol.*, vol. **25**, 2016.
[133] M. F. Zhukov and I. M. Zasypkin, *Thermal plasma torches - Design, Characteristics, Applications*. Cambridge: Cambridge International Science, 2006.
[134] M. Ramakers, J. A. Medrano, G. Trenchev, F. Gallucci, and A. Bogaerts, "Revealing the arc dynamics in a gliding arc plasmatron: A better insight to improve CO_2 conversion," *Plasma Sources Sci. Technol.*, vol. **26**, no. 12, 2017.
[135] T. P. Nunnally, "Application of Low Current Gliding Arc Plasma Discharges for Hydrogen Sulfide Decomposition and Carbon Dioxide Emission Reduction, PhD Dissertation, Drexel University," Drexel University, 2011.
[136] S. Pradeep, "Design and preliminary characterization of the magnetically stabilized gliding arc discharge," Drexel University, 2007.
[137] A. Berthelot and A. Bogaerts, "Modeling of CO_2 Splitting in a Microwave Plasma: How to Improve the Conversion and Energy Efficiency," *J. Phys. Chem. C*, vol. **121**, no. 15, pp. 8236–8251, 2017.
[138] R. Pothiraja, N. Bibinov, and P. Awakowicz, "Pulsed corona plasma source characterization for film deposition on the inner surface of tubes," *J. Phys. D. Appl. Phys.*, vol. **43**, no. 49, p. 496201, 2010.
[139] G. M. Elaragi and H. S. Elaraby, "Characterization of an Atmospheric-pressure Cold Plasma Jet," *IJEAS*, vol. **2**, no. 9, pp. 67–70, 2015.
[140] J. Schäfer, F. Sigeneger, R. Foest, D. Loffhagen, and K. D. Weltmann, "On plasma parameters of a self-organized plasma jet at atmospheric pressure," *Eur.*

Phys. J. D, vol. **60**, no. 3, pp. 531–538, 2010.
[141] N. Bibinov, D. Dudek, P. Awakowicz, and J. Engemann, "Characterization of an atmospheric pressure dc plasma jet," *J. Phys. D. Appl. Phys.*, vol. **40**, no. 23, pp. 7372–7378, 2007.
[142] A. Yu, "Non-equilibrium constricted dc glow discharge in N2 flow at atmospheric pressure: stable and unstable regimes," *J. Phys. D Appl. Phys. 4*, vol. **43**, p. 075202, 2010.
[143] A. Bogaerts and E. C. Neyts, "Plasma Technology: An Emerging Technology for Energy Storage," *ACS Energy Lett.*, vol. **3**, no. 4, pp. 1013–1027, 2018.
[144] A. Berthelot and A. Bogaerts, "Modeling of plasma-based CO_2 conversion: Lumping of the vibrational levels," *Plasma Sources Sci. Technol.*, vol. **25**, no. 4, p. 045022, 2016.
[145] D. Staack, B. Farouk, A. F. Gutsol, and A. A. Fridman, "Spectroscopic studies and rotational and vibrational temperature measurements of atmospheric pressure normal glow plasma discharges in air," *Plasma Sources Sci. Technol.*, vol. **15**, no. 4, pp. 818–827, 2006.
[146] Y. Akishev, M. Grushin, V. Karalnik, A. Petryakov, and N. Trushkin, "On basic processes sustaining constricted glow discharge in longitudinal N_2 flow at atmospheric pressure," *J. Phys. D. Appl. Phys.*, vol. **43**, no. 21, p. 215202, 2010.
[147] N. Hasan, D. S. Antao, and B. Farouk, "DC negative corona discharge in atmospheric pressure helium: Transition from the corona to the 'normal' glow regime," *Plasma Sources Sci. Technol.*, vol. **23**, no. 3, p. 035013, 2014.
[148] D. Staack, B. Farouk, A. Gutsol, and A. Fridman, "Characterization of a dc atmospheric pressure normal glow discharge," *Plasma Sources Sci. Technol.*, vol. **14**, no. 4, pp. 700–711, 2005.
[149] D. Dudek, N. Bibinov, J. Engemann, and P. Awakowicz, "Direct current plasma jet needle source," *J. Phys. D. Appl. Phys.*, vol. **40**, no. 23, pp. 7367–7371, 2007.
[150] C. O. Laux, T. G. Spence, C. H. Kruger, and R. N. Zare, "Optical diagnostics of atmospheric pressure air plasmas," *Plasma Sources Sci. Technol.*, vol. **12**, no. 2, pp. 125–138, 2003.
[151] M. Ramakers, G. Trenchev, S. Heijkers, W. Wang, and A. Bogaerts, "Gliding Arc Plasmatron: Providing an Alternative Method for Carbon Dioxide Conversion," *ChemSusChem*, vol. **10**, no. 12, pp. 2642–2652, 2017.
[152] J. Cheng, L. Du, and W. Xiang, "Incompressible Jet Flows in a de Laval Nozzle with Smooth Detachment," *Arch. Ration. Mech. Anal.*, vol. **232**, no. 2, pp. 1031–1072, 2019.
[153] J. R. Roth, *Industrial Plasma Engineering*. London UK: CRC Press, 2004.
[154] P. Scherz, *Practical Electronics for Inventors*. McGraw-Hill, 2000.
[155] N. Dye and H. Granberg, *Radio Frequency Transistors*. Newnes, USA, 2016.
[156] J. Zhu *et al.*, "Sustained diffusive alternating current gliding arc discharge in atmospheric pressure air," *Appl. Phys. Lett.*, vol. **105**, no. 23, p. 234102, 2014.
[157] LTWiki, "LTspice Genealogy - The Heritage of Simulation Ubiquity," 2018. [Online]. Available: http://ltwiki.org/index.php?title=LTspice_Genealogy_-_The_Heritage_of_Simulation_Ubiquity.
[158] M. Lasure, "Turbulence improvement of a reverse vortex flow gliding arc reactor for CO_2 conversion," University of Antwerp, 2019.

[159] N. A. Dyatko *et al.*, "Experimental and theoretical study of the transition between diffuse and contracted forms of the glow discharge in argon," *J. Phys. D. Appl. Phys.*, vol. **41**, no. 5, p. 055204, 2008.
[160] K. Bartschat and V. Zeman, " Electron-impact excitation from the (3p54s) metastable states of argon ," *Phys. Rev. A*, vol. **59**, no. 4, pp. R2552–R2554, 1999.
[161] H. A. Hyman, "Electron-impact ionization cross sections for excited states of the rare gases (Ne, Ar, Kr, Xe), cadmium, and mercury," *Phys. Rev. A*, vol. **20**, no. 3, pp. 855–859, 1979.
[162] J. Jonkers, M. Van De Sande, A. Sola, A. Gamero, A. Rodero, and J. Van Der Mullen, "The role of molecular rare gas ions in plasmas operated at atmospheric pressure," *Plasma Sources Sci. Technol.*, vol. **12**, no. 3, pp. 464–474, 2003.
[163] A. J. Cunningham, T. F. O'Malley, and R. M. Hobson, "On the role of vibrational excitation in dissociative recombination," *J. Phys. B At. Mol. Phys.*, vol. **14**, no. 4, pp. 773–782, 1981.
[164] M. K. and M. M. Casta˜nos-Martinez E, Kabouzi Y, "Modeling of microwave-sustained plasmas at atmospheric pressure with application to discharge contraction," *Phys. Rev. E*, vol. **70**, p. 066405, 2004.
[165] F. Kannari, A. Suda, M. Obara, and T. Fujioka, "Theoretical Simulation of Electron-Beam-Excited Xenon-Chloride (XeCI) Lasers," *IEEE J. Quantum Electron.*, vol. **19**, no. 10, pp. 1587–1600, 1983.
[166] A. Bultel, B. van Ootegem, A. Bourdon, and P. Vervisch, "Influence of [formula presented] in an argon collisional-radiative model," *Phys. Rev. E - Stat. Physics, Plasmas, Fluids, Relat. Interdiscip. Top.*, vol. **65**, no. 4, p. 16, 2002.
[167] J. Gregório, P. Leprince, C. Boisse-Laporte, and L. L. Alves, "Self-consistent modelling of atmospheric micro-plasmas produced by a microwave source," *Plasma Sources Sci. Technol.*, vol. **21**, no. 1, p. 015013, 2012.
[168] M A Lieberman and A. Lichtenberg, *Principles of Plasma Discharges and Materials Processing*, 1st ed. Hoboken:NJ: Wiley, 2005.